Study of the transverse mode coupling instability in the CERN Large Hadron Collider

David Amorim

THÈSE

Pour obtenir le grade de

DOCTEUR DE LA COMMUNAUTÉ UNIVERSITÉ GRENOBLE ALPES

Spécialité : **Physique Subatomique et Astroparticules**

Arrêté ministériel : 25 mai 2016

Présentée par

David Amorim

Thèse dirigée par **Jean-Marie De Conto, Université Grenoble-Alpes**, et codirigée par **Nicolò Biancacci, CERN**

préparée au sein de **l'Organisation Européenne pour la Recherche Nucléaire** et du **Laboratoire de Physique Subatomique et de Cosmologie**
dans **l'École Doctorale de Physique de Grenoble**

Étude de l'instabilité de couplage des modes transverses dans le Grand Collisionneur de Hadrons du CERN

Study of the Transverse Mode Coupling Instability in the CERN Large Hadron Collider

Thèse soutenue publiquement le **7 octobre 2019**,
devant le jury composé de :

Monsieur Ryutaro Nagaoka
Ingénieur de Recherche, SOLEIL, Rapporteur
Monsieur Mauro Migliorati
Professeur associé, Université de Rome « La Sapienza », Rapporteur
Monsieur Patrick Puzo
Professeur, Université Paris-Sud, Examinateur
Monsieur Johann Collot
Professeur, Université Grenoble-Alpes, Président
Monsieur Benjamin Trocmé
Directeur de recherche, Laboratoire de Physique Subatomique et de Cosmologie, Examinateur

Communauté UNIVERSITÉ Grenoble Alpes

Thèse
pour obtenir le grade de

Docteur de la communauté Université Grenoble-Alpes

Présentée par

David Amorim

Thèse dirigée par Jean-Marie De Conto, Université-Grenoble Alpes,
et codirigée par Nicolò Biancacci, CERN.

Préparée au sein de
l'Organisation Européenne pour la Recherche Nucléaire
et du
Laboratoire de Physique Subatomique et de Cosmologie

École Doctorale de Physique 47
Spécialité : Physique Subatomique et Astroparticules

Étude de l'instabilité de couplage des modes transverses dans le Grand Collisionneur de Hadrons du CERN

Study of the Transverse Mode Coupling Instability in the CERN LHC

Thèse soutenue publiquement le 7 octobre 2019, devant le jury composé de:

Monsieur Jean-Marie De Conto Professeur des Universités, Université Grenoble-Alpes	Directeur de thèse
Monsieur Nicolò Biancacci Ingénieur de Recherche, CERN	Co-directeur de thèse
Monsieur Mauro Migliorati Professeur associé, Università degli studi di Roma "La Sapienza"	Rapporteur
Monsieur Ryutaro Nagaoka Ingénieur de Recherche, SOLEIL	Rapporteur
Monsieur Johann Collot Professeur des Universités, Université Grenoble-Alpes	Président
Monsieur Patrick Puzo Professeur des Universités, Université Paris-Sud	Examinateur
Monsieur Benjamin Trocmé Directeur de Recherche, Laboratoire de Physique Subatomique et de Cosmologie	Examinateur

Arrêté ministériel du 25 mai 2016

Abstract

The High-Luminosity upgrade of the CERN LHC will increase the performance of the accelerator and the potential physics discoveries. The beam intensity will be multiplied by two to increase the collider luminosity. With such high intensities, collective effects and in particular beam coupling impedance are a possible performance limitation for the accelerator.

After an introduction to accelerator physics and wake-fields, two collective effects codes will be detailed: PyHEADTAIL, a time-domain macro-particle code, and DELPHI, a Vlasov equation solver. Both are important to estimate coherent beam stability margins in the CERN accelerator complex, therefore a detailed comparison for different wakes and impedances, including the LHC model, will be presented.

The current LHC stability limits will then be investigated with DELPHI simulations. In particular the Transverse Mode Coupling Instability, a fast instability occurring for high intensity beams with chromaticities close to zero, will be studied. The results will then be compared to measurements performed in the accelerator. Beam based measurements of several collimators will also be presented and compared to predictions from the impedance model. Combining these measurements and their comparison to simulations, we will estimate the uncertainty on the LHC impedance model.

To cope with the increased beam intensity, the impedance of the High Luminosity upgrade of the LHC will be reduced. The impact of different upgrade scenarios will be studied from the Transverse Mode Coupling Instability perspective. The potential benefits of an impedance reduction will be demonstrated through measurements in the LHC. Measurements performed in the LHC on a low impedance prototype collimator, the key component to the impedance reduction, will also be presented. These simulations and measurements will confirm the increase in the mode coupling threshold towards a value three times higher than the nominal bunch intensity.

Résumé

Le projet de LHC Haute Luminosité sera une amélioration majeure de l'accélérateur visant à accroître ses performances et son potentiel de découvertes. L'intensité du faisceau sera multipliée par deux pour augmenter la luminosité du collisionneur. À de telles intensités, les effets collectifs et en particulier l'impédance de couplage du faisceau sont une limitation possible des performances du LHC.

Après une introduction à la physique des accélérateurs et aux effets des champs électromagnétiques induits, deux codes de simulation des effets cohérents du faisceau seront détaillés : PyHEADTAIL, un code macro-particulaire temporel, et DELPHI, un solveur de l'équation de Vlasov. Ces derniers sont importants pour estimer les marges de stabilité dans les accélérateurs du CERN, c'est pourquoi une comparaison détaillée pour différentes impédances, y compris celle du LHC, sera présentée.

Les limites de stabilité actuelles du LHC seront ensuite étudiées à l'aide de simulations DELPHI. En particulier, l'instabilité de couplage des modes transversaux, une instabilité rapide se produisant dans les faisceaux de haute intensité pour des chromaticités proches de zéro, sera étudiée. Les résultats seront ensuite comparés à des mesures réalisées dans l'accélérateur. Des mesures de plusieurs collimateurs réalisées avec le faisceau seront également présentées et comparées aux prédictions du modèle d'impédance. L'association de ces différentes mesures et leur comparaison avec les simulations nous permettra d'estimer l'incertitude sur le modèle d'impédance du LHC.

Pour faire face à l'augmentation de l'intensité du faisceau, une réduction d'impédance est prévue pour le projet de LHC Haute Luminosité. L'impact de différents scénarios sera étudié du point de vue de l'instabilité de couplage des modes transversaux. L'effet bénéfique d'une réduction d'impédance sera démontré par des mesures sur le LHC. Les mesures effectuées dans le LHC sur un prototype de collimateur d'impédance réduite, un élément clé du projet, seront également présentées. Ces simulations et mesures confirmeront l'augmentation du seuil de couplage des modes à une valeur trois fois supérieure à l'intensité nominale des paquets.

Contents

1 Introduction 1
- 1.1 CERN and the CERN accelerator complex 1
- 1.2 Principles of accelerator physics 6
  - 1.2.1 Equations of transverse motion without momentum offset 6
  - 1.2.2 Equations of transverse motion with momentum offset 15
  - 1.2.3 Smooth approximation in the transverse plane 17
  - 1.2.4 Particle acceleration 17

2 Impedance induced instabilities 23
- 2.1 Notions and examples of beam coupling impedance 23
  - 2.1.1 Wake fields and impedances 23
  - 2.1.2 Resistive wall impedance 27
  - 2.1.3 Broadband resonator impedance 29
  - 2.1.4 The LHC impedance model 29
- 2.2 A simplified approach to beam instabilities: the two-particle model 37
- 2.3 Treatment of coherent beam instabilities 44
  - 2.3.1 Macroparticle formalism for instability simulations 45
  - 2.3.2 Vlasov's formalism for instability simulations 47
  - 2.3.3 Approximate solution of Sacherer's integral equation 53
  - 2.3.4 Post-processing of PyHEADTAIL data 54
- 2.4 Head-Tail instability 56
  - 2.4.1 Mode spectra with inductive impedance 56
  - 2.4.2 Head-tail instability with a resistive wall impedance 59
  - 2.4.3 Head-tail instability with the LHC impedance model 68
- 2.5 Transverse Mode Coupling Instability 76
  - 2.5.1 TMCI with a broadband resonator impedance 76
  - 2.5.2 TMCI with the LHC impedance model 82

3 The Transverse Mode Coupling Instability in the LHC 91
- 3.1 Motivations of the study 91
- 3.2 Simulations of the Transverse Mode Coupling in the LHC 93
  - 3.2.1 Impedance model, beam parameters and assumptions made 93
  - 3.2.2 Simulations results for a corrected chromaticity 94
  - 3.2.3 Results for a positive chromaticity 95
  - 3.2.4 Results for tighter collimator gaps 97

3.3 Assessment of the LHC impedance and stability limits with beam based measurements 100
3.3.1 Measurement of the TMCI threshold in the LHC 100
3.3.2 Measurement of individual collimators impedance at top energy 109
3.3.3 Measurement of the instability growth rate versus chromaticity at injection energy 113
3.3.4 Summary of the impedance related measurements performed in 2016, 2017 and 2018 114

4 The Transverse Mode Coupling Instability in future machines 117
4.1 Simulations of the Transverse Mode Coupling Instability in the High Luminosity LHC 117
4.2 Study of the collimation upgrade impact with beam measurements 123
4.2.1 Measurement of the machine tune shift 123
4.2.2 Measurement with the low impedance collimator prototype 127
4.3 Impedance and beam stability considerations for the High Energy LHC study 131
4.3.1 Impedance model for the HE-LHC 131
4.3.2 Mode coupling instability in the HE-LHC 135

5 Conclusion 137

A Impedance of two collimators with different orientations 139
A.1 Introduction 139
A.2 Simple derivation of the total impedance of the structure 139
A.3 Impedance of the single vertical collimator 141
A.4 Case of two collimators with identical Twiss beta functions 142
A.5 Case of two collimators with different Twiss beta functions 143
A.6 Conclusion 145

B Beam parameters for instability simulations 147
B.1 Parameters for simulations with an inductive impedance model 147
B.2 Parameters for TMCI simulations with the LHC impedance model 147
B.3 Comparison of collimator gaps for the TMCI measurement 148
B.4 Collimator gaps and beam parameters for the HL-LHC TMCI simulations 149
B.5 Collimator gaps and beam parameters for the HE-LHC impedance model and stability simulations at injection energy 150
B.6 Collimator gaps and beam parameters for the HE-LHC impedance model and stability simulations at injection energy 151

C Results of collimators measurements 155
C.1 Results of TCP measurements 155
C.2 Results of TCSG measurements 157

D Effect of beam distribution slicing in PyHEADTAIL simulations 161
D.1 Introduction 161
D.2 Slicing in the PyHEADTAIL code 161
D.3 Effect of slicing on the LHC stability simulations 164

D.4 Conclusion 167
Acronyms 169
Glossary 171

1 Introduction

1.1 CERN and the CERN accelerator complex

The European Organization for Nuclear Research was founded in 1954 by 12 European states. It had the purpose to rebuild the European nuclear physics landscape which had been shattered by the Second World War, and to share the increasing cost of research instruments among its members. The first accelerator, the Synchro-Cyclotron (SC), accelerated its first beam in 1957. A second accelerator, the Proton Synchrotron (PS) was already under construction. In 1959, its first proton beam was accelerated. While the SC was shutdown in 1990, the PS still runs after 60 years of operation and delivers beams to fixed target experiments as well as to the Super Proton Synchrotron (SPS) and the Large Hadron Collider (LHC).

As high energy physics required larger instruments to reach higher energies, a 7 km long accelerator was designed. In 1976, the Super Proton Synchrotron was inaugurated. Five years later, it was converted to a proton-antiproton collider, leading to the discovery of the W an Z bosons. More than forty years after its start, the SPS continues to deliver protons and heavy-ions beams to fixed targets and to the LHC.

As the understanding of the standard model progressed further, the energy reached by colliders became insufficient to explore rare phenomena. In consequence, CERN designed in the 1980s the 27 km long Large Electron Positron (LEP) collider. The LEP helped further investigate the properties of the W and Z bosons discovered beforehand in the SPS.

Meanwhile the first ideas of the Large Hadron Collider (LHC) came to life in the late 1980s. At the beginning of the 2000s, the LEP was dismantled to make room for the LHC. From the beginning the LHC design foresaw the use of cutting-edge technologies: 8 T superconducting magnets to guide the beam along the 27 km ring. The two counter rotating beams are kept separate from one another, requiring twin-aperture magnets and they are accelerated by superconducting radiofrequency cavities. The magnets cold bore are maintained at $\approx$2 K with a flow of super-fluid helium created by large cryogenics plants. Of course the LHC is the last element of the vast complex of CERN accelerators:

1. After the proton source, a linear accelerator, the Linac 2, regroups the protons in bunches and accelerates them up to a kinetic energy of 50 MeV.

2. The Proton Synchrotron Booster accelerates the proton beams from 50 MeV to 1.4 GeV kinetic energy. It is also in the Booster that the proton bunches intensities and transverse sizes are defined.

3. The Proton Synchrotron accelerates the beams from 1.4 GeV to 26 GeV. The PS is also a key accelerator: thanks to its various RF systems, one bunch can be split in multiples bunches, they can be merged or shortened to provide finely tuned beams for the SPS and the LHC.

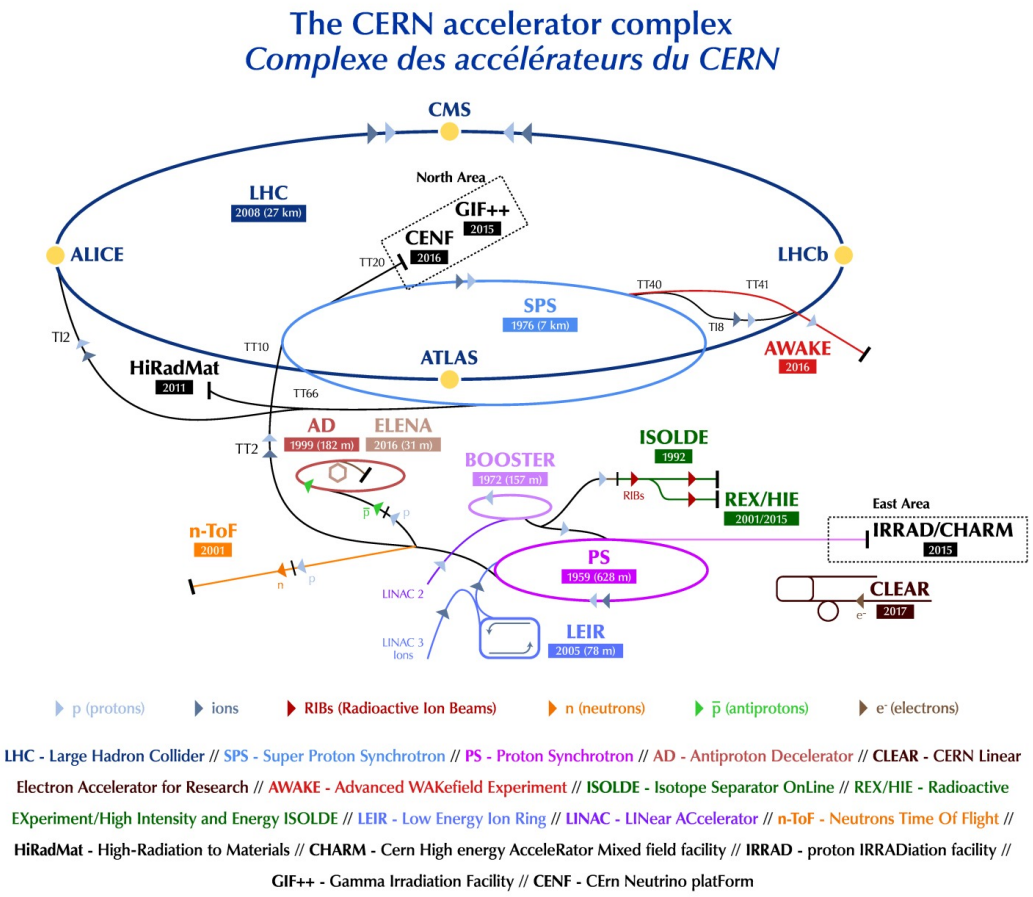

Figure 1.1: The CERN accelerator complex in August 2018 [97]. The circumference and first year of operation of each accelerator are indicated, as well the particle species which can be accelerated.

4. The Super Proton Synchrotron is the last stage before the LHC: the bunches are accelerated from 26 GeV to 450 GeV.

These accelerators also have their own physics program, serving fixed target experiments or antimatter production. Operation with ion beams is also possible and involves additional accelerators, the Linac 3 and the Low Energy Ion Ring (LEIR) at the beginning of the chain. The beams are then accelerated in the PS and SPS before reaching the LHC where they can be collided. Other experiments require antiproton or heavy-ions beams. The full accelerator complex operated at CERN is shown in Fig. 1.1.

The LHC was designed to host 2808 bunches, with 1.15×10^{11} protons per bunch (p.p.b.)[39]. The bunches are injected in the accelerator from the SPS in multiples trains, each containing multiples batches of proton bunches coming from the PS and PSB before it. Figure 1.2 schematizes the injection process of the LHC. Once all the trains have been injected, the two LHC beams are accelerated from 450 GeV to 6.5 TeV, ramping the magnets from 0.5 T to 7.7 T. After reaching their top energy, the two beams are brought into collision in the four experiments, ATLAS, ALICE, CMS and LHCb. The

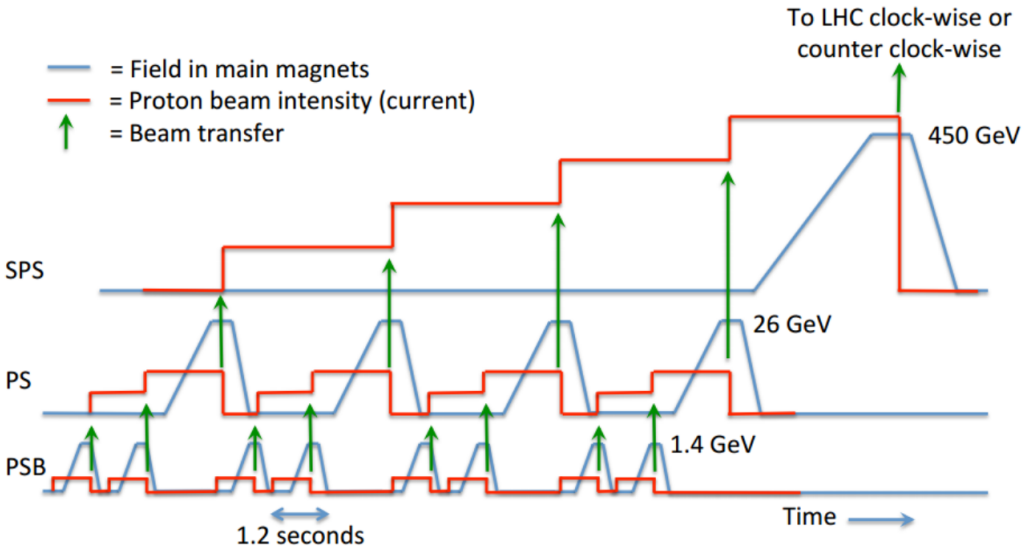

Figure 1.2: The LHC beam injection process. Batches of proton bunches are first accelerated in the PSB and ejected towards the PS. Once the PS contains two of these batches, they are accelerated and transferred to the SPS. This process is repeated until the SPS contains four of these PS trains of bunches. These four trains contain in total 144 bunches which are then accelerated to 450 GeV and injected in one of the two LHC rings. Picture from [55].

beams keep circulating and colliding for ∼12 h for the experiments to acquire data. After this period, if the beam quality is too poor, they are dumped and the magnets fields are ramped down. A new injection can then start. Figure 1.3 summarises the supercycle for particle physics operations.

A figure of merit for a particle collider is the instantaneous luminosity $\mathcal{L}$. It links the number of physics events per second $\frac{\mathrm{d}R}{\mathrm{d}t}$ to the cross-section of this event σ_{event}

$$\frac{\mathrm{d}R}{\mathrm{d}t} = \mathcal{L}\sigma_{event}\,. \tag{1.1}$$

Assuming that the two LHC beams have the same number of bunches M and that each bunch has the same number of protons N_b and the same transverse size, the luminosity can be written

$$\mathcal{L} = \frac{f_0 M N_b^2}{4\pi\sigma_x\sigma_y} F\,, \tag{1.2}$$

where f_0 is the is the beam revolution frequency and σ_x and σ_y are the RMS transverse beam size of the bunches, assuming those have a Gaussian profile. The transverse beam sizes at the collision point are determined by the focusing strength applied to the bunches and by the particle distribution divergence. A reduction factor F is applied because the beams do not collide head-on. Instead they collide with a small crossing angle which reduces the overlap of the two bunches at the interaction point. In turn the number of events which could happen is reduced during the crossing. The LHC design peak luminosity in ATLAS and CMS is 10^{34} cm^{-2} s^{-1}.

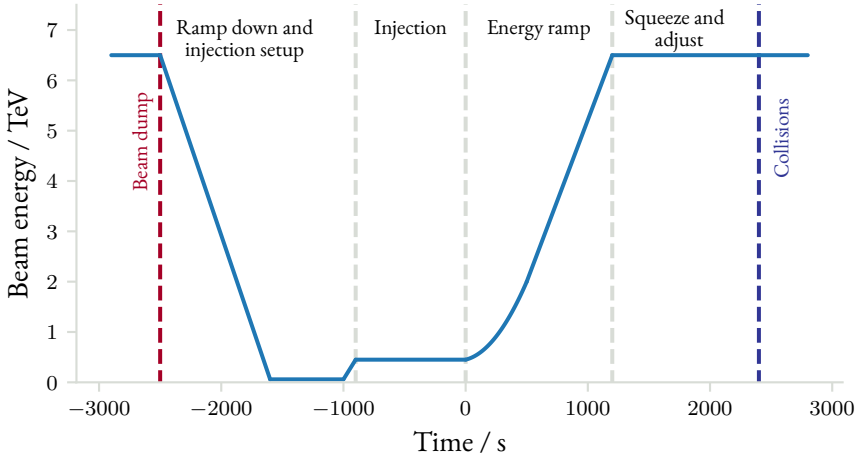

Figure 1.3: The LHC cycle as a function of time. The start of the energy ramp is taken as the time reference. Before this ramp, the machine is configured for injection and then the trains of bunches are injected from the SPS. Once the ramp is finished, the beams are focused to reduce their size at the experiment points and are then adjusted in collision. After ∼12 h of collisions, the beams are dumped and the magnets are ramped down to start a new cycle.

In 2018, despite a number of bunches reduced to 2556 compared to the design value of 2808, the LHC peak luminosity could reach up to 2×10^{34} cm^{-2} s^{-1}. This performance was made possible by the smaller beam sizes at the collision points, as well as the increased bunch intensities, and thus could not have been possible without the great flexibility of the CERN accelerators preparing the beam for the LHC.

An upgrade of the LHC, the High-Luminosity LHC, aims at increasing the peak luminosity as well as the integrated luminosity, i.e the total number of events recorded by the experiments. This will allow to further investigate the properties of the Higgs boson, as well as other rare physics processes. Equation 1.2 shows that to increase the luminosity, different parameters can be improved:

- The number of bunches can be increased: in HL-LHC it will reach 2760 bunches for the standard beam where the bunches are separated by 25 ns [94].

- The bunch intensity can also be increased: in HL-LHC it will be increased to 2.3×10^{11} p.p.b. at injection, more than two times the design value.

- The transverse beam sizes at the interaction points can also be reduced, which will be achieved in HL-LHC by using stronger focusing magnets before the interaction points and by reducing the beam divergence.

- The factor F coming from the crossing angle of the bunches can be optimized. In HL-LHC specific radiofrequency cavities called crab cavities will deflect the beam before the ATLAS and CMS detectors so that the two bunches fully overlap at the center of the experiments.

In HL-LHC the top energy of the beam will also be increased from 6.5 TeV to 7 TeV after an extensive training campaign for the superconducting magnets. Most of the hardware implementation for HL-LHC will occur during the Long Shutdown 3 in 2024 and 2025.

To obtain these smaller and more intense beams, the LHC injector chain must also be upgraded. In the framework of the LHC Injectors Upgrade (LIU), major hardware changes to CERN accelerators will occur during the Long Shutdown 2 in 2019 and 2020:

1. The Linac 2 will be replaced by the Linac 4 which will accelerate H^- ions up to 160 MeV kinetic energy.

2. In the Proton Synchrotron Booster the H^- electrons will be stripped out and the proton beams will be accelerated from 160 MeV to 2 GeV.

3. The Proton Synchrotron will accelerate the beams from 2 GeV to 26 GeV.

4. The SPS injection and top energy remain unchanged but the accelerating RF cavities power will be increased to cope with the more intense beams.

This increase in performance of the LHC poses many challenges in different fields. Among those challenges we can cite:

- Machine protection: each LHC beam has a stored energy of 360 MJ, which will rise to 700 MJ in HL-LHC. Collimators are used to protect the superconducting magnets from proton losses. New materials will be deployed for some of them to increase their robustness against beam losses. The collimation and protection layout close to the ATLAS and CMS interaction points will also be redesigned to withstand the damages caused by high energy collisions debris.

- Beam induced heat-load which affects the surrounding environment of the beam when it circulates in the accelerator. It is caused by synchrotron radiation, impedance as well as electron-cloud, a parasitic avalanche effect generated during the passage of the beam. The cryogenics plants having a limited cooling capacity, heating must be contained within nominal values.

- Coherent beam instabilities: the charged particle bunches interact with their environment, creating electromagnetic wakes after their passage. These wakes can then perturb the following bunches or the bunch itself. As the bunch intensity will increase by a factor of two in HL-LHC, these fields will become stronger. These perturbations have thus to be reduced through hardware changes or machine parameters optimisations.

Coherent beam instabilities are indeed one of the major concern for the LHC and HL-LHC as they can lead to beam quality degradation, beam losses and equipment damage. Their study is therefore of importance to reach and go beyond the luminosity target. We will now introduce elements of accelerator physics useful to understand how an accelerator works. This will be followed by an introduction to the concept of wake fields and impedances needed to study coherent beam instabilities.

1.2 Principles of accelerator physics

We will now derive the equations of motion in the transverse and longitudinal planes for a single particle. Several parameters essential to the study of collective effects such as transverse and synchrotron tune or chromaticity will be introduced. The full details of the derivations can be found in [52, 56, 74, 75, 87, 148, 149]. These references also provide further insight on single particle dynamics in the presence of machine imperfections, a critical aspect of beam dynamics.

1.2.1 Equations of transverse motion without momentum offset

Let us consider a charged particle travelling at a speed $v = \beta c$ along a circular orbit of radius ρ. We also consider an arbitrary position along the orbit as a reference for the curvilinear position s of the particle at an instant t, we then have $s = vt$. This reference for the curvilinear position is also used as the zero for the particle azimuthal angle θ. The reference frame is pictured in Fig. 1.4.

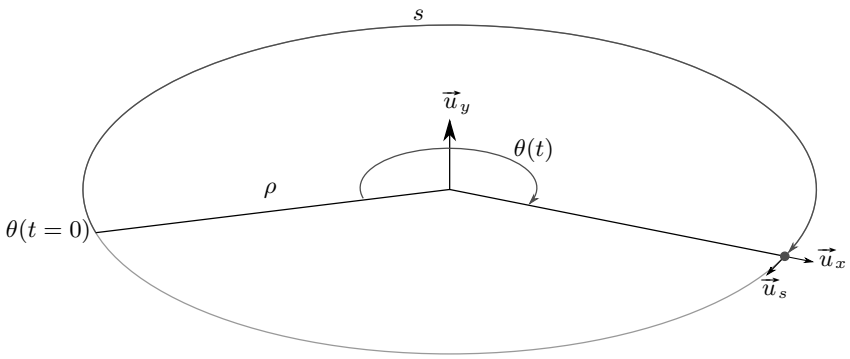

Figure 1.4: Coordinate system used to derive the equation of single particle motion. The gray circle represents the machine circumference on which the reference particle circulates. The coordinate system is defined with respect to this particle.

Let us now consider an other particle which has a position offset from the reference particle. Its coordinates with respect to the reference particle are detailed in Fig. 1.5.

The particle position vector with respect to the accelerator center $\vec{r}$ can be written

$$\vec{r} = (\rho + x)\,\vec{u}_x + y\,\vec{u}_y + z\,\vec{u}_s\,, \tag{1.3}$$

and its momentum $\vec{p}$ is decomposed as $\vec{p} = p_x\,\vec{u}_x + p_y\,\vec{u}_y + p_z\,\vec{u}_s$.

We now assume that the reference particle stays on the design orbit and energy. Its coordinates are $(x = 0, y = 0, z = 0)$ and its momentum is $(p_x = 0, p_y = 0, p_z = p_0)$. Here $p_0 = \gamma m_0 v$ is the particle momentum at the design energy, where $\gamma = \frac{1}{\sqrt{1-\beta^2}}$ and m_0 is the proton rest mass. This particle will be referred to as the synchronous particle.

The position offset of the other particle is assumed to be small compared to the machine radius: $x, y \ll \rho$. The transverse momenta are also small compared to the total momentum: $p_x, p_y \ll p_0$. The particle has a longitudinal offset z. Its total momentum p is assumed to be slightly different from the design one and is written $p = (1 + \delta)p_0$ where $\delta \ll 1$.

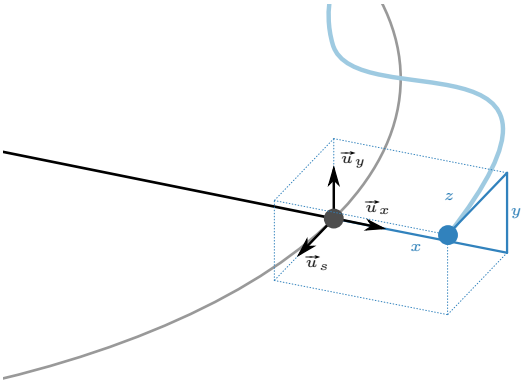

Figure 1.5: Detail of the coordinate system used to derive the equation of single particle motion. The gray circle represents the machine circumference and the the black dot the reference particle. The mobile coordinate system is defined with respect to this particle. A blue dot shows a particle with an offset from the reference particle. It circulates on the blue path called the closed orbit.

The particle state can then be represented by the 6D phase space vector $(x, x', y, y', z, \delta)$ with

$$x' = \frac{\mathrm{d}x}{\mathrm{d}s} = \frac{\mathrm{d}x}{\mathrm{d}t}\frac{\mathrm{d}t}{\mathrm{d}s} = \frac{v_x}{v_z} = \frac{p_x}{p_z} \approx \frac{p_x}{p}\,, \tag{1.4}$$

$$y' = \frac{\mathrm{d}y}{\mathrm{d}s} = \frac{\mathrm{d}y}{\mathrm{d}t}\frac{\mathrm{d}t}{\mathrm{d}s} = \frac{v_y}{v_z} = \frac{p_y}{p_z} \approx \frac{p_y}{p}\,, \tag{1.5}$$

$$\delta = \frac{p - p_0}{p_0}\,. \tag{1.6}$$

We will now concentrate on the transverse motion of the particle. It is assumed that there is no coupling between the longitudinal and transverse plane: the coordinate z with respect to the reference particle will be taken equal to zero, as well as the momentum deviation δ. We then have $\vec{r} = (\rho + x)\,\vec{u}_x + y\,\vec{u}_y = r\,\vec{u}_x + y\,\vec{u}_y$.

For the particle submitted to a magnetic field $\vec{B}$ only we have

$$\frac{\mathrm{d}\vec{p}}{\mathrm{d}t} = \vec{F}_{Lorentz} = q\,\vec{v} \times \vec{B}\,, \tag{1.7}$$

with q the particle charge. We will assume in the following that $q = +e$ where e is the elementary positive charge.

The right hand side term can be written

$$e\,\vec{v} \times \vec{B} = e(-v_z B_y\,\vec{u}_x + v_s B_x\,\vec{u}_y + (v_x B_y - v_y B_x)\,\vec{u}_s)\,, \tag{1.8}$$

assuming that the magnetic field has only transverse components, and can therefore be written as $\vec{B} = B_x\,\vec{u}_x + B_y\,\vec{u}_y$.

For the left hand side we have $\vec{p} = \gamma m_0 \vec{v}$, and assuming that the particle energy does not change, its γ remains constant in time. Then the left hand side of the equation becomes

$$\frac{\mathrm{d}\vec{p}}{\mathrm{d}t} = \gamma m_0 \frac{\mathrm{d}\vec{v}}{\mathrm{d}t} = \gamma m_0 \ddot{\vec{r}}\,, \tag{1.9}$$

where a dot means taking the derivative with respect to time.

The first derivative of $\vec{r}$ can be written

$$\dot{\vec{r}} = \dot{r}\,\vec{u}_x + r\,\dot{\vec{u}}_x + \dot{y}\,\vec{u}_y \tag{1.10}$$

$$= \dot{r}\,\vec{u}_x + r\dot{\theta}\,\vec{u}_s + \dot{y}\,\vec{u}_y \tag{1.11}$$

where $\dot{\theta} = v_s/r$. The second derivative is then

$$\ddot{\vec{r}} = \ddot{r}\,\vec{u}_x + \left(r\ddot{\theta} + 2\dot{r}\dot{\theta}\right)\vec{u}_s + r\dot{\theta}\,\dot{\vec{u}}_s + \ddot{y}\,\vec{u}_y \tag{1.12}$$

$$= \left(\ddot{r} - r\dot{\theta}^2\right)\vec{u}_x + \left(r\ddot{\theta} + 2\dot{r}\dot{\theta}\right)\vec{u}_s + \ddot{y}\,\vec{u}_y\,. \tag{1.13}$$

Combining Eq. 1.8 and 1.13 we obtain for the projection on the $\vec{u}_x$ axis

$$\ddot{r} - r\dot{\theta}^2 = -\frac{e v_s B_y}{\gamma m_0}\,, \tag{1.14}$$

It was assumed that $p_x, p_y \ll p_0$, and since $\vec{p_0} = \vec{p_x} + \vec{p_y} + \vec{p_z}$ we get $p_z \approx p_0$, leading in turn to $\gamma m_0 v_z \approx p_0$. The former equation becomes

$$\frac{\mathrm{d}^2 r}{\mathrm{d}t^2} - r\left(\frac{\mathrm{d}\theta}{\mathrm{d}t}\right)^2 = -\frac{e v_s^2 B_y}{p_0}\,. \tag{1.15}$$

At order zero, we must keep the proton on its design orbit $r = \rho$ which requires to have $\ddot{r} = 0$. Since $x \ll \rho$ we obtain $r = \rho + x \approx \rho$. Equation 1.15 then becomes

$$-\rho\left(\frac{v_s}{\rho}\right)^2 = -\frac{e v_s^2 B_y^0}{p_0}\,, \tag{1.16}$$

which can be written

$$B_y^0 \rho = \frac{p_0}{e}\,, \tag{1.17}$$

where B_y^0 is the constant component of the vertical magnetic field. Equation 1.17 is the basic equation to design a magnet based circular accelerator. It states that to increase the particle energy $E = \sqrt{p_0^2 c^2 + m_0^2 c^4}$, either the magnetic field or the machine radius has to be increased. We assume that the accelerator is planar and thus only the constant vertical magnetic field is used to guide the particles i.e $B_x^0 = 0$. The quantity $B_y^0 \rho$ is often considered as a single value called the magnetic rigidity of the accelerator and it will be noted $(B\rho)$. The constant vertical magnetic field is provided by dipole magnets, thus its name of dipolar field.

Because the accelerator must host other types of magnets such as quadrupoles or sextupoles, the radiofrequency cavities to accelerate the beam, the kicker magnets to inject and extract it as well as the particle detectors, the bending radius ρ is in practice smaller than the accelerator radius itself. We will have an effective bending radius $\rho = \eta_{dipole}\frac{L_{acc}}{2\pi}$ where L_{acc} is the total accelerator length and η_{dipole} is the fraction of it occupied by dipole magnets. Table 1.1 details the magnetic rigidity and the energy reached by various accelerators operated at CERN, as well as for projected ones [20, 27, 142].

Table 1.1: Magnetic parameters for protons beams of various accelerators in operation or projected at CERN. Unless noted, the parameters correspond to the maximum energy reached by the beam in the accelerator.

Accelerator	Mag. field / T	L_{acc} / m	η_{dipole} / %	$(B\rho)$ / T m	p / GeV/c
LHC	7.73[1]	26 658	66	32 818	6500
LHC injection	0.54	26 658	66	2270	450
SPS	2.02	6911	68	2222	450
PS	1.24	628	70	124	26
PSB[2]	1.12	157	33	28	2.8
HL-LHC	8.33	26 658	66	35 342	7000
FCC-hh	16	97 750	67	248 920	50 000

[1] Magnetic field reached in the main dipoles during Run II (2015-2018). During Run I (2009-2012), the field was first limited to 4.2 T for an energy reach of 3.5 TeV per beam. The field was then slightly increased to 4.8 T and the beam energy could reach 4 TeV.

[2] The beam kinetic energy assumed here is 2 GeV/c^2. It will be the energy used for LHC beams extracted to the PS after the LIU upgrade of the machine.

We must now switch from t to s for the independent variable, which leads to

$$\frac{\mathrm{d}}{\mathrm{d}t} = \frac{\mathrm{d}s}{\mathrm{d}t}\frac{\mathrm{d}}{\mathrm{d}s} \tag{1.18}$$

$$\frac{\mathrm{d}^2}{\mathrm{d}t^2} = \frac{\mathrm{d}}{\mathrm{d}t}\left(\frac{\mathrm{d}s}{\mathrm{d}t}\right)\cdot\frac{\mathrm{d}}{\mathrm{d}s} + \frac{\mathrm{d}s}{\mathrm{d}t}\frac{\mathrm{d}}{\mathrm{d}t}\left(\frac{\mathrm{d}}{\mathrm{d}s}\right). \tag{1.19}$$

Using $\mathrm{d}s = \rho\,\mathrm{d}\theta$ and $\mathrm{d}\theta = \frac{v_s}{r}\,\mathrm{d}t$ yields

$$\frac{\mathrm{d}s}{\mathrm{d}t} = \frac{\rho v_s}{r}. \tag{1.20}$$

Equation 1.19 then becomes

$$\frac{\mathrm{d}^2}{\mathrm{d}t^2} = \frac{\mathrm{d}^2 s}{\mathrm{d}t^2}\frac{\mathrm{d}}{\mathrm{d}s} + \left(\frac{\mathrm{d}s}{\mathrm{d}t}\right)^2\frac{\mathrm{d}^2}{\mathrm{d}s^2}, \tag{1.21}$$

and assuming $\frac{\mathrm{d}^2 s}{\mathrm{d}t^2} = 0$ i.e that the particle is neither accelerated nor decelerated we obtain

$$\frac{\mathrm{d}^2}{\mathrm{d}t^2} = \left(\frac{\mathrm{d}s}{\mathrm{d}t}\right)^2 \frac{\mathrm{d}^2}{\mathrm{d}s^2} = \left(\frac{\rho v_s}{r}\right)^2 \frac{\mathrm{d}^2}{\mathrm{d}s^2} \,. \tag{1.22}$$

The equation of motion 1.15 is now written

$$\left(\frac{\rho v_s}{r}\right)^2 \frac{\mathrm{d}^2 r}{\mathrm{d}s^2} - r\left(\frac{v_s}{r}\right)^2 = -\frac{e v_s^2 B_y}{p_0} \,, \tag{1.23}$$

and substituting r by $r = \rho + x$ it can be simplified to

$$\frac{\mathrm{d}^2 x}{\mathrm{d}s^2} - \frac{\rho + x}{\rho^2} = -\frac{e B_y}{p_0}\left(\frac{\rho + x}{\rho}\right)^2 . \tag{1.24}$$

The derivation is similar for the vertical plane motion, and yields

$$\frac{\mathrm{d}^2 y}{\mathrm{d}s^2} = \frac{e B_x}{p_0}\left(\frac{\rho + y}{\rho}\right)^2 . \tag{1.25}$$

These equations of a single particle motion are valid for any kind of magnetic field $\vec{B}$ at a position s along the accelerator: $\vec{B} = B_x(x, y, s)\,\vec{u}_x + B_y(x, y, s)\,\vec{u}_y$. They are generally non-linear. The magnetic field can be expanded in a Taylor series

$$B_x(x, y) = B_x(0, 0) + \sum_{i=0}^{\infty}\sum_{j=0}^{\infty} \frac{x^i y^j}{i!\, j!} \frac{\partial^{i+j} B_x(x, y)}{\partial x^i \partial y^i}\bigg|_{0,0} \,, \tag{1.26}$$

$$B_y(x, y) = B_y(0, 0) + \sum_{i=0}^{\infty}\sum_{j=0}^{\infty} \frac{x^i y^j}{i!\, j!} \frac{\partial^{i+j} B_y(x, y)}{\partial x^i \partial y^i}\bigg|_{0,0} \,. \tag{1.27}$$

It is assumed in these equations that the magnetic elements do not generate a field which depends on the curvilinear position s.

We will now keep only the linear terms in x and y for the magnetic field, as well as for the equations of motion. The field components can then be written

$$B_x = B_x(0, 0) + \frac{\partial B_x(x, y)}{\partial x} x + \frac{\partial B_x(x, y)}{\partial y} y \,, \tag{1.28}$$

$$B_y = B_y(0, 0) + \frac{\partial B_y(x, y)}{\partial x} x + \frac{\partial B_y(x, y)}{\partial y} y \,. \tag{1.29}$$

The terms $\frac{\partial B_y}{\partial y}$ and $\frac{\partial B_x}{\partial x}$ are assumed to be zero. This is to ensure that there is no coupling between the two planes of motion: only magnetic fields along the $\vec{u}_y$ axis will act on the horizontal motion and vice-versa. The $B_y(0,0)$ component is the one entering into the magnetic rigidity formula

$$(B\rho) = B_y^0\rho = B_y(0,0)\rho = \frac{p_0}{e}\,, \tag{1.30}$$

and it is assumed to be independent of the curvilinear position s.

Maxwell-Ampere's law in vacuum states that

$$\overrightarrow{\mathrm{rot}}\vec{B} = \mu_0\vec{j} + \mu_0\varepsilon_0\frac{\partial\vec{E}}{\partial t} \tag{1.31}$$

and in our case no time varying electric field $\vec{E}$ is present, and the current $\vec{j}$ induced by the single particle is negligible compared to the fields induced by the accelerator magnets[1]. Thus we have

$$\overrightarrow{\mathrm{rot}}\vec{B} = \left(\frac{\partial B_y}{\partial x} - \frac{\partial B_x}{\partial y}\right)\vec{u}_s = \vec{0}\,. \tag{1.32}$$

Therefore $\frac{\partial B_y}{\partial x} = \frac{\partial B_x}{\partial y}$ and the fields expressions 1.28 and 1.29 can then be simplified to

$$B_x = \frac{\partial B_y}{\partial x}y\,, \tag{1.33}$$

$$B_y = B_y^0 + \frac{\partial B_y}{\partial x}x\,, \tag{1.34}$$

which are in turn inserted in the equations of motion 1.24 and 1.25, yielding for the horizontal plane one

$$x'' - \frac{x}{\rho^2} - \frac{1}{\rho} = -\frac{e}{p_0}B_y^0\left(1+\frac{x}{\rho}\right)^2 - \frac{e}{p_0}\frac{\partial B_y}{\partial x}x\left(1+\frac{x}{\rho}\right)^2\,, \tag{1.35}$$

Using $(B\rho) = B_y^0\rho = \frac{p_0}{e}$ it can be simplified to

$$x'' - \frac{x}{\rho^2} - \frac{1}{\rho} = -\frac{1}{\rho}\left(1+\frac{x}{\rho}\right)^2 - \frac{1}{(B\rho)}\frac{\partial B_y}{\partial x}x\left(1+\frac{x}{\rho}\right)^2\,. \tag{1.36}$$

We only keep linear terms, thus $\left(1+\frac{x}{\rho}\right)^2 \approx 1 + 2\frac{x}{\rho}$ and the equation becomes

$$x'' = \frac{x}{\rho^2} + \frac{1}{\rho} - \frac{1}{\rho}\left(1+2\frac{x}{\rho}\right) - \frac{1}{B\rho}\frac{\partial B_y}{\partial x}x\left(1+2\frac{x}{\rho}\right) \tag{1.37}$$

$$= -\left(\frac{1}{\rho^2} + \frac{1}{B\rho}\frac{\partial B_y}{\partial x}\right)x\,, \tag{1.38}$$

[1] This assumption is made for the derivation of the single particle motion. We will see that electromagnetic fields are generated by the beam current when considering a collection of particles. These fields can then perturb the beam motion

where the term in x^2 has been neglected to obtain the second line.

A similar derivation for the vertical plane equation 1.25 completes the set of two equations:

$$x'' + \left(\frac{1}{\rho^2} + \frac{1}{(B\rho)}\frac{\partial B_y}{\partial x}\right)x = 0\,, \tag{1.39}$$

$$y'' - \frac{1}{(B\rho)}\frac{\partial B_y}{\partial x}y = 0\,. \tag{1.40}$$

Equations 1.39 and 1.40 are called Hill's equations and are similar to those of an harmonic oscillator. The difference with respect to the harmonic oscillator is that the spring constant depends on the curvilinear position s along the ring. These spring constants will be noted as K_x for the horizontal plane and K_y for the vertical plane

$$K_x(s) = \frac{1}{\rho^2} + \frac{1}{(B\rho)}\frac{\partial B_y}{\partial x}\,, \tag{1.41}$$

$$K_y(s) = -\frac{1}{(B\rho)}\frac{\partial B_y}{\partial x}\,. \tag{1.42}$$

For the horizontal plane, two terms enter the spring constant: the $\frac{1}{\rho^2}$ term is a weak focusing coming from the beam bending alone. The other term

$$\frac{1}{(B\rho)}\frac{\partial B_y}{\partial x}\,, \tag{1.43}$$

is stronger than the first one especially in large accelerators. These two components are usually created by different kind of magnets: dipole magnets to bend the trajectory of the beam, quadrupole magnets to focus it. When writing the expressions of the magnetic fields in Eq. 1.28 and 1.29, coupling and non linear terms were neglected. In a real machine such fields can be created by magnet misalignments, manufacturing imperfections or roll angles among others. Higher order magnets such as sextupoles, octupoles or decapoles and skewed magnets are thus needed to compensate these errors.

In our case the spring constant K is also periodic which means that a distance L exists such that

$$K(s+L) = K(s) \tag{1.44}$$

The distance L can be the circumference of the accelerator or a fraction of it. Studied by George Hill in the 19$^{\text{th}}$ century, the solutions for this class of differential equations resemble the ones of a harmonic oscillator [65]. The results for the horizontal plane and the vertical plane are similar. The solution for the equation of motion in the horizontal plane can be written as

$$x(s) = \sqrt{\beta_x(s)J_x}\cos(\mu_x(s) + \mu_{x,0})\,, \tag{1.45}$$

$$x'(s) = -\sqrt{\frac{J_x}{\beta_x(s)}}(\alpha_x(s)\cos(\mu_x(s) + \mu_{x,0}) + \sin(\mu_x(s) + \mu_{x,0}))\,, \tag{1.46}$$

where J_x and $\mu_{x,0}$ are integration constants determined by the initial conditions, $\alpha_x(s) = -\frac{1}{2}\beta'_x(s)$ and where $\beta_x(s)$ is a periodic function determined by the magnetic elements assembly. The function $\mu_x(s)$ is the phase advance from the $s = 0$ position to s and is equal to

$$\mu_x(s) = \int_0^s \frac{1}{\beta_x(s)} \mathrm{d}s \,. \tag{1.47}$$

The transverse tune Q_{x0} is defined as the number of oscillations per turn and derived from the phase advance

$$Q_{x0} = \frac{1}{2\pi} \oint \frac{1}{\beta_x(s)} \mathrm{d}s \,. \tag{1.48}$$

From Eq. 1.45 we get $\cos(\mu(s) + \mu_{x,0}) = \frac{x(s)}{\sqrt{\beta_x(s) J_x}}$ which, when inserted in Eq. 1.46 provides

$$J_x = \gamma_x(s) x(s)^2 + 2\alpha_x(s) x(s) x'(s) + \beta_x(s) x'(s)^2 \,, \tag{1.49}$$

where $\gamma_x(s) = \frac{1+\alpha_x(s)^2}{\beta_x(s)}$. This equation is a parametric representation of an ellipse in the (x, x') phase-space. The action J_x is the Courant-Snyder invariant. The three parameters α_x, β_x and γ_x are called the Twiss parameters and they define the ellipse shape and orientation. They are a function of the curvilinear position s and derive from the magnetic elements configuration. At different locations along the accelerator, the ellipse will differ in shape and orientation but its area will remain the same. This area will be noted as A and it results that

$$A = \pi J_x \,. \tag{1.50}$$

Figure 1.6 represents the phase space ellipse at one location of the accelerator and its remarkable points. The particle ellipse Eq. 1.49 can also be written in a matrix form

$$X = \begin{pmatrix} x \\ x' \end{pmatrix} \tag{1.51}$$

$$\Omega = \begin{pmatrix} \beta_x & -\alpha_x \\ -\alpha_x & \gamma_x \end{pmatrix} , \tag{1.52}$$

$$X^T \mathbf{\Omega} X = J_x \,. \tag{1.53}$$

The $\mathbf{\Omega}$ matrix is called the Twiss matrix.

The derivation was made for a single particle, however a real beam is composed at least of several millions of protons. We can therefore consider a distribution of particles in the (x, x') phase space. The covariance matrix Σ of such a distribution is written

$$\mathbf{\Sigma} = \begin{pmatrix} \langle x^2 \rangle & \langle x x' \rangle \\ \langle x x' \rangle & \langle x'^2 \rangle \end{pmatrix} . \tag{1.54}$$

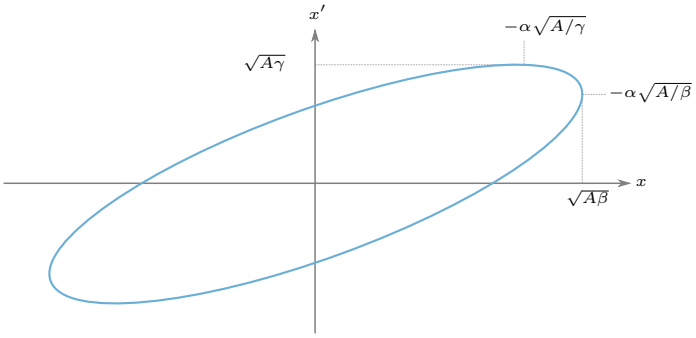

Figure 1.6: Ellipse in the (x, x') phase space described by a particle at a certain location in the accelerator.

The geometric emittance is defined as the square root of the covariance matrix determinant

$$\varepsilon_{geom} = \sqrt{\det \mathbf{\Sigma}} = \sqrt{\langle x^2 \rangle \langle x'^2 \rangle - \left(\langle x x' \rangle\right)^2} \,. \tag{1.55}$$

The covariance matrix $\mathbf{\Sigma}$ can also be expressed in terms of the Twiss matrix $\mathbf{\Omega}$ as

$$\mathbf{\Sigma} = \varepsilon_{geom} \mathbf{\Omega} \,. \tag{1.56}$$

A Gaussian beam distribution in x and x' is often encountered in lepton machines when the beam has reached an equilibrium state. It is also a good approximation for the LHC hadron beams at high energy [68, 109]. For these beams, an other definition of the beam emittance can be used: ε_F is defined as the area in the (x, x') phase space which contains a certain fraction F of all the particles. For a bi-Gaussian beam, the emittance is [56]

$$\varepsilon_F = -\frac{2\pi\sigma_x}{\beta_x} \ln(1 - F) \,. \tag{1.57}$$

where ln is the natural logarithm and σ_x is the standard deviation of the particle distribution. If the fraction $F = 15\,\%$, then the Gaussian beam emittance $\varepsilon_{F=0.15}$ equals the general definition of the emittance ε_{geom} from Eq. 1.55.

It can be shown that the betatron oscillations amplitude reduces when the particle energy increases [56, p.84]. Thus the emittance defined previously in Eq. 1.55 is not an invariant of motion if the beams are accelerated. The normalised emittance ε_n can be used instead

$$\varepsilon_n = \beta\gamma\varepsilon \,. \tag{1.58}$$

The normalised transverse emittance is the one which is preserved throughout the LHC acceleration chain and we will refer to this definition.

We now have the equation of motion for the ideal synchronous particle and its solution. We also defined a quantity to characterize an ensemble of particles and found an invariant of motion. We can now investigate the behavior of a particle with a small offset from the synchronous particle parameters.

1.2.2 Equations of transverse motion with momentum offset

We derived fundamental tools to study the unperturbed particle motion when the two transverse planes are uncoupled. The study was assuming that the longitudinal momentum of the particle was equal to the one of the reference particle. We will now highlight the effect a small momentum offset can have on the horizontal motion of the particle.

For this we start from Eq. 1.36, the equation of motion which included the linear terms of the magnetic field. In this case the particle had an momentum p equal to the reference particle momentum p_0. We now assume that its momentum is slightly different from the reference particle $p = p_0(1+\delta)$ with $\delta \ll 1$. Equation 1.36 is now written as

$$x'' - \frac{x}{\rho^2} - \frac{1}{\rho} = -\frac{e}{p_0(1+\delta)} B_y^0 \left(1 + \frac{x}{\rho}\right)^2 - \frac{e}{p_0(1+\delta)} \frac{\partial B_y}{\partial x} x \left(1 + \frac{x}{\rho}\right)^2 . \tag{1.59}$$

The term $\frac{e}{p_0}\frac{1}{1+\delta}$ can be approximated as

$$\frac{e}{p_0(1+\delta)} \approx \frac{e}{p_0}(1-\delta)\,, \tag{1.60}$$

and can in turn be expressed as a function of the magnetic rigidity $(B\rho) = \frac{p_0}{e}$ of the reference particle:

$$\frac{e}{p_0(1+\delta)} \approx \frac{1}{(B\rho)} - \frac{1}{(B\rho)}\delta\,. \tag{1.61}$$

Equation 1.59 then becomes

$$\begin{aligned} x'' - \frac{x}{\rho^2} - \frac{1}{\rho} = &- \frac{1}{(B\rho)} B_y^0 \left(1 + \frac{x}{\rho}\right)^2 - \frac{1}{(B\rho)} \frac{\partial B_y}{\partial x} x \left(1 + \frac{x}{\rho}\right)^2 \\ &+ \delta \frac{1}{(B\rho)} B_y^0 \left(1 + \frac{x}{\rho}\right)^2 + \delta \frac{1}{(B\rho)} \frac{\partial B_y}{\partial x} x \left(1 + \frac{x}{\rho}\right)^2 . \end{aligned} \tag{1.62}$$

This equation is similar to Eq. 1.36 except for the last two terms given by the momentum offset δ. The second or higher order terms are neglected, as well as the terms in $x\delta$ for now, leading to

$$x'' + \left(\frac{1}{\rho^2} + \frac{1}{(B\rho)} \frac{\partial B_y}{\partial x}\right) x = \frac{1}{\rho}\delta\,, \tag{1.63}$$

which is in turn similar to Eq. 1.38 and can also be written

$$x'' + K_x(s)x = \frac{1}{\rho}\delta\,. \tag{1.64}$$

This equation is the inhomogeneous Hill's equation. Its solutions are the sum of the deviation from the closed orbit caused by betatron oscillation $x_\beta(s)$ and the deviation caused by the momentum offset $x_D(s)$

$$x(s) = x_\beta(s) + x_D(s)\,. \tag{1.65}$$

The term $x_\beta(s)$ is the solution of the homogeneous Hill's equation derived previously. We write $x_D(s) = D(s)\delta$ where $D(s)$ is called the dispersion function which is the solution of equation

$$D'' + K_x(s)D(s) = \frac{1}{\rho}\,. \tag{1.66}$$

If the mean value of the machine dispersion is positive, a particle with a positive momentum offset will have a larger bending radius than the reference particle and will therefore travel a longer distance along the machine. The difference between the path length $C = C_0 + \Delta C$ of an off-momentum particle and the one of the reference particle is characterised by the momentum compaction factor α_p

$$\frac{\Delta C}{C_0} = \alpha_p \delta\,. \tag{1.67}$$

It can be shown that [56]

$$\alpha_p = \frac{1}{C_0}\oint \frac{D(s)}{\rho}\mathrm{d}s \approx \frac{1}{Q_{x0}^2}\,. \tag{1.68}$$

In Eq. 1.64 the terms in δx were neglected. We will now include them in the equation. Since $\frac{1}{\rho^2} \ll \frac{1}{(B\rho)}\frac{\partial B_y}{\partial x}$ we have

$$\frac{2}{\rho^2} + \frac{1}{(B\rho)}\frac{\partial B_y}{\partial x} \approx \left(\frac{1}{\rho^2} + \frac{1}{(B\rho)}\frac{\partial B_y}{\partial x}\right)\delta = K_x(s)\delta\,, \tag{1.69}$$

and Eq. 1.64 can be written

$$x'' + (K_x(s) - \delta K_x(s))x = \frac{1}{\rho}\delta\,, \tag{1.70}$$

This equation shows that a particle with a momentum offset will have a different focusing strength. This difference in focusing strength leads to a change of the betatron tune Q_{x0} by an amount ΔQ_{x0}. The chromaticity ξ characterises the variation of the betatron tune with respect to the particle momentum offset

$$\frac{\Delta Q_{x0}}{Q_{x0}} = \xi\delta\,. \tag{1.71}$$

The particle tune is then written $Q_x = Q_{x0} + \xi Q_{x0}\delta$. The quantity $Q'_x = \xi Q_{x0}$ will also be called chromaticity and we will also use the chromatic angular frequency $\omega_\xi = Q'_x\omega_0$, where ω_0 is the particle angular revolution frequency.

1.2.3 Smooth approximation in the transverse plane

For the study of beam motion perturbed by intensity effects, we will use the smooth approximation: the focusing term in Hill's equation will be considered constant. The average value of the betatron functions $\langle\beta_{x,y}\rangle$ will be used. The wavelength of the particle betatron oscillation is $2\pi\langle\beta_x\rangle$ and the tune Q_{x0} simplifies to

$$Q_{x0} = \frac{1}{2\pi\langle\beta_x\rangle}\oint \mathrm{d}s = \frac{C_0}{2\pi\langle\beta_x\rangle} = \frac{R_0}{\langle\beta_x\rangle}\,. \tag{1.72}$$

We derived fundamental concepts of transverse linear motion in a particle accelerator. Notions such as the Twiss functions, dispersion and chromaticity were introduced. We must now complete the picture with the motion in the longitudinal plane before introducing the concepts of impedance and collective effects.

1.2.4 Particle acceleration

The Lorentz force acting on the particle shows that the magnetic field components result in a deflecting force perpendicular to the particle velocity. The acceleration of the proton beam can therefore only be performed with electric fields. The Lorentz force acting on a particle submitted to a field $\vec{\mathcal{E}}$ is written

$$\vec{F}_{Lorentz} = e\vec{\mathcal{E}}\,. \tag{1.73}$$

The electric field can be electrostatic or time varying. In high energy accelerators, the field is time varying and is created by a set of radiofrequency (RF) cavities through which the particle passes every turn. To accelerate the particles, the electric field must be in the $\vec{u}_s$ direction: $\vec{F}_{Lorentz} = e\mathcal{E}_s\vec{u}_s$. The time varying electric field $\mathcal{E}_s$ felt by a particle travelling in a cavity of length g can be written

$$\mathcal{E}_s = \mathcal{E}_0\sin(\phi_{RF}(t)+\phi_0) = \mathcal{E}_0\sin(h\omega_0 t+\phi_0)\,, \tag{1.74}$$

where $\mathcal{E}_0$ is the electric field amplitude, $\phi_{RF}(t)$ is the phase of the field in the cavity and ϕ_0 is the phase angle of the synchronous particle with respect to the RF wave and ω_0 is the particle angular revolution frequency. In the RF phase $\phi_{RF}(t) = h\omega_0 t$, h an integer called the harmonic number.

The energy ΔE_0 gained by the synchronous particle during its passage in the cavity is

$$\Delta E_0 = e\int_{-g/2}^{+g/2}\mathcal{E}_0\sin(h\omega_0 t+\phi_0)\,\mathrm{d}(\beta c t) \tag{1.75}$$

$$= e\mathcal{E}_0\beta c\int_{-g/2\beta c}^{+g/2\beta c}\sin(h\omega_0 t+\phi_0)\,\mathrm{d}t \tag{1.76}$$

$$= e\mathcal{E}_0 g\frac{\sin(h\omega_0 g/2\beta c)}{(h\omega_0 g/2\beta c)}\sin(\phi_0)\,. \tag{1.77}$$

To go from the first to the second line, it was assumed that the particle velocity increase per turn in the cavity gap is small compared to its longitudinal speed, hence $\mathrm{d}s = \beta c\mathrm{d}t$. Because the particle travels

through the cavity at a finite speed, the electric field it feels is not constant: it will experience an average electric field $V = \mathcal{E}_0 g T$. We call transit time factor T the quantity

$$T = \frac{\sin(h\omega_0 g/2\beta c)}{(h\omega_0 g/2\beta c)} \,. \tag{1.78}$$

The transit time factor can be kept close to one by having a small cavity gap g. At each passage in the cavity, the synchronous particle will gain an energy $\Delta E_0 = eV\sin(\phi_0)$. Its energy change rate is therefore $\dot{E}_0 = \frac{\omega_0}{2\pi} eV\sin(\phi_0)$, assuming no other device or phenomena affect the particle energy during its revolution. A particle with a momentum offset will be non-synchronous. It will have a RF phase ϕ instead of ϕ_0. Its energy gain will be $\Delta E = eV\sin(\phi)$ and its energy change rate $\dot{E} = \frac{\omega_0}{2\pi} eV\sin(\phi)$.

We saw that the momentum compaction factor α_p relates the change of the particle path length to its momentum offset with respect to the reference particle. The slip factor η is an other parameter which links the change of the non-synchronous particle revolution frequency ω to its momentum offset:

$$\frac{\omega - \omega_0}{\omega_0} = -\eta\delta \,. \tag{1.79}$$

The momentum compaction factor and the slip factor are related: taking the logarithm-differentiate of the expression $\omega = 2\pi v/C = 2\pi\beta c/C$ gives

$$\frac{\mathrm{d}\omega}{\omega} = \frac{\mathrm{d}\beta}{\beta} - \frac{\mathrm{d}C}{C_0} \tag{1.80}$$

$$= \frac{1}{\gamma^2}\frac{\mathrm{d}p}{p_0} - \frac{\mathrm{d}C}{C_0} \tag{1.81}$$

$$= \left(\frac{1}{\gamma^2} - \alpha_p\right)\frac{\mathrm{d}p}{p_0} \,, \tag{1.82}$$

where we used $p = \beta m_0 c/\sqrt{1-\beta^2}$ which gives $\frac{\mathrm{d}\beta}{\beta} = \frac{1}{\gamma^2}\frac{\mathrm{d}p}{p}$. The slip factor can then be written

$$\eta = \alpha_p - \frac{1}{\gamma^2} \,. \tag{1.83}$$

A particle with a positive momentum offset will have a higher velocity than the synchronous particle. However its bending radius is also increased and thus it will travel a longer distance compared to the synchronous particle. These two effects compete to either increase or decrease the particle revolution frequency. One can see that the slippage factor η changes sign at a certain energy $\gamma_t = \sqrt{1/\alpha_p}$. Three different situations can be distinguished according to the particle energy γ:

1. If $\gamma < \gamma_t$ then $\eta < 0$. A momentum increase will lead to an increase of the particle revolution frequency.
2. If $\gamma = \gamma_t$ then $\eta = 0$. At first order, a momentum increase or decrease will not change the particle revolution frequency.
3. If $\gamma > \gamma_t$ then $\eta > 0$. A momentum increase will lead to a decrease of the particle revolution frequency.

The last case can seem counter-intuitive: a momentum, and thus a velocity increase leads to a lower revolution frequency. This is because the path length of the particle has been increased by an amount that the particle velocity increase can not compensate. The quantity γ_t is called the transition energy and it is determined by the optics design, in particular by the dispersion function. For a regular lattice design based on alternating focusing and defocusing elements, $\gamma_t \approx Q_{x0}$. The transition crossing, i.e acceleration from $\gamma < \gamma_t$ to $\gamma > \gamma_t$ requires special measures to avoid beam quality deterioration. In the LHC the transition energy is at $\gamma_t \approx 53$ and is therefore never crossed since the injection occurs at $\gamma = 480$. Instead the transition crossing occurs in the PS: the beams are injected at $\gamma = 2.5$, extracted at $\gamma = 27.7$ and the transition occurs at $\gamma \approx 6$. To mitigate instabilities close to this energy, a transition crossing scheme was put in place [89].

Energy-phase equations

We now have all the elements to obtain the equation of motion in the longitudinal plane. We will establish a first relation between the particle energy and the RF phase it experiences inside the RF cavity. Similarly to the derivation done for the transverse motion, we assume that the particle parameters have a small deviation from the synchronous particle parameters which are denoted with a zero subscript

$$\begin{aligned} \theta &= \theta_0 + \Delta\theta\,, \quad R = R_0 + \Delta R\,, \quad E = E_0 + \Delta E\,, \\ p &= p_0 + \Delta p\,, \quad \omega = \omega_0 + \Delta\omega\,, \quad \phi = \phi_0 + \Delta\phi\,, \end{aligned} \tag{1.84}$$

with respectively the azimuthal angle, the closed orbit radius $R = C/2\pi$, the energy, the momentum, the angular revolution frequency and the synchrotron phase. We have $\Delta\theta = -\omega_0\Delta t$ where $\Delta t = t - t_0$ is the time delay between the off-momentum particle and the synchronous particle. Therefore the delayed proton arrives at the center of the RF cavity with a phase delay $\Delta\phi = h\omega_0\Delta t$. Combining these two relations gives

$$\Delta\phi = -h\Delta\theta\,. \tag{1.85}$$

In turn we have

$$\Delta\omega = \frac{\mathrm{d}}{\mathrm{d}t}\Delta\theta = -\frac{1}{h}\frac{\mathrm{d}}{\mathrm{d}t}\Delta\phi = -\frac{1}{h}\frac{\mathrm{d}\phi}{\mathrm{d}t}\,, \tag{1.86}$$

where it is assumed that the synchronous particle phase ϕ_0 varies slowly in time with respect to ϕ. Since $\frac{\Delta\omega}{\omega_0} = -\eta\frac{\Delta p}{p_0}$ we obtain

$$\Delta p = \frac{p_0}{h\eta\omega_0}\frac{\mathrm{d}\phi}{\mathrm{d}t}\,. \tag{1.87}$$

The total particle energy is $E^2 = E_{rest}^2 + (pc)^2$ so $\mathrm{d}E = v\mathrm{d}p$[2]. The energy deviation ΔE is thus $\Delta E = v\Delta p = \omega_0 R_0 \Delta p$. Combining this relation with Eq. 1.87 we obtain the first energy-phase equation:

$$\frac{\Delta E}{\omega_0} = \frac{R_0 p_0}{h\eta\omega_0}\frac{\mathrm{d}\phi}{\mathrm{d}t}\,. \tag{1.88}$$

To obtain the second energy-phase relation, we start from the energy change rate for the synchronous and off-momentum particles:

$$\dot{E} = \frac{\omega}{2\pi}\sin(\phi)\,, \tag{1.89}$$

$$\dot{E}_0 = \frac{\omega_0}{2\pi}\sin(\phi_0)\,, \tag{1.90}$$

which can be simplified to

$$R\frac{\mathrm{d}p}{\mathrm{d}t} = \frac{1}{2\pi}\sin(\phi)\,, \tag{1.91}$$

$$R_0\frac{\mathrm{d}p_0}{\mathrm{d}t} = \frac{1}{2\pi}\sin(\phi_0)\,, \tag{1.92}$$

if we assume that the particle velocity increase per turn is small. These two equations lead to

$$2\pi\left(R\frac{\mathrm{d}p}{\mathrm{d}t} - R_0\frac{\mathrm{d}p_0}{\mathrm{d}t}\right) = eV(\sin(\phi) - \sin(\phi_0))\,. \tag{1.93}$$

The left hand side can be expanded and simplified to the first order

$$R\frac{\mathrm{d}p}{\mathrm{d}t} - R_0\frac{\mathrm{d}p_0}{\mathrm{d}t} = (R_0 + \Delta R)\left(\frac{\mathrm{d}p_0}{\mathrm{d}t} + \frac{\mathrm{d}\Delta p}{\mathrm{d}t}\right) - R_0\frac{\mathrm{d}p_0}{\mathrm{d}t} \tag{1.94}$$

$$\approx R_0\frac{\mathrm{d}\Delta p}{\mathrm{d}t} + \Delta R\frac{\mathrm{d}p_0}{\mathrm{d}t}\,. \tag{1.95}$$

Assuming the parameter offsets are small, we have $\Delta R \approx \frac{\mathrm{d}R_0}{\mathrm{d}p_0}\Delta p$ and then

$$R_0\frac{\mathrm{d}\Delta p}{\mathrm{d}t} + \Delta R\frac{\mathrm{d}p_0}{\mathrm{d}t} = R_0\frac{\mathrm{d}\Delta p}{\mathrm{d}t} + \Delta p\frac{\mathrm{d}R_0}{\mathrm{d}t} = \frac{\mathrm{d}(R_0\Delta p)}{\mathrm{d}t}\,, \tag{1.96}$$

and using $R_0\Delta p = \frac{\Delta E}{\omega_0}$, Eq. 1.93 yields the second energy-phase equation

$$2\pi\frac{\mathrm{d}(\Delta E/\omega_0)}{\mathrm{d}t} = eV(\sin(\phi) - \sin(\phi_0))\,. \tag{1.97}$$

[2] Since $\mathrm{d}(E^2) = 2E\mathrm{d}E$ on one hand and $\mathrm{d}(E^2) = \mathrm{d}(E_{rest}^2) + \mathrm{d}((pc)^2) = 2c^2p\mathrm{d}p = 2c\beta E\mathrm{d}p$ on the other hand, we obtain $2E\mathrm{d}E = 2c\beta E\mathrm{d}p$.

Equation of motion for small amplitude oscillations

Combining Eq. 1.88 and 1.97 finally provides

$$2\pi \frac{\mathrm{d}}{\mathrm{d}t}\left(\frac{R_0 p_0}{h\eta\omega_0}\frac{\mathrm{d}\phi}{\mathrm{d}t}\right) = eV(\sin(\phi) - \sin(\phi_0))\,. \tag{1.98}$$

This is a non linear equation in ϕ. The synchronous particle parameters inside the left hand term are also time dependent. However if ones assumes that those parameters are slowly varying in time, the equation simplifies to

$$2\pi \frac{R_0 p_0}{h\eta\omega_0}\frac{\mathrm{d}^2\phi}{\mathrm{d}t^2} = eV(\sin(\phi) - \sin(\phi_0))\,. \tag{1.99}$$

This equation has analytic solutions if one further assumes that the oscillations have a small amplitude. Since $\phi = \phi_0 + \Delta\phi$, the term $(\sin(\phi) - \sin(\phi_0))$ can be expanded to the first order in $\Delta\phi$

$$\begin{aligned}(\sin(\phi) - \sin(\phi_0)) &= \sin(\phi_0)\cos(\Delta\phi) + \sin(\Delta\phi)\cos(\phi_0) - \sin(\phi_0) &(1.100)\\ &\approx \Delta\phi\cos(\phi_0)\,, &(1.101)\end{aligned}$$

and the equation of motion 1.99 simplifies to

$$\frac{\mathrm{d}^2\Delta\phi}{\mathrm{d}t^2} - \frac{eVh\eta\omega_0\cos(\phi_0)}{2\pi R_0 p_0}\Delta\phi = 0\,, \tag{1.102}$$

where it was assumed that the synchronous particle phase ϕ_0 varies slowly with time so that $\dot{\phi_0} \approx 0$. The motion is stable and the equation corresponds to an harmonic oscillator only if $\eta\cos(\phi_0) < 0$. The angular revolution frequency of the oscillations in the longitudinal plane is called the synchrotron frequency ω_s

$$\omega_s = \sqrt{\frac{eVh\omega_0|\eta\cos(\phi_0)|}{2\pi R_0 p_0}}\,, \tag{1.103}$$

and the synchrotron tune Q_s is defined as

$$Q_s = \frac{\omega_s}{\omega_0} = \sqrt{\frac{eVh|\eta\cos(\phi_0)|}{2\pi v_0 p_0}}\,. \tag{1.104}$$

This equation was derived by assuming that the phase offset of the particle is small and that the synchronous particle parameters vary slowly in time. For a larger energy offset or for quick changes in the longitudinal beam parameters, Eq. 1.99 must be solved numerically. The treatment can of course lead to important differences in the beam physics results. As we now have seen the elements needed to understand single particle motion in an circular accelerator, we can investigate the impact of collective effects on the beam dynamics.

2 Impedance induced instabilities

We will now study in more detail the effect of the electromagnetic fields generated by the beam itself on the particles motion. A first part will detail the concept of beam coupling impedance and showcase simple examples which can be encountered in circular accelerators. The second part will make use of these examples to study two different beam instability regimes: the head-tail instability which is a chromaticity dependent effect and the Transverse Mode Coupling Instability, a stronger instability observed for chromaticities close or equal to zero.

2.1 Notions and examples of beam coupling impedance

2.1.1 Wake fields and impedances

Until now we studied the unperturbed particle motion in the longitudinal and transverse planes. The study focused on a single particle and we assumed that only the external magnetic and electric fields used to guide and bunch the particles were present. However the beam is not composed of a single particle but of several billions of them. It also travels in an environment which is not perfectly conducting, thus the image currents induced on the beam pipe boundaries will generate parasitic electromagnetic fields. These fields will in turn perturb the other particles present in the bunch itself or the following bunches if present. The more particles the bunch contains, the stronger these fields get and thus the stronger are the perturbations. These perturbations can be included in the equations of motion derived previously to study their impact on the beam dynamic.

We will now introduce the concepts of wake fields and impedances which are used to describe these beam induced electromagnetic fields. Detailed explanations of the concept of wake-fields and derivations for different structures can be found in [35, 49, 79, 90, 105, 108, 127, 137].

We saw that for the beam to circulate inside the accelerator, a set of external electromagnetic fields is needed. These fields generate a Lorentz force $\vec{F}_{ext}$ which writes

$$\vec{F}_{ext} = e\left(\vec{E}_{ext} + \vec{v} \times \vec{B}_{ext}\right). \tag{2.1}$$

This relation is valid for a single particle travelling inside the machine, and the equations of motion were previously derived in this framework. However the charged particle beam interacts with its environment, creating images charges and currents in the accelerator components. They generate in turn electromagnetic fields which will act back on the beam. These fields are called wake fields. We then have a force $\vec{F}_{wake}$ acting on the beam

$$\vec{F}_{wake} = e\left(\vec{E}_{wake} + \vec{v} \times \vec{B}_{wake}\right). \tag{2.2}$$

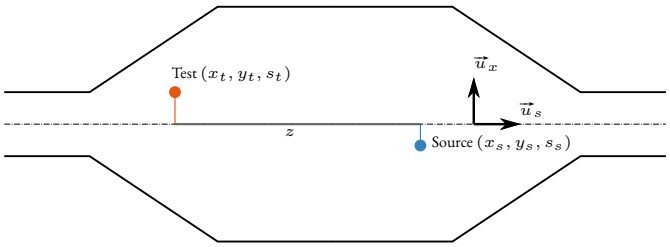

Figure 2.1: Coordinate system used for the source and test particles traveling through an accelerator element.

Let us consider an accelerator equipment through which two charged particles are travelling. Figure 2.1 shows the situation under study: a source particle with charge q_s enters first the structure. We assume that it travels with a speed $\vec{v} = \beta c \vec{u}_s$ parallel to the structure axis. It also has a transverse offset in both horizontal and vertical planes $\vec{r}_s = x_s \vec{u}_x + y_s \vec{u}_y$. During its passage in the structure, the particle will generate electromagnetic fields and lose some of its energy. Now a test particle with charge q_t enters the structure after the source particle. We assume that its velocity and direction are the same as the source particle and its offset with respect to the structure axis is $\vec{r}_t = x_t \vec{u}_x + y_t \vec{u}_y$. In the figure, the positions along the ring of the two particles are denoted s_s and s_t.

We will make a second assumption: we assume that the wake field perturbation is small enough so that it does not affect the motion of the beam during its passage in the structure. In this rigid beam approximation, the distance between the two particles stays constant and is therefore noted z. As we assumed that the two particles travel at the same speed $\vec{v} = \beta c \vec{u}_s$, we can write $s_s = \beta c t$ and $s_t = \beta c t - z$. If $z > 0$, then the test particle is behind the source particle.

The Lorentz force $\vec{F}_{wake}$ created by the source particle and acting on the test particle is thus a function of the two particles offsets $\vec{r}_s$ and $\vec{r}_t$, of their positions s_s and s_t and of time t

$$\begin{aligned} \vec{F}_{wake} &= \vec{F}_{wake}(\vec{r}_s, \vec{r}_t, s_s, s_t) \\ &= q_t \Big(\vec{E}_{wake}(\vec{r}_s, \vec{r}_t, s_s, s_t) + \beta c \vec{u}_s \times \vec{B}_{wake}(\vec{r}_s, \vec{r}_t, s_s, s_t) \Big) . \end{aligned} \tag{2.3}$$

This force will create a momentum change $\Delta \vec{p}_t$ for the test particle which can be written

$$\Delta \vec{p_t}(\vec{r}_s, \vec{r}_t, z) = \int_{-\infty}^{+\infty} \vec{F}_{wake}(\vec{r}_s, \vec{r}_t, s_s = \beta c t, s_t)|_{s_t = s_s - z} \, \mathrm{d}t \, , \tag{2.4}$$

and can be projected on the longitudinal plane $\Delta p_\parallel$ and on the transverse planes $\Delta \vec{p}_\perp$

$$\Delta p_\parallel(\vec{r}_s, \vec{r}_t, z) = q_t \int_{-\infty}^{+\infty} E_{wake,\parallel}(\vec{r}_s, \vec{r}_t, s_s = \beta c t, s_t)\big|_{s_t = s_s - z} \, \mathrm{d}t \, , \tag{2.5}$$

$$\begin{aligned} \Delta \vec{p}_\perp(\vec{r}_s, \vec{r}_t, z) = q_t \int_{-\infty}^{+\infty} & \vec{E}_{wake,\perp}(\vec{r}_s, \vec{r}_t, s_s = \beta c t, s_t) \\ & + \beta c \vec{u}_s \times \vec{B}_{wake,\perp}(\vec{r}_s, \vec{r}_t, s_s = \beta c t, s_t)\Big|_{s_t = s_s - z} \mathrm{d}t \, , \end{aligned} \tag{2.6}$$

The Lorentz force components have been projected on the longitudinal and transverse planes which for the electric field gives $\vec{E}_{wake} = E_{wake,\parallel}\,\vec{u}_s + \vec{E}_{wake,\perp}$, the magnetic field decomposition being similar. The wake functions are defined for the longitudinal and transverse planes as

$$w_\parallel(\vec{r}_s, \vec{r}_t, z) = -\frac{\beta c}{q_s q_t}\Delta p_\parallel(\vec{r}_s, \vec{r}_t, z)\,, \tag{2.7}$$

$$\vec{w}_\perp(\vec{r}_s, \vec{r}_t, z) = -\frac{\beta c}{q_s q_t}\Delta \vec{p}_\perp(\vec{r}_s, \vec{r}_t, z)\,. \tag{2.8}$$

The wake functions $\left(w_\parallel, \vec{w}_\perp\right)$ can be Taylor expanded if the source and test particles offsets are small. For the longitudinal wake $w_\parallel$, the dependence on a transverse offset is neglected and the wake is expanded to zero order, yielding

$$w_\parallel(\vec{r}_s, \vec{r}_t, z) = w_\parallel\left(\vec{0}, \vec{0}, z\right) + O(\vec{r}_s) + O(\vec{r}_t)\,. \tag{2.9}$$

The $w_\parallel\left(\vec{0}, \vec{0}, z\right)$ function will be called the longitudinal wake.

For the transverse wake functions $\vec{w}_\perp = w_{\perp,x}\,\vec{u}_x + w_{\perp,y}\,\vec{u}_y$, the expansion can be made to the first order, yielding for example in the horizontal plane

$$\begin{aligned} w_{\perp,x}(\vec{r}_s, \vec{r}_t, z) \approx & w_{\perp,x}\left(\vec{0}, \vec{0}, z\right) \\ & + \left.\frac{\partial w_{\perp,x}}{\partial x_s}\right|_{\vec{0},\vec{0}} x_s + \left.\frac{\partial w_{\perp,x}}{\partial y_s}\right|_{\vec{0},\vec{0}} y_s \\ & + \left.\frac{\partial w_{\perp,x}}{\partial x_t}\right|_{\vec{0},\vec{0}} x_t + \left.\frac{\partial w_{\perp,x}}{\partial y_t}\right|_{\vec{0},\vec{0}} y_t\,. \end{aligned} \tag{2.10}$$

In this decomposition, the first term is a constant which is equal to zero if the structure is symmetric. If not it will cause a shift of the closed orbit path of the particles as they travel through the device [152]. The second and third terms are the dipolar or driving wake fields. These terms correspond to an offset of the source particle while the test particle remains on axis. For these terms the force experienced by the test particle is independent of its transverse position, like in a dipole magnet. The fourth and fifth terms are the quadrupolar or detuning wake fields. These terms correspond to an offset of the test particle while the source particle remains on axis. In this case the force experienced by the test particle is proportional to its transverse offset, as in a quadrupole magnet. This force would therefore change the particle tune, hence its name of detuning wake.

We will use the notations

$$w_{x,dip} = \left.\frac{\partial w_{\perp,x}}{\partial x_s}\right|_{\vec{0},\vec{0}}, \qquad w_{xy,dip} = \left.\frac{\partial w_{\perp,x}}{\partial y_s}\right|_{\vec{0},\vec{0}}, \tag{2.11}$$

$$w_{x,quad} = \left.\frac{\partial w_{\perp,x}}{\partial x_t}\right|_{\vec{0},\vec{0}}, \qquad w_{xy,quad} = \left.\frac{\partial w_{\perp,x}}{\partial y_t}\right|_{\vec{0},\vec{0}}, \tag{2.12}$$

for the different terms of the Taylor expansion. The cross terms $w_{xy,dip}$ and $w_{xy,quad}$ will be neglected as well since they only become important in asymmetric structures and with large displacements of the source and test particles [152].

By definition, the wake functions are the response of the device to an impulse excitation, thus it is equivalent to a Green function. The wake potential $\vec{W}$ created by a line charge density $\lambda(z)$ travelling inside the structure is therefore the convolution of the distribution with the wake function $\vec{w}(\vec{r}_s, \vec{r}_t, z) = \left(w_{\parallel}, w_{\perp,x}, w_{\perp,y}\right)$

$$\vec{W}(\vec{r}_s, \vec{r}_t, z) = \int_{-\infty}^{+\infty} \vec{w}\left(\vec{r}_s, \vec{r}_t, z - z'\right)\lambda\left(z'\right) \mathrm{d}z' \,. \tag{2.13}$$

For some element geometries, the wake functions can be computed analytically. Exact derivations are often limited to simple geometries such as circular or flat beam pipes. For more complex structures such as cavities or corrugations, approximate models can be found. The wake functions for various elements are derived in detail in [154] and an overview can be found in [105]. For complex devices installed in accelerators, the wake functions can also be obtained with simulations codes such as CST Particle Studio [54]. In this case the source charge can not be a pure impulse: a line charge density is used and the wake function is computed by deconvoluting the simulation results. The simulation set-up must be carefully thought of to obtain accurate results in a reasonable computation time.

The beam coupling impedance is defined as the Fourier transform of the wake fields

$$Z_{\parallel}(\vec{r}_s, \vec{r}_t, \omega) = \frac{1}{\beta c}\int_{-\infty}^{+\infty} w_{\parallel}(\vec{r}_s, \vec{r}_t, z) e^{j\omega z/\beta c} \mathrm{d}z \,, \tag{2.14}$$

$$Z_{\perp,x}(\vec{r}_s, \vec{r}_t, \omega) = -j\frac{1}{\beta c}\int_{-\infty}^{+\infty} w_{\perp,x}(\vec{r}_s, \vec{r}_t, z) e^{j\omega z/\beta c} \mathrm{d}z \,, \tag{2.15}$$

$$Z_{\perp,y}(\vec{r}_s, \vec{r}_t, \omega) = -j\frac{1}{\beta c}\int_{-\infty}^{+\infty} w_{\perp,y}(\vec{r}_s, \vec{r}_t, z) e^{j\omega z/\beta c} \mathrm{d}z \,. \tag{2.16}$$

They are defined for negative and positive frequencies and they follow the relations [49]

$$Z_{\parallel}(-\omega) = Z_{\parallel}^{*}(\omega) \,, \tag{2.17}$$

$$Z_{\perp}(-\omega) = -Z_{\perp}^{*}(\omega) \,, \tag{2.18}$$

where Z^* denotes the complex conjugate of the beam coupling impedance function.

The beam coupling impedance, which will be referred to as impedance, is more adapted to circular machines where the periodicity can help simplify the expressions. Similarly to the wake functions, the impedance can be Taylor expanded and the same notations apply. Again the main terms considered are the longitudinal impedance $Z_{\parallel}$, the transverse dipolar impedances $Z_{x,dip}$ and $Z_{y,dip}$ and the transverse quadrupolar impedances $Z_{x,quad}$ and $Z_{y,quad}$.

The longitudinal wake is in units of V C^{-1}, the transverse dipolar and quadrupolar wakes in V C^{-1} m^{-1}, the longitudinal impedance in Ω and the transverse dipolar and quadrupolar impedances in Ω m^{-1}.

We saw that the wake is a space or time domain quantity. Physically, the larger the wake functions are, the stronger the kicks to the beam will be. If the wake is short-ranged, the particles closer to the

source will be affected. In that case the wake will mainly act on the bunch itself. On the contrary if the wake is long-ranged, then the following bunches will also be affected. A very long ranged wake can have a multi-turn effect: the wake generated during a first passage will affect the bunch after it has performed a full revolution of the machine.

Since the impedance is the Fourier transform of the wake, a short ranges wake will give a broadband impedance spanning over a large frequency range. On the contrary a long ranged wake will give a sharply peaked impedance.

We now have an overview of the wake field and beam coupling impedance concepts. Their impact on the beam dynamics will be further explored in the following parts. Before we will show the wake and impedance functions for two specific cases, the resistive wall and the broadband resonator. We will then focus on the LHC transverse impedance model which will be the basis for beam stability studies.

2.1.2 Resistive wall impedance

An accelerator requires a vacuum chamber to keep the beam circulating. Depending on the materials used, the dimensions and the geometry of the chamber, the main source of wake fields can be caused by this vacuum chamber. Maxwell's equations are used to derive analytically the impedance generated by such element. Details on the derivation are given in [49, 95, 105, 154]. The longitudinal and transverse dipolar resistive wall impedances for a circular pipe can be written [95]

$$Z_{\parallel,RW}(\omega) = (1 + j\,\mathrm{sgn}(\omega))\frac{L}{2\pi b\sigma_c\delta_{skin}}\,, \tag{2.19}$$

$$Z_{\perp,RW}(\omega) = (\mathrm{sgn}(\omega) + j)\mu c\delta_{skin}\frac{L}{2\pi b^3}\,, \tag{2.20}$$

and the longitudinal and transverse wakes are written

$$w_{\parallel}(z) = -\frac{\beta c}{4\pi b}\sqrt{\frac{\mu c}{\pi\sigma_c}}\frac{L}{|z|^{3/2}}\,, \tag{2.21}$$

$$w_{\perp}(z) = -\frac{\beta c}{\pi b^3}\sqrt{\frac{\mu c}{\pi\sigma_c}}\frac{L}{|z|^{1/2}}\,, \tag{2.22}$$

where b is the beam pipe radius and L its length, σ_c is the beam pipe material conductivity and $\mathrm{sgn}(\omega)$ means the sign of the angular frequency ω. $\delta_{skin} = \sqrt{\frac{2}{|\omega|\mu\sigma_c}}$ is the skin depth and μ the magnetic permeability of the beam chamber material. These relations are an exact expression of the chamber impedance only in a certain range of frequencies [95, 104]

$$\begin{gathered}\frac{\chi c}{b} \ll \omega \ll \frac{\chi^{-1/3}c}{b}\,,\\ \chi = \frac{1}{Z_0\sigma_c b}\,,\end{gathered} \tag{2.23}$$

where Z_0 is the free space impedance. For the wake function the previous condition becomes

$$2\pi b\chi^{1/3} \ll z \ll \frac{2\pi b}{\chi}\,. \tag{2.24}$$

Figure 2.2a shows the transverse wake as a function of the distance between the source and test particle. Time is used here as a variable since $t = z/\beta c$. The corresponding impedance as a function of frequency $f = \omega/2\pi$ is plotted in figure 2.2b. The vacuum chamber properties used to obtain these functions are given in Tab. 2.1. Following the conditions given in Eq. 2.23 and 2.24 the resistive wall model will be valid in the 140 Hz to 18.1 THz range, equivalent to a wake ranging between 100 μm and 13×10^6 m. This specific resistive wall impedance model will later be used in the benchmark of two instability codes

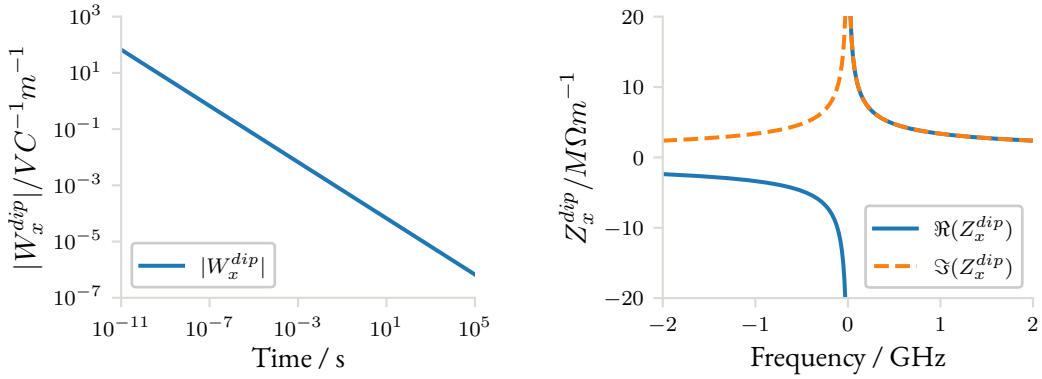

(a) Wakefield

(b) Impedance

Figure 2.2: Left plot represents the resistive wall horizontal dipolar wake function versus time after the source particle, obtained for a cylindrical copper beam pipe. The right plot represents the corresponding beam coupling impedance as a function of frequency.

Table 2.1: Beam chamber parameters used to obtain the resistive wall wake and impedance functions.

Parameter	Value
Geometry	Cylindrical
Radius b	10 mm
Length L	27 km
Material	Copper at 300 K
Conductivity[1] σ_c	58.8 MS m^{-1}

[1] Conductivity obtained from the copper resistivity at 300 K $\rho_c = 17$ nΩ m [121].

2.1.3 Broadband resonator impedance

A second simple wake and impedance model is the broadband resonator. It can be used as a first approximation to account for the various cross-section changes occurring in the vacuum chamber. A broadband impedance means a quickly decayed wake field. The wake will mainly affect the bunch itself and not the following ones, leading to so-called single bunch instabilities. The longitudinal and transverse broadband impedance as a function of angular frequency can be written

$$Z_{\parallel,BB}(\omega) = \frac{R_s}{1 - jQ\left(\frac{\omega_r}{\omega} - \frac{\omega}{\omega_r}\right)}\,, \tag{2.25}$$

$$Z_{\perp,BB}(\omega) = \frac{c}{\omega}\frac{R_s}{1 - jQ\left(\frac{\omega_r}{\omega} - \frac{\omega}{\omega_r}\right)}\,, \tag{2.26}$$

where ω_r is the angular resonance frequency of the resonator, R_s the shunt impedance, Q the quality factor. For the wake function, the formulas for the longitudinal and transverse components are [154]

$$\begin{aligned} W_{\parallel,BB}(z) &= \frac{R_{s,\parallel}\omega_r}{Q}\exp\left(-\frac{\alpha z}{c}\right)\left(\cos\left(\frac{\sqrt{|\omega_r^2 - \alpha^2|}z}{c}\right) - \frac{\alpha}{2Q}\sin\left(\frac{\sqrt{|\omega_r^2 - \alpha^2|}z}{c}\right)\right)\,, \\ W_{\perp,BB}(z) &= \frac{R_{s,\parallel}\omega_r^2}{Q\sqrt{|\omega_r^2 - \alpha^2|}}\exp\left(-\frac{\alpha z}{c}\right)\sin\left(\frac{\sqrt{|\omega_r^2 - \alpha^2|}z}{c}\right)\,, \\ \alpha &= \frac{\omega_r}{2Q}\,. \end{aligned} \tag{2.27}$$

Figure 2.3a shows the wake function as a function of the distance between the source and test particles. The parameters for this wake are $\omega_r = 2\pi \times 2 \times 10^9$ GHz, $R_s = 25\,\mathrm{M\Omega\,m^{-1}}$ and $Q = 1$. The time scale in ns highlights that for the broadband resonator the wake quickly decays. This decay time is comparable to the RMS bunch length of LHC beams: 8.1 cm, equivalent to 0.27 ns. The impedance function is pictured in figure 2.3b. As highlighted before a short range wake implies a large frequency range with an impedance extending up to 10 GHz.

The broadband resonator model presented here will be used to study single bunch effects and in particular study and benchmark two codes in the Transverse Mode Coupling Instability regime. We will now detail the LHC impedance and the elements that compose it. Only the main elements with a strong impact on the machine impedance will be detailed.

2.1.4 The LHC impedance model

The LHC impedance model was developed in 2012 [103] and has been completed and improved over the years. It was also extended to cope with the new or upgraded equipments of the High-Luminosity upgrade of the LHC and now includes a large part of the different elements present in the machine [8]. The contributions are frequency dependent and are also changing according to the accelerator configuration. Figure 2.4 shows the transverse impedance as a function of frequency at the injection energy of 450 GeV and the top energy of 6.5 TeV. The impedance at top energy is larger than at injection energy by a factor of $\sim$10.

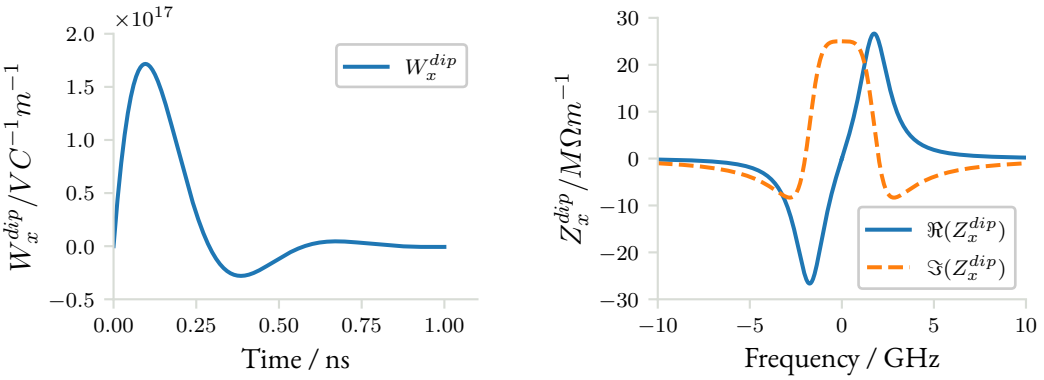

(a) Wakefield

(b) Impedance

Figure 2.3: Left plot represents the horizontal dipolar wake function of a broadband resonator versus time after the source particle. The horizontal axis is in ns, highlighting the quick decay of the wake for these resonator parameters. The right plot represents the corresponding beam coupling impedance as a function of frequency. For frequencies below 1 GHz, the impedance is mainly inductive i.e $\Re\left(Z_x^{dip}\right) \approx 0$ and $\Im\left(Z_x^{dip}\right) \approx$ constant.

The real part and imaginary part of the LHC impedance at top energy are detailed in figures 2.5a and 2.5b. These plots show the impedance functions of the various elements included in the model. They highlight the major contribution of the collimators and the beam screen on a large portion of the frequency range. The models used for these two parts will now be further detailed.

The cold beam screen

The cold beam screens are the tubes shielding the magnets cold bore from synchrotron radiation and beam induced heating from image currents [39]. Figures 2.6b and 2.6a show the assembly of the beam screen in the cold bore and their location in a dipole magnet. The beam screens are stainless steel tubes with a 75 µm copper lamination, cooled between 5 K and 20 K [8]. Thanks to the copper coating and the low operating temperature, the impedance per unit length of the cold beam screens is small. But because they cover 21 km out of the 27 km circumference of the LHC [8], their contribution to the impedance becomes sizeable at injection and top-energy.

Oblong perforations are made on the top and bottom parts of the cold beam screens, as pictured in Fig. 2.6b. They allow reaching equivalent pressures in the 10^{-9} Pa to 10^{-8} Pa range, ensuring a beam lifetime of ∼100 h [39]. They cover 4% of the beam screen surface, and their position and length was semi-randomised to minimise their impact on longitudinal impedance [39]. Their impedance depends on the perforations geometry and the beam pipe radius [70, 99]. Their relative contribution at injection energy is high, in particular for the imaginary part of the impedance. At top energy, the total impedance of the machine increases because of the collimators and therefore the pumping holes have a smaller relative contribution.

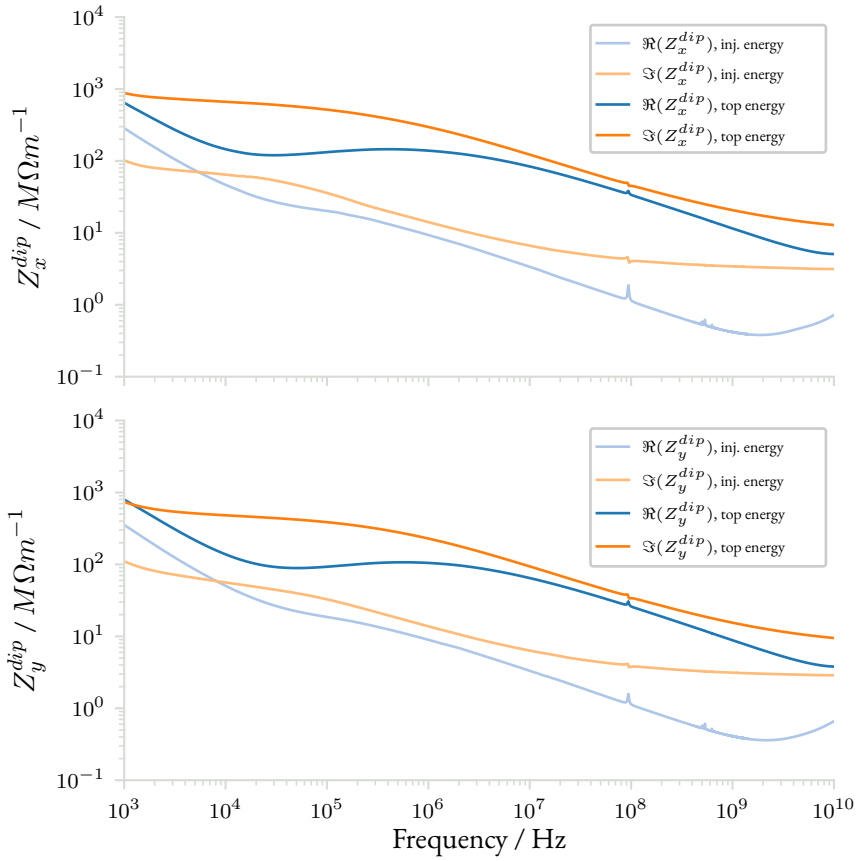

Figure 2.4: Transverse dipolar beam coupling impedance of the LHC as a function of frequency. The top plot shows the horizontal impedance and the bottom plot the vertical impedance. The impedance at injection energy is plotted with light colors and the one at top energy with dark colors.

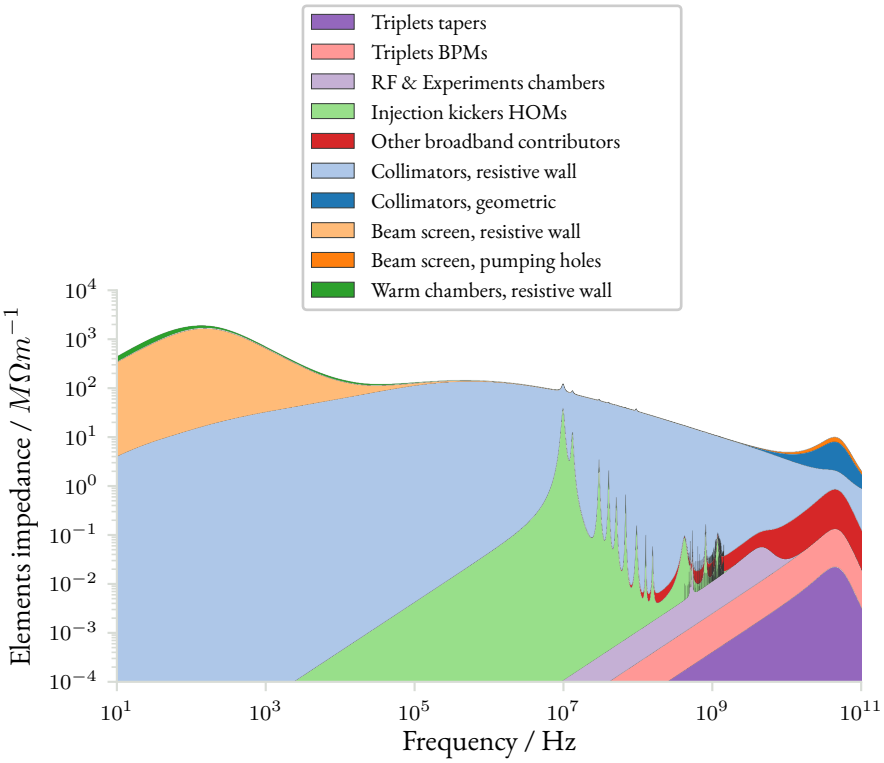

(a) $\Re\left(Z_x^{dip}\right)$ at top energy.

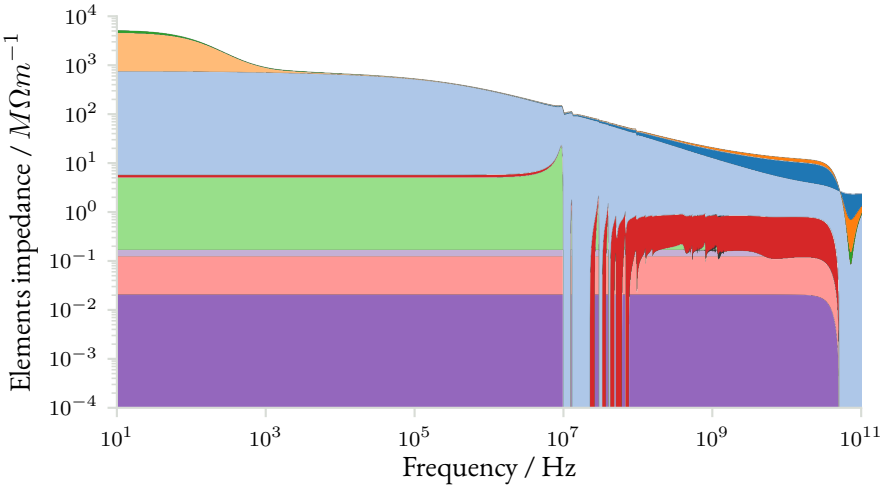

(b) $\Im\left(Z_x^{dip}\right)$ at top energy.

Figure 2.5: Contribution to the horizontal dipolar impedance of the different accelerator elements at top energy versus frequency. The top plot shows the real part of the impedance whereas the bottom plot shows the imaginary part.

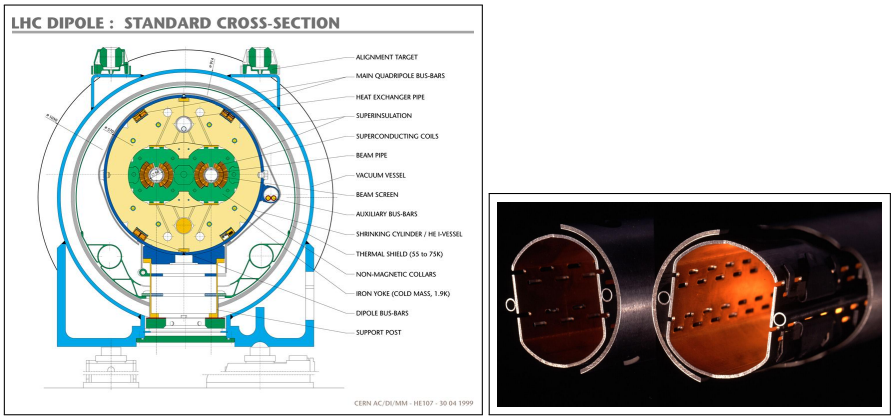

(a) Cross-section of a LHC dipole magnet [53]. (b) Picture of a cut of the LHC beam screen inserted in the cold bore [39, 80].

Figure 2.6: The beam screen (left) is a racetrack shaped tube inserted in the magnet cold bore (right). It is cooled between 5 K and 20 K and serves as a heating shield for the cold bore, cooled to 2 K.

The collimators

In 2018 a single LHC beam had a stored energy of 320 MJ (2556 bunches of 1.2×10^{11} protons at 6.5 TeV). In HL-LHC this energy will reach 710 MJ (2760 bunches of 2.3×10^{11} protons at 7 TeV) [94]. Particles at the fringes of the beam core form a halo that may be lost in the superconducting magnet coils. High loss levels can lead to an unwanted quench, and might damage equipment. The collimators are beam cleaning devices required to mitigate particle losses. Figure 2.7 shows the assembly of a single collimator. The two jaws are positioned close to the beam and must be made of robust materials such as Carbon Fiber-reinforced Carbon (CFC) [39, p. 480].

To improve the cleaning efficiency, 57 of these devices are installed for each of the LHC beam [39, 115]. The system is multi-staged [115]: primary collimators (TCP[1]) will intercept the main halo, secondary collimators (TCSG[2]) located downstream will intercept the secondary halo and the particle showers created by the interaction of high energy particles with the primary collimators. The principle is repeated with tertiary collimators (TCT) and particle showers absorbers (TCL and TCLA[3]). Figure 2.8 schematizes the multistage cleaning principle used in the LHC [1], and Fig. 2.9 shows the location along the two beams of the collimators.

[1] The collimator names follow this convention: T stands for target, the general category for the equipment, C for collimator, the subcategory, P for primary, the type of collimator.
[2] For a TCSG, S stands for secondary and G for Graphite
[3] The L designates auxiliary collimators and the A designates absorbers. TCL collimators are located close to the interaction points and TCLA are located in the betatron and dispersion cleaning regions.

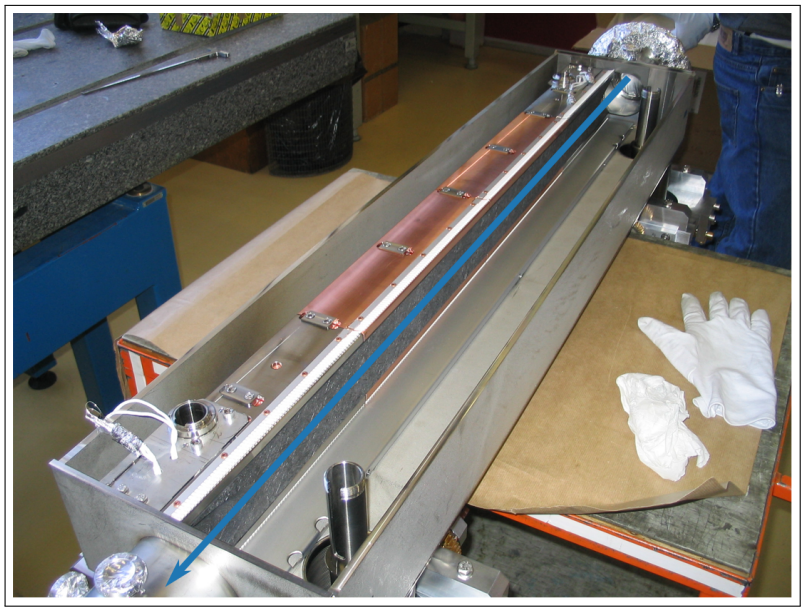

Figure 2.7: Top view of an LHC collimator during assembly. The beam trajectory in the device is represented with the blue arrow. In this picture only the left jaw has been installed. It is made of a CFC block mounted on stainless steel frame. Once the two jaws are assembled, the beam passes in a tight gap and the particles in the transverse beam halo are intercepted by the jaws. Picture from [61].

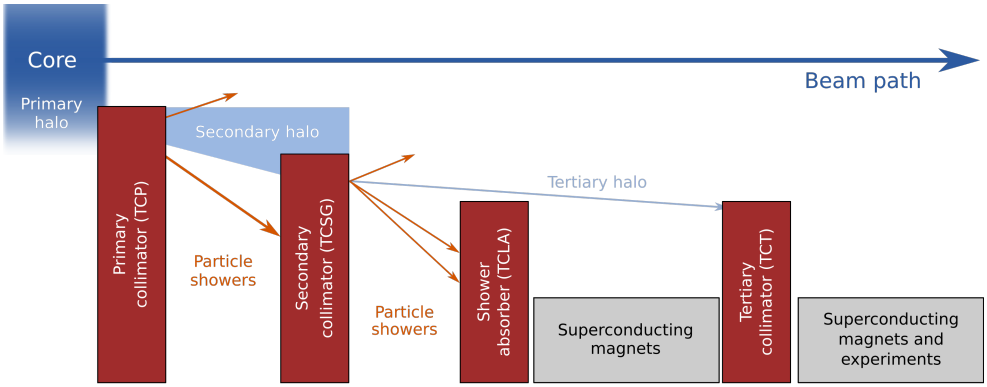

Figure 2.8: Principle of the multi-stage beam cleaning used in the LHC [1, 115].

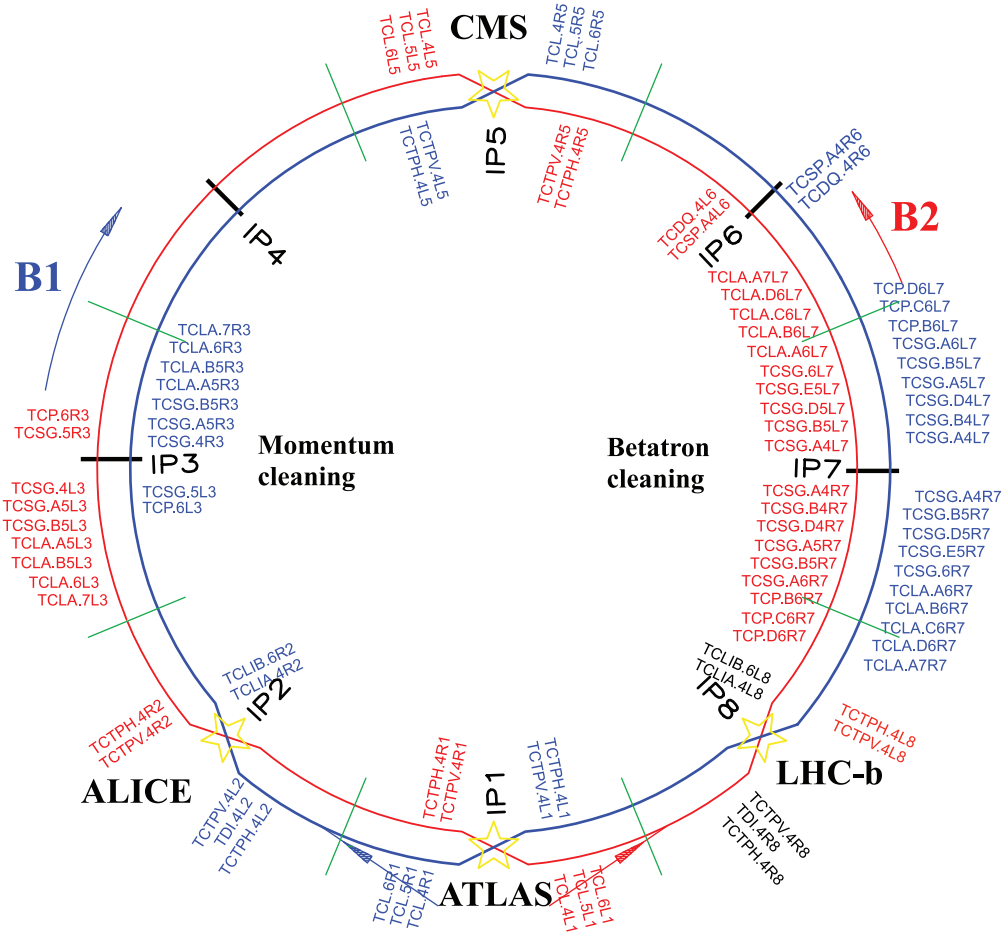

Figure 2.9: Layout and names of the collimators installed in the LHC, for both ring 1 (blue) and ring 2 (red).

The collimators apertures are set to intercept the fringes particles without intercepting the beam core. The physical gap g of each collimator in m is computed from the RMS beam size at the collimator. The beam size σ_i in the plane $i \in (x, y)$ is given by

$$\sigma_i = \sqrt{\beta_i \frac{\varepsilon}{\beta\gamma} + (D_i \delta)^2}\,, \tag{2.28}$$

where β_i and D_i are the Twiss beta and the dispersion values at the collimator position. Only the betatron part is kept to compute the horizontal and vertical beam sizes in the collimator [38]

$$\sigma_{i,coll} = \sqrt{\beta_i \frac{\varepsilon}{\beta\gamma}}\,. \tag{2.29}$$

The collimators are also oriented with an angle θ with respect to the horizontal plane. An effective beam size in the collimation plane is then computed with the beam sizes from 2.29 and the collimator angle θ [114, 115]

$$\sigma_{coll} = \sqrt{\left(\sigma_x \cos(\theta)\right)^2 + \left(\sigma_y \sin(\theta)\right)^2}\,. \tag{2.30}$$

Moreover, the normalised beam emittance used to compute the collimators gaps is fixed to 3.5 μm rad for the LHC [126] and will be fixed to 2.5 μm rad for HL-LHC [94].

Finally, the collimator jaws are set at a certain number of the effective beam σ_{coll}. Since the collimators settings are symmetric, this setting is the collimator half-gap $g/2$

$$g = 2 n_\sigma \sigma_{coll}\,. \tag{2.31}$$

The various collimators families (primary, secondary, tertiary and absorbers) will have different gaps which are then reported in number of effective beam size n_σ. Table 2.2 reports a selection of collimators gaps and the associated beam parameters.

Name	Family	β_x	β_y	θ / rad	σ_{coll}	n_σ	g / mm
TCP.B6L7	Primary	142	87	2.215	0.232	5	1.16
TCSG.D4L7	Secondary	333	69	1.571	0.186	6.5	1.21
TCLA.B6R7	Shower absorber	160	76	0	0.284	10	2.84
TCTPH.4L2	Tertiary	85	104	0	0.207	37	7.65

Table 2.2: Example of LHC beam 1 collimator settings with their Twiss beta values β_x and β_y, their collimation angle θ, their effective beam size in the collimation plane σ_{coll}, their settings n_σ in number of σ_{coll} and their physical gap g in mm. The settings are taken from the 2017 top energy table [77].

Equations 2.29 and 2.30 show that as the beam energy increases, the beam size at the collimator decreases. Since the collimators settings are defined for a certain normalized emittance, their gaps must follow the beam size and therefore are reduced as the energy increases. The collimators then become the main contributors to the impedance at top energy, as shown in Fig. 2.5.

The jaws materials are also a key element to explain their predominance on the beam impedance. Most of them are made of graphite based materials, resulting from mechanical and vacuum compatibility considerations [39, p. 481]. Their electric conductivity is rather poor: 0.2 MS m^{-1} for CFC [103] against 58.8 MS m^{-1} for copper at room temperature [103, 121]. All-in-all the beam coupling impedance in LHC is higher at top energy than at injection energy, as can be seen in Fig. 2.4.

Because of their tight gaps, as shown in Table 2.2, each collimator has a measurable impact on the impedance. Methods were developed to measure their individual contribution which can then be compared to predictions from the LHC impedance model. The results will be detailed in part 3.3.

Because they are the main impedance source at top energy, the betatron cleaning collimators located in IR7 will be upgraded in the framework of the HL-LHC project. The scope and the impact of this impedance reduction on the mode coupling instability will be investigated in chapter 4.

The simple impedance models presented at the beginning of the section and the LHC impedance model will now be used to study transverse beam instabilities. But before benchmarking two beam instability simulation codes with those impedance models, we will first give a qualitative overview of beam instabilities for a model with two particles.

2.2 A simplified approach to beam instabilities: the two-particle model

The simplest way to study beam instabilities is to use a two-particle model: the bunch is divided in two macroparticles each containing half the bunch intensity. This approach also enables to derive approximate formulas which can then be compared to more involved models. This model was suggested by R.Kohaupt [69] and R.Talman [138] and detailed derivations can be found in [49, 105]. We will first investigate the beam instability qualitatively before giving the main results from the aforementioned references.

The study starts by dividing the bunch in two macroparticles, one at the head of the bunch and one at the tail. Their charge is $N_b/2$ where N_b is the total number of protons in the bunch . The particle at the head of the bunch generates a wake field which perturbs the particle at the tail of the bunch. This initial situation is depicted in Fig. 2.10a. The particles are initially located at $z_1 = 75\,\mathrm{mm}$, $z_2 = -75\,\mathrm{mm}$, $x_1 = 0.3\,\mu\mathrm{m}$ and $x_2 = 0.3\,\mu\mathrm{m}$. Their individual intensity is 2.5×10^{11} p.p.b. The summary of the parameters for these simulation is given in Table 2.3. Macroparticle 1 (MP1) at the head of the bunch creates a wake field depicted by the solid line. Initially the wake felt by the macroparticle 2 (MP2) trailing behind is small and thus has little impact on its transverse motion.

The two particles execute synchrotron oscillations: they periodically exchange their longitudinal position, the period being the synchrotron tune Q_s. Figure 2.11 shows the longitudinal position of the two macroparticles as a function of the turn number. For this simple example the synchrotron tune has been chosen so that $Q_s = 1/500$ i.e the particles execute a full synchrotron oscillation in 500 turns.

Because of the synchrotron oscillations, the trailing particle which was affected by the wake will become the leading particle after $1/(4Q_s)$ turns. This is depicted in Figs. 2.10b and 2.10c which show the position of the macroparticles at turn 120 and at turn 130, before and after $1/(4Q_s)$. At turn 120, MP2 at the tail is strongly affected by the wake created by MP1 at the head, as can be seen in Fig. 2.10b. It is kicked by the wake as long as it remains behind MP1. At turn 130, the two macroparticles have just exchanged their longitudinal position. Figure 2.10c shows that MP2 is now at the head and is the one

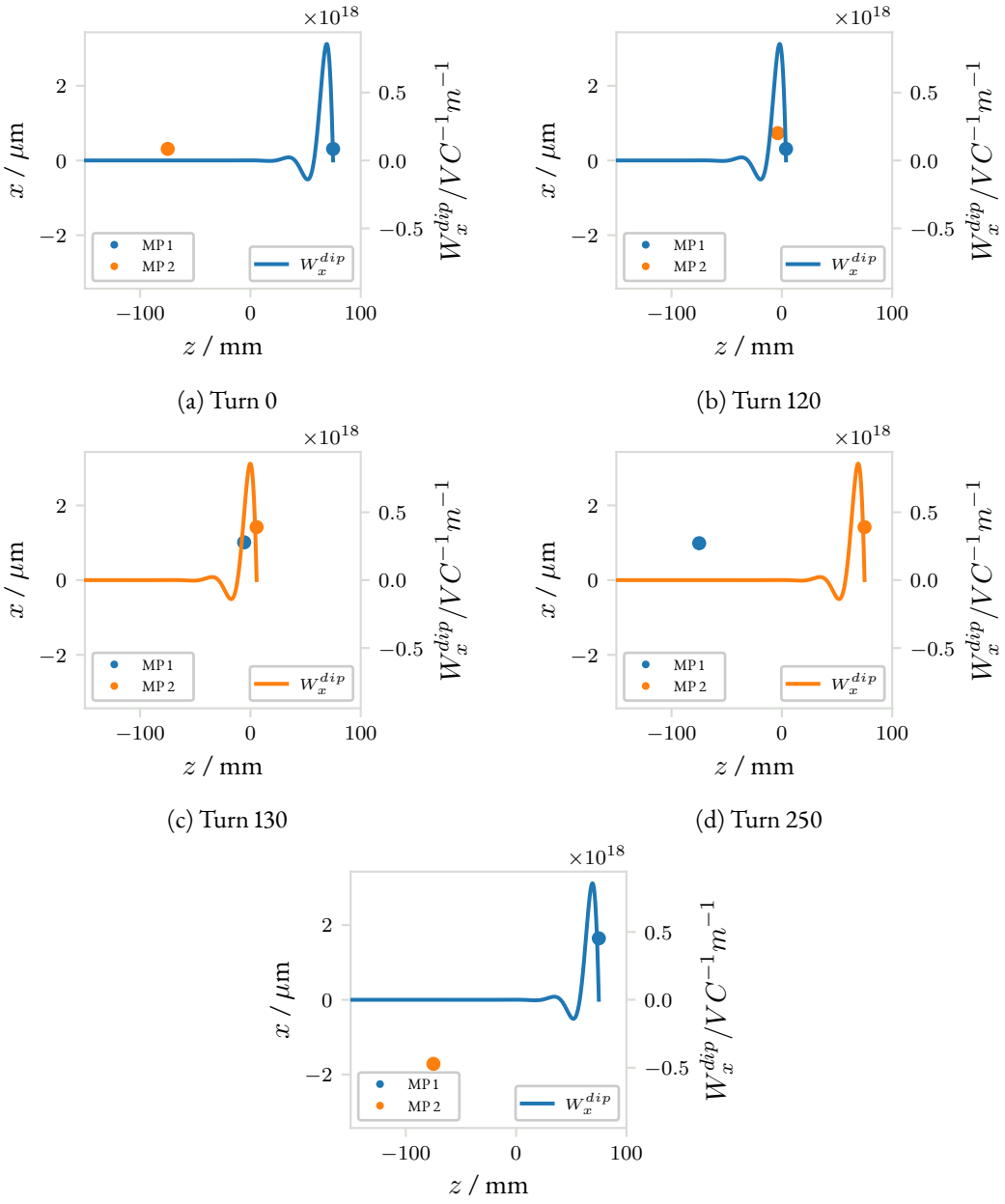

(a) Turn 0

(b) Turn 120

(c) Turn 130

(d) Turn 250

(e) Turn 500

Figure 2.10: Transverse and longitudinal position x and z of the two macroparticles at different periods of the synchrotron oscillation cycle. They perform a full synchrotron oscillation in 500 turns. The total bunch intensity in this case is 5×10^{11} p.p.b., each particle has half the bunch intensity 2.5×10^{11} p.p.b. The kick felt by the trailing particle is caused by the wake generated by the head particle. It is depicted here in a solid line the same colour as the macroparticle generating it.

Table 2.3: Impedance and beam parameters for the two-particle model simulations.

Parameter	Value
Impedance model	Transverse broad-band resonator[1]
Machine	
Circumference / m	26 658.8832
Transverse tune Q_{x0}[2]	50.2
Momentum compaction factor α_c	1.0×10^{-4}
Synchrotron tune Q_s	2×10^{-3}
Beam	
Number of bunches	1
Number of macroparticles	2
4 σ bunch length τ_b / ns	1.0
Bunch intensity / p.p.b.	10^{10} and 5×10^{11}
Chromaticity Q'	0

[1] Resonator impedance with resonance frequency $f_{res} = 10\,\mathrm{GHz}$, shunt impedance $R_s = 25\,\mathrm{M\Omega\,m^{-1}}$ and quality factor $Q = 1$. Only the horizontal plane is used.

[2] This tune value is chosen so that a particle executes a full revolution in the (x, x') phase space in five turns $(1/0.2 = 5)$. That is after five turns the transverse position of the particle is the same if the motion is unperturbed. This is impossible to set in a real machine because magnet imperfections would create a resonance at this tune value.

generating the wake. In turn this wake strongly affects MP1 transverse position. After $1/(2Q_s)$ turns, MP1 is at the tail of the bunch and MP2 at the head, as showed in Fig. 2.10d. The transverse position of both macroparticles has been affected by the wake field. While they both started with a transverse offset of 0.3 μm, they end at ∼1 μm after half a synchrotron oscillation. In this case the kicks to the trailing particle are piling up and create an exponentially growing transverse oscillation. Figure 2.10e shows the situation after one full synchrotron oscillation. The two macroparticles are far from their original position: ±2 μm, a factor ~ 7 compared to the 0.3 μm original position.

This simple description highlights the important role of the synchrotron tune in the instability mechanism. Indeed if the particles exchange their position quickly enough, the trailing particle is affected for a shorter time. The kicks to the transverse position do not have the time to accumulate and the beam remains stable.

An other important parameter is of course the bunch intensity. Since the wake strength is proportional to the head particle intensity, the instability is more likely to appear for high bunch intensities. Figure 2.12 shows the same snapshots of the particles motion at different periods of the synchrotron oscillation but for a bunch intensity reduced to 10^{10} p.p.b. The kicks to the trailing particle do not accumulate and the motion remains stable.

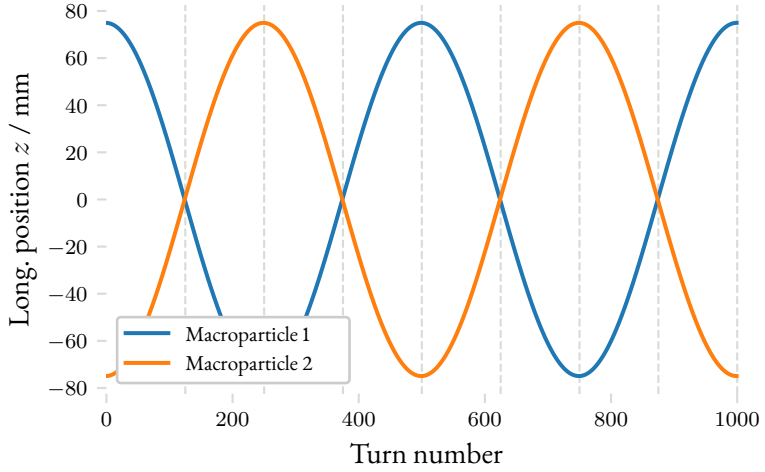

Figure 2.11: Longitudinal position of the two macroparticles as a function of turn number. The synchrotron tune is $Q_s = 0.002$ and dashed lines at $1/(4Q_s)$ multiples are plotted. As the synchrotron period is 500 turns, each macroparticle comes back to its initial longitudinal position after this period.

The transverse position of the two macroparticles during 1000 turns are plotted in Figs. 2.13 and 2.14, for both the unstable and the stable case. In the unstable case, the transverse excursions of the particles are clearly increasing because of the wake field kicks. In the stable case, these kicks are not strong enough and the transverse motion remains regular.

The two-particle model can easily be put in equations as detailed in [49, 56, 105], and approximations can be made using it. The situation presented before is further simplified:

- The two macroparticles are assumed to be separated by a distance z for the first half of the synchrotron period $T_s = 1/Q_s$. MP1 is at the head of the bunch, MP2 at the tail. At $T_s/2$, their longitudinal position are instantaneously switched. MP2 is now at the head of the bunch and MP1 at the tail.
- The wake force $W_x^{dip}(z)$ acting on the tail macroparticle located at position z behind the head particle is assumed to be constant.
- The machine is assumed to be smooth i.e transverse focusing is constant along the accelerator. The transverse tune Q_{x0} is then equal to $Q_{x0} = C_0/2\pi\langle\beta_x\rangle$.

Using these assumptions, the equations of motion of the head and the tail particles are written [49]

$$\ddot{x_1} + (\omega_{\beta_x})^2 x_1 = 0\,, \tag{2.32}$$

$$\ddot{x_2} + (\omega_{\beta_x})^2 x_2 = \frac{e^2 N_b W_x^{dip}}{2C_0\gamma m_0} x_1\,, \tag{2.33}$$

where $\omega_{\beta_x} = Q_{x0}\omega_0$. x_1 corresponds to the transverse position of the macroparticle which starts at the head of the bunch. x_2 is the transverse position of the macroparticle which starts at the tail of the bunch. In the equations, the tail particle MP2 motion is perturbed by a force generated by the wake field of the head particle MP1. This force is also proportional to the charge of the particle.

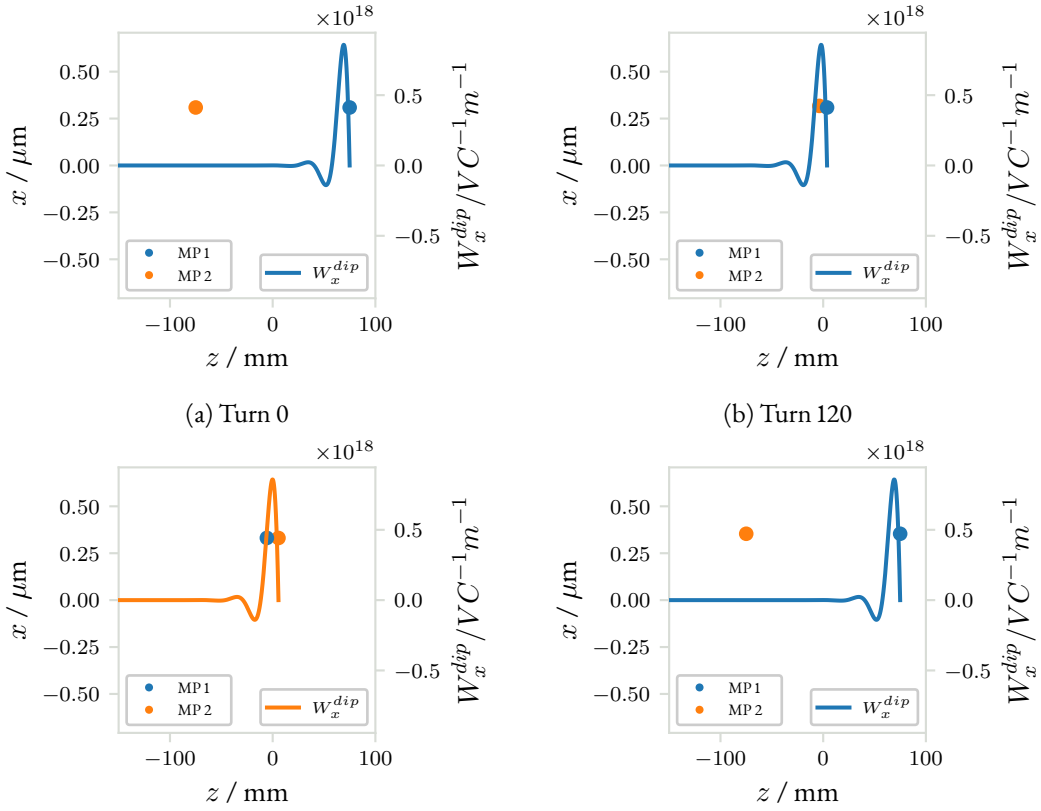

(a) Turn 0

(b) Turn 120

(c) Turn 130

(d) Turn 500

Figure 2.12: Transverse and longitudinal position of the two macroparticles MP1 and MP2 at different periods of the synchrotron oscillation cycle. The total bunch intensity in this case is now 10^{10} p.p.b., each particle has half the bunch intensity 0.5×10^{10} p.p.b. The kicks do not accumulate and the motion remains stable: the two macroparticles recover their initial position after a full synchrotron period.

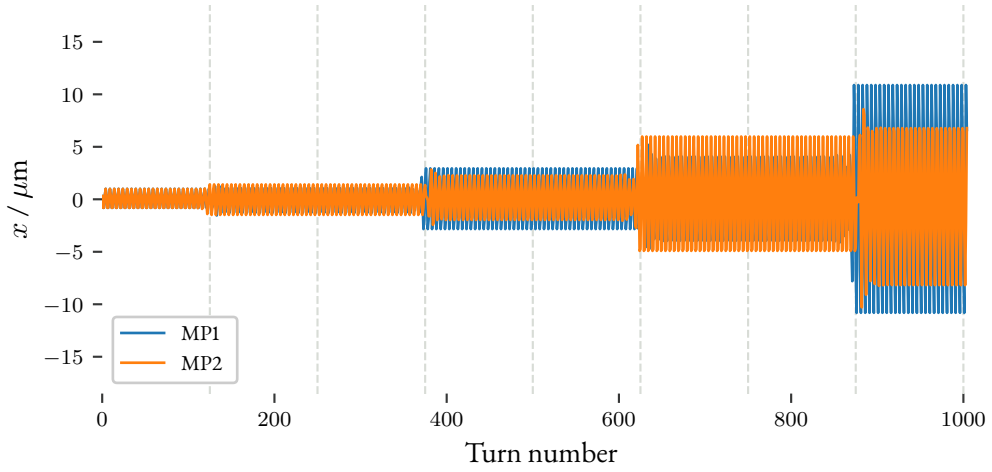

Figure 2.13: Transverse position of the two macroparticles as a function of turn number. The synchrotron tune is $Q_s = 0.002$ and dashed lines at $1/(4Q_s)$ multiples are plotted. The total bunch intensity is 5×10^{11} p.p.b. The effect of the wake field is visible when the two particles are close longitudinally, at 125, 375, 625 and 875 turns. At these time periods, the wake is strong enough to create a displacement of the trailing particle which accumulates with time.

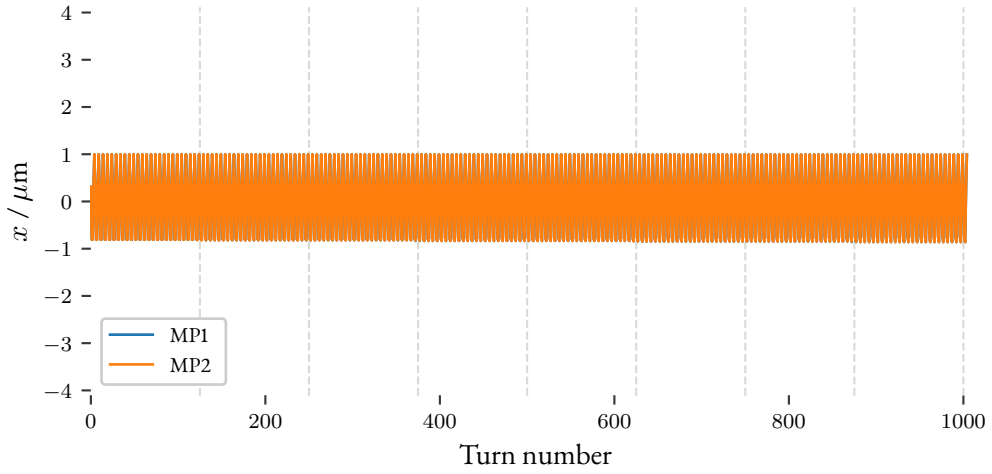

Figure 2.14: Transverse position of the two macroparticles as a function of turn number. The total bunch intensity is reduced to 10^{10} p.p.b. The wake is therefore weaker and the transverse displacements do not accumulate. The transverse position of the particles remains in a bounded region and the beam stays stable.

After a time $T_s/2$, the positions of the two particles are switched, and so are the equations

$$\ddot{x_1} + (\omega_{\beta_x})^2 x_1 = \frac{e^2 N_b W_x^{dip}}{2C_0 \gamma m_0} x_2 \,, \tag{2.34}$$

$$\ddot{x_2} + (\omega_{\beta_x})^2 x_2 = 0 \,. \tag{2.35}$$

In the first half of the synchrotron period, equations 2.32 and 2.33 govern the particles motion. Introducing the phasors of the two particles [49]

$$\tilde{x}_{1,2} = x_{1,2} - j\frac{1}{\omega_{\beta_x}} \dot{x}_{1,2} \tag{2.36}$$

allows to write the system of equations in the matrix form

$$\begin{pmatrix} \tilde{x}_1(T_s/2) \\ \tilde{x}_2(T_s/2) \end{pmatrix} = e^{j\omega_{\beta_x} T_s/2} \mathbf{A} \begin{pmatrix} \tilde{x}_1(0) \\ \tilde{x}_2(0) \end{pmatrix} . \tag{2.37}$$

During the second half of the synchrotron period, MP1 and MP2 are simply switched. The corresponding equations 2.34 and 2.35 lead to the matrix system

$$\begin{pmatrix} \tilde{x}_1(T_s) \\ \tilde{x}_2(T_s) \end{pmatrix} = e^{j\omega_{\beta_x} T_s/2} \mathbf{B} \begin{pmatrix} \tilde{x}_1(T_s/2) \\ \tilde{x}_2(T_s/2) \end{pmatrix} . \tag{2.38}$$

Combining the two former systems of equations allows to find the transverse positions of the two particles after one full synchrotron period

$$\begin{pmatrix} \tilde{x}_1(T_s) \\ \tilde{x}_2(T_s) \end{pmatrix} = e^{j\omega_{\beta_x} T_s} \mathbf{M} \begin{pmatrix} \tilde{x}_1(0) \\ \tilde{x}_2(0) \end{pmatrix} . \tag{2.39}$$

where the matrices $\mathbf{A}$, $\mathbf{B}$ and $\mathbf{M}$ are written

$$\begin{aligned} \mathbf{A} &= \begin{pmatrix} 1 & 0 \\ -j\Upsilon & 1 \end{pmatrix} \\ \mathbf{B} &= \begin{pmatrix} 1 & -j\Upsilon \\ 0 & 1 \end{pmatrix} \\ \mathbf{M} &= \mathbf{B} \cdot \mathbf{A} \\ \Upsilon &= \frac{e^2 N_b T_s W_x^{dip}}{8\omega_{\beta_x} C_0 \gamma m_0} \,. \end{aligned} \tag{2.40}$$

The system is stable if the matrix trace $|\mathrm{Tr}(\mathbf{M})| = |2 - \Upsilon^2| < 2$. This condition leads in turn to $\Upsilon < 2$ also written

$$\frac{e^2 N_b T_s W_x^{dip}}{8\omega_{\beta_x} C_0 \gamma m_0} < 2 \,. \tag{2.41}$$

This condition confirms the qualitative observations which were made before. Decreasing the synchrotron period and thus exchanging more often the positions of the head and tail particles helps stabilize the beam. A higher beam energy also contributes to the stabilization: if the beam is more rigid, the perturbation caused by the head particle has less impact on the tail. On the other hand an increased beam intensity or a stronger wake will reduce the beam stability.

This result can be applied to the simple case presented beforehand. The beam parameters entering in the stability criterion are

$$\begin{aligned} &W_x^{dip} \approx 8 \times 10^{17}\,\mathrm{V\,C^{-1}\,m^{-1}}\,, \\ &Q_s = 1/500\,, \\ &Q_{x0} = 50.2\,, \\ &\omega_0 = 2\pi \times 11\,250\,\mathrm{Hz}\,, \\ &\gamma = 6930\,, \\ &m_0 = 1.67 \times 10^{-27}\,\mathrm{kg}\,. \end{aligned} \tag{2.42}$$

Two bunch intensities were considered, $N_b = 10^{10}$ p.p.b. and $N_b = 5 \times 10^{11}$ p.p.b. which led respectively to a stable motion and an unstable motion. In the first case $\Upsilon \approx 1$ and in the second case $\Upsilon \approx 51$. The stability criteria predicts indeed an intensity threshold for the instability at $\Upsilon = 2$ which gives to $N_b \approx 1.9 \times 10^{10}$ p.p.b..

We have seen that a two-particle model of the bunch allows to derive a stability criteria which depends on the bunch intensity, the synchrotron and betatron tunes, the wake field strength and the beam energy. This model is valid for the zero chromaticity case where the betatron and synchrotron motions are independent. Chromaticity can however be introduced in the model as showed in [105]. In this case a two-particle beam can have two oscillation modes: a σ mode where the head and the tail of the bunch oscillate in phase and a π mode where the head and the tail have opposite phase. The sum of the modes growth rates is equal to zero so one of the two mode is always unstable [49].

The two-particle model is however limited when more than two degrees of freedom are needed to describe the bunch behavior. A N-particle model can then be used to simulate the beam dynamics. We will now briefly introduce the physics underlying one of such code, PyHEADTAIL. The Vlasov formalism, which is an other approach to treat beam instabilities, will then also be introduced.

2.3 Treatment of coherent beam instabilities

We saw that the perturbation to the beam transverse motion caused by a wake field can be treated analytically using a simple two-particle model. However analytic models are more difficult to obtain when more than two degrees of freedom are required. The two-particle model method has therefore to be extended to a multi-particle problem where the 10^{11} particles of the bunch are considered. The movement of each particle is tracked along time, using the single particle equations of motion. The kicks induced by the wake fields are then applied at every turn to each particle. With this method a computational limit is quickly encountered: it is impossible to track 10^{11} particles for enough turns to see the instability rising. The solution is to regroup them: instead of tracking 10^{11} particles of charge e, the code will track for example 10^6 macroparticles of charge $10^5\,e$. Despite the code optimisation

and progress made on computing power, simulation time remains the main limitation of this method. Studying different machine parameters for many turns can be resource-intensive and thus the simulations parameters have to be carefully chosen. Macroparticle codes can also be extended to include many other effects such as RF manipulations of the bunches (acceleration, splitting, rotation), direct space-charge, electron cloud or synchrotron radiation among others. This versatility makes macroparticle codes powerful tools to study the beam dynamics in accelerators. The code PyHEADTAIL [113] is used at CERN to study coherent instabilities in the presence of wake fields, space-charge or feedbacks among others. Its implementation in the case of wake field induced instabilities will be briefly presented in part 2.3.1.

With the macroparticle approach, tracking 10^6 macroparticles implies that 10^6 modes of motion will be studied for each transverse and longitudinal coordinate. The tracking is unconcerned by the fact that many of these modes describe microscopic motions, thus irrelevant to coherent beam instabilities. It is the macroscopic motion, i.e modes with wavelengths in the order of the beam pipe or the bunch length dimensions that are of interest. So instead of considering the beam as a collection of macroparticles in time domain, the bunch can be studied as a whole and its modes of oscillation can be studied in the frequency domain. This approach relies on Vlasov equation [145] and was first applied to bunched beams by F.Sacherer [122, 123, 124, 125]. Different methods to solve the equation were developed along the years [31, 32, 33, 34, 50, 51, 60, 72, 91]. We will present the method used in the code DELPHI [100, 143] in part 2.3.2.

2.3.1 Macroparticle formalism for instability simulations

We will briefly introduce the underlying mechanisms of PyHEADTAIL interesting for the study of impedance induced instabilities. Further details on PyHEADTAIL implementation and functionalities can be found in [78, 131]. A simulation follows these main steps:

1. Machine initialization: the accelerator parameters (circumference, particle used, Twiss and dispersion values) are loaded. The ring is divided into K segments each separated by an interaction point IP.

2. Beam initialization: a beam made of N macroparticles is generated at interaction point IP0. Typically 10^6 macroparticles are used. The initial transverse and longitudinal distributions of the macroparticles can be specified. A macroparticle with index $i \in [1, N]$ now has a set of six coordinates $(x_i, x_i', y_i, y_i', z_i, \delta_i)$, a charge q_i and a mass m_i.

3. Linear tracking: using Hill's equation solution detailed in part 1.2.1, the macroparticle transverse coordinates are transported from IP0 to IP1. This transport for macroparticle i can be written in a matrix form [56, 74, 75]

$$\begin{aligned} \begin{pmatrix} x_i \\ x_i' \end{pmatrix}\Big|_1 &= \mathbf{M} \begin{pmatrix} x_i \\ x_i' \end{pmatrix}\Big|_0 , \\ \mathbf{M} &= \begin{pmatrix} \sqrt{\beta_1} & 0 \\ -\frac{\alpha_1}{\sqrt{\beta_1}} & \frac{1}{\sqrt{\beta_1}} \end{pmatrix} \begin{pmatrix} \cos(\Delta\mu_{0\to1}) & \sin(\Delta\mu_{0\to1}) \\ -\sin(\Delta\mu_{0\to1}) & \cos(\Delta\mu_{0\to1}) \end{pmatrix} \begin{pmatrix} \frac{1}{\sqrt{\beta_0}} & 0 \\ -\frac{\alpha_0}{\sqrt{\beta_0}} & \sqrt{\beta_0} \end{pmatrix} , \end{aligned} \tag{2.43}$$

where $\alpha_{0,1}$ and $\beta_{0,1}$ are the Twiss functions values at the IP and $\Delta\mu_{0\to1}$ the phase advance from IP0 to IP1. The smooth approximation is used in PyHEADTAIL linear tracking so the phase advance $\Delta\mu_{0\to1} = Q_{x0}L_{0\to1}/C$ where $L_{0\to1}$ is the first segment length.

4. Chromaticity and detuning effects: these effects are implemented as a change of each macroparticle phase advance. Amplitude detuning is the dependence of the particle tune with its Courant-Snyder invariant $2J_{x,y}$. It is an important effect for beam stabilization through Landau damping [64, 73]. The phase advance $\Delta\mu_{0\to1}$ for macroparticle i is derived from the phase advance $\Delta\mu_{0\to1}$ which was used for all macroparticles

$$\Delta\mu_{i,0\to1} = \Delta\mu_{0\to1} + (\xi_x\delta_i + a_{xx}J_{x,i} + a_{xy}J_{y,i})\frac{\Delta\mu_{0\to1}}{2\pi Q_{x0}} \tag{2.44}$$

where a_{xx} and a_{xy} are the detuning coefficients, $J_{x,i}$ and $J_{y,i}$ the transverse actions of the particle.

5. Synchrotron motion: the longitudinal coordinates (z_i, δ_i) of the macroparticle are updated once every turn using the equations of longitudinal motion. The motion can be linear or not and complex RF systems can be modeled, allowing for bunch acceleration, splitting or rotation among others.

6. Collective effects: they are applied at each interaction point. PyHEADTAIL implements wake fields effects but also feedbacks and space charge. For wake fields, we saw that the particles in front generate a wake which provides a momentum kick to the following particles. The dipolar wake kick $\Delta x'_i$ on macroparticle i caused by the other macroparticles j is thus

$$\Delta x'_i = -\frac{e^2}{\beta^2 E_0}\sum_{j=1}^{N} W_x^{dip}(z_i - z_j)\Delta x_j \,. \tag{2.45}$$

If the beam is made of 10^6 macroparticles, applying this formula for each particle, at multiple interaction points along the ring and for several thousands of turns would be computationally impossible. Instead the bunch is sliced longitudinally as schematized in Fig. 2.15.

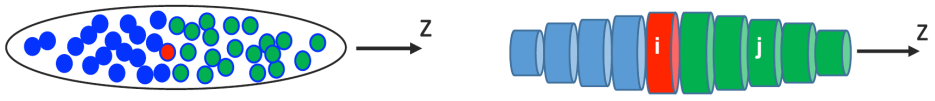

(a) Bunch before slicing. (b) Bunch after slicing.

Figure 2.15: Principle of beam slicing for in PyHEADTAIL. On the left the bunch is represented as a collection of macroparticles. The effect of the wakefield generated by all the macroparticles on the red one must be evaluated. To decrease computation time, the bunch is instead sliced as pictured on the right. Each slice contains several thousands of macroparticles, and it is the effect of all slices on the red one which is computed. Pictures courtesy of M.Schenk [131].

For thin enough slices, the wake can be considered constant inside the slice. The wake kick $\Delta x'_i$ generated by all the slices j located upstream of slice i are then computed and summed to obtain the wake kick acting on slice i

$$\Delta x'_i = -\frac{e^2}{\beta^2 E_0} \sum_{j=1}^{N_{slices}} \langle x \rangle_j W_x^{dip}(i-j)\,, \tag{2.46}$$

where $\langle x \rangle_j$ is the mean value of all the transverse offsets of macroparticles in slice j.

This whole process is then repeated for several thousands of turns depending on the beam revolution frequency. For example in the LHC the revolution frequency is ∼10 kHz, so an instability with a rise time of 1 s would be seen after 3×10^4 turns of simulation. On the other hand in the PSB the revolution frequency at injection energy is ∼1 MHz so an instability with the same rise-time of 1 s would require 3×10^6 turns of simulation. The simulation length must therefore be chosen carefully to ensure that eventual instabilities can develop properly. The wake slicing is also crucial since it assumes that the wake is constant within a slice. If the wake has sharp peaks, a very thin slicing has to be used to resolve it correctly.

We saw that PyHEADTAIL is a flexible simulation code implementing the particle equations of motion and adding the chromaticity and the wake field induced effects on top of it. However computing power remains a limit of such code. Performing large parameters scans and studying slow instabilities can be time consuming. We will now see an other way to treat the instability problems which relies on Vlasov's equation.

2.3.2 Vlasov's formalism for instability simulations

In the macroparticle approach the beam is treated as a collection of individual particles interacting with each other and transported along the ring. The limit case would be to consider a beam made of an infinite number of particles and apply the results to a subsystem of 10^{11} particles. In this approach the beam is described as a superposition of modes rather than a collection of particles. The basic tool is Vlasov's equation which describes the evolution of an arbitrary distribution of particles along time [49, 105]. The code DELPHI [100] implements this approach which will now be detailed.

Let us consider two conjugate variables q and p, where q is the coordinate and p the momentum. (q, p) forms the phase space, longitudinal or transverse. Vlasov's equation states that if we follow a local particle distribution $\Psi(q, p, t)$ along time, the phase space area will not change. It can be written as

$$\frac{\mathrm{d}\Psi}{\mathrm{d}t} = 0\,. \tag{2.47}$$

We now consider that the distribution Ψ is a function of the horizontal coordinate x and momentum p_x, the longitudinal coordinate z and momentum offset δ and of the curvilinear position along the accelerator s which encloses the time dependence as $s = vt$

$$\Psi = \Psi(x, p_x, z, \delta, s)\,. \tag{2.48}$$

Equation 2.47 can then be rewritten [49]

$$\frac{\partial \Psi}{\partial s} + x' \frac{\partial \Psi}{\partial x} + p_x' \frac{\partial \Psi}{\partial p_x} + z' \frac{\partial \Psi}{\partial z} + \delta' \frac{\partial \Psi}{\partial \delta} = 0\,. \tag{2.49}$$

The transverse plane coordinates can be changed from the position and momentum variables (x, p_x) to the action and angle variables (J_x, θ_x)

$$\begin{aligned} x &= \sqrt{2J_x \frac{R}{Q_{x0}}} \cos(\theta_x)\,, \\ p_x &= \sqrt{2J_y \frac{Q_{x0}}{R}} \sin(\theta_x)\,, \end{aligned} \tag{2.50}$$

where Q_{x0} refers to the transverse betatron tune from single particle dynamics without momentum offset. Vlasov's equation 2.47 becomes

$$\frac{\partial \Psi}{\partial s} + J_x' \frac{\partial \Psi}{\partial J_x} + \theta_x' \frac{\partial \Psi}{\partial \theta_x} + z' \frac{\partial \Psi}{\partial z} + \delta' \frac{\partial \Psi}{\partial \delta} = 0\,. \tag{2.51}$$

The Hamiltonian H describing the motion of a single particle, including the effect of wake fields, can be written [49, 100]

$$H = \frac{Q_x}{R} J_x - \frac{1}{2\eta} \left(\frac{\omega_s}{v}\right)^2 z^2 - \frac{\eta}{2} \delta^2 - \frac{x F_x^{dip}(z,s)}{E_0}\,. \tag{2.52}$$

The first term describes the transverse betatron motion of the beam in the smooth approximation. The effect of chromaticity ξ is accounted for in $Q_x = Q_{x0}(1 + \xi_x \delta)$. The second and third terms of Eq. 2.52 describe the linear synchrotron motion of the beam. The last term corresponds to the force created by the dipolar wake field at the position s along the accelerator acting on the particle at longitudinal coordinate z. The derivatives with respect to s can be expressed

$$J_x' = -\frac{\partial H}{\partial \theta_x} = \frac{\partial x}{\partial \theta_x} \frac{F_x^{dip}(z,s)}{E_0}\,, \tag{2.53}$$

$$\theta_x' = \frac{\partial H}{\partial J_x} = \frac{Q_x}{R} - \frac{\partial x}{\partial J_x} \frac{F_x^{dip}(z,s)}{E_0}\,, \tag{2.54}$$

$$z' = \frac{\partial H}{\partial \delta} = -\eta \delta\,, \tag{2.55}$$

$$\delta' = -\frac{\partial H}{\partial z} = \left(\frac{\omega_s}{v}\right)^2 \frac{z}{\eta}\,, \tag{2.56}$$

and Vlasov's equation 2.51 is now written

$$\frac{\partial \Psi}{\partial s} + \frac{F_x^{dip}(z,s)}{E_0}\frac{\partial x}{\partial \theta_x}\frac{\partial \Psi}{\partial J_x} + \left(\frac{Q_x}{R} - \frac{F_x^{dip}(z,s)}{E_0}\frac{\partial x}{\partial J_x}\right)\frac{\partial \Psi}{\partial \theta_x} - \eta\delta\frac{\partial \Psi}{\partial z} + \left(\frac{\omega_s}{v}\right)^2 \frac{z}{\eta}\frac{\partial \Psi}{\partial \delta} = 0\,. \tag{2.57}$$

To write the particle Hamiltonian, different assumptions were made. The longitudinal motion is assumed to be linear, thus the formalism can not handle particles with large synchrotron amplitudes, accelerated beams or complex beam manipulations. Also only the transverse dipolar wake is taken into account.

Perturbation formalism

The perturbation formalism will now be used to solve the differential equation. We assume that the phase space distribution can be decomposed in a sum of an unperturbed distribution ψ_0 and a small perturbation ψ_1. This perturbation develops itself at a complex frequency $\omega_c = Q_c\omega_0$ where Q_c is the perturbed tune value associated with the mode. The total distribution can thus be written [49, 100]

$$\psi(s, J_x, \theta_x, z, \delta) = \underbrace{f_0(J_x)g_0(r)}_{\text{unperturbed distribution}} + \underbrace{f_1(J_x,\theta_x)g_1(z,\delta)\exp\left(\frac{j\omega_c s}{v}\right)}_{\text{perturbation to be found}}, \tag{2.58}$$

where $r = \sqrt{z^2 + \left(\frac{\eta v \delta}{\omega_s}\right)^2}$. Using polar coordinates $z = r\cos\phi$ and $\delta = \frac{\omega_s}{\eta v} r\sin\phi$, Vlasov's equation 2.57 simplifies to

$$\begin{aligned}\left(f_1 g_1 \frac{j\omega_c s}{v} + \frac{Q_x}{R} g_1 \frac{\partial f_1}{\partial \theta_x} + \frac{\omega_s}{v} f_1 \frac{\partial g_1}{\partial \phi}\right)\exp\left(\frac{j\omega_c s}{v}\right) = \\ \frac{\sin\theta_x}{E}\sqrt{2J_x\frac{R}{Q_{x0}}}F_x^{dip}(z,s)g_0(r)f_0'(J_x)\,.\end{aligned} \tag{2.59}$$

The function $f_1(J_x, \theta_x)$ can be Fourier expanded as

$$f_1(J_x,\theta_x) = \sum_{k=-\infty}^{k=+\infty} f_1^k(J_x)e^{-jk\theta_x}\,, \tag{2.60}$$

but only the term $f_1^{k=1}$ term is non-zero [100]. Therefore $f_1(J_x, \theta_x)$ is expressed as $f(J_x)\exp(-j\theta_x)$. The term $g_1(r,\phi)$ is also Fourier expanded as

$$g_1(r,\phi) = \exp\left(-\frac{jQ_x' z}{\eta R}\right)\sum_{m=-\infty}^{m=+\infty} R_m(r)e^{-jm\phi}\,, \tag{2.61}$$

where $R_m(r)$ is the azimuthal mode m function. This leads to

$$\sum_{m=-\infty}^{m=+\infty} R_m(r) e^{-jm\phi} \left(\frac{f(J_x)(Q_c - Q_{x0} - mQ_s)}{f_0'(J_x)\sqrt{2J_x \frac{R}{Q_{x0}}}} \right) = \frac{R}{2E} F_x^{dip}(z,s) \exp\left(-j\frac{Q_c s}{R}\right) \exp\left(-j\frac{Q_x' z}{\eta R}\right). \tag{2.62}$$

The wake force $F_x^{dip}(z,s)$ for a dipolar impedance Z_x^{dip} is proportional to

$$F_x^{dip}(z,s) \propto \exp\left(j\frac{Q_c s}{R}\right) \sum_{m=-\infty}^{+\infty} j^{-m} \sum_{p=-\infty}^{+\infty} \left[\exp\left(-j(Q_c+p)\frac{z}{R}\right) Z_x^{dip}(-\omega_0(Q_c+p)) \int_0^\infty r R_m(r) \mathrm{J}_m\left((\omega_\xi - \omega_0(Q_c+p))\frac{r}{v}\right), \mathrm{d}r \right]. \tag{2.63}$$

The transverse damper can be treated as a single turn wake acting on the dipole motion of the bunch [100]. A damper force term can be added to the wake force term

$$F_x^{dip}(z,s) \propto \exp\left(j\frac{Q_c s}{R}\right) \sum_{m=-\infty}^{+\infty} j^{-m} \int_0^\infty r R_m(r) \mathrm{J}_m\left(\frac{\omega_\xi r}{v}\right), \mathrm{d}r\,. \tag{2.64}$$

Combining equations 2.62, 2.63 and 2.64, integrating over ϕ and taking $\tau = \frac{r}{v}$ yields

$$(\omega_c - Q_{x0}\omega_0 - m\omega_s) R_m(\tau) = -\kappa g_0(\tau) \sum_{m'=-\infty}^{\infty} j^{m'-m} \int_0^\infty \mathrm{d}\,, \tau'\tau' R_{m'}(\tau') \left(\overbrace{\frac{\mu}{\omega_0} \mathrm{J}_m(-\omega_\xi \tau) \mathrm{J}_{m'}(-\omega_\xi \tau')}^{\text{damper term}} + \underbrace{\sum_{p=-\infty}^{\infty} Z_x^{dip}(\omega_p) \mathrm{J}_m((\omega_\xi - \omega_p)\tau) \mathrm{J}_{m'}((\omega_\xi - \omega_p)\tau')}_{\text{impedance term}} \right). \tag{2.65}$$

Equation 2.65 is called Sacherer's integral equation [72]. It includes as well a damping term treated as an impedance. It is an eigensystem since the radial function $R_m(\tau)$ of azimuthal mode m is itself a function of all the radial functions.

Eigenvalues problem

Sacherer's integral equation 2.65 can be solved for different shapes of the longitudinal phase space distribution [105]. The code DELPHI assumes that the unperturbed longitudinal distribution is Gaussian with a RMS bunch length σ

$$g_0(r) = \frac{1}{2\pi\sigma}\exp\left(-\frac{r^2}{2\sigma^2}\right). \tag{2.66}$$

This type of distribution leads to an expansion over Laguerre polynomials of Sacherer's integral. It becomes in the end an eigenvalue problem, which is then solved numerically. The radial functions $g_0(\tau)$ and $R_m(\tau)$ are decomposed over Laguerre polynomials [100]

$$R_m(\tau) = \left(\frac{\tau}{\tau_b}\right)^{|l|} e^{-b\tau^2}\sum_{n=0}^{\infty} c_{m,n}\mathrm{L}_n^{|m|}\left(a\tau^2\right), \tag{2.67}$$

$$g_0(\tau) = e^{-b\tau^2}\sum_{k=0}^{n_0} g_k\mathrm{L}_k^0\left(a\tau^2\right), \tag{2.68}$$

which are then substituted in Eq. 2.65. An integration over the variable τ then leads to an eigenvalue problem [100, 105]

$$(\omega_c - Q_{x0}\omega_0)c_{m,n} = \sum_{m'=-\infty}^{\infty}\sum_{n'=0}^{\infty} c_{m',n'}\left(\delta_{mm'}\delta_{nn'}m\omega_s + \mathbf{M}_{m,n,m',n'}\right), \tag{2.69}$$

where $\mathbf{M}$ is the combined impedance and damper matrix. The eigenvalues problem presents a two fold infinity with l the azimuthal mode number and n the radial mode number. When the problem is numerically solved, the matrix is truncated and only some modes are taken into account.

Signal created by the perturbation

The eigenvalue $(\omega_c - Q_{x0}\omega_0)$ associated with the mode (m, n) is the complex frequency shift of this mode. The real part $\Re(\omega_c - Q_{x0}\omega_0)$ will provide the coherent betatron frequency shift of the mode caused by the impedance. The imaginary part $\Im(\omega_c)$ will give the rise or damping time of the oscillation mode. If $\Im(\omega_c) < 0$, the mode is unstable and the time needed for the oscillation amplitude to grow by a factor e^1 is $\frac{1}{\Im(\omega_c)}$. If $\Im(\omega_c) \geq 0$ the mode remains stable.

The eigenvector associated to mode (m, n) can be used to retrieve the mode frequency spectrum. After a Fourier transformation, the spectrum gives the signal observable at a fixed location in the accelerator [5, 9]. This signal represents the bunch shape when it is disturbed by the impedance. The bunch profile can be obtained from the eigenvectors by reconstructing the transverse perturbation $g_1(r, \phi)$. From [49] the distribution spectrum $\tilde{\lambda}(\omega')$ can be written as

$$\tilde{\lambda}(\omega') = \frac{\omega_s}{\eta c}\int_{r=0}^{r=+\infty}\int_{\phi=0}^{\phi=2\pi} r\exp\left(j\frac{\omega' r\cos\phi}{c}\right)g_1(r,\phi)\,\mathrm{d}r\,\mathrm{d}\phi\,, \tag{2.70}$$

where $\omega' = p\omega_0 + \omega_c$ and $p \in \mathbb{Z}$. Inserting Eq. 2.67 in Eq. 2.70 then yields

$$\tilde{\lambda}(\omega') = \frac{\omega_s}{\eta c} \sum_{m=-\infty}^{+\infty} \int_{r=0}^{r=+\infty} r R_m(r)\,\mathrm{d}r \int_{\phi=0}^{\phi=2\pi} \exp\left(-jm\phi + j\left(\frac{\omega' r}{c} - \frac{Q'_x r}{\eta R}\right)\cos\phi\right)\mathrm{d}\phi\,. \tag{2.71}$$

With the relations

$$\frac{1}{2\pi}\int_0^{2\pi} \exp(jm\phi - jx\cos\phi)\,\mathrm{d}\phi = j^{-m}\mathrm{J}_m(x)\,, \tag{2.72}$$

$$\mathrm{J}_{-m}(x) = \mathrm{J}_m(-x)\,, \tag{2.73}$$

we obtain

$$\tilde{\lambda}(\omega') = \frac{2\pi\omega_s}{\eta c} \sum_{m=-\infty}^{+\infty} j^m \int_0^{+\infty} r R_m(r)\mathrm{J}_m\left(\frac{\omega' r}{c} - \frac{Q'_x r}{\eta R}\right)\mathrm{d}r\,. \tag{2.74}$$

This function is the spectrum of the unstable mode. A Fourier transform then allows to obtain the time domain profile of the bunch. The signal can be reconstructed from DELPHI's output following these steps:

1. An eigenvalue ω_c is selected and its corresponding eigenvector is retrieved.

2. From equation 2.67 $R_m\left(\tau = \frac{r}{c}\right)$ is reconstructed for each azimuthal mode m. The retrieved eigenvector gives the coefficient $c_{m,n}$ of the decomposition.

3. Equation 2.74 is computed for a range of ω'.

The signals obtained by simulations can be compared to those measured in an accelerator. In the SPS and the LHC, the head-tail monitor system is used to acquire these beam profiles [76]. It employs a set of strip-line bunch position monitors to record the bunch longitudinal profile. The baseline profile is then subtracted to obtain the oscillation pattern of the bunch. We will see in parts 2.4 and 2.5 examples of profiles for different oscillation modes and instability types.

Vlasov formalism allows for a fast treatment of the instability problem: it is reduced to an eigenvalue problem, which is computationally interesting. This allows to perform simulation scans over a large range of beam parameters such as bunch intensity, transverse and synchrotron tunes, chromaticity or impedance model. However many assumptions have been made during the problem derivation: for instance only linear synchrotron and betatron motions are kept, the transverse motions are assumed to be decoupled, and only the dipolar term of the impedance is used. These assumptions will matter when the results from PyHEADTAIL and DELPHI will be compared.

We saw that DELPHI fully solves Sacherer's integral equation, including azimuthal and radial modes. However some of the modes can be very weak and neglected as a first approximation. We will now give the results of a simpler treatment of Sacherer's integral which allows to estimate the mode frequency shifts and growth rates.

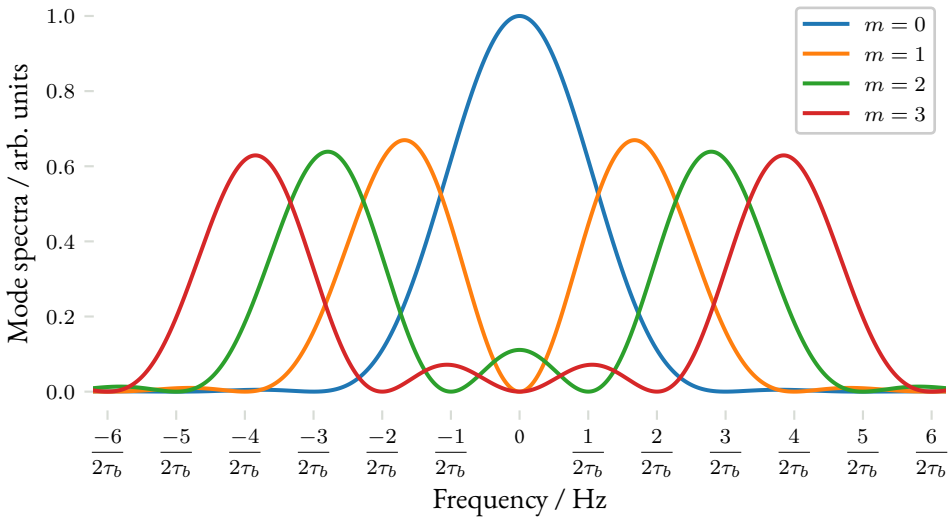

Figure 2.16: Mode spectra obtained with Sacherer's formula treatment. The modes are represented here for zero chromaticity. Mode 0 is peaked at $f = 0$ GHz whereas the other modes are peaked at $f \approx \frac{(|m|+1)}{2\tau_b}$. Chromaticity would shift all the modes by f_ξ.

2.3.3 Approximate solution of Sacherer's integral equation

In DELPHI, many of the computed matrix elements will correspond to weak modes with very slow growth rates and frequencies far from the unperturbed tune. In a first approximation, the treatment of Sacherer's integral equation 2.65 can be further simplified. Only the modes with the same azimuthal and radial number are kept. The longitudinal beam distribution can also be considered constant $g_0(\tau) = \frac{4}{\pi^2\tau_b^2}$ where τ is the longitudinal coordinate expressed in time unit and τ_b is the full bunch length i.e $\tau_b = 4\sigma_z/\beta c$. These assumptions allow to get a simple expression for the complex frequency shift $\omega_{c,m}$ of azimuthal mode m for a low intensity bunch and outside the mode coupling regime [90, 105]

$$(\omega_{c,m} - Q_{x0}\omega_0 - mQ_s\omega_0) = \frac{1}{|m|+1}\frac{je^2N_b}{4\pi\gamma m_0 c Q_{x0}\tau_b}\frac{\sum_{k=-\infty}^{+\infty} Z_x(\omega_k)h_m(\omega_k - \omega_\xi)}{\sum_{k=-\infty}^{+\infty} h_m(\omega_k - \omega_\xi)} \tag{2.75}$$

where Z_x is the transverse dipolar impedance and $\omega_k = (k + Q_{x0})\omega_0 + m\omega_s$. The mode m spectrum h_m is

$$h_m(\omega_k - \omega_\xi) = \frac{(|m|+1)^2\tau_b^2}{2\pi^4}\frac{1 + (-1)^{|m|}\cos((\omega_k - \omega_\xi)\tau_b)}{\left(\frac{\tau_b^2}{\pi^2}(\omega_k - \omega_\xi)^2 - (|m|+1)^2\right)^2} \tag{2.76}$$

Figure 2.16 represents the spectra of different azimuthal modes. It is the interaction of these mode spectra with the impedance which determines the coherent frequency shift of the modes.

A quantity called the effective impedance appears in Sacherer's formula

$$Z_{x,eff} = \frac{\sum_{k=-\infty}^{+\infty} Z_x(\omega_k) h_m(\omega_k - \omega_\xi)}{\sum_{k=-\infty}^{+\infty} h_m(\omega_k - \omega_\xi)} \,. \tag{2.77}$$

This value represents the interaction of each mode with the beam coupling impedance. It can be computed for different modes, chromaticities or bunch lengths and can be used to compare different machines and their configurations. Sacherer's formula 2.75 is therefore written

$$(\omega_{c,m} - Q_{x0}\omega_0 - mQ_s\omega_0) = \frac{1}{|m|+1} \frac{je^2 N_b}{4\pi\gamma m_0 c Q_{x0} \tau_b} Z_{x,eff} \,. \tag{2.78}$$

A few observations can be drawn from Eq. 2.77 and 2.78

- The mode shifts and growth rates are proportional to the bunch intensity and inversely proportional to the beam energy.
- Azimuthal modes different from zero have a smaller amplitude and an instability is more difficult to drive.
- The complex mode frequency shift is proportional to $jZ_{x,eff}$. In consequence the imaginary part (inductive or capacitive) of the impedance will affect the mode frequency shift whereas the real part (resistive) of the impedance will affect the mode growth rate. An instability can only appear if the real part of the impedance is non-zero.

Sacherer's formula 2.78 is useful to obtain a first estimate of the mode frequency shifts for a given impedance. However, effects such as mode coupling are not taken into account. We will compare the complex mode frequencies as a function of intensity obtained with DELPHI and Sacherer's formula to highlight their differences. We will also compare them to PyHEADTAIL results. However a post-processing of PyHEADTAIL output is necessary: the code yields time domain data whereas DELPHI and Sacherer's formula directly give the mode complex frequencies. We will now detail these post-processing steps.

2.3.4 Post-processing of PyHEADTAIL data

PyHEADTAIL being a tracking code, it records the turn-by-turn positions and momentas for the six phase space coordinates of all macropaticles. This data must be post-processed to allow comparisons with DELPHI output

An example of an instability obtained with PyHEADTAIL is plotted in Fig. 2.17. The horizontal mean position of the bunch is plotted versus the turn number. To obtain the instability growth rate, one can fit an exponential function to the position signal envelope as shown in the plot. The simulation was performed with a resistive wall impedance for a chromaticity $Q' = +14$ and a bunch intensity of 6×10^{11} p.p.b.. This type of instability will be detailed in part 2.4. We will see that for this chromaticity the most unstable mode has an oscillation frequency shifted by $2Q_s$ from the unperturbed tune.

To obtain the frequencies of the beam oscillation modes, a fast Fourier transform of the signal can be performed. Figure 2.18 shows the frequency spectrum obtained with the instability signal represented in Fig. 2.17. The amplitude of the Fourier transform $A = |\mathcal{F}(\langle x \rangle)(t)|$ is represented. It has been

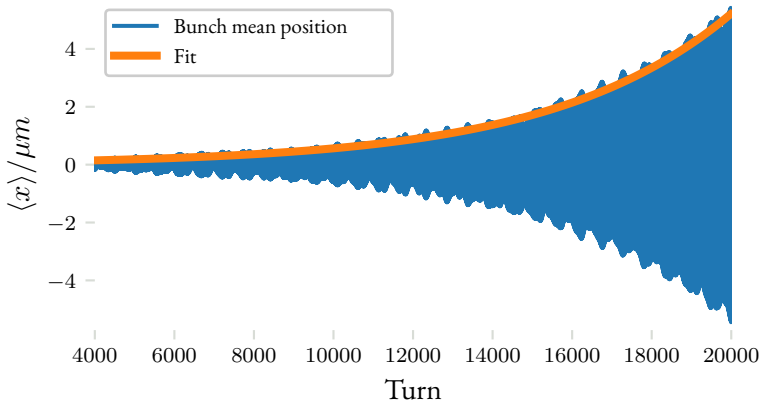

Figure 2.17: Example of an instability signal obtained with PyHEADTAIL. The mean value of the bunch horizontal position is plotted against the turn number in blue. The exponential fit of the signal envelope is plotted in orange.

normalised to the maximum amplitude value A_0 which corresponds to the most unstable mode. One can see that the oscillation mode with the largest amplitude develops at a frequency corresponding to $Q_{x0} - 2Q_s$. Other modes with smaller amplitudes are present at $Q_{x0} - 3Q_s$, $Q_{x0} - Q_s$, Q_{x0} and $Q_{x0} + Q_s$.

The mode spectrum can also be obtained with the SUSSIX algorithm [24] or the Harpy code [107]. These tools can provide more accurate results than the FFT for shorter signal lengths, which will be useful during measurements with the LHC beam for example.

We now have the elements to compare DELPHI and PyHEADTAIL results for different impedance models and beam parameters. Instability growth rates, modes frequency shifts and head-tail profiles will be investigated. The first instability studied will be the head-tail one.

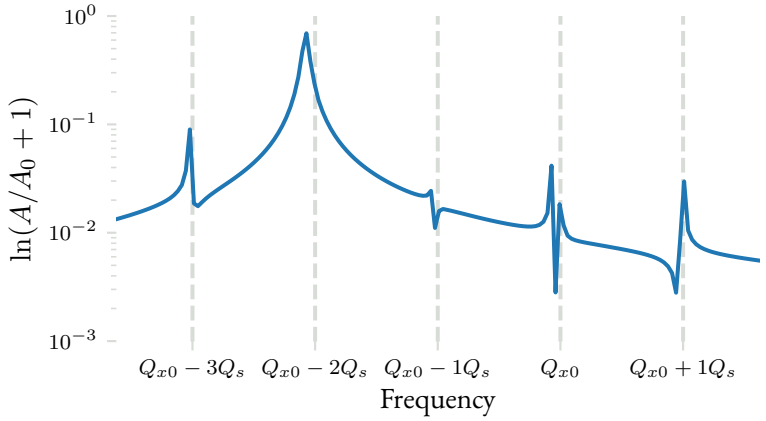

Figure 2.18: Mode spectrum amplitude as a function of the transverse tune frequency. The amplitude A is normalized to the maximum amplitude A_0. The unperturbed transverse tune is Q_{x0}. Positive and negative synchrotron side-bands are plotted as dashed lines. The most unstable mode is at the second negative sideband $Q_{x0} - 2Q_s$. Other modes are present at the other side-bands.

2.4 Head-Tail instability

We saw in the previous part that two main approaches are possible to study beam instabilities: the macroparticle formalism and the mode formalism. The mode formalism and its implementation in the solver DELPHI have been detailed. We will now compare DELPHI and PyHEADTAIL for two types of bunched beam instabilities: the head-tail and the Transverse Mode Coupling Instability. We start with the head-tail instability: it is a chromaticity dependent instability which was encountered early in the history of circular accelerators [67, 111, 128]. Indeed we will see that this instability appears for any bunch intensity and can be quite strong for some chromaticity values.

We will first investigate the case of a purely inductive impedance model. Then in parts 2.4.2 and 2.4.3 the head-tail instability will be studied with a resistive wall impedance model and the LHC impedance model.

2.4.1 Mode spectra with inductive impedance

The Sacherer integral equation 2.65 written before holds for any bunch intensity and any impedance function. Approximations can however be made in the low intensity case as shown in [72]. In this case the different oscillation modes are decoupled. Solving the eigenvalue problem will provide a set of complex frequency shifts ω_c. We saw in part 2.3.3 that the imaginary part of the beam coupling impedance is responsible for the frequency shift whereas the real part is responsible for the growth rate. As a result, if the impedance is purely inductive, the oscillation modes only have a frequency shift and no instability appears.

Let us take a transverse dipolar impedance $Z_x^{dip}(\omega)$ constant and purely inductive at $j25\,\mathrm{M\Omega\,m^{-1}}$. The code DELPHI was used to obtain the complex frequencies ω_c of the oscillation modes, with a beam intensity of 10^5 p.p.b. The other relevant beam parameters are detailed in Table B.1 reported in appendix B. Since the beam intensity is low, the oscillation modes are independent. The Gaussian bunch power spectra as a function of frequency for several azimuthal modes are plotted in Fig. 2.19 with the

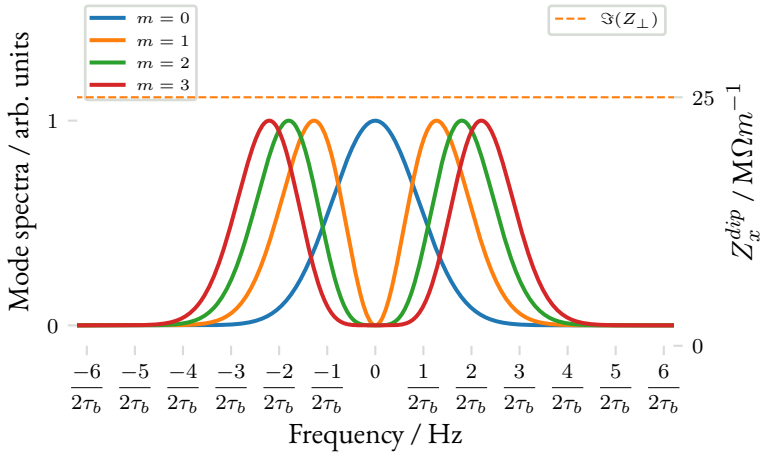

Figure 2.19: Azimuthal mode power spectra for a low intensity bunch in a purely inductive impedance, computed with DELPHI. Several modes are represented, they all have been normalized to their maxima. The imaginary part of the impedance function is plotted alongside as a dashed line. Each mode frequency shift and growth rate result from the convolution of its respective spectra with the impedance function.

constant inductive impedance plotted alongside. All spectra have been normalized to their respective maxima. This case is for a chromaticity $Q'_x = 0$: all the spectra are centered on $f = 0$ GHz. The mode 0 spectrum is peaked at zero frequency while the higher order modes have extrema at higher frequencies. The bunch longitudinal particle distribution is Gaussian with $\sigma_z = 7.5$ cm bunch length. We will also refer to the full bunch length τ_b which corresponds to the $\pm 2\sigma_z$ extent of the bunch expressed in seconds. In this case $\tau_b = \frac{4\sigma_z}{\beta c} = 1$ ns and we can see in Fig. 2.19 that the mode 0 spectra extends to $\frac{1}{\tau_b} = 1$ GHz. The modes obtained with DELPHI are similar to those used in Sacherer's approach represented in Fig.2.16, except for their amplitude.

The Fourier transform of the spectra provides the bunch profile as explained in part 2.3.2. Figure 2.20 shows a series of 15 consecutive snapshots of the head-tail profile for an observer located at a fixed position in the accelerator. The profiles correspond to azimuthal modes $|m| = 0, 1, 2, 3$ oscillations. At $Q'_x = 0$ the mode 0 represented in Fig. 2.20a corresponds to a pure dipolar oscillation of the bunch. Mode 1 represented in Fig. 2.20b corresponds to an oscillation where the head and the tail of the bunch have an opposite phase which can be inferred by the presence of a single node in the signal. These two modes can be described with the simple two-particle model developed in part 2.2. Modes 2 and 3 correspond to more complex motion where multiple fixed points appear along the bunch profile.

When the chromaticity is non-zero, the modes power spectra are shifted by a frequency $\omega_\xi = \xi \frac{\omega_\beta}{\eta}$. Figure 2.21 represents the same modes and impedance as in Fig. 2.19 but with a chromaticity $Q' = -10$. The corresponding chromatic frequency shift is therefore $f_\xi = -350$ MHz. The shift towards the negative frequencies can clearly be seen in Fig. 2.21.

This frequency shift affects the longitudinal profile of the bunch as can be observed in Fig. 2.22 for azimuthal modes $|m| = 0, 1$. In this case the mode 0 is not a pure dipolar oscillation anymore: a traveling wave pattern is present. The envelope of all the profiles remains however similar to the one

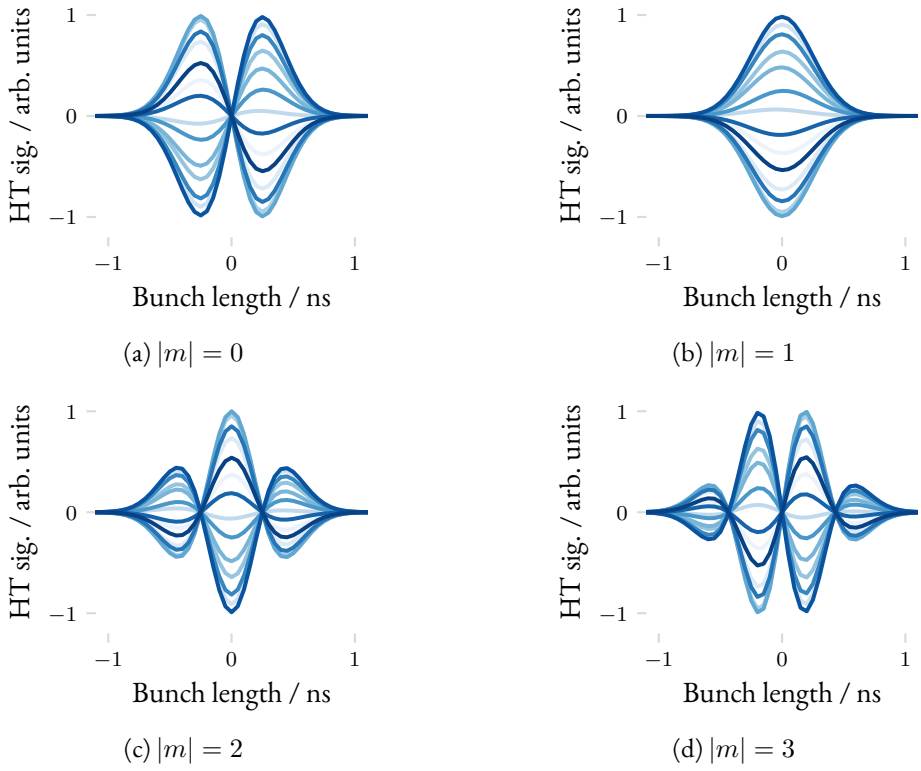

Figure 2.20: Head-tail profiles obtained with DELPHI at $Q'_x = 0$ in an inductive impedance model. The profiles corresponding to azimuthal modes $|m| = 0, 1, 2, 3$ are represented.

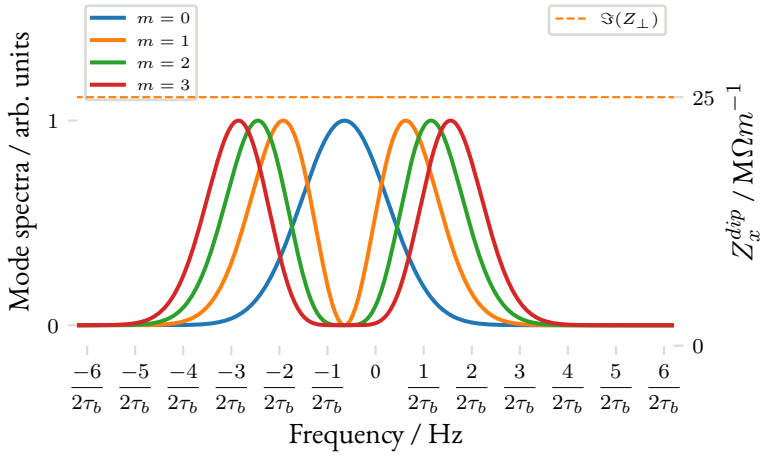

Figure 2.21: Azimuthal modes power spectrum for a low intensity bunch in a purely inductive impedance at $Q' = -10$. All the mode spectra are shifted towards negative frequency values and they interact with a different frequency range of the impedance function.

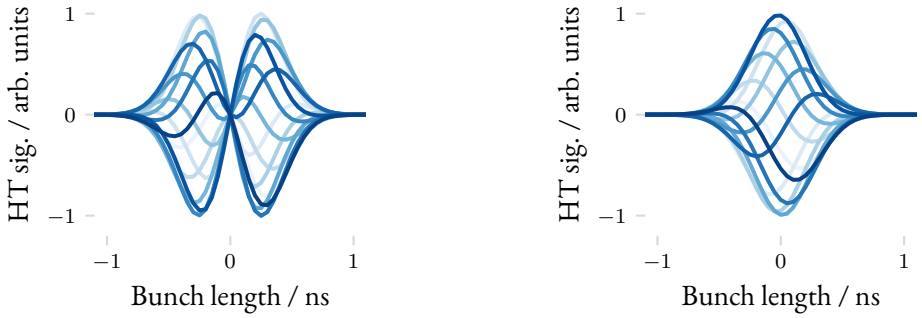

(a) $|l| = 0$ (b) $|l| = 1$

Figure 2.22: Head-tail profiles obtained with DELPHI for $Q' = -10$ and an inductive impedance model. The profiles corresponding to azimuthal modes $|m| = 0, 1$ are represented.

obtained when $Q' = 0$. The same observation can be made for mode 1: the head and the tail are not in phase opposition anymore at a specific turn but superimposing multiple signals reveals the single-node structure observed in the $Q' = 0$ case.

These results are similar to those obtained in the past with analytic derivations or measured in the PS and PSB [59, 72]. In J.-L. Laclare and J.-P.Garnier analytic approach [60, 72] the modes at low intensity are used as a basis for the high intensity stability eigenvalue problem. This approach was implemented in the Valsov solver GALACTIC [91].

We will now study with DELPHI the head-tail instability for a range of chromaticities. As we saw the chromaticity shifts the mode spectra, changing their interaction with the impedance. For a certain chromaticity value, some oscillation modes will interact more strongly with the impedance while others can be stabilised.

2.4.2 Head-tail instability with a resistive wall impedance

We start the study of the head-tail instability with the resistive wall impedance model. As seen in part 2.1.2, both impedance and wake functions can be written exactly given the beam chamber properties. This model is valid for an intermediate frequency regime specified in part 2.1.2. For the study we will take the same cylindrical copper beam pipe as in part 2.1.2. Its radius is $b = 10\,\mathrm{mm}$, its length $L = 27\,\mathrm{km}$ and copper resistivity at 300 K is $1/\sigma_c = 17\,\mathrm{n\Omega\,m}$. The impedance and wake functions were plotted in Fig. 2.2b and 2.2a. The resistive wall impedance is larger at frequencies close to zero: the mode spectrum sampling this frequency region will drive a strong instability. Changing the chromaticity will shift the mode spectra and therefore changes the most unstable mode.

The beam and machine parameters for DELPHI and PyHEADTAIL simulations are detailed in Table 2.4. The PyHEADTAIL and DELPHI convergence parameters are detailed in Table 2.5. They correspond to a

modified version of the LHC top energy beam parameters. Both codes use the smooth approximation for the Twiss beta functions. The average beta functions in the machine are

$$\langle \beta_x \rangle = \frac{R}{Q_{x0}} = \frac{26658.8832}{2\pi \times 62.31} \approx 68.1\,\mathrm{m}\,, \tag{2.79}$$

$$\langle \beta_y \rangle = \frac{R}{Q_{y0}} = \frac{26658.8832}{2\pi \times 60.32} \approx 70.3\,\mathrm{m}\,. \tag{2.80}$$

Table 2.4: Machine and beam parameters for DELPHI and PyHEADTAIL simulations for the head-tail instability study.

Parameter	Value
Impedance	
Impedance model	LHC 2017 flat-top[1] Resistive wall[2]
Machine	
Circumference / m	26 658.8832
Transverse tunes $Q_{x,y}$	62.31/60.32
Momentum compaction factor α_c	3.48×10^{-4}
RF voltage / MV	12
Harmonic number	35 640
Synchrotron tune Q_s	1.909×10^{-3}
Beam	
Number of bunches	1
4 σ bunch length / ns	1.0
Bunch intensity / 10^{11} p.p.b.	2 and 6[3]
Chromaticity Q'	−50 to 50

[1] Impedance and wake model as described in [8, 103] and available at [143].
[2] Resistive wall impedance and wake computed analytically assuming a 27 km long cylindrical beam pipe of radius $r = 10\,\mathrm{mm}$, made of copper at room temperature.
[3] An intensity of 2×10^{11} p.p.b. was used for simulations with the LHC impedance model, whereas the intensity was increased to 6×10^{11} p.p.b. for the resistive wall impedance model.

We first investigate the head-tail instability when the transverse damper is deactivated. The study is made for a fixed bunch intensity, scanning the horizontal chromaticity from $Q' = -50$ to $Q' = 50$. These corresponds to chromatic frequencies of $f_\xi = \pm 1.6\,\mathrm{GHz}$. The RMS bunch length used is $\sigma_z = 7.5\,\mathrm{cm}$ which corresponds to a full bunch length of $\tau_b = 1\,\mathrm{ns}$. The wake field and the impedance in the vertical plane are set to zero so that the instability develops only in the horizontal plane.

Figure 2.23 represents the real part of the mode complex frequency shifts as a function of chromaticity. DELPHI output is represented with blue dots. The mode with the largest negative imaginary part is highlighted in the plots. PyHEADTAIL results are plotted in a yellow-purple gradient, where purple

Table 2.5: DELPHI and PyHEADTAIL specific parameters for the head-tail instability study.

Parameter	Value
PyHEADTAIL	
Software version	1.13.1
Number of slices for the longitudinal distribution	100
Longitudinal cut / σ_z	± 8
Number of macroparticles	10^6
Number of turns	500×10^3
DELPHI	
Plane simulated	Horizontal
Convergence criterion[1]	5×10^{-3}

[1] DELPHI convergence criterion crit checks at a given iteration i the imaginary part of the mode imaginary part. If $|\frac{\Im(\omega_i)-\Im(\omega_{i-1})}{\Im(\omega_{i-1})}| < \text{crit}$, the computation is stopped. Otherwise the matrix size is increased by computing new azimuthal and radial modes.

indicates the modes which have the largest spectral amplitude. The same color scale will be used for similar plots within the chapter. The modes were obtained using Harpy for the post-treatment [107].

Figure 2.24 shows the growth rates of the modes $-\Im(\omega_{c,x})$ as a function of chromaticity. For DELPHI simulations only the most unstable mode growth rate is represented. For PyHEADTAIL we saw in part 2.3.4 that the growth rate is directly obtained with the turn-by-turn transverse position data of the bunch. The positive chromaticities part is magnified in Fig. 2.25. An excellent agreement between the two codes over the whole chromaticity range is achieved.

Figure 2.24 shows that for negative chromaticities a quick instability develops. Associated with the most unstable mode in Fig. 2.23, we can deduce that it is the mode 0 which is the most unstable at negative frequencies. For negative chromaticities and above the transition energy, the modes spectra are shifted towards negative frequencies. The mode 0 spectra will therefore sample an impedance Z_x which has $\Re(Z_x) < 0$ and $\Im(Z_x) > 0$ as Eq. 2.20 and Fig. 2.2b show. From Sacherer's formula 2.78, we saw that the mode complex shift is proportional to jZ_x so the mode will have a large imaginary component, hence the quick instability.

For positive chromaticities, mode 0 samples an impedance which has $\Re(Z) > 0$ and $\Im(Z) > 0$. The mode frequency will now have a positive imaginary part and therefore will be stable. The higher order modes however will become unstable as they are now sampling more of the negative frequency region of the impedance. When the chromaticity becomes higher, the most unstable mode changes and the instability growth rate becomes smaller.

The head-tail profile of all modes can be obtained with DELPHI and PyHEADTAIL for the different simulated chromaticities. Figure 2.26 shows a selection of signals for the most unstable mode obtained with DELPHI. We can see that the profile is modified by chromaticity:

- At $Q' = -3$, mode 0 is the most unstable mode and the profile has no node as seen in Fig. 2.26a.

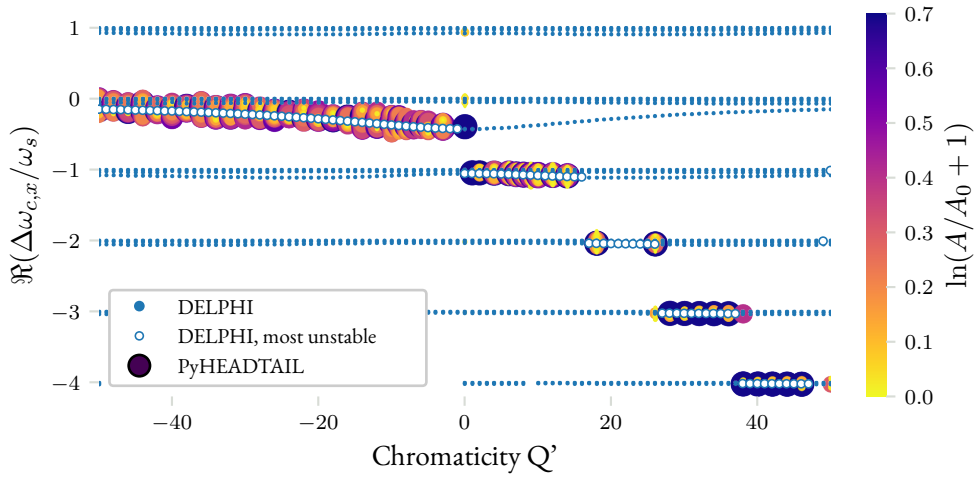

Figure 2.23: Real part of the complex mode frequency shifts as a function of chromaticity, comparing `PyHEADTAIL` and `DELPHI` simulations. The resistive wall impedance is used and the damper is deactivated.

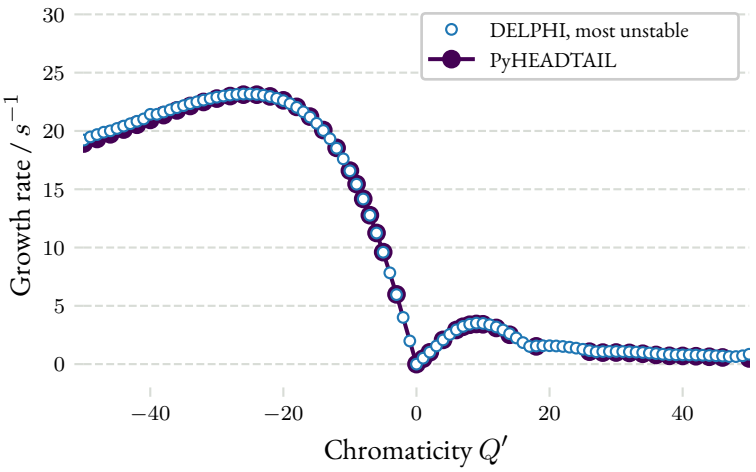

Figure 2.24: Instability growth rate as a function of chromaticity, comparing `PyHEADTAIL` and `DELPHI` simulations. Only the most unstable mode is figured in this case. The resistive wall impedance is used and the damper is deactivated.

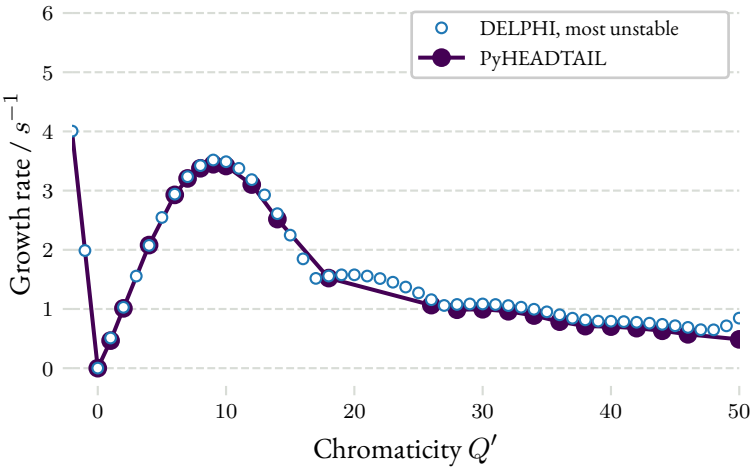

Figure 2.25: Zoom on the positive chromaticities of the instability growth rate of Fig. 2.24.

- At $Q' = 5$, mode -1 is the most unstable and the profile contains one node as seen in Fig. 2.26b.
- At $Q' = 25$, mode -2 is the most unstable and the profile contains two nodes as seen in Fig. 2.26c.
- At $Q' = 35$, mode -3 is the most unstable and the profile contains three nodes as seen in Fig. 2.26d.

All the signals also exhibit the profile modulation caused by chromaticity. The higher the chromaticity, the faster this modulation gets.

These signals can be compared to those obtained with PyHEADTAIL. Figure 2.27 shows the comparison for a chromaticity of $Q' = -3$ and Fig. 2.28 for $Q' = 26$. Excellent agreement is also reached on the head-tail profiles obtained with the two methods.

We will now study the effect of the transverse damper on beam stability. The transverse damper is a feedback system: it detects the transverse position of a bunch which is becoming unstable, then computes and applies an electromagnetic kick to restore its transverse position [81, 150]. In an ideal feedback the kick would be applied right after the position detection and would immediately restore the bunch position. But because of the hardware limitations, the feedback system will apply small kicks over several turns after a certain delay. The damper provides therefore a momentum kick x'_d proportional to the bunch dipole moment

$$x'_d = \frac{g\langle x \rangle \sin \phi_d}{\beta_d} \tag{2.81}$$

where g is damper gain, $\langle x \rangle$ is the mean position of the bunch, ϕ_d is the damper phase and β_d is the Twiss beta function value at the damper location. A damper gain $g = 0$ corresponds to the absence of a transverse damper whereas a gain $g = 1$ corresponds to an instantaneous damping. The damping time τ_D computed in unit of turns is the inverse of the damping gain $\tau_D = 1/g$.

In the LHC the transverse damper (ADT) is a bunch-by-bunch feedback: each bunch in the beam will receive a correction kick. The system bandwidth of 20 MHz [66] guarantees that the kick affects

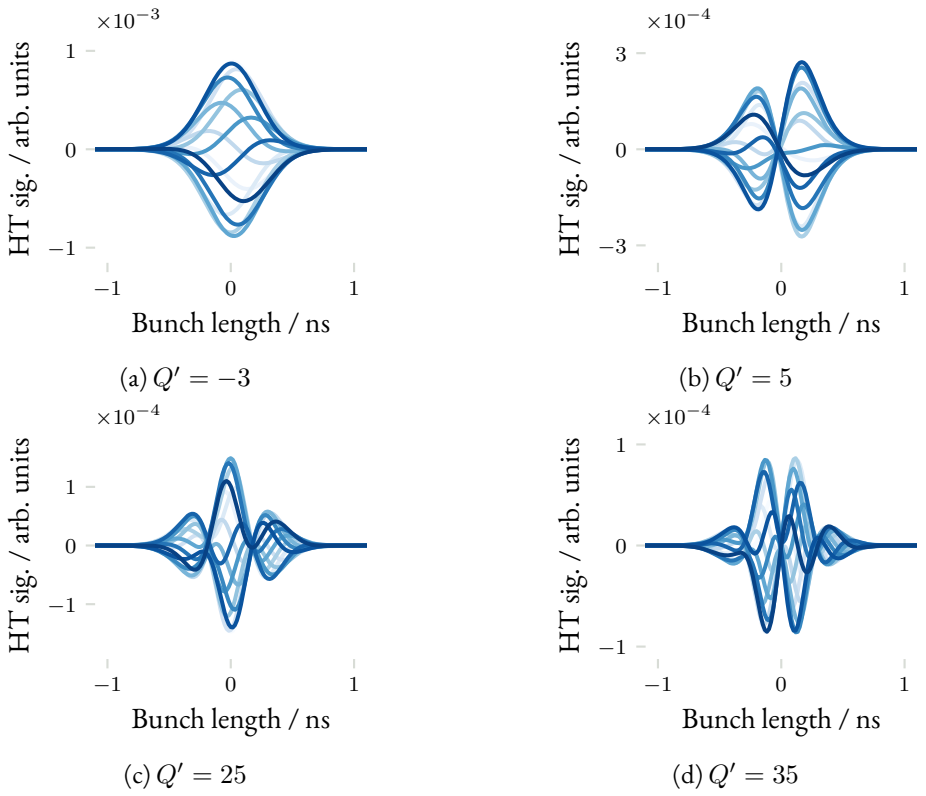

(a) $Q' = -3$ (b) $Q' = 5$

(c) $Q' = 25$ (d) $Q' = 35$

Figure 2.26: Head-tail profiles obtained with DELPHI for different chromaticities, at a fixed bunch intensity of 6×10^{11} p.p.b. The resistive wall impedance is used and the damper is deactivated.

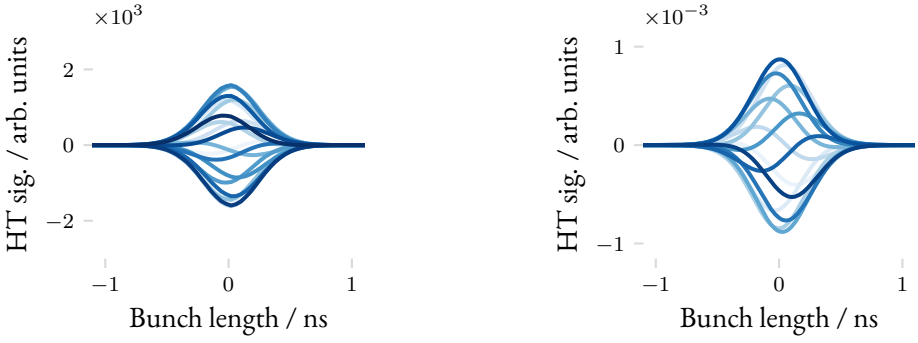

(a) PyHEADTAIL (b) DELPHI

Figure 2.27: Head-tail profiles obtained with PyHEADTAIL (left plot) and DELPHI (right plot) for a chromaticity of $Q' = -3$. The resistive wall impedance is used and the damper is deactivated.

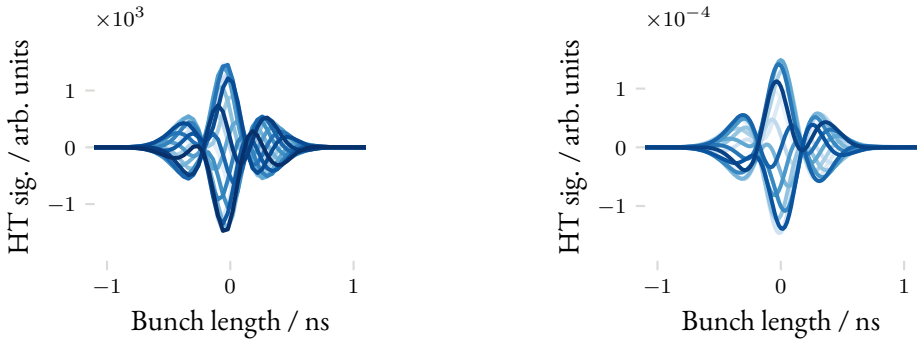

(a) PyHEADTAIL (b) DELPHI

Figure 2.28: Head-tail profiles obtained with PyHEADTAIL (left plot) and DELPHI (right plot) for a chromaticity of $Q' = 26$. The resistive wall impedance is used and the damper is deactivated.

only the selected bunch. The ADT was designed to damp injection oscillations and coupled bunch instabilities [39] but is now routinely used in operation to stabilize both coupled and single bunch instabilities [66]. It can also be used to excite the beam for measurement purposes and its beam position monitors can be used to record the turn-by-turn position of all bunches for several thousands of turns [144].

In the tracking code PyHEADTAIL the behavior of the damper is implemented following the previous formula. More complex cases are also available: the feedback phase can be changed so that the ADT can affect the bunch tune or drive an instability.

In DELPHI, the transverse damper is implemented as a delta function impedance [101], corresponding to a constant wake. Because of the limited bandwidth of the ADT hardware, the damper is more efficient at damping mode 0, a rigid bunch oscillation when $Q' = 0$, than higher order modes of oscillation.

Figure 2.29 shows the real part of the mode frequency shifts as a function of chromaticity when the transverse damper has been activated. The agreement between DELPHI and PyHEADTAIL is again excellent over the full chromaticity range. One can see that the transverse damper strongly affects the beam instabilities by acting on the dipolar motion of the bunch. For $Q' \in [-20, 0]$, mode 0 is not the most unstable one anymore. For positive chromaticities, the damper also affects the higher-order modes due to the dipole moment produced by chromaticity.

Looking at the instability growth rate in Figs. 2.30 and 2.31, we can see that they are reduced compared to the case without damper. For $Q' \in [-20, 0]$ the mode 0 growth rate is reduced to almost zero. For chromaticities $Q' < -20$, a positive growth rate is still present and comparable to the case without damper. At positive chromaticities, the growth rates of higher order modes are reduced by a factor ~ 2 compared to the case without damper, as can be observed by comparing Figs. 2.24 and 2.30.

We can examine the head-tail profiles obtained with DELPHI and compare them to those obtained with PyHEADTAIL. Figure 2.32 shows the profiles for the same chromaticities as the case without damper. We can see that for the negative chromaticity case in Fig. 2.32a, the most unstable mode obtained with DELPHI is different from the one obtained when the damper was deactivated in Fig. 2.26a. The transverse feedback damps the mode 0 oscillation and an other mode becomes the most unstable, but with a much lower growth rate.

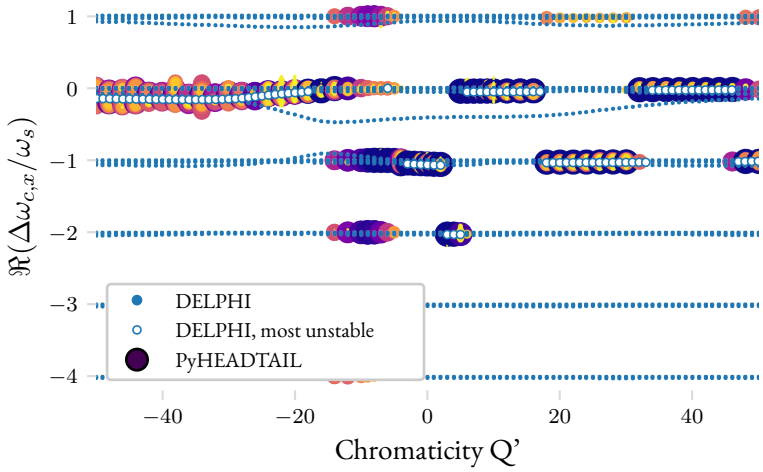

Figure 2.29: Real part of the complex mode frequency shifts as a function of chromaticity, comparing PyHEADTAIL and DELPHI simulations. The resistive wall impedance is used and the damper is activated with a damping time of 100 turns.

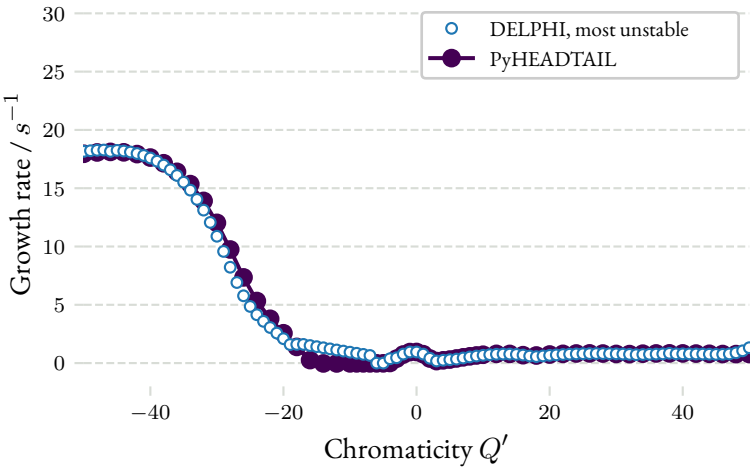

Figure 2.30: Instability growth rate as a function of chromaticity, comparing PyHEADTAIL and DELPHI simulations. Only the most unstable mode is figured in this case. The resistive wall impedance is used and the damper is activated with a damping time of 100 turns.

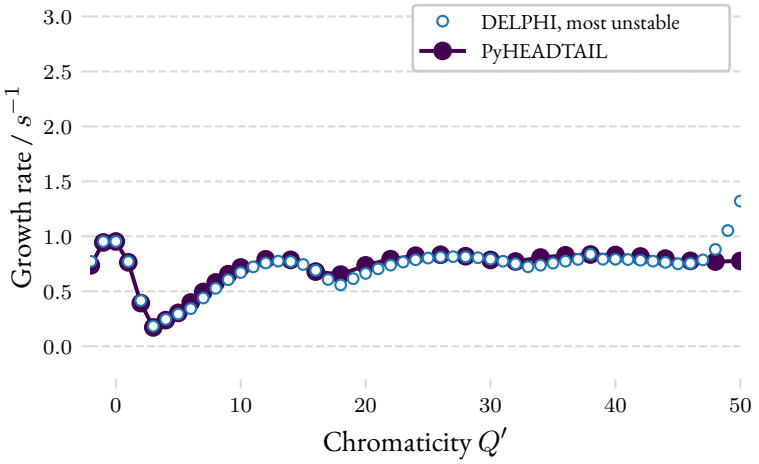

Figure 2.31: Zoom on the positive chromaticities of Fig. 2.30.

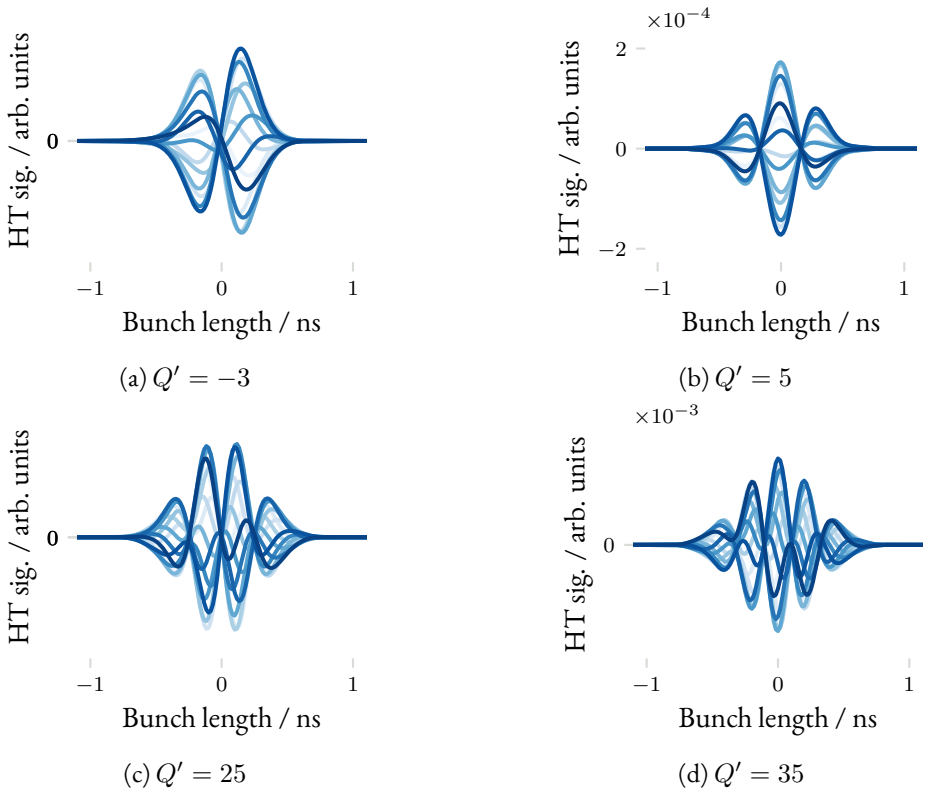

Figure 2.32: Head-tail profiles obtained with DELPHI for different chromaticities, at a fixed bunch intensity of 6×10^{11} p.p.b. The resistive wall impedance is used and the damper is activated with a damping time of 100 turns.

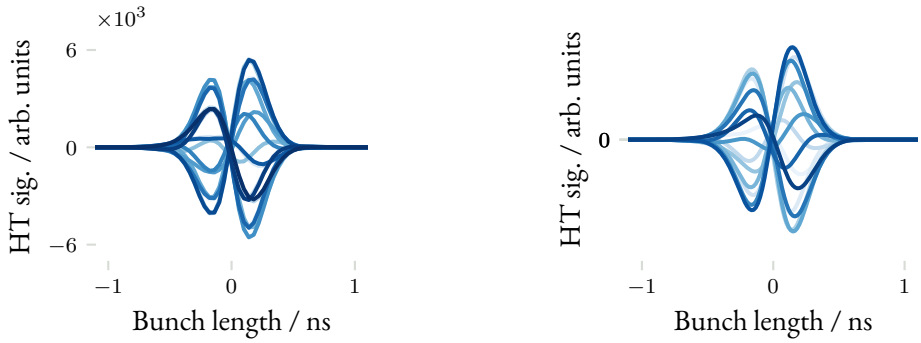

(a) PyHEADTAIL (b) DELPHI

Figure 2.33: Head-tail profiles obtained with PyHEADTAIL (left plot) and DELPHI (right plot) for a chromaticity of $Q' = -3$. The resistive wall impedance is used and the damper is activated with a damping time of 100 turns.

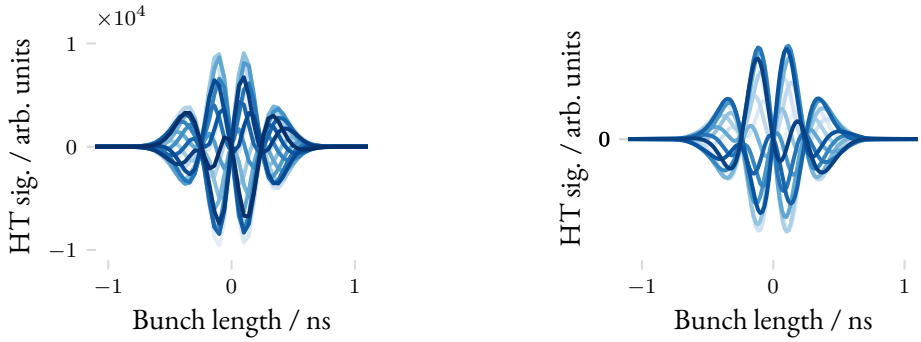

(a) PyHEADTAIL (b) DELPHI

Figure 2.34: Head-tail profiles obtained with PyHEADTAIL (left plot) and DELPHI (right plot) for a chromaticity of $Q' = 26$. The resistive wall impedance is used and the damper is activated with a damping time of 100 turns.

Again the results of DELPHI and PyHEADTAIL are in good agreement for the head-tail profile as can be observed for example at $Q' = -3$ in Fig. 2.33 and at $Q' = 26$ in Fig. 2.34.

We have seen with the simple resistive wall impedance model that the two approaches, macro-particle tracking and Vlasov's equation solver, provide consistent results both without and with the damper activated. We can now use the more complex and realistic impedance model of the LHC.

2.4.3 Head-tail instability with the LHC impedance model

As for the previous case we will start the analysis with the damper deactivated. Figure 2.35 compares the real parts of the modes. The results of a third code, Nested Head-Tail Vlasov Solver (NHTVS) [42] are also plotted in green triangles. This Vlasov solver uses a different approach from DELPHI to solve Sacherer's integral equation. The longitudinal distribution is assumed to be a sequence of equally charged concentric rings. A basis of head-tail modes is computed for each of these rings and grouped

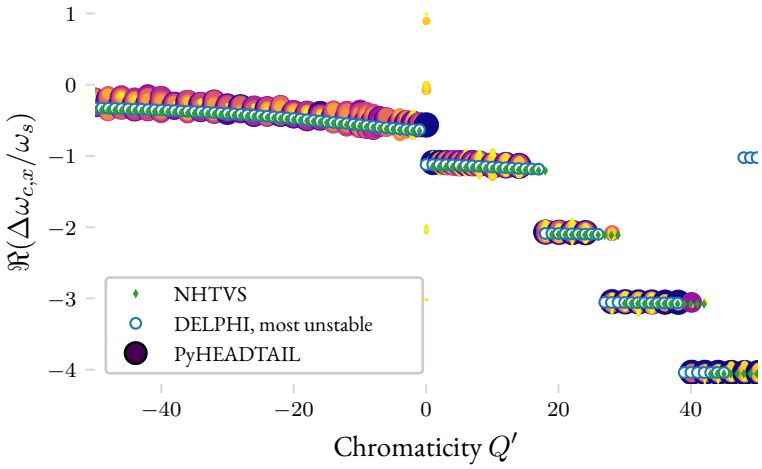

Figure 2.35: Real part of the complex mode frequency shifts as a function of chromaticity, comparing PyHEADTAIL and DELPHI simulations. The LHC impedance is used and the damper is deactivated.

in an eigenvalue problem. Figures 2.36 and 2.37 show the most unstable mode growth rate obtained with the codes. Both plots confirm the excellent agreement which was obtained in the resistive wall impedance case. Minor discrepancies on the mode growth rate between DELPHI and PyHEADTAIL are present for chromaticities $Q' \sim 45$. These are potentially caused by DELPHI convergence scheme: the convergence criteria checks the most unstable mode imaginary part. To reach the convergence on this value, DELPHI increases both the number of azimuthal and radial modes to be computed. If the computation is stopped because of too large matrices, the modes remain potentially non-converged.

We can see that bunch behavior is similar to the resistive wall impedance case, with the shift of head-tail modes at positive chromaticities and the mode 0 dominating the negative chromaticities. The head-tail profiles are also very similar, and the two codes results are again consistent. Figure 2.38 shows DELPHI and PyHEADTAIL reconstructions of the profiles for $Q' = -3$, and Fig. 2.39 for $Q' = 20$.

Activating the transverse damper with the same damping time of 100 turns as done previously results in a behavior similar to the resistive-wall case. Results are plotted in Figs. 2.40, 2.41 and 2.42.

At negative chromaticities the mode 0 is damped by the feedback for $Q' \in [-30, 0]$, as can be seen in Fig. 2.40. But when the chromaticity is set to a large negative value, mode 0 becomes unstable again. Figure 2.43 shows the signal reconstructed with DELPHI for $Q' = -35$ and $Q' = -45$ The signals envelope corresponds to a mode 0 instability and the head-tail profiles show a large phase shift because of the chromaticity value.

Similarly to the resistive wall impedance case, some minor discrepancies remain between the two codes. In the $Q' \in [-30, -10]$ and in the $Q' \in [40, 50]$ ranges, the growth rate obtained with DELPHI are different from the ones obtained with PyHEADTAIL. The discrepancy for these chromaticities can also be observed on the real part of the modes frequencies in Fig. 2.40. The source of these discrepancies was confirmed to be DELPHI convergence scheme [102]. Overall the agreement between DELPHI and PyHEADTAIL is excellent for the LHC impedance model for both cases without and with the transverse damper.

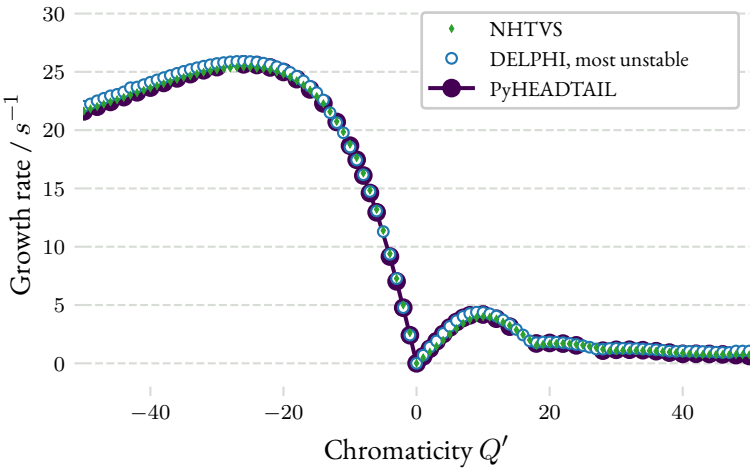

Figure 2.36: Instability growth rate as a function of chromaticity, comparing `PyHEADTAIL` and `DELPHI` simulations for the LHC impedance without transverse damper. Only the most unstable mode is represented. The LHC impedance is used and the damper is deactivated.

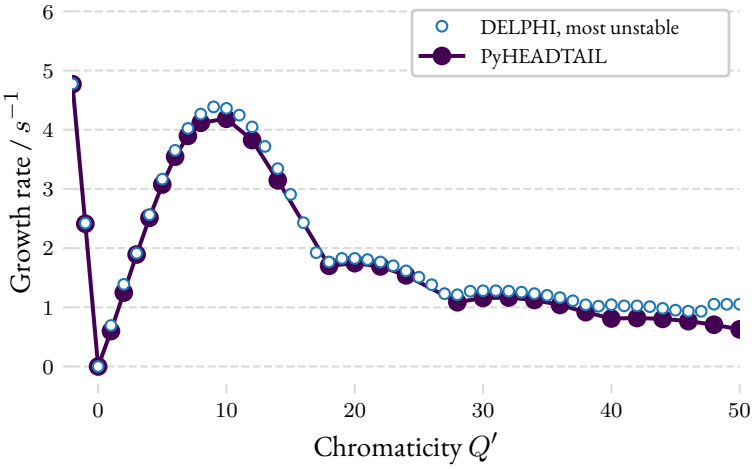

Figure 2.37: Zoom on the positive chromaticities of the instability growth rate of Fig. 2.36.

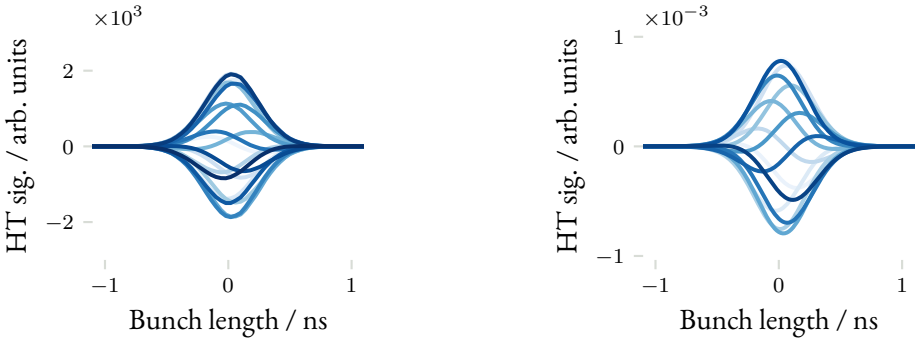

(a) PyHEADTAIL (b) DELPHI

Figure 2.38: Head-tail profiles obtained with PyHEADTAIL (left plot) and DELPHI (right plot) for a chromaticity of $Q' = -3$ with the LHC impedance model. The LHC impedance is used and the damper is deactivated.

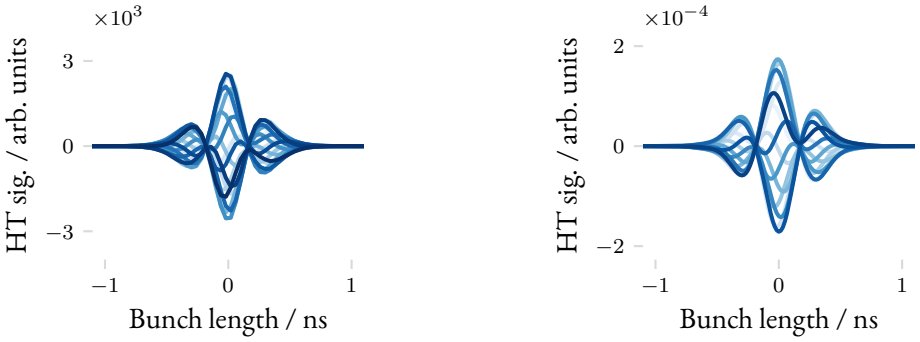

(a) PyHEADTAIL (b) DELPHI

Figure 2.39: Head-tail profiles obtained with PyHEADTAIL (left plot) and DELPHI (right plot) for a chromaticity of $Q' = 20$ with the LHC impedance model. The LHC impedance is used and the damper is deactivated.

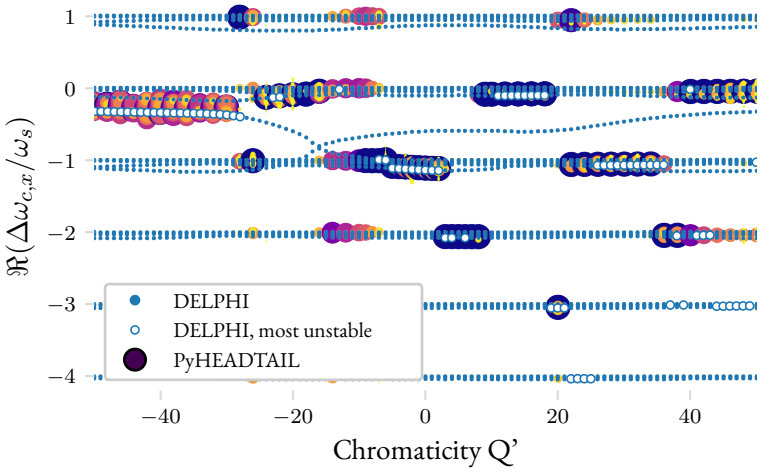

Figure 2.40: Real part of the complex mode frequency shifts as a function of chromaticity, comparing PyHEADTAIL and DELPHI simulations. The LHC impedance is used and the damper is activated with a damping time of 100 turns.

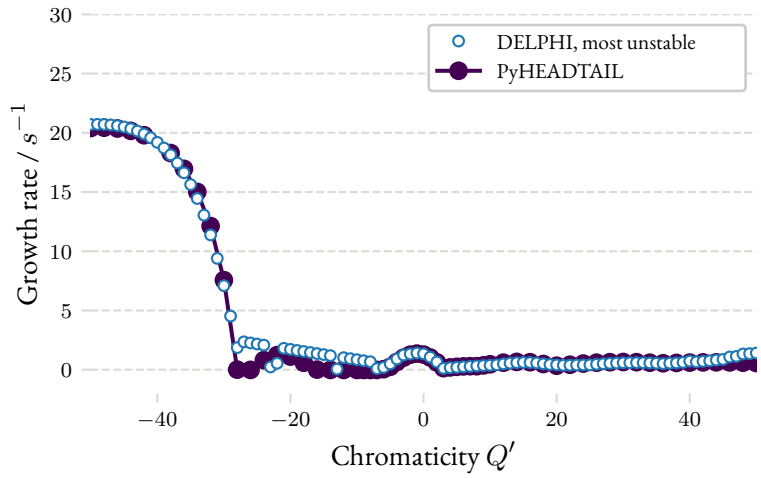

Figure 2.41: Instability growth rate as a function of chromaticity, comparing PyHEADTAIL and DELPHI simulations. Only the most unstable mode is represented. The LHC impedance is used and the damper is activated with a damping time of 100 turns.

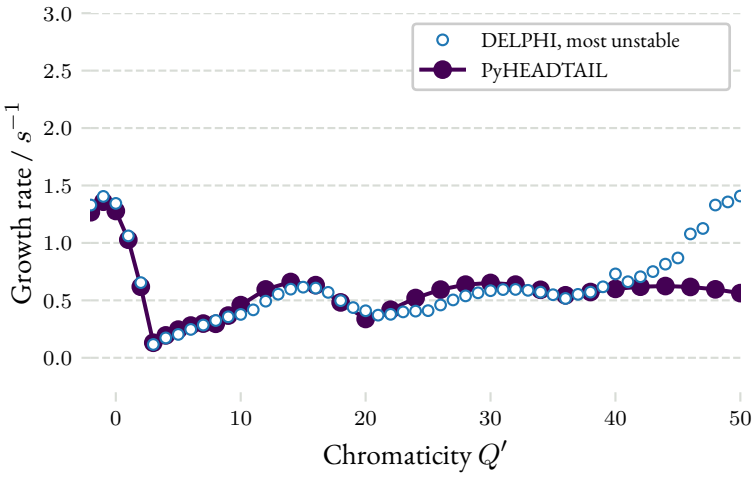

Figure 2.42: Zoom on the positive chromaticities of the instability growth rate of Fig. 2.41.

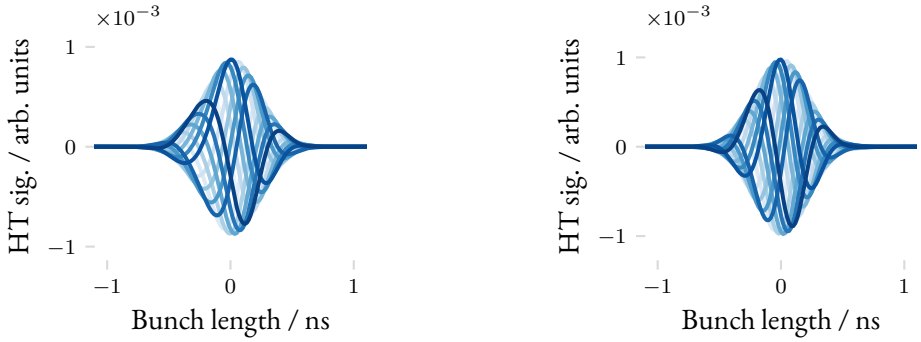

(a) $Q' = -35$ (b) $Q' = -45$

Figure 2.43: Head-tail profiles obtained with DELPHI at negative chromaticities. The LHC impedance is used and the damper is activated with a damping time of 100 turns.

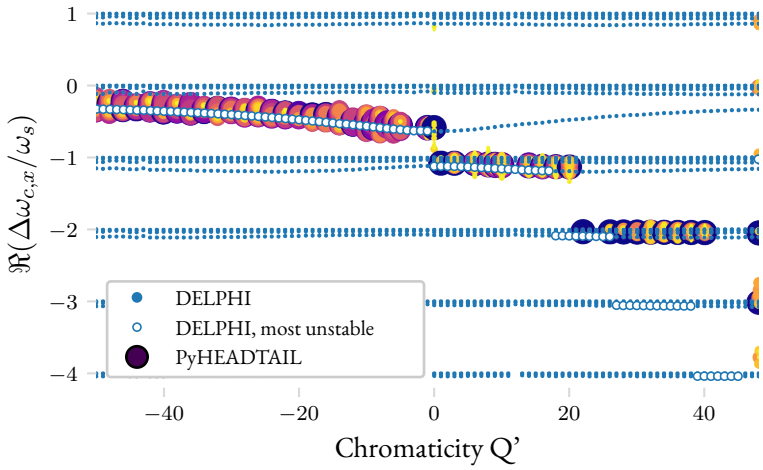

Figure 2.44: Real part of the complex mode frequency shifts as a function of chromaticity, comparing PyHEADTAIL and DELPHI simulations. The LHC impedance is used and the damper is deactivated. Non-linear longitudinal motion is activated in PyHEADTAIL.

Effect of non-linear longitudinal motion on the head-tail instability

We saw in part 2.3.2 that DELPHI assumes that the bunch synchrotron motion is linear. In reality synchrotron motion is non-linear and those effects can be simulated with PyHEADTAIL. The effect of non-linear synchrotron motion will be investigated with PyHEADTAIL for the LHC impedance without damper and compared to DELPHI results. Figure 2.44 shows the real part of the modes frequency for the same beam parameters and chromaticity range as before. The imaginary parts of the modes are plotted in Figs. 2.45 and 2.46.

The effect of non-linear synchrotron motion is noticeable for chromaticities $Q' \geq 18$. In Fig. 2.44 we can observe with DELPHI a shift of the most unstable mode from $m = -1$ to $m = -2$ at $Q' = 18$. With PyHEADTAIL this shift occurs at $Q' = 20$. The effect is even more visible for the $m = -2$ to $m = -3$ shift: while DELPHI predicts it at $Q' = 26$, PyHEADTAIL predicts it at $Q' \approx 50$. In Fig. 2.46, for $Q' = 10$, we see that the growth rate obtained with PyHEADTAIL is reduced by ∼20 % compared to DELPHI simulations. The effect of non-linear synchrotron motion is therefore visible, even though the LHC bunch is rather short (1 ns full bunch length in a 2.5 ns long RF bucket) and thus is less sensitive to the non-linear synchrotron motion. Since the synchrotron motion affects the longitudinal phase, and thus the bunch length, the modes spectrum are affected and their interaction with the impedance affects in turn the modes frequencies and growth rates. This effect could be more important when the bunch is filling up the RF bucket, for example in the PSB beams [96].

We saw with the head-tail instability a first important type of coherent beam instability. This is in fact the most commonly encountered in accelerators since the chromaticity is usually different from zero. For a machine operating above the transition energy, the chromaticity is often chosen to be slightly positive. Then it is a mode $l = -1$ or $l = -2$ which is unstable. These modes can be damped by a transverse damper as we saw or by the accelerator non-linearities which creates a spread of the particle tunes.

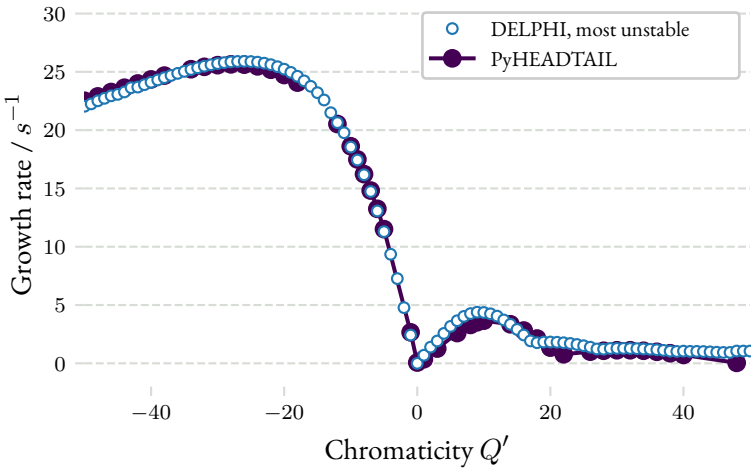

Figure 2.45: Instability growth rate as a function of chromaticity, comparing PyHEADTAIL and DELPHI simulations. The LHC impedance is used and the damper is deactivated. Non-linear longitudinal motion is activated in PyHEADTAIL.

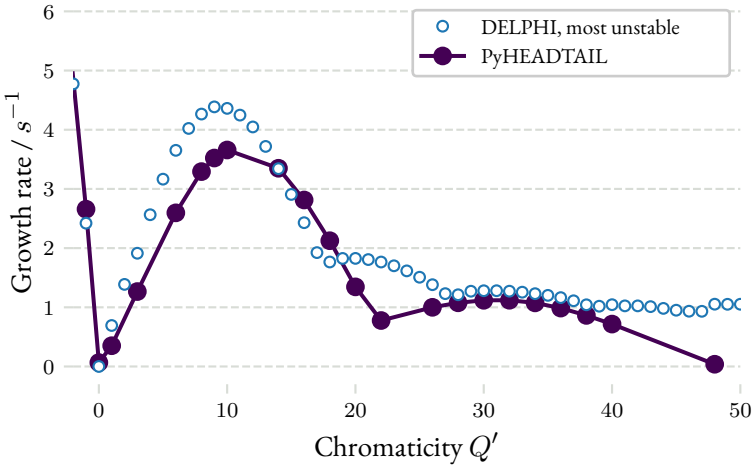

Figure 2.46: Zoom on the positive chromaticities of Fig. 2.45.

The head-tail instability occurs for any bunch intensity as Sacherer's formula 2.78 shows. In this approximation the growth rate and mode frequency shifts are linear with the bunch intensity and the effective impedance. In the case studied previously, we saw that for $Q' = 0$ the instability is much weaker than for $Q' \neq 0$ and therefore easier to mitigate. However at $Q' = 0$, when the bunch intensity is increased, a fast instability can develop. The two codes DELPHI and PyHEADTAIL will now be compared in this configuration.

2.5 Transverse Mode Coupling Instability

We saw that the head-tail instability is chromaticity dependent but occurs for any bunch intensity. The instability was however weaker for chromaticities close to zero. For $Q' = 0$ we will see that this observation is valid for a certain intensity range and that above a certain threshold a fast instability, the Transverse Mode Coupling Instability, appears. We will start the study with the simple broadband resonator model, comparing the results of PyHEADTAIL and DELPHI without and with the transverse damper. We will then use this model to investigate the very high intensity behavior where the instability rise-time becomes comparable to the synchrotron period. Finally we will perform the study with the LHC impedance model.

2.5.1 TMCI with a broadband resonator impedance

The first comparison between DELPHI and PyHEADTAIL is made for the case of a broadband resonator impedance. This impedance model was described in 2.1.3 and shown in Fig. 2.3b, and can be used to study single bunch instabilities. The low quality factor used for the resonator ensures that the wake fields remaining after the bunch passage are negligible.

The beam parameters are the same as those used for the head-tail instability study found in Table 2.4. Table 2.6 only lists the parameters which have been modified for this study. The parameters specific to DELPHI and PyHEADTAIL are listed in Table 2.7.

Table 2.6: Machine and beam parameters for DELPHI and PyHEADTAIL simulations.

Parameter	Value
Impedance	
	LHC 2017 flat-top[1]
Impedance model	Broad-band resonator[2]
Beam	
Number of bunches	1
4 σ bunch length τ_b / ns	1.0
Bunch intensity / 1×10^{11} p.p.b.	0 to 10
Chromaticity Q'	0

[1] LHC impedance and wake model as described in [103] and available at [143].
[2] Resonator impedance with resonance frequency $f_{res} = 2\,\mathrm{GHz}$, shunt impedance $R_s = 25\,\mathrm{M\Omega\,m^{-1}}$ and quality factor $Q = 1$.

Table 2.7: DELPHI and PyHEADTAIL specific parameters for the TMCI simulations.

Parameter	Value
PyHEADTAIL	
Software version	1.13.1
Number of slices for the longitudinal distribution	100
Longitudinal cut / σ_z	± 8
Number of macroparticles	10^6
Number of turns	70×10^3
DELPHI	
Plane simulated	Horizontal
Convergence criterion	5×10^{-3}

We saw with the two particle model in part 2.2 that the head and the tail of the bunch regularly exchange their position, mitigating the destabilizing effect of the impedance. However when the bunch intensity is too high or the wake field too strong, the bunch becomes unstable. Figure 2.47 shows the real part of the complex mode frequency shifts obtained with PyHEADTAIL and DELPHI as a function of bunch intensity. We can see that the mode 0 is shifted down as intensity increases. On the other hand the mode -1 stays almost constant with intensity. When the bunch intensity reaches 5×10^{11} p.p.b., the two modes have an identical oscillation frequency, they couple and a fast instability arises.

The instability growth rate in Fig. 2.48 confirms this threshold at 5×10^{11} p.p.b.. A growth rate of $10\,\mathrm{s}^{-1}$ corresponds to a rise-time of 100 ms, whereas the revolution period is $T_0 = \frac{1}{f_0} = 89\,\mu\mathrm{s}$. The instability therefore develops in approximately 1000 turns. The growth rate increases with the beam intensity, and at 7.5×10^{11} p.p.b., a second step is present. A close examination of the real part of the modes frequency in Fig. 2.47 shows that a second mode coupling occurs at this intensity, between modes -1 and -2.

The TMCI intensity threshold can be approximated using Sacherer's formula 2.78. With this model the mode 0 frequency shift is linear with intensity and proportional to the effective impedance $Z_{eff,0}$. Using Sacherer's mode expression from Eq. 2.76, for a chromaticity $Q' = 0$ we obtain an effective impedance $Z_{eff,0} = 24.9\mathrm{j}\,\mathrm{M}\Omega\,\mathrm{m}^{-1}$. The mode 0 frequency needs to be shifted by $-\omega_s$ to reach and couple with the mode -1 frequency. Using Sacherer's formula 2.78 this leads to the condition

$$N_b^{thresh} = -j \frac{1}{Z_{eff,0}} \frac{4\pi\gamma m_0 c Q_{x0} \tau_b \omega_s}{e^2} \,. \tag{2.82}$$

This simple formula gives for this first case a threshold intensity of 5.5×10^{11} p.p.b., close to the value of 5×10^{11} p.p.b. obtained with DELPHI and PyHEADTAIL. The difference is mainly caused by the fact that the mode 0 shift is not linear anymore when the intensity is close to the TMCI threshold and that mode -1 also has a small shift as can be seen in Fig. 2.47.

A series of signals obtained with DELPHI for various bunch intensities are reported in Fig. 2.49. For an intensity below the TMCI threshold, Fig. 2.49a shows the mode 0 executing a dipolar oscillation,

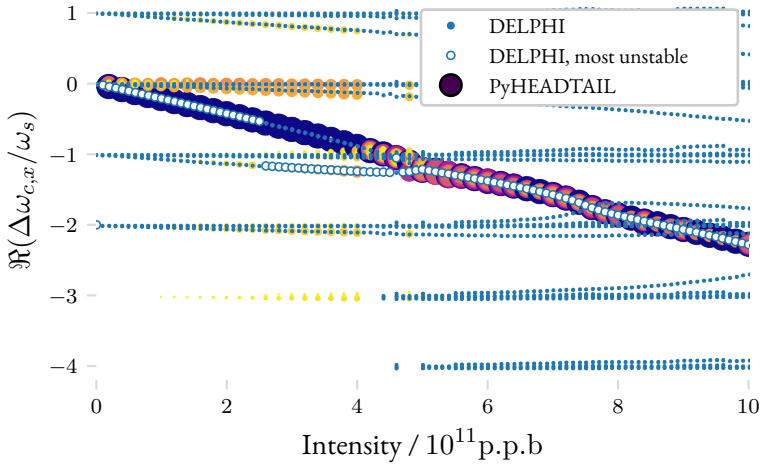

Figure 2.47: Real part of the complex mode frequency shifts as a function of bunch intensity, comparing PyHEADTAIL and DELPHI simulations. The broadband impedance is used and the damper is deactivated.

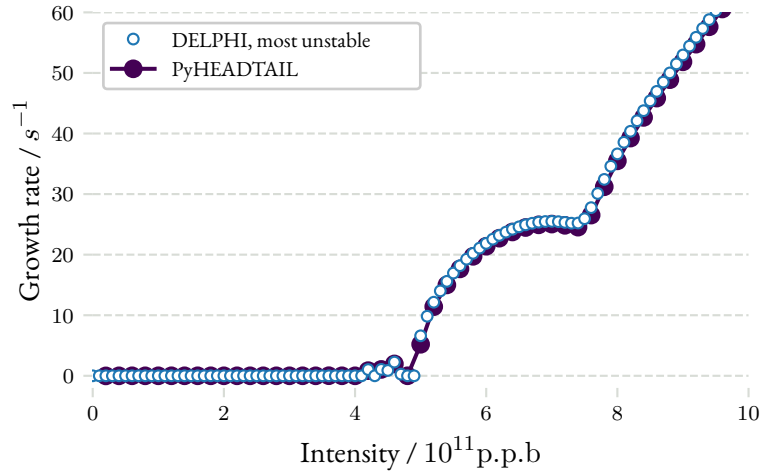

Figure 2.48: Instability growth rate as a function of bunch intensity, comparing PyHEADTAIL and DELPHI simulations. Only the most unstable mode are compared in this case. The broadband impedance is used and the damper is deactivated.

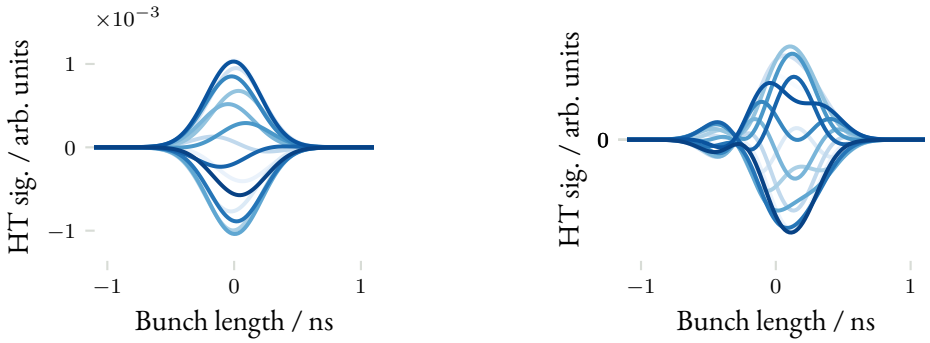

(a) 0.6×10^{11} p.p.b.

(b) 4.6×10^{11} p.p.b.

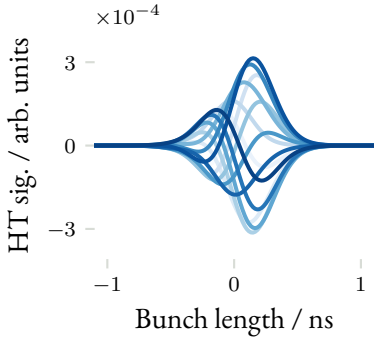

(c) 5.6×10^{11} p.p.b.

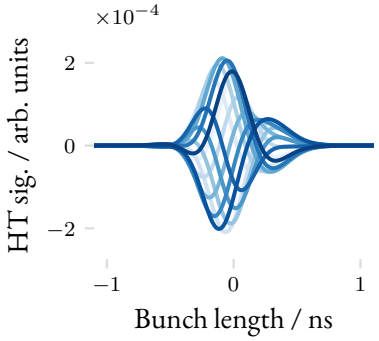

(d) 9.6×10^{11} p.p.b.

Figure 2.49: Head-tail profiles obtained with DELPHI for different bunch intensities below and above the TMCI threshold. The broadband impedance is used and the damper is deactivated.

appearing as a signal with no node and with a standing wave structure turn after turn. As the bunch intensity increases and becomes close to the TMCI threshold, a travelling wave pattern starts to appear, as shown in Fig. 2.49b. Above the TMCI threshold, this travelling wave pattern is clearly present as can be observed in Figs. 2.49c and 2.49d. Below the instability the threshold, the two modes are decoupled and have an independent standing-wave pattern. When the intensity is increased, the two modes start to influence each other and the travelling wave appears. Above the mode coupling threshold, the beam pattern is the superposition of the standing-wave patterns of mode 0 and mode -1.

The signals obtained with the two codes can now be compared. Because below the TMCI threshold the motion is stable, the oscillation signal obtained with PyHEADTAIL is within the numerical noise. The two codes have to be compared for intensities above the TMCI threshold.

Figure 2.50 shows the profile for a bunch intensity of 5.6×10^{11} p.p.b., just above the TMCI threshold, whereas figure 2.51 shows the profiles for a bunch intensity of 9.6×10^{11} p.p.b. Again the two codes give results in good agreement for this impedance model.

These simulations were also extended to a bunch intensity of 100×10^{11} p.p.b.. For such high intensities, the instability rise time is comparable or faster than the synchrotron period. The mode coupling instability is then similar to a beam-break-up instability encountered in linear accelerators in which there is no synchrotron motion [88]. The results of DELPHI and PyHEADTAIL are again in excellent

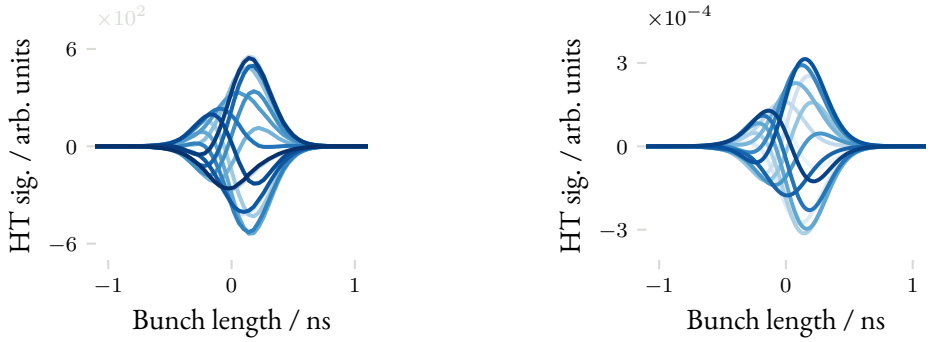

(a) PyHEADTAIL (b) DELPHI

Figure 2.50: Head-tail profiles obtained with PyHEADTAIL (left plot) and DELPHI (right plot) for a bunch intensity of 5.6×10^{11} p.p.b. The broadband impedance is used and the damper is deactivated.

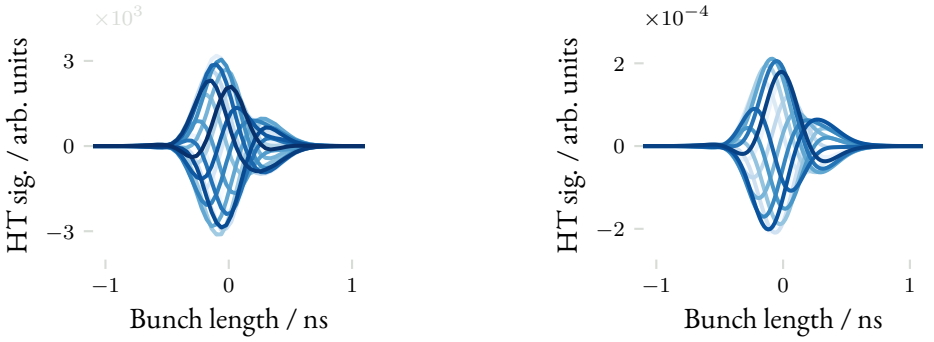

(a) PyHEADTAIL (b) DELPHI

Figure 2.51: Head-tail profiles obtained with PyHEADTAIL (left plot) and DELPHI (right plot) for a bunch intensity of 9.6×10^{11} p.p.b. The broadband impedance is used and the damper is deactivated.

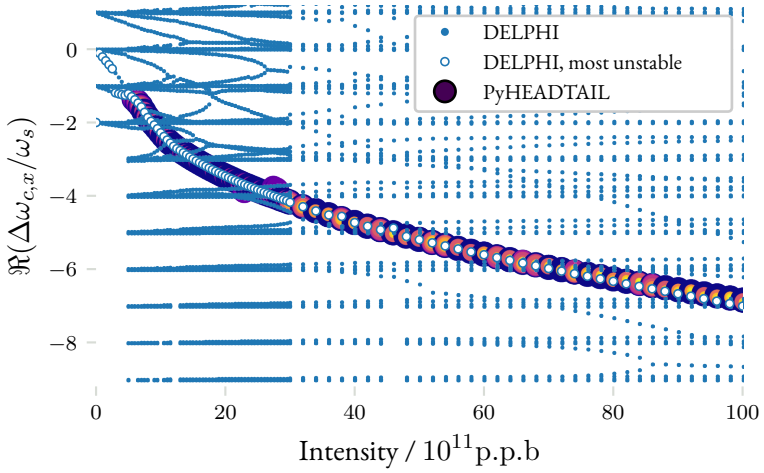

Figure 2.52: Real part of the complex mode frequency shifts as a function of bunch intensity, comparing PyHEADTAIL and DELPHI simulations. The broadband impedance is used and the damper is deactivated.

agreement for intensities up to 70×10^{11} p.p.b., as shown in Figs. 2.52 and 2.53. A discrepancy starts however to arise at intensities close to 70×10^{11} p.p.b..

A simple model describing the instability with two oscillation modes provides a scaling law for the growth rate GR [88]

$$GR = \frac{\pi}{T_s} \frac{N_b}{N_b^{thresh}} , \tag{2.83}$$

where $T_s = \frac{1}{Q_s f_0}$ is the synchrotron period and N_b^{thresh} the TMCI intensity threshold. In this case, at $N_b = 60 \times 10^{11}$ p.p.b., the scaling law gives

$$GR = \pi \times 1.909 \times 10^{-3} \times 11245 \times \frac{60}{7.5} = 540\,\mathrm{s}^{-1} \tag{2.84}$$

whereas the growth rate found with DELPHI and PyHEADTAIL at this intensity is $600\,\mathrm{s}^{-1}$. Figure 2.53 compares the results obtained with the scaling law to those obtain with DELPHI and PyHEADTAIL

Some of the longitudinal beam profile obtained with DELPHI for these high intensities are shown in figure 2.54. As the intensity is increased, the oscillation amplitude becomes larger towards the tail of the bunch. This is an other indication that the bunch entered a break-up like regime.

We saw that without damper the bunch motion is stable below a well defined intensity threshold, found at 5×10^{11} p.p.b.. Activating the transverse damper will however introduce a slow instability of the mode -1 below the TMCI threshold. This instability is created by a coupling of the two modes through the interaction with the damper. This result was found with the Vlasov solver GALACTIC [84] and the results could be reproduced with DELPHI [3, 7] and NHTVS [17].

Figures 2.55 and 2.56 show DELPHI and PyHEADTAIL results when the transverse damper is activated with a damping time of 100 turns. The slow instability below the TMCI threshold of 5×10^{11} p.p.b. is clearly visible on Fig. 2.56. Its growth rate is non-zero but remains small in comparison to the values

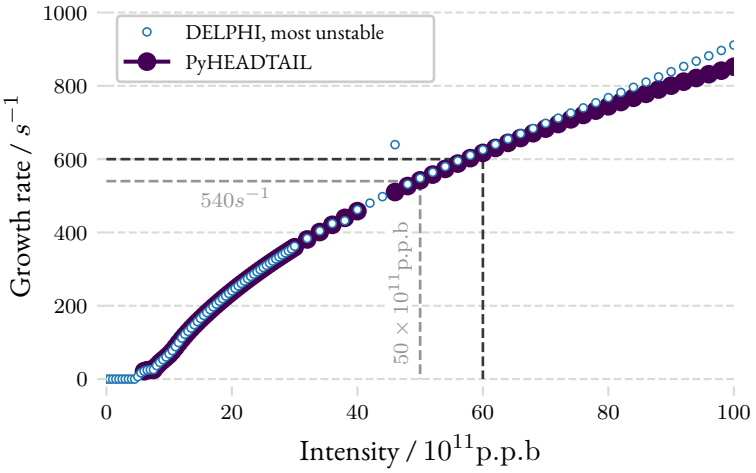

Figure 2.53: Instability growth rate as a function of bunch intensity, comparing PyHEADTAIL and DELPHI simulations. Only the most unstable mode is compared in this case. The broadband impedance is used and the damper is deactivated. The dashed black line corresponds to the growth rate at $N_b = 60 \times 10^{11}$ p.p.b., the dashed grey line represents the intensity value corresponding to a 540 s^{-1} growth rate.

reached in the mode coupling regime. Combined with Fig. 2.55, we can see that it is mode -1 which is unstable while mode 0 is damped by the transverse feedback. The mode 0 and -1 coupling is also suppressed by the feedback. A stronger instability still appears at 7.5×10^{11} p.p.b. when the modes -1 and -2 couple, the transverse damper being less efficient at damping these modes.

An excellent agreement between PyHEADTAIL and DELPHI is again obtained with the mode coupling instability for the simple broadband resonator model, both without and with the transverse damper active. We can now perform the same study using the LHC impedance model.

2.5.2 TMCI with the LHC impedance model

For the study with the LHC impedance model, the beam and machine parameters remain the same as those presented in Tables 2.6 and 2.7. The instability will again be studied for the case without and with damper. Furthermore, the effect of the horizontal quadrupolar impedance on tune shifts and beam stability will also be investigated, and compared to Sacherer's formula.

For the first case of the LHC impedance without damper, the comparison results are shown in Figs. 2.57 and 2.58. The TMCI threshold is found at 3×10^{11} p.p.b.. A second coupling of modes -2 and -3 is found at $N_b = 9 \times 10^{11}$ p.p.b. with DELPHI but is not observed with PyHEADTAIL.

Agreement between the two codes is good for intensities up to 5×10^{11} p.p.b.. For larger intensity values, a discrepancy which was not seen in the previous broadband resonator case is present. This discrepancy was addressed by changing then slicing method used for PyHEADTAIL simulations from an `UniformBinSlicer` to a `UniformChargeSlicer`. More details on the different slicing methods and results of the convergence study can be found in appendix D.

For the bunch profile, the agreement between the codes remains satisfactory, as can be seen in Fig. 2.59 for bunch intensities of 4×10^{11} p.p.b. and 9×10^{11} p.p.b.. Since the single bunch intensity reached in

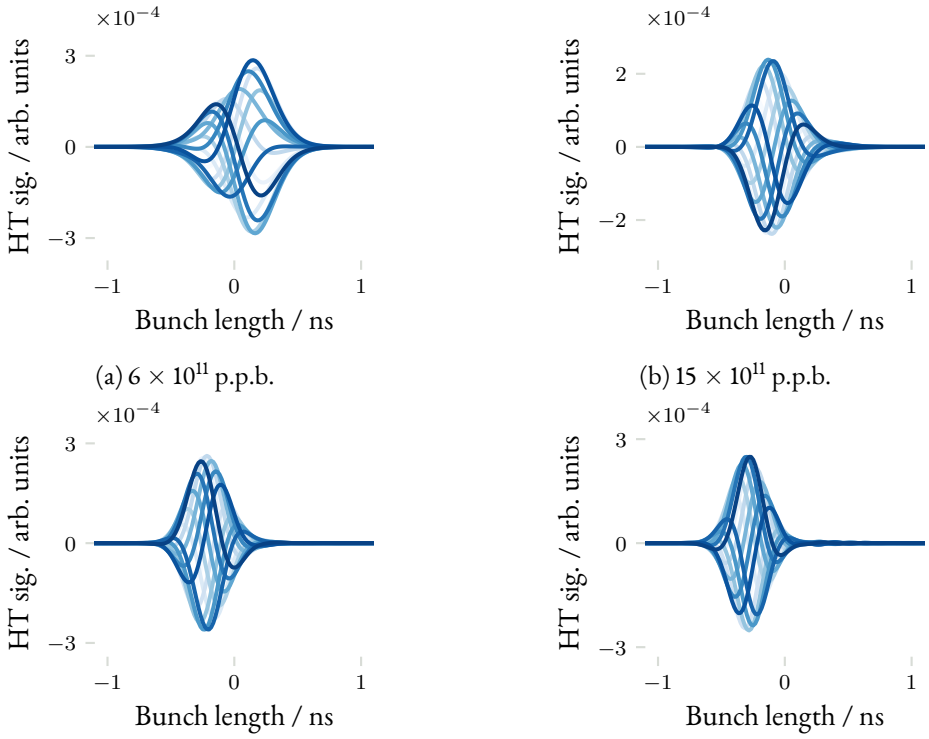

(a) 6×10^{11} p.p.b.

(b) 15×10^{11} p.p.b.

(c) 40×10^{11} p.p.b.

(d) 90×10^{11} p.p.b.

Figure 2.54: Head-tail profiles obtained with DELPHI for high bunch intensities, above the TMCI threshold. The broadband impedance is used and the damper is deactivated.

.

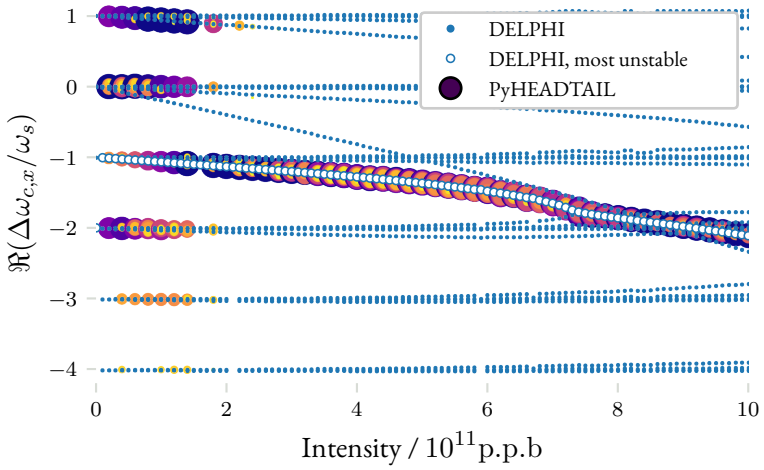

Figure 2.55: Real part of the complex mode frequency shift as a function of bunch intensity, for PyHEADTAIL and DELPHI simulations. The broadband impedance is used and the damper is activated with a damping time of 100 turns. Compared to Fig. 2.47, mode 0 is now stable at all intensities. Mode -1 is the most unstable, and it is coupling with mode -2 at an intensity of 7.5×10^{11} p.p.b.

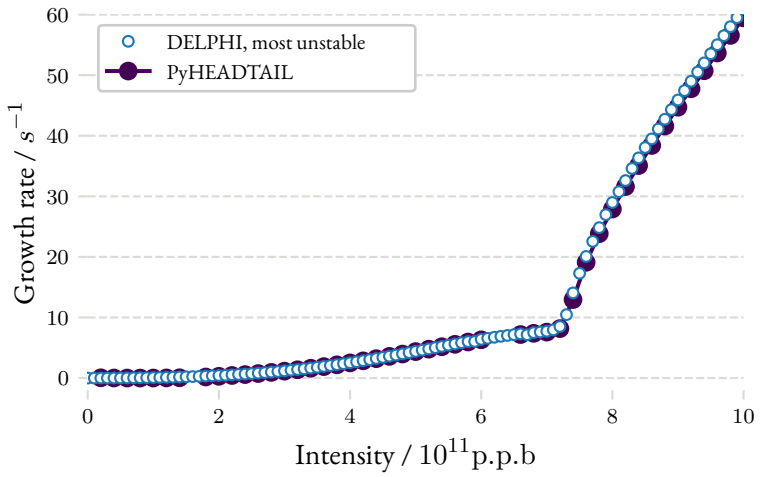

Figure 2.56: Instability growth rate as a function of bunch intensity for PyHEADTAIL and DELPHI simulations. The broadband impedance is used and the damper is activated with a damping time of 100 turns. When the damper is activated, a slow instability appears for intensities below the TMCI threshold of 5×10^{11} p.p.b.

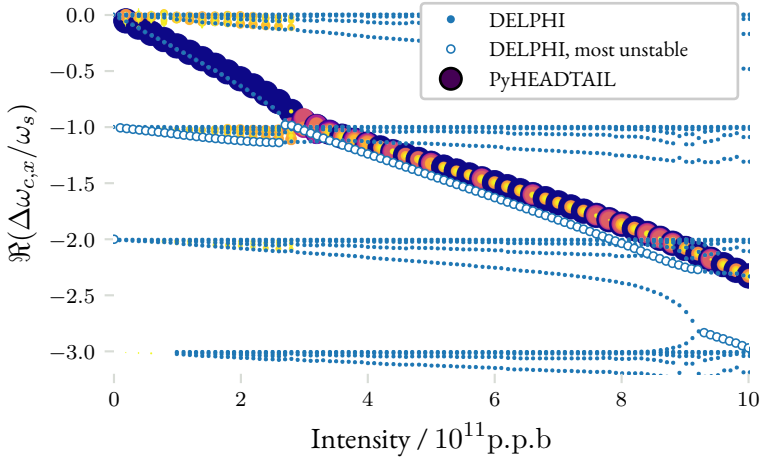

Figure 2.57: Real part of the complex mode frequency shifts as a function of bunch intensity, comparing PyHEADTAIL and DELPHI simulations. The LHC impedance is used and the damper is deactivated.

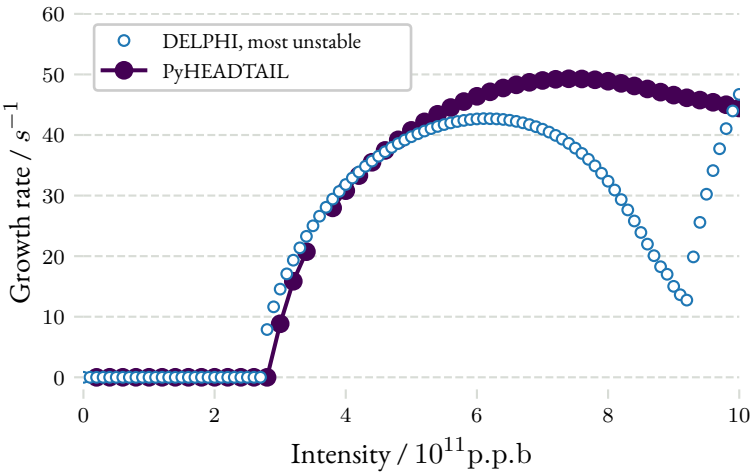

Figure 2.58: Instability growth rate as a function of bunch intensity, comparing PyHEADTAIL and DELPHI simulations. Only the most unstable mode is compared in this case.

the LHC after the High-Luminosity upgrade will not exceed 2.3×10^{11} p.p.b., the discrepancies found for higher bunch intensity are not critical.

The transverse damper will now be activated with a damping time of 100 turns. Figures 2.60 and 2.61 show the comparison of the real and the imaginary part of the modes shifts. As in the case without damper, the agreement between the two codes is good below an intensity of 5×10^{11} p.p.b. Beyond this value, both real and imaginary parts of the modes diverge, as observed already in the previous case without damper.

The effect of the transverse damper is clear: the mode 0 is no longer the most unstable below the TMCI threshold previously found. As with the broadband resonator case, there is no sharp threshold for the mode coupling instability. The bunch is instead unstable at all intensities, and the mode -1 is the one driving the instability.

The bunch profile obtained for the intensities of 2×10^{11} p.p.b., 4×10^{11} p.p.b. and 9×10^{11} p.p.b. are shown in Fig. 2.62. For the latter, there is a clear difference with respect to the case without damper pictured in 2.59b: a node structure remains in the beam profile. This confirms that it is mode -1 which is the most unstable at all intensities, while the coupling with mode 0 is reduced by the action of the transverse feedback. We can also see that a travelling wave pattern starts to develop in the bunch for an intensity of 2×10^{11} p.p.b., confirming that a weak coupling of modes 0 and -1 occurs at this intensity because of the transverse damper.

In the cases presented until now, only the dipolar part of the beam impedance was taken into account. The quadrupolar part of the impedance has a detuning effect, which can increase or reduce the bunch tune shift among other effects. As seen previously, the code DELPHI only includes the effect of the dipolar impedance. PyHEADTAIL can however account for the effect of any component of the wake field. A comparison of PyHEADTAIL, including the quadrupolar wake of the LHC model, and DELPHI was thus made. This allows to estimate the error made on the tune shift when simulations are performed with DELPHI. The simulations were performed without the transverse damper, and also compared to

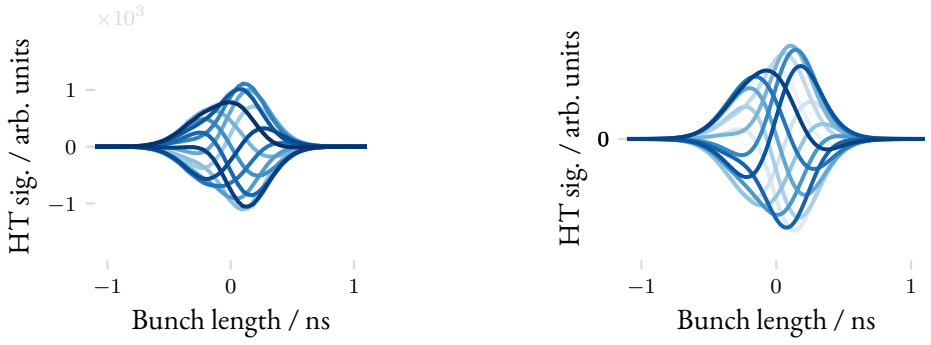

(a) PyHEADTAIL, 4×10^{11} p.p.b. (b) DELPHI, 4×10^{11} p.p.b.

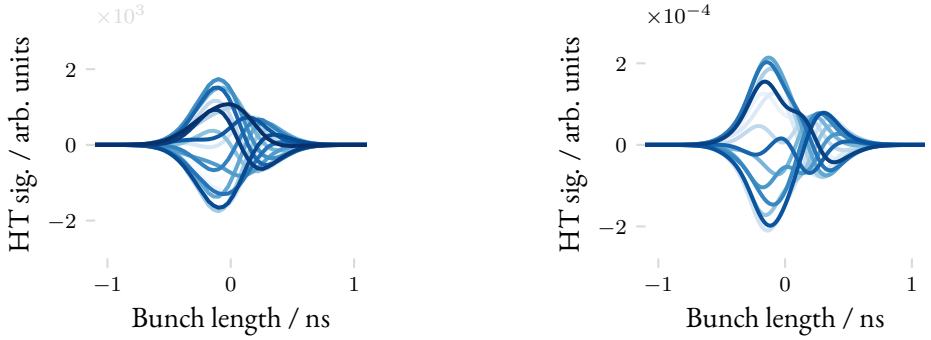

(c) PyHEADTAIL, 9×10^{11} p.p.b. (d) DELPHI, 9×10^{11} p.p.b.

Figure 2.59: Profiles obtained with PyHEADTAIL and DELPHI for bunch intensities of 4×10^{11} p.p.b. 9.0×10^{11} p.p.b. The LHC impedance is used and the damper is deactivated.

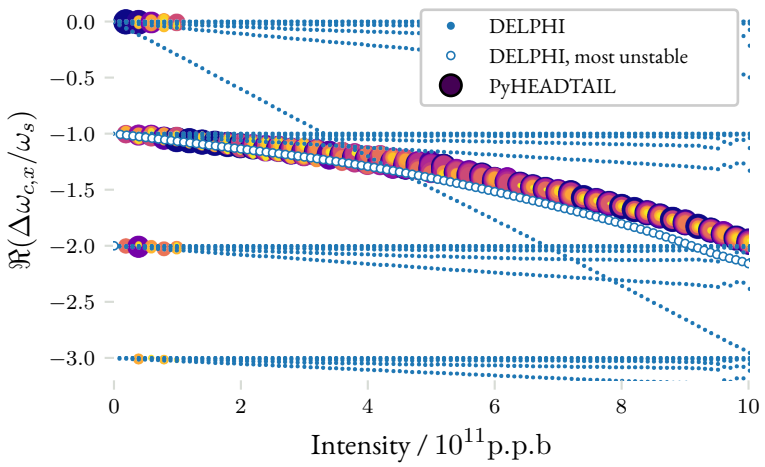

Figure 2.60: Real part of the complex mode frequency shifts as a function of bunch intensity, comparing PyHEADTAIL and DELPHI simulations. The LHC impedance is used and the damper is activated with a damping time of 100 turns.

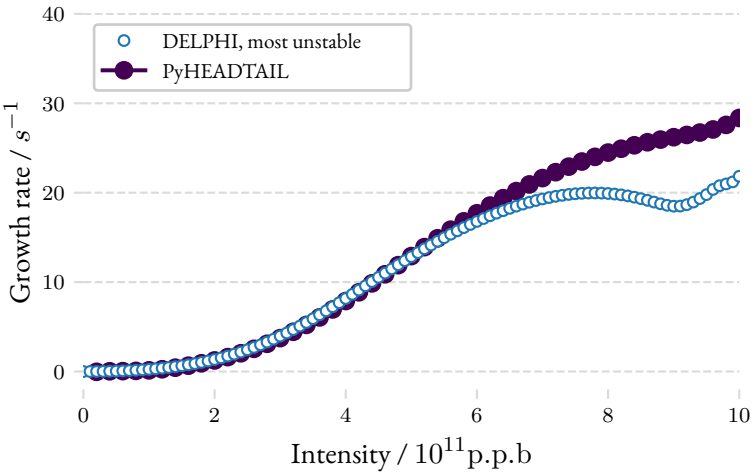

Figure 2.61: Instability growth rate as a function of bunch intensity, comparing PyHEADTAIL and DELPHI simulations. Only the most unstable mode is compared in this case. The LHC impedance is used and the damper is activated with a damping time of 100 turns.

Sacherer's formula results which in one case will account only for the dipolar tune shift and in the other for both dipolar and quadrupolar tune shifts.

Figure 2.63 compares the modes frequency shifts obtained with the two codes. Including the quadrupolar impedance in PyHEADTAIL (right plot) shifts the mode 0 slightly upward for intensities below the TMCI threshold compared to the case without the quadrupolar impedance (left plot). For intensities beyond this threshold, the 0/-1 coupled mode is also shifted upward. This shows that in the LHC the quadrupolar tune shift partially compensates the dipolar one in the horizontal plane. This comes from the combination of the collimators impedance. Because of their different orientations and Twiss beta functions, their dipolar and quadrupolar impedance can add or compensate each other. An illustrative example is given in appendix A.

The effect on the modes growth rates can be seen in figure 2.63. In this case the TMCI is not much affected by the horizontal quadrupolar impedance. The growth rates also remain similar in the three cases for intensities up to 5×10^{11} p.p.b.. Above this intensity DELPHI and PyHEADTAIL results start to diverge, as seen previously. However the quadrupolar impedance only affects the growth rates for intensities above 7×10^{11} p.p.b..

Sacherer's formula allows to estimate the mode frequency shifts by computing the effective impedance of the machine for the given beam parameters. The formula can also be used to estimate the detuning effect of the quadrupolar impedance. Applying it to the LHC impedance model, one obtains the horizontal dipolar Z_{eff}^{dip} and quadrupolar Z_{eff}^{quad} effective impedances

$$Z_{eff}^{dip} = 37\mathrm{j}\,\mathrm{M}\Omega\,\mathrm{m}^{-1}\,, \tag{2.85}$$

$$Z_{eff}^{quad} = -5.8\mathrm{j}\,\mathrm{M}\Omega\,\mathrm{m}^{-1}\,. \tag{2.86}$$

$$\tag{2.87}$$

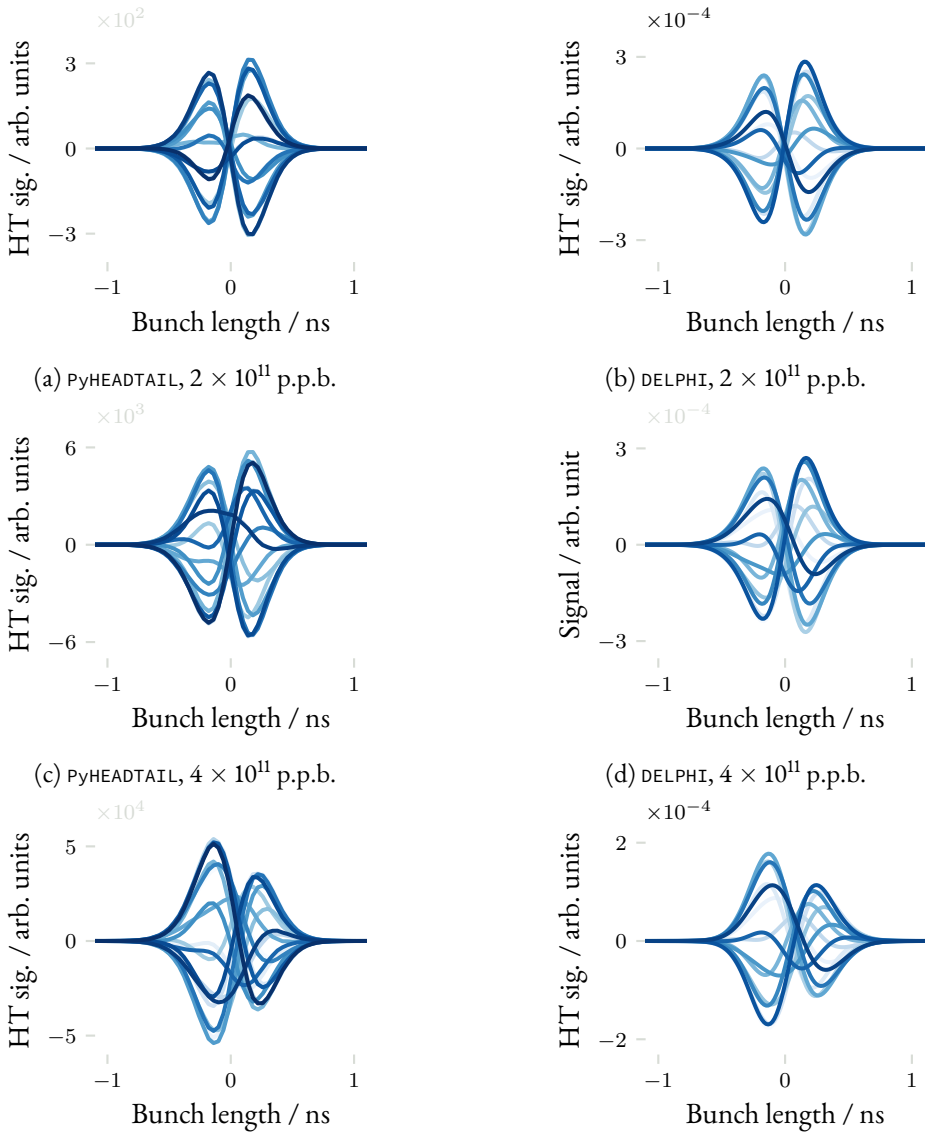

(a) PyHEADTAIL, 2×10^{11} p.p.b.

(b) DELPHI, 2×10^{11} p.p.b.

(c) PyHEADTAIL, 4×10^{11} p.p.b.

(d) DELPHI, 4×10^{11} p.p.b.

(e) PyHEADTAIL, 9×10^{11} p.p.b.

(f) DELPHI, 9×10^{11} p.p.b.

Figure 2.62: Head-tail profiles obtained with PyHEADTAIL and DELPHI for bunch intensities of 2×10^{11} p.p.b., 4.0×10^{11} p.p.b. and 9×10^{11} p.p.b. The LHC impedance is used and the damper is activated with a damping time of 100 turns.

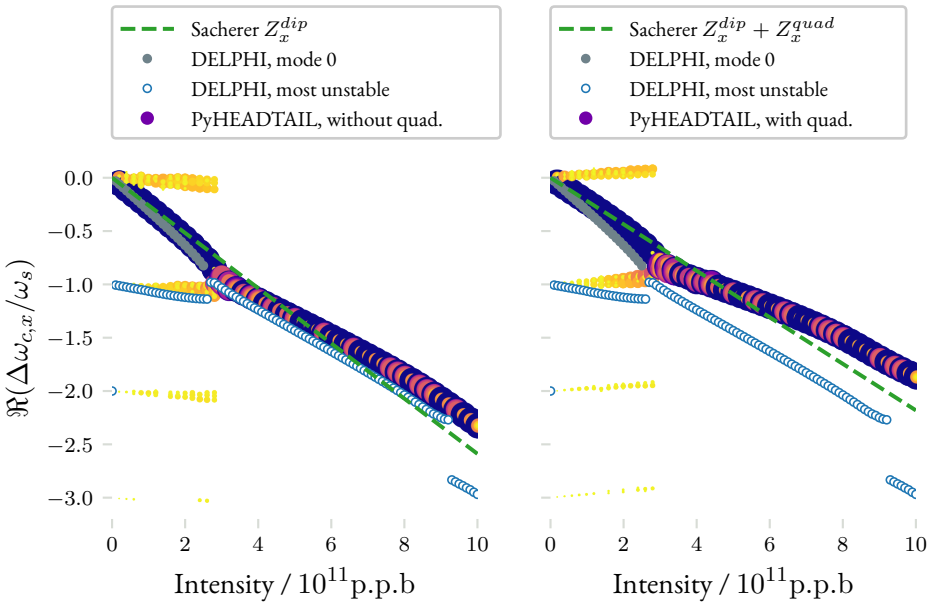

Figure 2.63: Real part of the complex mode frequency shifts as a function of bunch intensity, comparing PyHEADTAIL and DELPHI simulations. The LHC impedance is used and the damper is deactivated. On the left, PyHEADTAIL simulations include only the dipolar wake and Sacherer's tune shift is computed for the effective dipolar impedance only. On the right, PyHEADTAIL simulations include both dipolar and quadrupolar wakes and Sacherer's tune shift is computed by adding the dipolar and quadrupolar effective impedances. In both plots DELPHI only includes the dipolar impedance effect.

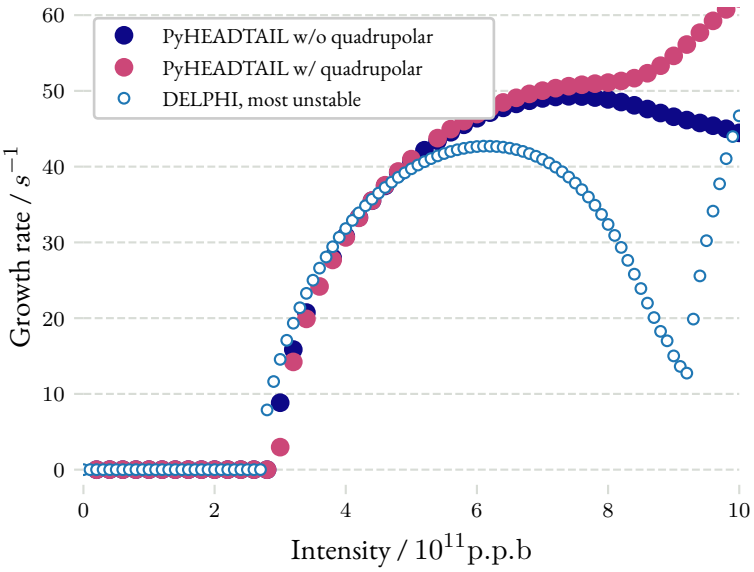

Figure 2.64: Instability growth rate as a function of bunch intensity, comparing PyHEADTAIL and DELPHI simulations. Only the most unstable mode is compared in this case. The LHC impedance is used and the damper is deactivated.

The estimated tune shift $\Delta\omega_{c,0}$ for mode 0 induced by the dipolar and quadrupolar impedance is then proportional to the sum of the effective impedances [127]

$$\Delta\omega_{c,0} \propto jN_b\left(Z_{eff}^{dip} + Z_{eff}^{quad}\right). \tag{2.88}$$

The left plot of Fig. 2.63 shows the case without quadrupolar impedance. For intensities below 10^{11} p.p.b., the tune shifts are the same for the three methods. However as the intensity increases, the mode 0 starts to interact with other modes and its frequency shift diverges from the linear model of Sacherer's formula.

The right plot shows the case where the quadrupolar wake is included in PyHEADTAIL and Sacherer's formula sums the effective impedances. Mode 0 frequency is shifted upwards because of the quadrupolar impedance contribution. PyHEADTAIL and Sacherer's formula results remain in good agreement for intensities below 10^{11} p.p.b.. The tune shift obtained with DELPHI is now overestimated by ∼15 %, the ratio of the horizontal quadrupolar and dipolar effective impedances. This ratio obtained with Sacherer's formula can therefore be used as a correction for DELPHI simulations.

We studied the head-tail instability and the transverse mode coupling instability for different impedance models and compared the results of two simulations codes. We saw that they both are in good agreement except for some specific cases. DELPHI now also permits to reconstruct the beam profile which would be observed at a fixed location in the accelerator. The signals were cross-checked with those obtained with PyHEADTAIL for the different studies, validating the implementation. For the head-tail instability we also investigated with PyHEADTAIL the effect non-linear synchrotron motion can have on beam instabilities and compared the results with DELPHI. Some differences were found, notably for large positive chromaticity values where the head-tail mode change was affected by the non-linear motion. For the transverse mode coupling instability, we studied the very high intensity regime where the instability growth rate becomes linear with the bunch intensity and observed the beam-break-up like behavior of the bunch. In this regime, the chromaticity is assumed to be perfectly corrected to 0. The effect of quadrupolar impedance on the mode frequency shifts was also investigated. We could see that in the LHC impedance case the horizontal quadrupolar component compensates the mode 0 dipolar tune shift by ∼15 %. Moreover PyHEADTAIL results are close to those obtained with Sacherer's formula for low intensities. Correction factors can therefore be computed using Sacherer's approximation and applied to the mode 0 shift obtained with DELPHI.

We will now investigate the impact of impedance on the beam dynamics in the LHC. In particular the effect of slightly positive chromaticity on the mode coupling regime will be investigated through simulations. We will compare the results of these simulations with beam based measurements performed in the accelerator.

3 The Transverse Mode Coupling Instability in the LHC

We investigated two types of coherent beam instabilities: the head-tail and the transverse mode coupling. We saw that the two simulation codes used, PyHEADTAIL and DELPHI, are in good agreement and we investigated their limits. We will now use DELPHI simulations to simulate beam stability margins in the LHC. They will rely on the accelerator impedance model described in part 2.1.4. The comparison between measurements and simulations will allow to estimate the uncertainty on the impedance model.

A first part will be dedicated to a general overview of stability limits encountered during the machine Run II (2015-2018). We will then investigate the Transverse Mode Coupling Instability in the LHC with simulations and measurements in parts 3.2 and 3.3. Beam based measurements of individual collimators and head-tail instability measurements at injection energy will also be presented in part 3.3.

3.1 Motivations of the study

We saw in the previous chapter that the transverse damper and chromaticity can be effective ways to reduce the instability growth rate. However in the LHC the beam configuration process takes several minutes. The energy ramp takes ∼20 min, the flat-top phase during which the transverse tunes are modified takes ∼5 min, the squeeze and adjust process during which the tranverse size of the bunches at the interaction points are reduced and the beams brought into collision takes ∼30 min [135]. The beams are then stored for several hours, colliding at the experimental points. The beam stability needs to be ensured at all stages in order to preserve the beam quality.

A mechanism called Landau damping helps keeping the beam stable [64, 73]. A spread in the individual particle oscillation frequencies i.e the transverse tunes is introduced. When a coherent excitation of the bunch is applied, the particles cannot organize themselves to provide a coherent response. Over time their average response is zero and no instability develops.

The frequency spread is introduced by the machine non-linearities resulting from the magnets misalignment and mechanical errors. But the spread they provide is often not sufficient to keep the beam stable. Dedicated octupole magnets called Landau octupoles are therefore installed in the machine. They provide a frequency spread which is function of the particles betatron oscillations amplitude [18, 58, 140]. In the LHC, 168 of these magnets are installed [39]. The nominal current they can reach is 550 A. Because their number and the current they can sustain are limited, they can only stabilize the beam up to a certain threshold.

The frequency spread needed from the octupoles can be predicted from the coherent mode frequency shifts [29]. This frequency spread corresponds to a certain current in the octupole magnets. This simulated current can be compared to the value set during machine operation or the values found during dedicated measurements [40, 47, 48].

Figure 3.1 compares the results of instability threshold measurements and simulations in terms of Landau octupoles current as a function of chromaticity. The results are for the horizontal plane of beam 1 in the year 2017. They show that a systematically higher octupole current than predicted from the impedance model was required to stabilize the beam.

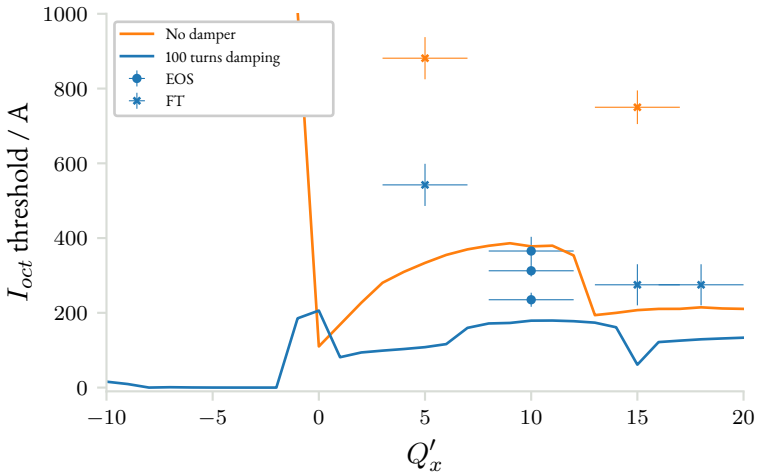

Figure 3.1: Current in the Landau octupoles magnets required to stabilize the horizontal plane of beam 1 (solid lines) as a function of chromaticity during the year 2017. The results for a case without damper (in blue) and with the transverse damper activated with a damping time of 100 turns (in orange) are presented. Those are compared to measurements for different chromaticities, represented in the same color code. A dot denotes a measurement made at the end of squeeze, i.e when the beams are ready to be collided. A cross represents a measurement made a flat-top, i.e after the end of the energy ramp and before the tune change. All results have been normalized to a bunch intensity of 10^{11} p.p.b.

Measurements during Run II (2015-2018) and daily monitoring of transverse beam instabilities in the LHC during the year 2018 have shown that a factor two on the octupole current is required to ensure the beam stability [40]. Figure 3.2 shows the octupole current used in LHC operation during Run II. It is compared to the one predicted with DELPHI simulations. The octupole current margin could be reduced over the years as the understanding of various instability mechanisms improved [46, 48].

The margin remains however tight to cope with the bunch intensity increase foreseen in HL-LHC. The octupole current scales linearly with the bunch intensity, therefore a factor two on the bunch intensity would bring the 2018 operational scenario to the limit of available octupole current. No margin would be left in case new instability phenomena appear.

The factor two existing between simulations and measurements needs therefore to be investigated. Impedance effects, including the mode coupling instability mechanism, are possible candidates to explain a part of this factor. We will now focus on impedance related simulations and measurements performed in the LHC. This will allow us to estimate the uncertainty on the impedance model.

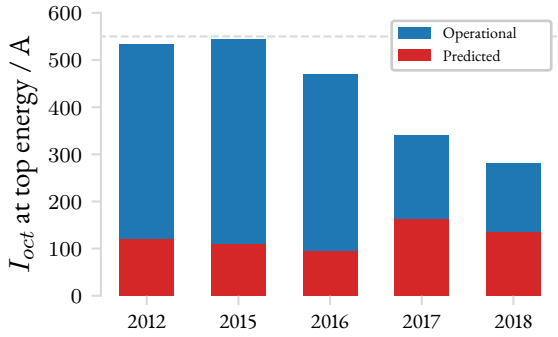

Figure 3.2: Octupoles current used in operation (in blue) versus predicted from the impedance model (in red) during Run II. The maximum current of 550 A which can be reached in the magnets is highlighted as a dashed line. Courtesy X.Buffat [40]

3.2 Simulations of the Transverse Mode Coupling in the LHC

As seen in part 2.5, the Transverse Mode Coupling Instability is a fast instability which arises at high bunch intensity and at a chromaticity corrected to zero. The LHC currently operates with a high chromaticity of $Q' \sim 15$ to mitigate electron-cloud induced instabilities [120]. Moreover instabilities in this region of small chromaticities were observed during the LHC Run I (2009-2013) [93]. Operation at small positive chromaticities would however be preferred to optimize the beam lifetime and reduce the Landau octupole current. We will now investigate the mode coupling instability in the LHC with DELPHI simulations for different chromaticities and collimator settings.

3.2.1 Impedance model, beam parameters and assumptions made

The TMCI simulations were performed with the 2017 LHC impedance model. The year indication is essential since the collimators gaps can be modified during the run to match the beam size reduction at the interaction points. The collimator gaps for the specified year were provided by the LHC Collimation team [77]. The simulation parameters are similar to those presented in part 2.5, only the beam parameters are different to reproduce the real machine configuration. The parameters correspond to the flat-top phase, before the tune change and are summarised in Table 3.1.

The TMCI simulations presented in the previous chapter assumed a chromaticity corrected to 0 units. However because of the uncertainty over the parameters set in the accelerator, the chromaticity has an error range of ±2 units [146]. To guarantee that the beam remains stable, the chromaticity should be kept at a positive value. Therefore a measurement on the LHC should be performed with a chromaticity set to ∼5 units to keep the beam stable. For the same purpose the transverse damper is also kept activated. The effect of these two elements, chromaticity and damper, on the TMCI must be simulated for the LHC in order to plan a machine measurement.

Table 3.1: Machine and beam parameters for TMCI simulations with DELPHI.

Parameter	Value
Machine	
Impedance model	LHC 2017 flat-top[1]
Circumference / m	26 658.8832
Transverse tunes $Q_{x,y}$	62.31/60.32
Momentum compaction factor α_c	3.225×10^{-4}
RF voltage / MV	12
Harmonic number	35 640
Synchrotron tune Q_s	1.838×10^{-3}
Beam	
Number of bunches	1
$4\,\sigma$ bunch length / ns	1.08
Bunch intensity / 1×10^{11} p.p.b.	0 to 10
Chromaticity Q'	0 to 5

[1] LHC impedance and wake model as described in [103] and available at [143].

3.2.2 Simulations results for a corrected chromaticity

The first simulations cover the case of $Q' = 0$ without the transverse damper. Figure 3.3a shows the mode frequency shifts and growth rates as a function of bunch intensity. One can see that the TMCI threshold is reached at an intensity of 2.8×10^{11} p.p.b..

Figure 3.3b shows the same simulation but with the transverse damper activated with a damping time of 100 turns. One can see that the mode frequency shift of the mode 0 remains unaffected by the damper for low intensities. At intensities closer to the TMCI threshold found before, modes 0 and -1 influence each other but no strong coupling is found. These observations are in agreement with the ones made for the comparison of DELPHI and PyHEADTAIL in part 2.5.

These results were computed for the case of a chromaticity perfectly corrected to zero units. Since an uncertainty always remains on the operationally set value of chromaticity, we will now look at the effect of a positive chromaticity on the TMCI threshold.

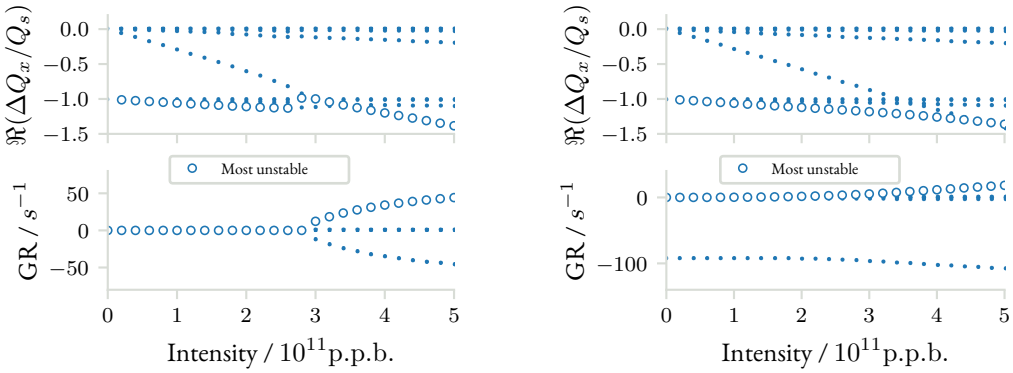

(a) $Q' = 0$ without damper

(b) $Q' = 0$ with damper

Figure 3.3: Real part of the mode frequency shifts (top plots) and instability growth rate (bottom plots) as a function of bunch intensity. On the left the damper is deactivated, on the right it is activated with a damping time of 100 turns. In both cases the chromaticity is corrected to $Q' = 0$.

3.2.3 Results for a positive chromaticity

To understand the effect of chromaticity on the TMCI, the same simulations as in the previous part were performed with $Q' = 5$, both without and with damper. Figure 3.4b shows the results for $Q' = 5$ in a case where the damper is deactivated. It is compared to the reference TMCI case at zero chromaticity and without damper pictured in Fig. 3.4a. The frequency shift of mode 0 remains unaffected for intensities below the TMCI threshold found before at 2.8×10^{11} p.p.b.. A coupling between modes 0 and -1 can still be observed at a similar bunch intensity as before, 3×10^{11} p.p.b.. An examination of the growth rates shows that below this intensity a slow instability develops: it is the head-tail instability which is present because of the non-zero chromaticity.

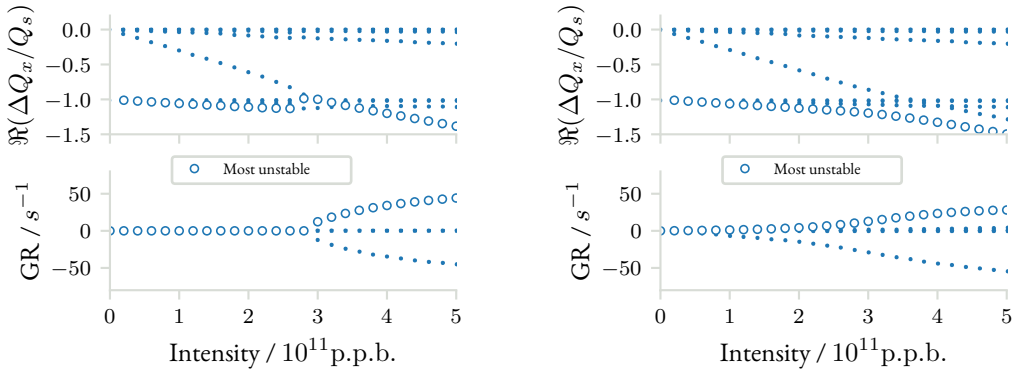

(a) $Q' = 0$ without damper

(b) $Q' = 5$ without damper

Figure 3.4: Real part of the mode frequency shifts (top plots) and instability growth rate (bottom plots) as a function of bunch intensity. Both left and right plots are for a deactivated damper. On the left the chromaticity is corrected to $Q' = 0$ and on the right it is positive at $Q' = 5$.

We saw that a small positive value for the chromaticity doesn't change drastically the mode coupling behaviour at high bunch intensity. We now need to check the effect of the transverse damper: Fig. 3.5b depicts the results of simulations for a damping time of 100 turns, with $Q' = 5$. It is again compared to the reference TMCI case without damper and at $Q' = 0$ in Fig. 3.5a.

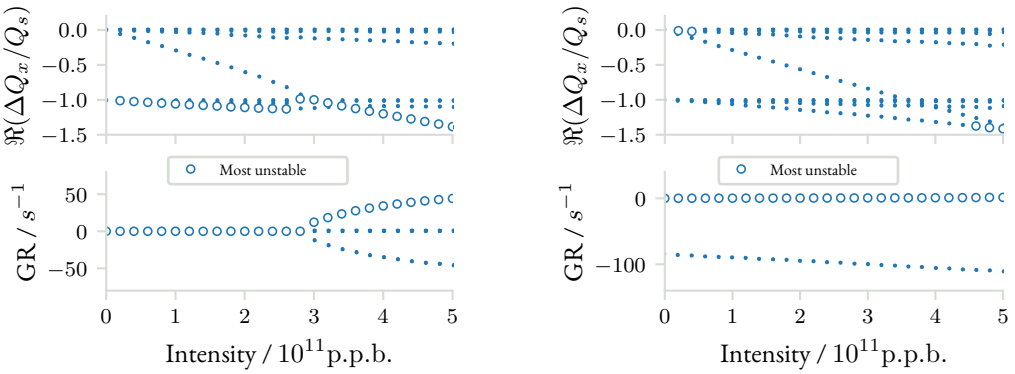

(a) $Q' = 0$ without damper

(b) $Q' = 5$ with damper

Figure 3.5: Real part of the mode frequency shifts (top plots) and instability growth rate (bottom plots) as a function of bunch intensity. On the left the chromaticity is corrected to $Q' = 0$ and the damper is deactivated, on the right the chromaticity is positive at $Q' = 5$ and the damper is activated with a damping time of 100 turns.

The transverse damper, combined with the positive chromaticity, effectively removes the head-tail instability. The mode 0 frequency remains marginally affected by the presence of the damper and the positive chromaticity compared to the reference case.

From the different simulations presented, one can conclude that measuring the tune-shift as a function of intensity is a way to infer the TMCI threshold. Indeed the slope of the mode 0 shift versus bunch intensity is minimally affected by the inclusion of a positive chromaticity and the transverse damper: the difference is within 5 % which remains within the uncertainties of a tune-shift measurement in the LHC. Simulations also show that the machine currently operates with bunch intensities largely below the TMCI threshold. If one wants to try to reach the TMCI threshold, either the beam parameters have to be modified or the machine impedance should be increased.

From the beam parameters side, the synchrotron tune Q_s can be reduced to decrease the TMCI threshold. We saw with the two particle model that the TMCI threshold value is proportional to Q_s

$$N_b^{thres} = \frac{8E_0 C\omega_\beta \omega_s}{\pi e^2 W_0 v^2}\,. \tag{3.1}$$

A reduction of Q_s can be obtained by reducing the RF cavities voltage V_{RF}. As $Q_s \propto \sqrt{V_{RF}}$, a reduction of the RF by a factor of 2 would result in a TMCI threshold reduction of only 40 %. However a sharp reduction of the RF voltage could affect in turn the bunch length and increase non-linear effects from the RF bucket. The measurement could then be affected by this reduction of the RF voltage.

The previous equation shows that a simple way to decrease the TMCI threshold is to increase the machine impedance, here represented by the wake W_0. This increase can be obtained by tightening the

IR7 collimators gaps. As the resistive wall impedance of a flat structure is proportional to g^{-3} where g is the structure gap, decreasing the collimator gaps by ≈25 % would increase their impedance by a factor 2. The next part will detail the simulations results obtained for tighter settings of the LHC collimators.

3.2.4 Results for tighter collimator gaps

Simulations with tighter collimators gaps are based on the 2017 LHC impedance model with nominal gaps. The gaps settings are given in number of transverse beam size σ_{coll} in the plane of collimation. Since the transverse beam size is different at each collimator because of different Twiss beta functions, the physical collimator gaps change from one collimator to the other. Figure 3.6 shows the gaps for three of the LHC collimators and for the different scenarios investigated.

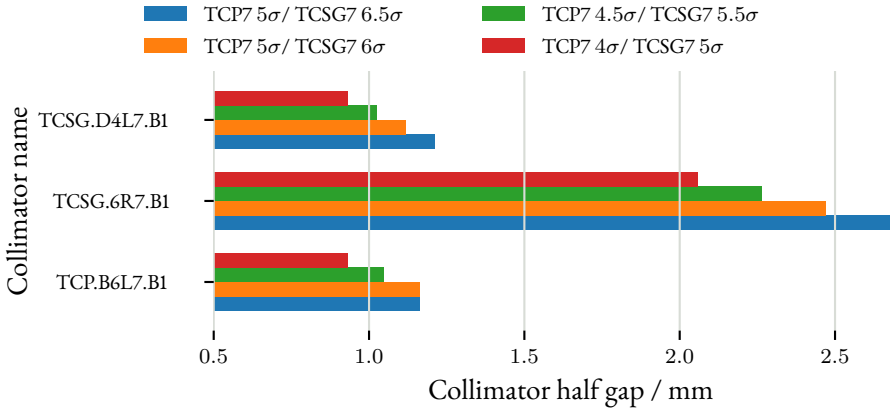

Figure 3.6: Physical gaps of three of the LHC IR7 collimators in mm for the different scenarios investigated. The nominal LHC configuration in 2017 is displayed in blue, whereas the other colors show tighter collimators settings. In the tightest setting presented here the collimator gaps are reduced by ≈25 %. The picture for all collimators gaps is reported in part B.2

The LHC impedance simulations were then performed with these tighter gap settings. The resulting horizontal dipolar impedance as a function of frequency is shown in Fig. 3.7. The collimators have a strong impact on the real part of the dipolar impedance in the 10 MHz to 10 GHz frequency range. For the imaginary part the impact is seen in an even broader frequency range, from 1 kHz to 10 GHz.

In this frequency range the impedance can be increased by up to a factor of 2 by closing the primary and secondary collimators gaps to 4.0σ and 5.0σ. Thus the TMCI intensity threshold could be reduced by the same factor. To confirm the impact on transverse beam stability, DELPHI simulations were performed for these sets of tighter collimators gaps. Figure 3.8b shows the results for the 4.0σ and 5.0σ configuration in the TCP and TCSG collimators. To obtain a clear TMCI effect, the chromaticity is taken equal to $Q' = 0$ and the damper is deactivated. It is again compared to the nominal reference case with nominal collimators gaps in Fig. 3.8a.

The impact of the impedance increase caused by the tighter gaps in the collimators is clearly visible. In this tightest configuration the TMCI threshold is reduced to 1.6×10^{11} p.p.b.. This bunch intensity becomes reachable in the accelerator. The mode 0 shift is also clearly affected. A measurement of the

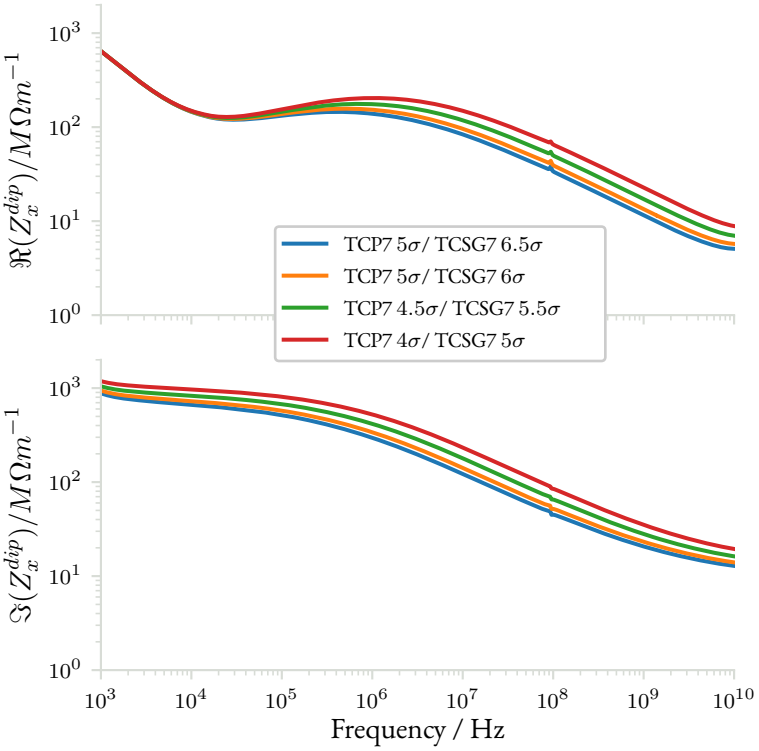

Figure 3.7: Real and imaginary part of the LHC horizontal beam coupling impedance for different collimator settings.

LHC tune shift versus intensity for different collimators settings could therefore provide more insight on the accuracy of the impedance model.

As for the previous study with nominal collimator gaps, a positive chromaticity is required because of operational uncertainties. The chromaticity is now at 5 units and the transverse damper has a damping time of 100 turns. Figure 3.9b shows the simulations results for this setup. They are compared to the results with a corrected chromaticity and no damper for the same tight collimator gaps in Fig. 3.9a.

As seen previously in the case with nominal collimators gaps, the tune shift is only slightly affected for intensities below the new TMCI threshold of 1.6×10^{11} p.p.b.. The presence of both chromaticity and damper affects however the mode coupling behavior. The fast instability characteristic to mode coupling disappears even for intensities above the threshold.

We saw that because of operational constraints and limitations, the machine setup used for TMCI simulations can not be exactly reproduced in measurements. However an observable can help infer the TMCI threshold value: the tune shift as a function of intensity. Measuring it can help to quantify the accuracy of the impedance model. This tune shift can also be increased by tightening the collimators settings, providing more data for an identical set of bunch intensities. A scenario with tight enough collimators gaps could also bring the TMCI threshold within the intensity reach of the machine. The next part will detail the measurement performed in the LHC, using the simulations detailed before.

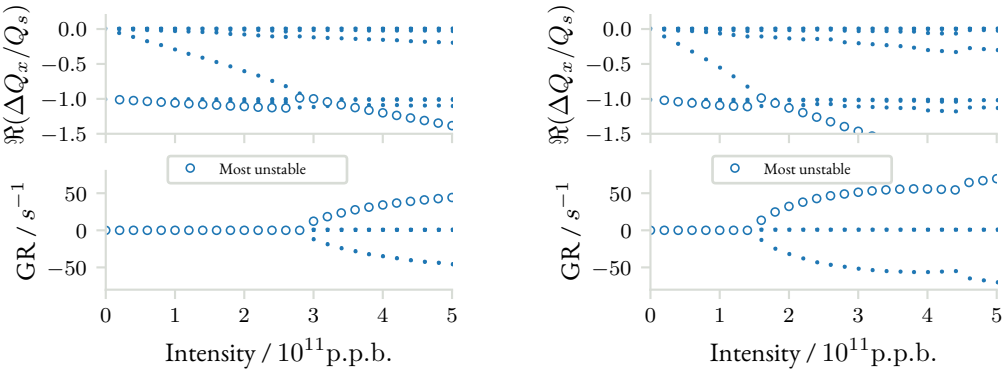

(a) Nominal collimator gaps

(b) Tighter collimator gaps

Figure 3.8: Real part of the mode frequency shifts (top plots) and instability growth rate (bottom plots) as a function of bunch intensity. Both left and right plots are for a deactivated damper and a chromaticity corrected to $Q' = 0$. On the left the collimator gaps are the nominal ones for 2017 whereas on the right they are tighter to increase the machine impedance.

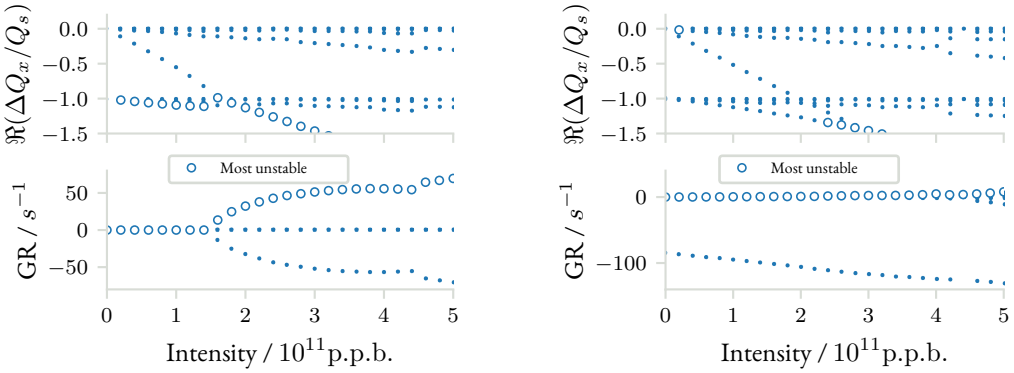

(a) $Q' = 0$, no damper

(b) $Q' = 5$, with damper

Figure 3.9: Real part of the mode frequency shifts (top plots) and instability growth rate (bottom plots) as a function of bunch intensity. Now in both left and right plot the collimators gaps are tighter at $5\sigma/6\sigma$ in the TCP7/TCSG7. In the left plot the chromaticity is at $Q' = 0$ and the damper is deactivated. In the right plot chromaticity is at $Q' = 5$ and the damper is activated with a damping time of 100 turns.

3.3 Assessment of the LHC impedance and stability limits with beam based measurements

3.3.1 Measurement of the TMCI threshold in the LHC

We saw with simulations that the TMCI threshold in the LHC is predicted to be at an intensity of 2.8×10^{11} p.p.b. However this bunch intensity can not be reached in the machine. The measurements will therefore aim to infer the TMCI threshold. Sacherer's formula developed in part 2.3.3 showed that at zero chromaticity, outside the mode coupling regime, the mode zero complex frequency shift $\Delta\omega_{c,0}$ is proportional to the effective impedance $Z_{\perp,eff}$ and the bunch intensity N_b

$$\Delta\omega_{c,0} \propto jZ_{\perp,eff}N_b\,. \tag{3.2}$$

The imaginary part of the mode complex shift will determine its growth rate and can be measured when the beam becomes unstable. The real part of the mode corresponds to the change of betatron frequency caused by the impedance. We saw in part 2.5 that this frequency change is small since it is in the order of $Q_s\omega_0$. It can however be measured precisely by coherently kicking the bunch and recording its turn-by-turn oscillations. With a properly controlled kick, these oscillations will then be damped by the transverse feedback. The transverse tune can be found by performing a Fourier transform or applying the Harpy algorithm to the bunch transverse position, in the same way as for the processing of `PyHEADTAIL` data.

In many machines the impedance at a given energy is fixed and the induced tune shift can be measured by injecting bunches of different intensities, as was done for example in the CERN SPS [25]. If a bunch becomes unstable and its quality degrade, the quick turn-over time allows to re-inject a new bunch and perform a new measurement.

However, in the LHC, the turn-over time is in the order of the hour. Moreover the time for a measurement is usually limited to 8 h since many different studies have to be performed in the accelerator during the year. In this limited time, two energy ramps and their consecutive measurements can be accommodated. Measurement repeatability is therefore limited and the experiment has to be carefully set-up.

As seen in part 3.1, the collimators have a strong impact on the transverse impedance. As they are movable devices, they can then be approached or moved away from the beam to increase or reduce the impedance. The collimators and bunch intensity parameters chosen for the experiment were based on the simulations detailed in the previous part and the machine limitations.

Moving the collimators allows to repeat the same measurement for different machine impedances, however it limits the number of bunches which can be injected in the machine. The total beam intensity must remain below 3×10^{11} p.p.b. if the collimators are moved from their nominal position at top energy. This constraint results from machine protection requirements and failing to keep the beam intensity within this limit would trigger a beam dump [147].

An experiment to infer the TMCI threshold for different collimator configurations was proposed and executed in the LHC during the MD block 3 of year 2017 [10], in the night of the 15$^{\text{th}}$ of September. The steps taken during the MD were the following:

1. Three single bunches of different intensities were injected in both rings. The bunch buckets were chosen so as no beam-beam effects would occur between the beam 1 and beam 2 bunches. The bunch intensities were 0.6×10^{11}, 1.0×10^{11} and 1.4×10^{11} p.p.b..

2. The energy was ramped-up to 6.5 TeV, keeping the Landau octupoles at maximum current to provide a sufficient tune-spread ensuring coherent stability.

3. The beam parameters were set-up: chromaticity was reduced to $Q' \sim 5$. This value has been chosen to stay close to $Q' = 0$ while remaining at a positive chromaticity. The transverse fractional tunes were kept at their injection values of 0.275 and 0.295 in the horizontal and vertical planes respectively.

4. The bunches were coherently kicked in both planes. The turn-by-turn position of all bunches is then recorded and the data post-processed to obtain the tune [136].

5. The kicks were then repeated for the configurations with tighter collimator gaps.

The time allocated for the measurement allowed to perform a second ramp for which the procedure was kept identical. Only the beam intensities used were different, with two bunches of 0.9×10^{11} and 1.9×10^{11} p.p.b. instead of three bunches. Four different collimator configurations were used to better probe the impedance model despite a limited number of bunches available. The collimators parameters are given in Table 3.2.

Table 3.2: Primary and secondary collimators gaps settings used during the tune shift versus intensity measurement.

Collimator setting / σ_{coll}			
TCP	TCSG	Configuration name	Remark
5	14	(5/14)	Relaxed setting, HL-LHC mock-up
5	6.5	(5/6.5)	2017 nominal setting
5	6	(5/6)	Tight settings
4.5	6	(4.5/6)	

The first configuration presented in Table 3.2 used larger collimator gaps than the nominal configuration. The gaps were chosen to reproduce the equivalent impedance reduction foreseen for HL-LHC. The results obtained in this configuration will be further detailed in part 4.

We highlighted in the previous parts that the collimators have a strong impact on the impedance. It is therefore important to obtain the gaps which were present in the machine. Those are logged in the CERN Accelerator Logging System (CALS) [119] during machine operation. Once retrieved, the machine impedance can be computed for these real gaps. In Fig. 3.10 the gaps retrieved from the CALS are compared to the ideal ones resulting from the scaling of the physical collimator gaps with the number of sigmas used for the configuration. The difference between the predicted gaps and measured gaps is small but visible. The measurement results will therefore be compared to the results of stability simulations performed with the impedance models derived from the real machine collimator gaps.

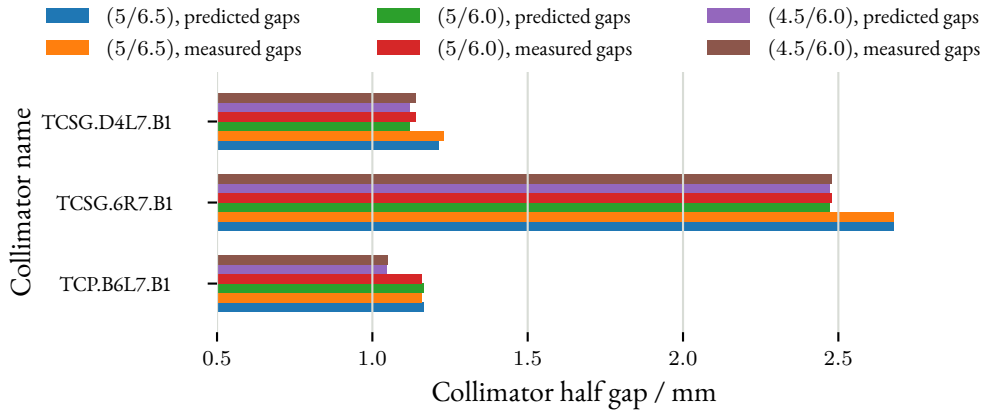

Figure 3.10: Physical gaps of three of the LHC IR7 collimators in mm for the configurations given in Table 3.2. The collimator gaps measured in the machine are compared to the one resulting from a scaling with $n_{\sigma,coll}$ of the gaps and which were used for instability predictions described in the previous part. The difference between the gaps measured in the machine and the predicted ones are of the order of 1 %. The picture for all collimators gaps is reported in part B.3

Once the top energy was reached, the tune measurement relied on the transverse damper (ADT). The bunches were coherently kicked with the ADT. The excitation strength was chosen to obtain clear bunch oscillations without provoking intensity losses caused by scrapping on the collimators. The damper gain was also reduced to obtain a longer decoherence time. An excitation was applied to both horizontal and vertical planes, with a delay of 2000 turns between the two, and all the bunches were coherently kicked at the same time. Their oscillation signal was recorded using the ADTObsBox [144], a system which can acquire the bunch-by-bunch and turn-by-turn transverse position of the beams using the ADT stripline pick-ups. An example of a set of acquired signals is given in Fig. 3.11 where the vertical axis unit is proportional to the bunch transverse position. The kicks were then repeated multiple times for each beam, spaced by 10 seconds. The transverse tune is then computed for each kick signal using a procedure similar to the one described in part 2.3.4 on the post-processing of `PyHEADTAIL` data.

Figure 3.12 shows ring 2 collimators gaps and beam parameters as well as the three bunches intensities, full lengths and vertical emittances over time. The times at which the kicks were sent are highlighted as well. The procedure started with the ADT setup, then a first set of kicks was applied. The collimators gaps were then tightened for a second measurement set, and again for a third set of kicks. The beam intensity losses, emittance growth and bunch lengthening were small during the tune measurements thanks to the controlled kick strength. A beam instability was induced at the end of the measurement by closing the gaps to tighter settings, leading to intensity losses and bunch lengthening.

Figure 3.13 shows the data processing steps made once the tune has been computed for each ADT signal. In the top plot all the vertical tune signals for the three bunches are represented. For each collimator configuration the values are then averaged. Knowing the individual bunch intensity over time, the tune shift as a function of intensity can be computed.

Figures 3.14 and 3.15 show the tune shift as a function of intensity compared to predictions from the impedance model. The unperturbed tune Q_0 has been subtracted from the measurements to allow the

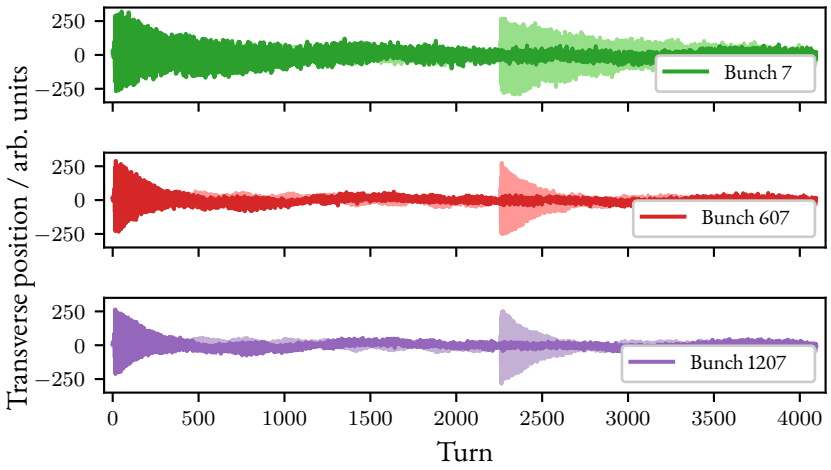

Figure 3.11: Example of turn-by-turn transverse beam position signals acquired with the ADTObsBox after an ADT kick. The three bunches present in beam 2 during the first fill are represented. For each bunch, the horizontal position is plotted with a darker color than the vertical position. All three bunches are kicked at the same time, first in the horizontal plane and after 2000 turns in the vertical plane. The bunch oscillations decay in $\lesssim 500$ turns.

comparison of the two fills data and the different collimators configurations. The points represent the average tune values whereas the lines show the tune shifts predicted from the impedance model.

The tune shifts as a function of intensity are reported in Table 3.3. They have been normalized to the accelerator synchrotron tune $Q_s = 1.838 \times 10^{-3}$.

We saw in the TMCI study with PyHEADTAIL and DELPHI done in part 2.5.2 that the quadrupolar impedance affects the tune shift. As DELPHI models only the dipolar impedance contribution, a correction should to be used to account for the quadrupolar impedance effect. The correction is based on Sacherer's formula. First the tune shifts induced by the dipolar and quadrupolar impedances, noted ΔQ_{dip} and ΔQ_{quad}, are computed separately. The ratio $\frac{\Delta Q_{dip}+\Delta Q_{quad}}{\Delta Q_{dip}}$ is then computed and applied to DELPHI simulations. The results with this correction factor are also reported in Table 3.3.

These measurements can then be used to infer the TMCI threshold. As we saw in the simulations from part 3.3 this instability results from the coupling of mode 0 and -1. The mode -1 frequency is weakly perturbed, therefore the TMCI threshold is approximately the intensity at which the real part of mode 0 and mode -1 complex frequencies cross. From the normalised tune shift versus intensity $\Delta Q/Q_s$, the TMCI intensity threshold N_b^{thres} is approximately found at

$$N_b^{thres} \approx -\frac{1}{\Delta Q/Q_s}\,. \tag{3.3}$$

The thresholds inferred from the measurements presented in Table 3.3 are reported in Table 3.4. The third column shows the TMCI threshold obtained with DELPHI simulations by reading the intensity value at which the growth rate becomes non-zero. The fourth and fifth columns give the threshold

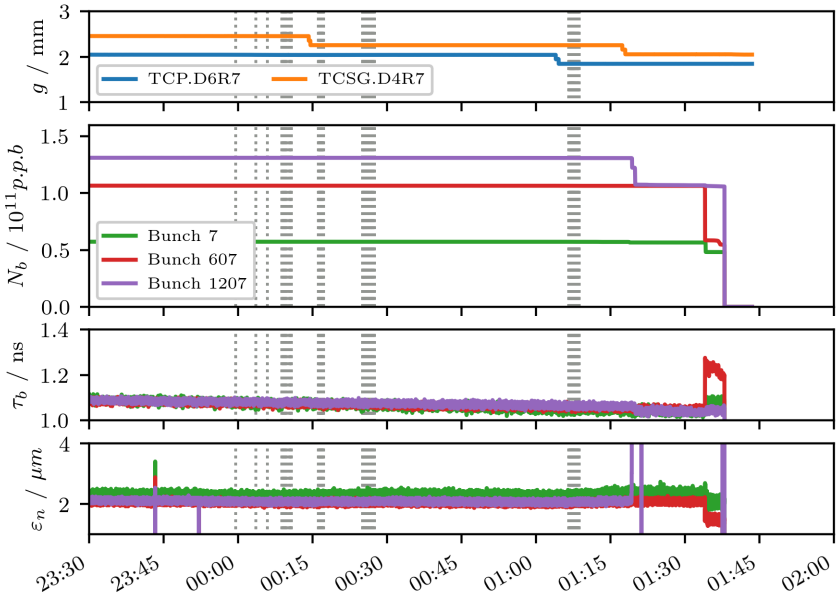

Figure 3.12: Overview of the beam parameters in ring 2 during the first ramp for the tune shift measurement at top energy on the 15th and 16th of September 2017. The top plot shows the gap of a primary (TCP.D6R7) and a secondary collimator (TCSG.D4R7). The second, third and fourth plot show the individual bunch intensities, full bunch lengths and the vertical emittances. The time at which the ADT kicks were sent are marked with dashed lines.

computed from Eq. 3.3 and using the tune shift obtained with DELPHI and the tune shift corrected for the quadrupolar impedance contribution. The last column shows the TMCI threshold inferred from the measurements.

The average ratio between measurements and simulations is calculated for the two beams and planes. The simulation results are from DELPHI with the quadrupolar tune shift effect taken into account via the correction factors. The results are reported in Table 3.5 and show that the tune shifts at top energy are underestimated by ∼20 % to 60 %.

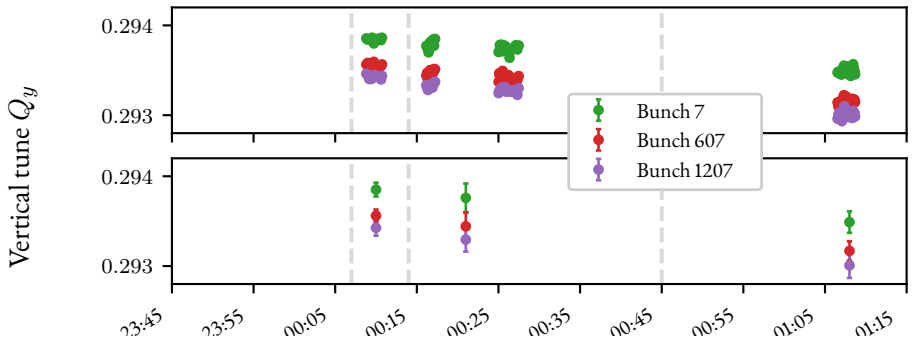

Figure 3.13: Tune signals obtained after the post-processing of the ADT kicks signals with SUSSIX (top plot). The data represented is for beam 2 vertical plane and the corresponding beam parameters shown in Fig. 3.12. Three collimators configuration, separated by a dashed line, were measured with this beam. The left part of the plot corresponds to the nominal collimators configuration (5/6.5), the central part to the tighter TCSG setting (5/6) and the right part to the tighter TCP setting (4.5/6). The bottom plot shows the average tune for each bunch in the three collimators configurations.

Table 3.3: Measured and simulated tune shifts as a function of beam intensity for the LHC nominal collimator settings and tighter configurations. The third column reports DELPHI simulations results. The fourth column is the correction factor to account for the quadrupolar impedance effect and the fifth column is the simulation results with the correction factor applied.

		Tune shift / $\left(10^{12}\,\text{p.p.b.} \times Q_s\right)^{-1}$			
	Conf.	Sim.	Correction / %	Sim. w/ quad.	Measured
B1H	(5/6.5)	−3.03	−12.7	−2.65	−3.37
	(5/6.0)	−3.42	−13.6	−2.99	−4.12
B1V	(5/6.5)	−2.34	−8.9	−2.13	−3.77
	(5/6.0)	−2.66	−8.2	−2.44	−3.84
B2H	(5/6.5)	−3.16	−12.2	−2.77	−3.70
	(5/6.0)	−3.56	−13.3	−3.08	−3.87
	(4.5/6.0)	−3.78	−14.3	−3.24	−4.48
B2V	(5/6.5)	−2.40	−8.7	−2.19	−2.70
	(5/6.0)	−2.73	−7.8	−2.51	−2.97
	(4.5/6.0)	−2.90	−6.2	−2.8	−2.98

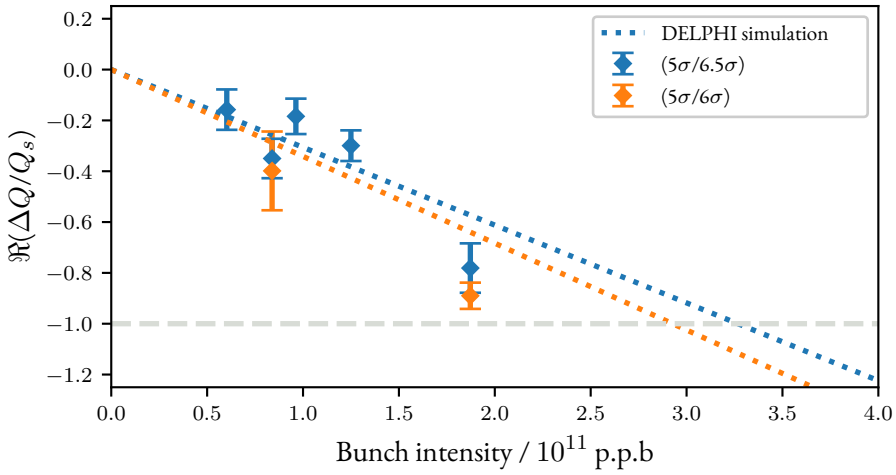

(a) B1H

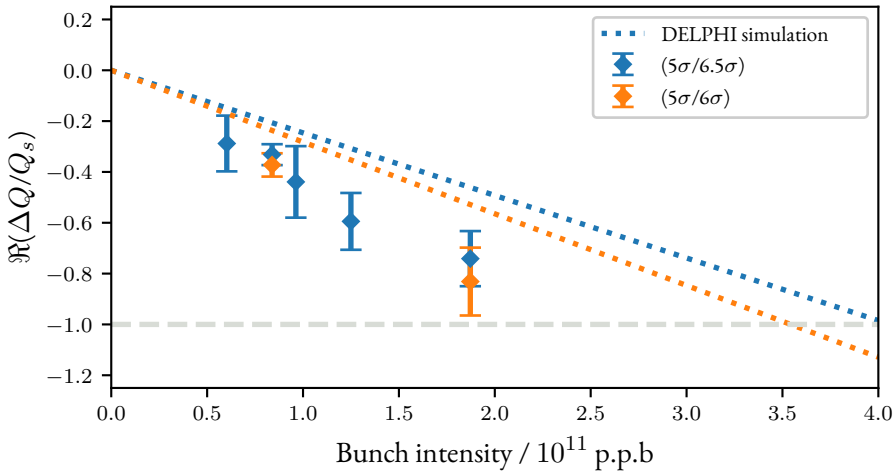

(b) B1V

Figure 3.14: Measured tune shift as a function of bunch intensity for beam 1, compared to DELPHI simulations corrected for the quadrupolar tune shift (dashed lines). The collimator settings measured during the MD are represented by different line and points colors.

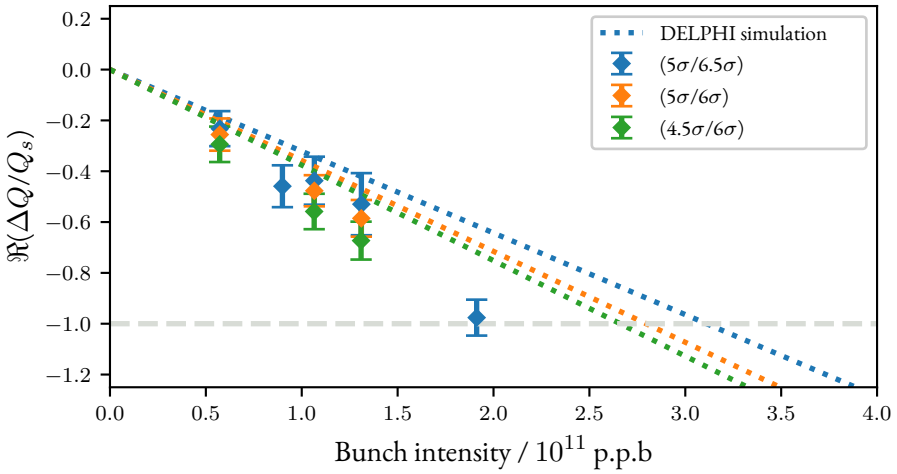

(a) B2H

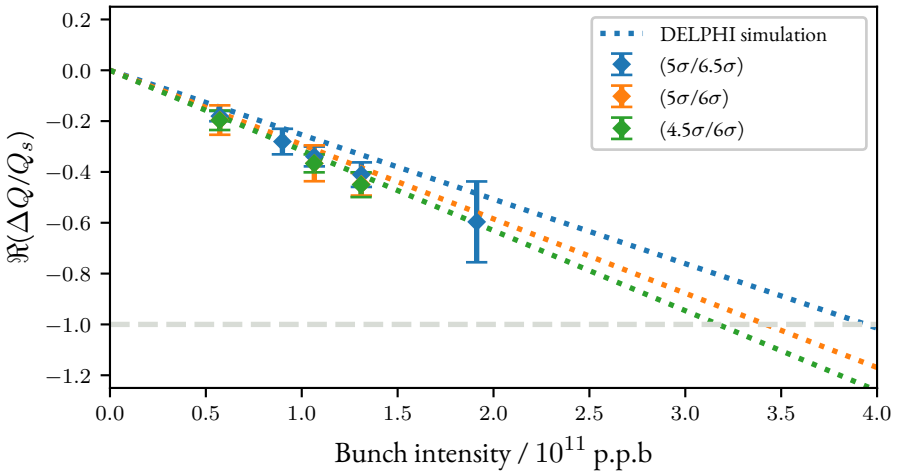

(b) B2V

Figure 3.15: Measured tune shift as a function of bunch intensity for beam 2, compared to DELPHI simulations corrected for the quadrupolar tune shift (dashed lines). The collimator settings measured during the MD are represented by different line and points colors.

Table 3.4: TMCI intensity threshold inferred from the measurements presented in Table 3.3 and from DELPHI simulations. The third column corresponds to DELPHI results. The fourth and fifth columns are the thresholds estimated from the mode 0 tune shift, without and with the correction for the quadrupolar tune shift effect. The last column shows the measurement results.

		Threshold / 10^{11} p.p.b.			
	Conf.	DELPHI	DELPHI tune shift	DELPHI tune shift corrected	Measured
B1H	(5/6.5)	2.8	3.3	3.8	2.9
	(5/6.0)	2.4	2.9	3.4	2.4
B1V	(5/6.5)	3.4	4.3	4.7	2.7
	(5/6.0)	3.0	3.7	4.1	2.6
B2H	(5/6.5)	2.8	3.2	3.6	2.7
	(5/6.0)	2.4	2.8	3.2	2.6
	(4.5/6.0)	2.2	2.6	3.1	2.2
B2V	(5/6.5)	3.4	4.1	3.5	3.7
	(5/6.0)	3.0	3.6	3.0	3.4
	(4.5/6.0)	2.8	3.4	2.8	3.3

Table 3.5: Measurement to simulation ratios of the tune shifts versus intensity in the LHC, for both beams and planes. The measurements for the different collimators configurations are averaged and compared to simulations results which account for the quadrupolar tune shift.

	Horizontal	Vertical
Beam 1	1.3	1.6
Beam 2	1.3	1.2

3.3.2 Measurement of individual collimators impedance at top energy

The measurement of tune shifts versus intensity detailed beforehand allows to compare the total machine impedance to the model. The effect of the collimators on the tune shift was clearly shown by closing further their gaps. It is therefore interesting to study the individual collimator contribution to the overall machine impedance budget. As seen previously, the LHC collimators can be moved from their nominal position, allowing to change the machine impedance at will. The position setting of a single collimator can be modified and its impact on the machine transverse tune measured.

Multiple machine development sessions were carried out during the years 2016, 2017 and 2018 to measure primary, secondary and tertiary collimators [11, 83]. The measurement principle is similar to the one carried out during the TMCI measurement described in part 3.3.1. For some cases in 2016, the tune kicker (MKQA) was used [23] instead of using the ADT to excite the beams. The collimator to be measured is further closed, then a series of kicks is applied. The collimator gap is then opened and a new series of kicks is made. This process is repeated one more time. Figure 3.16 shows the TCSG measurement process during the dedicated 2017 machine development. In this case seven different secondary collimators were measured.

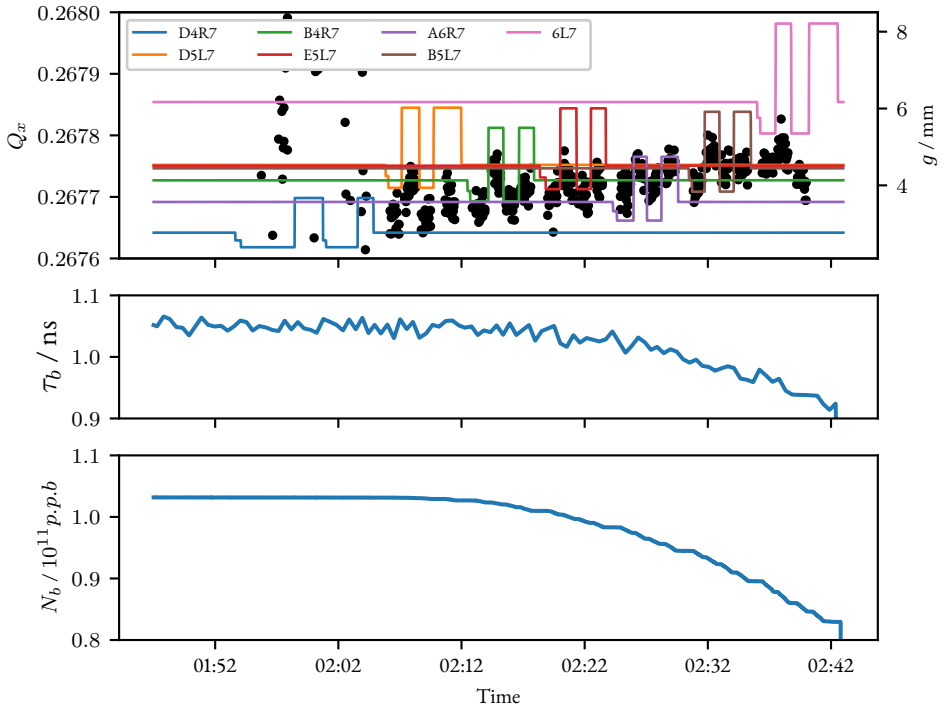

Figure 3.16: Overview of the secondary collimators measurements performed on the night of 27th to 28th of October 2016. The top plot shows the horizontal tune obtained from the ADT kicks (dots) correlated with the collimators gaps (solid lines) along time. The center and bottom plots show the full bunch length and the bunch intensity evolution.

The same process was used to measure primary and some of the tertiary collimators. Table 3.6 reports the names, location, and collimation plane of the collimators which were measured during Run II.

Table 3.6: List of single collimators measured during Run II.

Type	Collimator name	Location	Collimation plane
Primary	D6L7	IR7	Vertical
	C6L7	IR7	Horizontal
	B6L7	IR7	Skew
	6L3	IR3	Horizontal
Secondary	A6L7	IR7	Skew
	D4L7	IR7	Vertical
	B4L7	IR7	Horizontal
	B5R7	IR7	Skew
	D5R7	IR7	Skew
	E5R7	IR7	Skew
	6R7	IR7	Horizontal
Tertiary	TCTPV	IR2	Vertical
	TCTPH	IR2	Horizontal

Figure 3.16 also shows the beam parameters during one of the machine developments. Significant bunch intensity losses caused by too strong kicks affected the measurement. The full bunch length shrinks down and the tune drifts upwards over time. However the effect of the collimator impedance on the tune can still be observed, as detailed in Fig. 3.17. The tune is changed when opening and closing the collimator jaws. Similarly to the TMCI measurement data processing, an average tune value is computed for each period of time when the gaps were opened and close. The difference between the closed position and opened position can then be calculated and compared to simulations results..

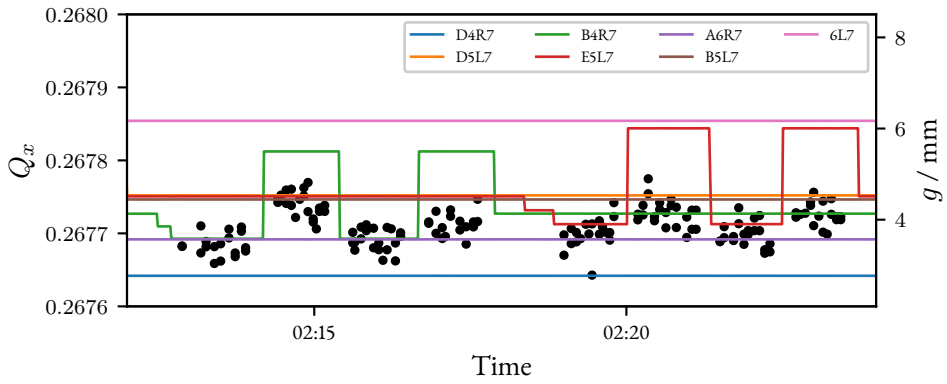

Figure 3.17: Detail of Fig. 3.16 showing the tune variation during the measurement of two collimators. Despite the overall upwards tune drift, the effect of the collimator gaps opening and closing remains visible and the induced tune shift can be computed.

The measurements and simulations results for the collimators impedance measurements are reported in appendix C. Figure 3.18 shows the ratios between measurement and simulation of the single collimator

induced tune shifts. The ratios are within a factor two for most of the collimators, which is consistent with the results of the full machine tune shift measurements.

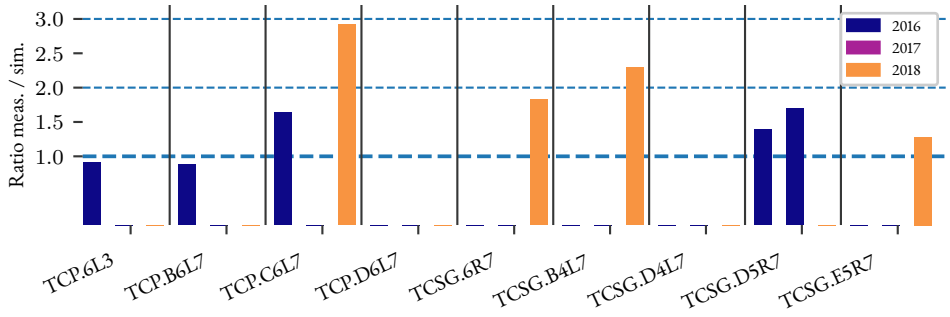

(a) Ratios B1H

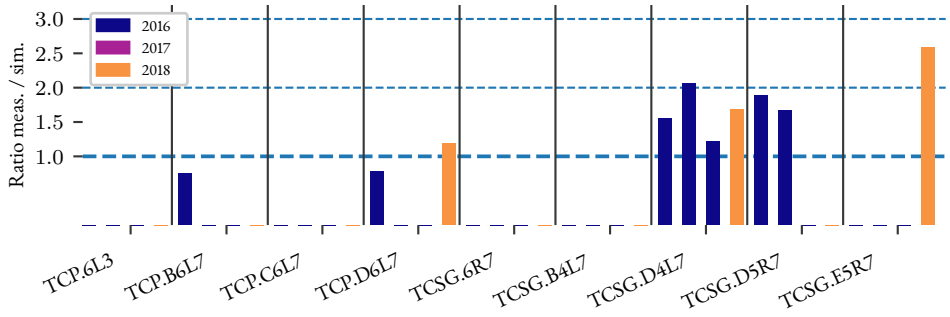

(b) Ratios B1V

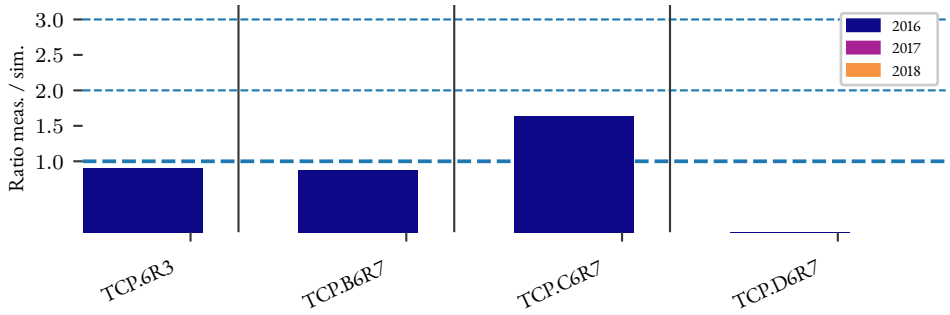

(c) Ratios B2H

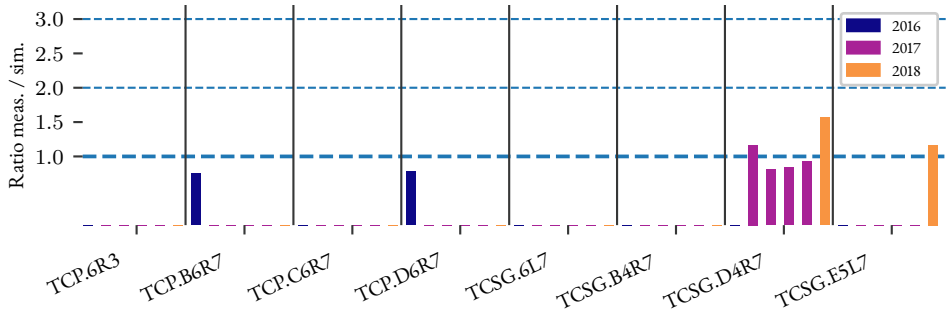

(d) Ratios B2V

Figure 3.18: Ratios between measured and predicted tune shifts induced by individual collimators of ring a and ring 2 at top energy. The measurement years are indicated by different colors.

3.3.3 Measurement of the instability growth rate versus chromaticity at injection energy

The measurements presented beforehand investigated the machine when it is in the most critical phase stability-wise. These measurements are time consuming and the limited periods dedicated to machine studies in the LHC reduce the measurement repeatability. The injection set-up, the energy ramp, the beam parameters and equipment configuration once the top energy is reached reduce considerably the quantity of data which can be acquired. The number and intensity of bunches present in the machine must also remain below a certain limit to protect the superconducting magnets and machine equipment. On the other hand experiments performed at injection energy can profit from a quick refilling time either to reproduce a measurement or to scan a certain parameter space.

A measurement of the single bunch instability growth rate as a function of chromaticity was planned and executed. The measurement took place during the MD block 3 of 2018, on the afternoon of the 14^{th} of September. With nominal bunches at the injection energy, the horizontal chromaticity was trimmed in the negative range, keeping the vertical chromaticity positive. The ADT was then switched off to let an instability develop. The turn-by-turn position signal was then recorded over 64 000 turns with the ADTObsBox. From these signals the instability rise time was found by fitting an exponential function.

The experiment was repeated for both beams and planes, and the results compared to DELPHI simulations using the LHC impedance model at injection. Figures 3.19 and 3.20 show the results for the horizontal and vertical plane of both beams. The impedance model for beam 1 and beam 2 being similar, only one set of DELPHI simulation is presented.

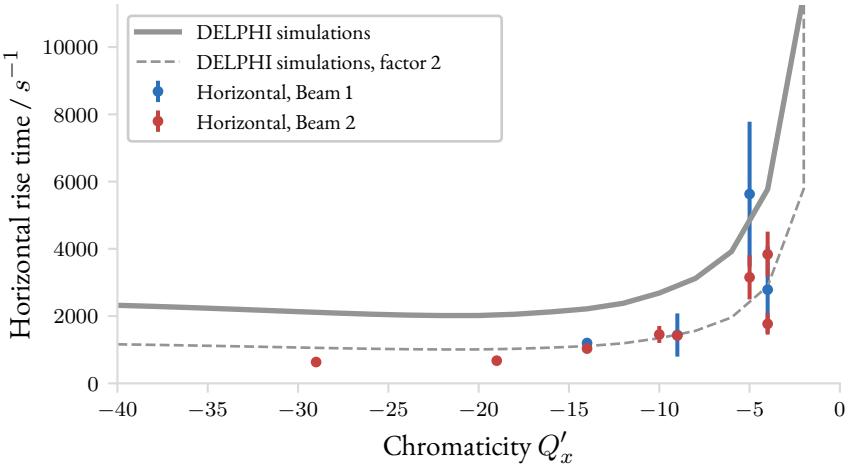

Figure 3.19: Instability rise time as a function of chromaticity measured in the LHC at injection energy, for the horizontal plane. The measurements were made for beam 1 (in blue) and beam 2 (in red). They are compared to DELPHI simulations represented with a solid grey line. The dashed grey line corresponds to the simulated rise times with a factor two applied.

The results are within a factor two from the predictions for both beams and planes, with the exception of the vertical plane of beam 1. In this case at large negative chromaticities the rise time is larger than

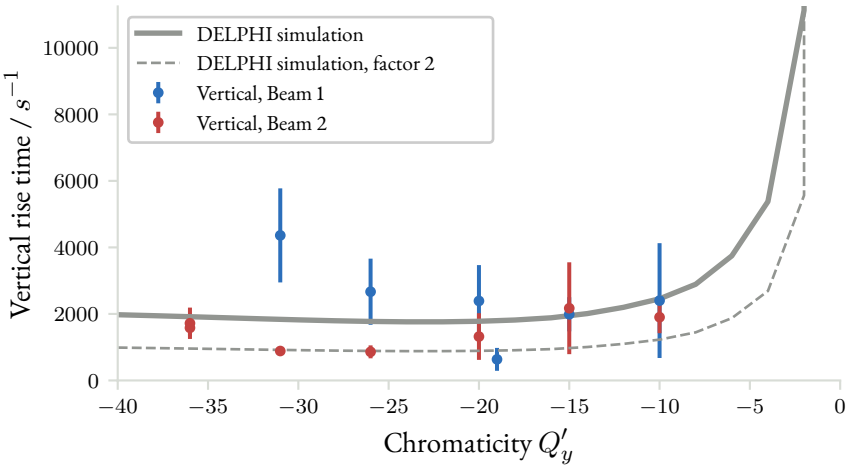

Figure 3.20: Instability rise time as a function of chromaticity measured in the LHC at injection energy, for the vertical plane. The measurements were made for beam 1 (in blue) and beam 2 (in red). They are compared to DELPHI simulations represented with a solid grey line. The dashed grey line corresponds to the same simulated rise times with a factor two applied.

predicted. For those points the instability signal is less clear and non-linear effects such as space-charge could play a stabilizing role [85, 92, 106]. An example of such signal is given in Fig. 3.21.

3.3.4 Summary of the impedance related measurements performed in 2016, 2017 and 2018

The results of the various stability measurements performed in the LHC during Run II can be summarized by computing the ratio between measurements and predictions from the impedance model. Those were shown for the TMCI measurements, the individual collimators measurements and the instability growth rate at injection energy. Table 3.7 reports those ratios for the different years [4].

Year	Measurement	B1H	B1V	B2H	B2V
2016	Tune shift vs. IR7 secondary collimators gaps[1]	1.3	1.4	1.1	1.4
2017	Tune shift vs. bunch intensity[2]	1.2	1.4	1.3	1.1
	Tune-shift vs. bunch intensity[3]	1.4	1.6	1.4	1.2
2018	Full machine tune shift at flat-top[4]	1.5	-	-	-
	Growth-rate vs. negative chromaticity	1.4	1.6	1.4	1.2

[1] Tune shifts measurements with all IR7 secondary collimators, detailed in [36].
[2] Quadrupolar impedance effect not taken into account.
[3] Quadrupolar impedance effect taken into account.
[4] Measurement from Beam Transfer Function (BTF) detailed in [139].

Table 3.7: List of ratios between measured and predicted tune shifts values for both beams and planes.

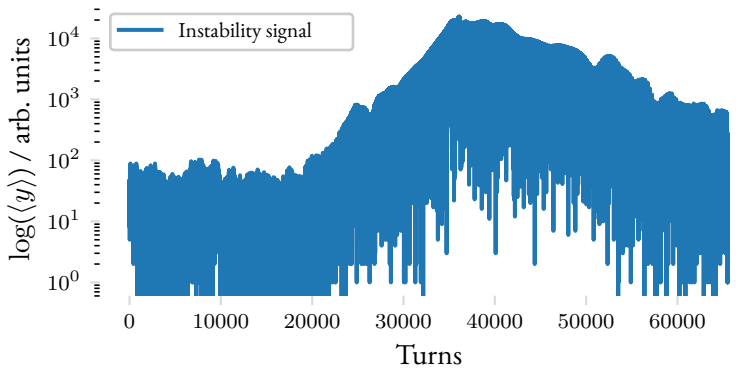

Figure 3.21: Example of a beam 1 vertical position signal. The y-axis is in logarithmic scale. With this scale the fit should be realized on an linearly growing part. However for this instability signal the part to fit is less clear as the instability seems to develop at different rates between turn 20 000 and 30 000 and turn 30 000 and 40 000.

Thanks to the different measurements methods, the impedance was investigated from different sides: individual elements and full machine, imaginary part and real part, injection and top energy. From 3.7 the factor between measurements and simulations can be estimated to be between 30 % and 50 %. This value can be compared to the factor two on the Landau octupoles current required to stabilize the beam: missing elements to the the impedance model need to be found. However the impedance is not the only contributor to the discrepancy. Studies are currently ongoing to investigate potential effects detrimental to beam stability: external noise affecting the transverse distribution [57], transverse damper [41] and its interplay with Landau damping [86] among others.

4 The Transverse Mode Coupling Instability in future machines

We investigated in the previous chapter the mode coupling instability in the LHC. Measurements performed in the machine also allowed to estimate the uncertainty on the accelerator impedance. We concluded from these measurements that the impedance is approximately 30 % to 50 % higher than predicted with the current model.

As the High-Luminosity upgrade of the LHC will use bunches with an intensity increased by a factor of two compared to the current value, impedance will be one of the critical aspects of the project. The mode coupling instability in the HL-LHC will be investigated and the impact of the impedance reduction assessed. We will first present the scope of the collimation upgrade and the simulations results for different scenarios in part 4.1. Measurements performed in the LHC to showcase the benefits of the impedance reduction will then be presented in part 4.2. One of the measurement focused on the full machine tune shift whereas the other characterised the impedance of a prototype collimator for the collimation upgrade.

We will conclude the chapter with an overview of the impedance and stability estimates realised for the High-Energy LHC study. The HE-LHC is a proposed collider which could succeed the HL-LHC and re-use the existing accelerator infrastructures. Part 4.3 will describe the project and the impedance and beam stability studies performed.

4.1 Simulations of the Transverse Mode Coupling Instability in the High Luminosity LHC

The impedance reduction for HL-LHC will target the IR7 betatron cleaning collimators since they are the main contributors to the impedance at top energy as we saw in part 2.1.4. Selected collimators among the three primaries and eleven secondaries will be replaced. The overall design of the collimators will remain similar, but the jaws materials will be changed. During the Long Shutdown 2 in 2019 and 2020, two primary collimators (TCP) per ring will be replaced in the framework of the LHC consolidation project. Four secondary collimators (TCSG) per ring will also be replaced by low impedance ones in the framework of the HL-LHC collimation upgrade [116, 117]. The remaining seven TCSGs per ring will be replaced during the Long Shutdown 3 in 2024 and 2025.

The new collimators will use a molybdenum-graphite composite [63, 118] instead of carbon-fiber reinforced carbon for the jaw materials. The upgraded primary collimators, the TCPPM[1], will use the molybdenum-graphite (MoGr) blocks over their 60 cm length. The new secondary collimators, the

[1] Here the M stands for a metallic material used for the jaws and the second P indicates that a beam position monitor is embedded in the collimator for orbit control.

TCSPM, will use molybdenum-graphite for the jaws materials and the blocks will also receive a 5 μm coating of pure molybdenum (Mo) [20].

These new materials were chosen to meet the challenges presented by both the impedance reduction and the machine protection. Their resistivities are reported in Table 4.1. The MoGr bulk material has a resistivity reduced by a factor 5 compared to the current jaw materials and the additional Mo coating would provide an other factor ∼20 reduction for the jaw resistivities. We saw in part 2.1.2 that the resistive wall transverse impedance $Z_{\perp,RW}$ scales as

$$Z_{\perp,RW}(\omega) \propto \delta_{skin}(\omega)\,, \tag{4.1}$$

with δ_{skin} the skin depth at the considered frequency. This simplifies in turn to

$$Z_{\perp,RW}(\omega) \propto \sqrt{\rho_c}\,, \tag{4.2}$$

where $\rho_c = 1/\sigma_c$ is the electrical resistivity. Therefore the use of MoGr will reduce by a factor 2.2 the transverse resistive wall impedance of the collimators. The Mo coating would provide a factor of ∼10 reduction on the resistive wall impedance compared to the current collimator design.

Table 4.1: Resistivity of the materials selected for the LHC collimation upgrade, compared to the current CFC.

Material	Resistivity / nΩ m
CFC[1]	5000
MoGr[2]	1000
TiN[2, 3]	400
Mo[2]	54

[1] Further data on the electric properties of materials currently used in the LHC can be found in [103].
[2] Further data on these materials can be found in [30, 63]
[3] TiN stands for titanium nitride. This material is a possible alternative to the Mo coating for the MoGr blocks.

The Landau octupole current is a limiting factor for coherent beam stability as we saw in part 3.1. The impedance reduction will allow to preserve stability margins in HL-LHC with the higher intensity beams [19, 20]. We will now study the impact of the collimation upgrade on the transverse mode coupling instability. Table 4.2 shows the different scenarios which were studied. Two additional cases in which the Mo coating of the secondary collimators is not present were also studied. The HL-LHC scenarios are compared to two scenarios with the LHC impedance model: the first one with the nominal collimator gaps and the second one with the secondary collimators opened to $14\sigma_{coll}$ to simulate an impedance reduction.

The collimator gaps used in the different simulation scenarios are reported in appendix B.4. The horizontal dipolar impedance as a function of frequency is plotted in Fig. 4.1 for the different cases. A clear impedance reduction with respect to the LHC 2017 nominal case can be observed. The final upgrade with all the TCSGs made of molybdenum coated molybdenum-graphite provides a reduction by a factor ∼5 over the 10 kHz to 10 GHz frequency range. The LHC scenario with the TCSGs opened

Table 4.2: Scenarios considered for the study of TMCI in HL-LHC. The table shows the materials used for the different collimators families and the number of collimators upgraded.

Scenario name	TCP	TCSG
LHC 2017	3 CFC	11 CFC
LHC 2017, TCSGs at $14\sigma_{coll}$	3 CFC	11 CFC
HL-LHC LS2, uncoated TCSGs	2 MoGr, 1 CFC	4 MoGr, 7 CFC
HL-LHC LS2, coated TCSGs	2 MoGr, 1 CFC	4 Mo+MoGr, 7 CFC
HL-LHC final, uncoated TCSGs	2 MoGr, 1 CFC	11 MoGr
HL-LHC final, coated TCSGs	2 MoGr, 1 CFC	11 Mo+MoGr

at $14\sigma_{coll}$, represented in orange, is close to the LS2 scenarios of the HL-HC collimation upgrade, represented in green and red, for the 10 MHz to 10 GHz range.

The scenarios were used to study the transverse mode coupling instability in HL-LHC. The beam parameters used for the simulations are similar to those used for the TMCI simulations in the LHC and are therefore reported in appendix B.4. The results for the horizontal plane of beam 1 will be reported since it is the most critical plane from the stability point of view [94, 117]. Figure 4.2 shows DELPHI results obtained for the LHC 2017 scenario and the HL-LHC final scenario with molybdenum coating. For the latter case the coupling of modes 0 and -1 still occurs but at an intensity of 8.4×10^{11} p.p.b. instead of 2.8×10^{11} p.p.b.

To facilitate the comparison of the different scenarios, the mode 0 shift is linearly fitted in the low intensity part as showed in Fig. 4.2. The TMCI intensity threshold can be obtained with the instability growth rate. Figure 4.3 shows the linear fits of the mode 0 real part and the instability growth rate for the different scenarios.

From these linear fits the tune shifts versus intensity can be computed. They are reported in Table 4.3. The first stage implementation of the collimation upgrade during the LS2 increases the TMCI intensity threshold by a factor 2.2, from 2.8×10^{11} p.p.b. to 6.3×10^{11} p.p.b. The final stage of the upgrade with the eleven secondary collimators coated in molybdenum increases the TMCI threshold by a factor 3.1 compared to the current LHC case. For all these scenarios the TMCI threshold reaches a value higher than the maximum bunch intensity of 2.3×10^{11} p.p.b. planned for HL-LHC.

Table 4.3: Results of DELPHI simulations for the LHC and HL-LHC impedance reduction scenarios. Both the tune shift versus intensity and the TMCI threshold are reported.

Scenario	Tune shift / $\left(10^{11}\text{ p.p.b.} \times Q_s\right)^{-1}$	TMCI
LHC 2017	−0.32	2.8
LHC 2017, TCSGs at $14\sigma_{coll}$	−0.18	5.0
HL-LHC LS2, uncoated TCSGs	−0.16	5.7
HL-LHC LS2, coated TCSGs	−0.14	6.3
HL-LHC final, uncoated TCSGs	−0.13	6.7
HL-LHC final, coated TCSGs	−0.11	8.7

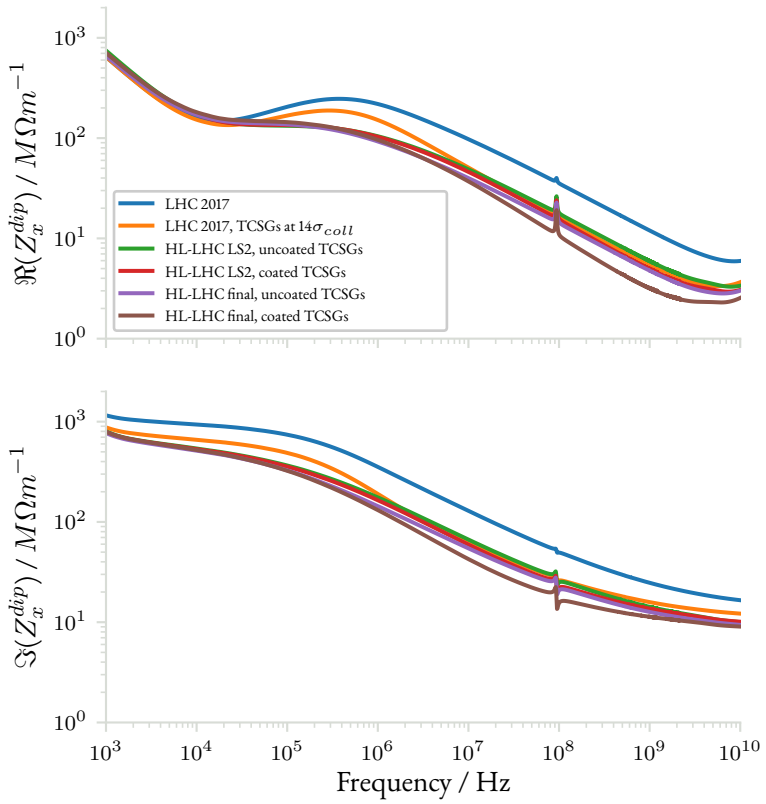

Figure 4.1: Horizontal dipolar impedance as a function of frequency for the different scenarios considered. The top plot shows the real part of the impedance, the bottom plot the imaginary part.

The molybdenum coating used for the secondary collimators helps to increase the TMCI threshold by 10 % for the LS2 upgrade and by 30 % for the final upgrade with respect to the uncoated versions of the collimators. The tune shifts versus intensity are similarly decreased for the different investigated cases.

We saw with simulations that the collimation upgrade of the LHC will increase the TMCI threshold and reduce the machine tune shift. These will provide margins to operate the machine at lower chromaticity. The benefits of the impedance reduction will now be investigated with beam based measurements performed in the LHC.

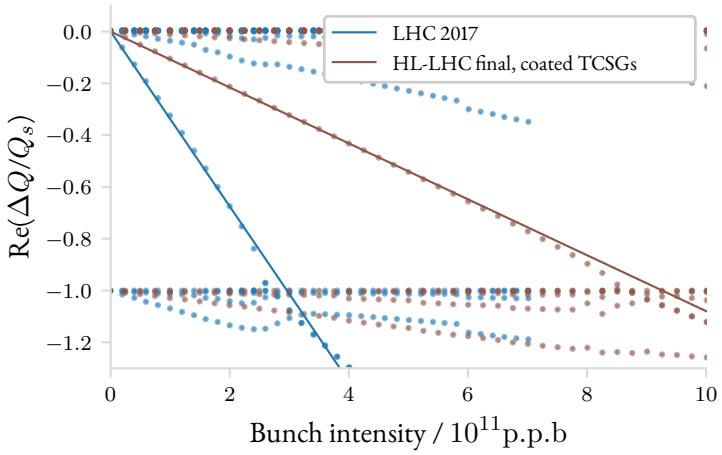

Figure 4.2: Horizontal mode frequency shifts as a function of bunch intensity for two of the HL-LHC scenarios considered. The modes are computed with DELPHI (points) and the mode 0 is then fitted in the low intensity part (solid lines).

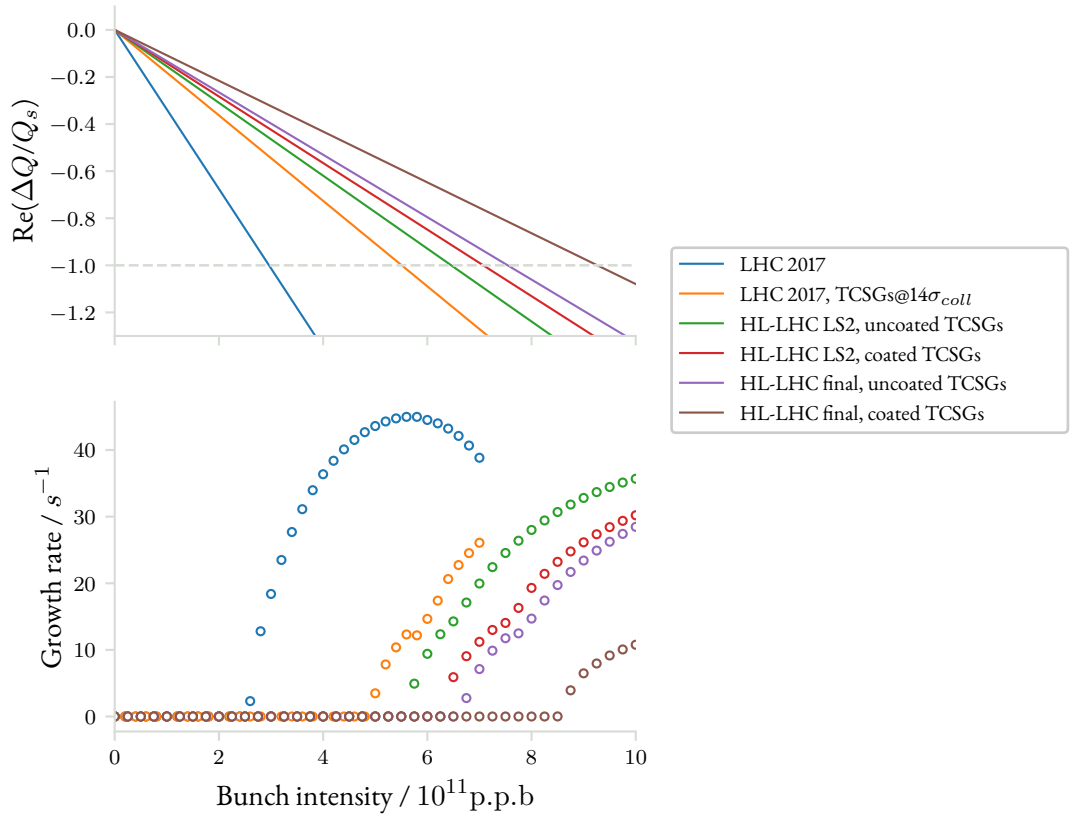

Figure 4.3: Mode 0 horizontal frequency shifts as a function of bunch intensity (top plot) for all scenarios considered in Table 4.2. The top plot shows the function fitted on the low intensity region as presented in Fig. 4.2. The bottom plot shows the associated growth rates obtained with DELPHI.

4.2 Study of the collimation upgrade impact with beam measurements

4.2.1 Measurement of the machine tune shift

We saw in the previous part that the impedance reduction planned for HL-LHC will have a visible impact on the coherent beam tune shift. To demonstrate the benefits of the impedance reduction targeted at the collimators, a measurement was performed in the LHC by opening the secondary collimators gaps. Simulations detailed in the the previous part showed that opening the secondary collimators of IR7 to $14\sigma_{coll}$ reduces the machine impedance to an intermediate level between the nominal configuration and the LS2 upgrade.

This configuration was measured during the TMCI machine development detailed in part 3.3.1. The measurement procedure and the data post-treatment method are therefore identical. Figure 4.4 shows the results for both planes of beam 1 and Fig. 4.5 the results for beam 2. The mode 0 frequency shift predicted by DELPHI has been corrected for the quadrupolar impedance contribution. In all cases the tune-shift is reduced compared to the nominal machine configuration.

The resulting tune shifts as a function of intensity are reported in Table 4.4 and the corresponding TMCI intensity thresholds are reported in Table 4.5. The tune shift is reduced by a factor of ∼1.3 in the horizontal plane and by a factor of ∼2 in the vertical plane. The TMCI threshold inferred from these measurements is increased by the same factors compared to the nominal LHC case.

Table 4.4: Measured and simulated tune shifts as a function of beam intensity for the LHC nominal collimator settings and the HL-LHC mock-up scenario. The third column reports DELPHI simulations results. The fourth column is the correction factor to account for the quadrupolar impedance effect and the fifth column is the simulation results with the correction factor applied.

		Tune shift / $\left(10^{12}\,\text{p.p.b.} \times Q_s\right)^{-1}$			
	Conf.	Sim.	Correction / %	Sim. w/ quad.	Measured
B1H	(5/14)	−1.93	−5.9	−1.82	−2.34
	(5/6.5)	−3.03	−12.7	−2.65	−3.37
B1V	(5/14)	−1.43	−14.9	−1.22	−1.9
	(5/6.5)	−2.34	−8.9	−2.13	−3.77
B2H	(5/14)	−2.06	−4.2	−1.97	−2.9
	(5/6.5)	−3.16	−12.2	−2.77	−3.70
B2V	(5/14)	−1.42	−15.6	−1.20	−1.46
	(5/6.5)	−2.40	−8.7	−2.89	−2.70

This tune shift versus intensity measurement highlights the predominant role of the collimators in the impedance model. They support the impedance reduction strategy for the HL-LHC collimation upgrade and the beneficial effect it will have for coherent beam stability.

Table 4.5: TMCI intensity threshold inferred from the measurements presented in Table 4.4 and from DELPHI simulations. The third column corresponds to DELPHI results. The fourth and fifth columns are the threshold estimated from the mode 0 tune shift, without and with the correction for the quadrupolar tune shift effect. The last column shows the measurement results. The nominal LHC case and the HL-LHC-like case are presented.

		Threshold / 10^{11} p.p.b.			
	Conf.	DELPHI	DELPHI tune shift	DELPHI tune shift corrected	Measured
B1H	(5/14)	5.2	5.2	5.5	4.3
	(5/6.5)	2.8	3.3	3.8	2.9
B1V	(5/14)	6.8	7.0	8.2	5.3
	(5/6.5)	3.4	4.3	4.7	2.7
B2H	(5/14)	4.8	4.8	5.1	3.4
	(5/6.5)	2.8	3.2	3.6	2.7
B2V	(5/14)	6.6	7.0	8.3	6.8
	(5/6.5)	3.4	4.1	3.5	3.7

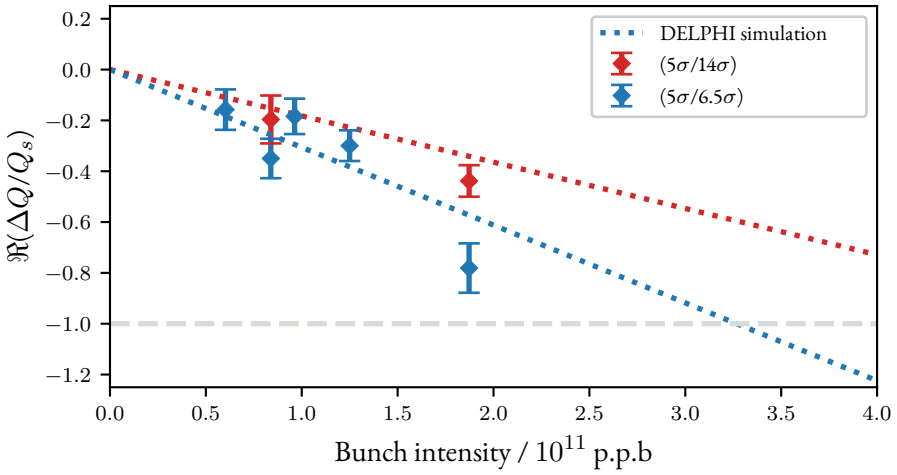

(a) B1H

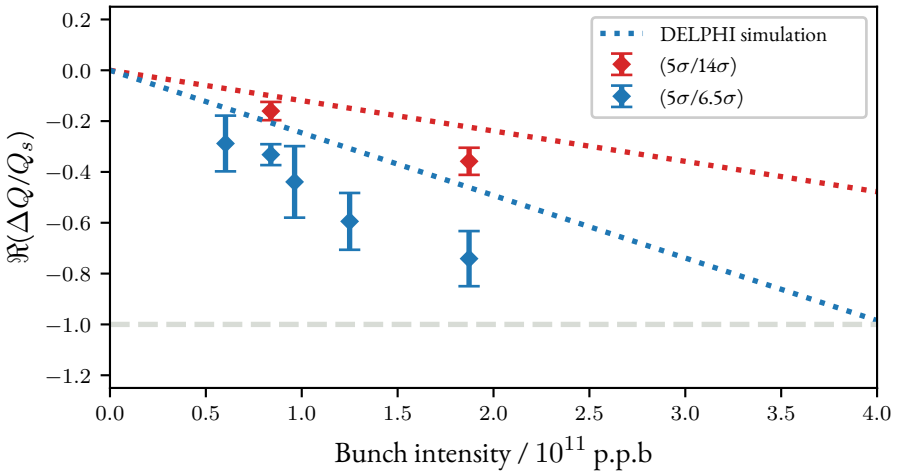

(b) B1V

Figure 4.4: Measured tune shift as a function of bunch intensity for beam 1, compared to DELPHI simulations corrected for the quadrupolar tune shift (dashed lines). The nominal LHC configuration is represented in blue, the low impedance configuration in red.

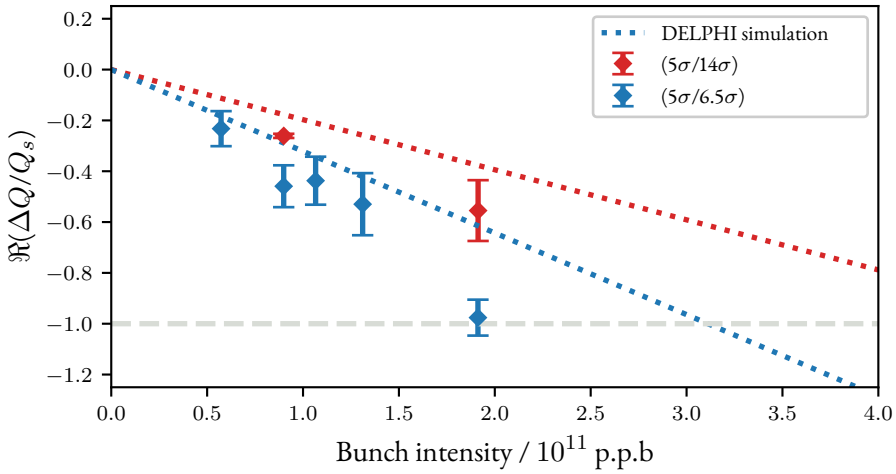

(a) B2H

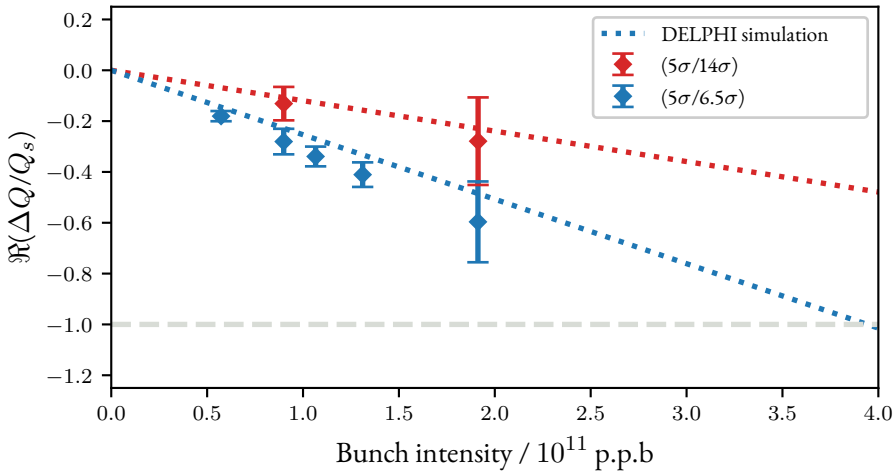

(b) B2V

Figure 4.5: Measured tune shift as a function of bunch intensity for beam 2, compared to DELPHI simulations corrected for the quadrupolar tune shift (dashed lines). The nominal LHC configuration is represented in blue, the low impedance configuration in red.

4.2.2 Measurement with the low impedance collimator prototype

To further validate the choice of low impedance collimators for the HL-LHC collimation upgrade, a prototype collimator was installed in the LHC during the 2016-2017 winter shutdown [116]. It was positioned in a spare slot of beam 2 adjacent to the TCSG.D4R7 [117]. This collimator, the TCSPM.D4R7, is a vertical collimator. Unlike the production version, this prototype does not have fully molybdenum coated jaws. As showed in Fig. 4.6, the jaws have three different materials: a molybdenum coating, the molybdenum-graphite bulk and a titanium-nitride coating. A motor can shift horizontally the jaws and expose a different stripe to the beam.

This prototype collimator was designed to validate with beam measurements the choice of materials for the collimation upgrade. The goal was to measure the tune shifts induced by the three different materials and compare the results to predictions from the impedance model. The adjacent collimator, the TCSG.D4R7 was also measured during the procedure.

A machine development session took place on the 30$^{\text{th}}$ of June and 1$^{\text{st}}$ of July 2017. The measurement procedure applied was identical to the one described in part 3.3.2 on the single collimator tune shift measurements. The beam was kicked with the transverse damper and the oscillations recorded with the ADTObsBox. As showed in Fig. 4.7a a series of kicks was performed for ∼2 min and the collimator gap was then changed. The procedure was repeated for a few cycles of the collimator gap. However the machine tune is also jittering with time. In the TCSPM case the tune jitter is comparable to the impedance induced tune shift. The measurement method was therefore slightly modified to bypass the tune jitter effects and reach the desired precision.

For this second attempt the collimator gap was changed in quick successions as showed in Fig. 4.7b. The beam was kicked in quick series with the ADT, decorrelating the kicks from the collimator gap. The tune jitter is still present as can be seen in Fig. 4.7b but two distinct lines appear as well in the time evolution of the tune. The upper one corresponds to kicks which were sent when the collimator gap was wider, the lower one to kicks applied when the gap was tighter.

The tune jitter effect could be removed and the tune shift induced by the TCSPM different materials computed [14]. This improved method allowed to reach a tune shift measurement precision in the order of a few 10×10^{-5}. The procedure was repeated for different lower positions of the collimation gap: $3.5\sigma_{coll}$, $4\sigma_{coll}$, $4.5\sigma_{coll}$ and $6\sigma_{coll}$. The subsequent data treatment is further detailed in [14, 16]. Figure 4.8 shows the tune shift as a function of the collimator gap for the different considered materials. From the resistive wall impedance model the tune shifts should scale in $1/n_\sigma^3$. The measured tune shifts include both the resistive wall impedance and the geometric impedance from the collimator elements. The contribution of the geometric impedance was therefore subtracted from the measured tune shifts [43, 44]. The measurements are compared to simulations results.. For carbon-fiber reinforced carbon, molybdenum-graphite and titanium-nitride, measurements are lower than predicted whereas for the molybdenum coating measurements are two times higher than the prediction.

Despite the discrepancy found between the model and measurements, the molybdenum coating on molybdenum-graphite jaws still provides the largest impedance reduction of all the investigated materials. Measurements of the electrical properties of molybdenum coatings are ongoing to systematically check and validate the production series of molybdenum coated blocks [2, 13, 62, 71, 82].

Figure 4.6: Top view of the prototype TCSPM jaw. Three stripes are visible: the top one is the molybdenum coating, the central one the molybdenum-graphite bulk and the bottom one the titanium-nitride coating. One the left a button beam position monitor is embedded in the transition taper. Picture from [45].

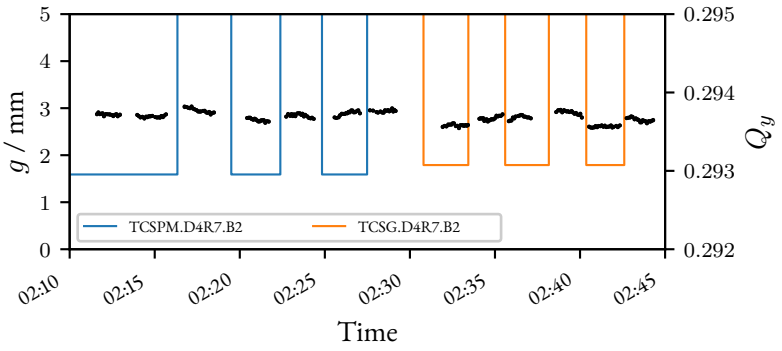

(a) Measurement with slow cycles of collimator gaps.

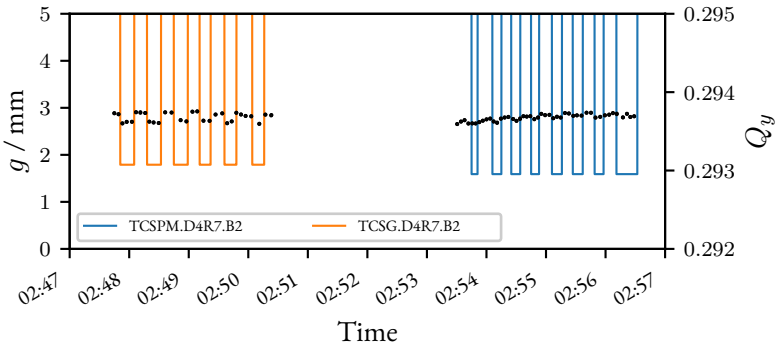

(b) Measurement with fast cycles of collimator gaps.

Figure 4.7: Tune and collimator gap versus time during the TCSPM measurement. The solid curves represent the collimator gaps. The TCSPM (in blue) and the adjacent TCSG (in orange) were both measured. During the first attempt (top plot), a tune shift induced by the collimator gap change is visible but the measurement precision is reduced by tune drifts. During the second attempt the collimator gap was opened and closed in quick successions while kicking the beam with the ADT (bottom plot). A tune drift was still present but could be fitted and the tune data corrected.

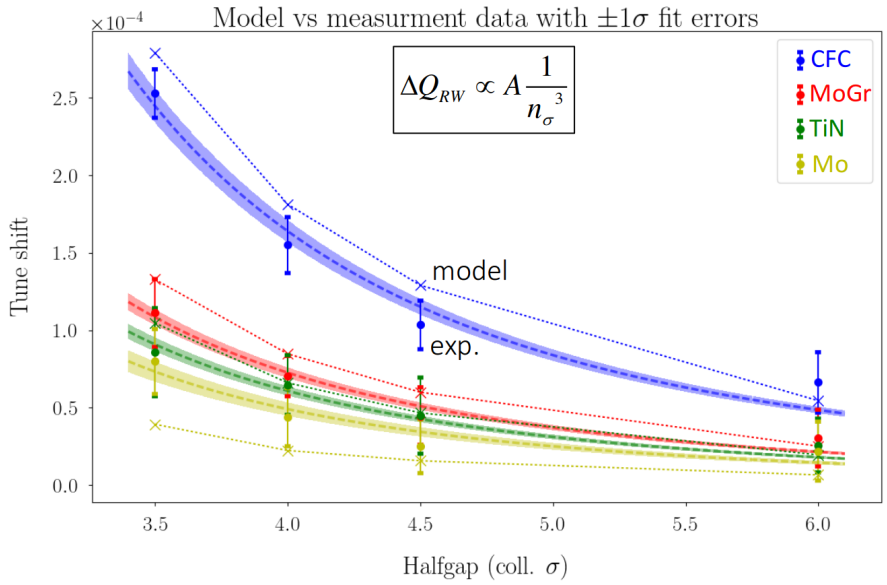

Figure 4.8: Tune shifts induced by the TCSPM as a function of collimator gap for the three different materials. Predictions from the impedance model are represented in dashed lines and measurements are represented with the 1σ error bar. The geometric impedance of the collimators has been removed of the measured values. Results courtesy of S.Antipov [16].

4.3 Impedance and beam stability considerations for the High Energy LHC study

We will now investigate the impedance model of the High-Energy LHC (HE-LHC) which was derived from the HL-LHC one. A quick overview of the Future Circular Collider Study and the HE-LHC impedance model at injection and top energy will be detailed in part 4.3.1. We will then use this model to study the mode coupling instability in part 4.3.2.

4.3.1 Impedance model for the HE-LHC

The High-Luminosity LHC is planned to operate until 2040 [20]. To follow it, two collider design studies have been launched at CERN: the Compact Linear Collider (CLIC), a multi-TeV linear electron-positron collider [141] and the Future Circular Collider (FCC). In the FCC study three different machines have been considered:

- The FCC-ee, a 100 km long electron-positron accelerator with collision energies ranging from 88 GeV to 365 GeV [28].
- The FCC-hh, a 100 TeV hadron collider (50 TeV per beam) which could follow the lepton collider, re-using the same infrastructures. High field magnets would be needed to reach the target energy [27].
- The High Energy LHC, a 27 TeV hadron collider which would re-use the LHC infrastructures with the high field magnets of FCC-hh to reach the collision energy [153].

The hadron colliders rely on high field magnets to obtain the desired energies. These magnets could reach a magnetic field of 16 T with $Nb Sn_3$ superconductors instead of the NbTi technology used in the LHC [26]. The machine protection requirements will become even more stringent as the beam energy increases. These requirements will in turn pose challenges for coherent beam stability from the very beginning of the machine design [21, 22].

The HE-LHC transverse impedance was derived from the HL-LHC impedance model [12]. The same optics function as in HL-LHC were used but the beam screen was replaced by the FCC-hh one, pictured in Fig. 4.9. This new beam screen design must cope with an increased synchrotron radiation power and the subsequent vacuum and cooling constraints [112] while keeping its impedance as low as possible.

Three injection energies options are considered for HE-LHC. The first at 450 GeV would allow to re-use the SPS as an injector without further modifications. The second and third options at 900 GeV and 1.3 TeV would require to replace the existing SPS by a superconducting machine. These two options are however more favorable in terms of available aperture for the beam injection [153]. For the impedance study the 450 GeV and the 1.3 TeV injection energies will be investigated.

For the collimators, the HL-LHC collimation layout was used. The collimator materials were assumed to be those of the fully upgraded HL-LHC which was detailed in part 4.1. The collimator gaps have been scaled with the beam energy and reference emitttance. Because of the higher energy, the transverse beam size will be reduced compared to LHC and HL-LHC and therefore the collimator gaps will also be smaller. The gap settings, their physical gaps and the beam parameters for stability simulations are reported in appendix B.5 and B.6.

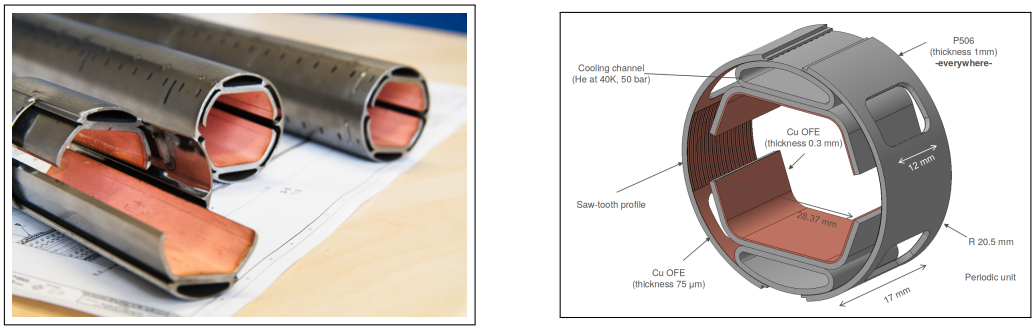

Figure 4.9: Picture of a beam screen prototype for the FCC-hh, and cross-section of the current design. Two slits are present to allow synchrotron radiation to escape from the main chamber. The pumping holes are shielded by the central chamber walls. Pictures from [37] and [98]

Figures 4.10 and 4.11 show the horizontal and vertical dipolar impedance at injection energy and top energy. The effect of the tighter collimator gaps in HE-LHC is clearly visible for both injection energy options. The collimators become a major contributor to the machine impedance in both cases [6]. For the 450 GeV option, even if the beam size is unchanged compared to HL-LHC, the impedance is higher because the collimators must be set closer to the beam to protect the magnets.

At top energy the impedance increases by a factor 10 compared to HL-LHC in the 100 kHz to 10 GHz frequency range. With a single bunch intensity for HE-LHC similar to the HL-LHC one, 2.3×10^{11} p.p.b., the stability margins in HE-LHC must be investigated and mitigation techniques proposed.

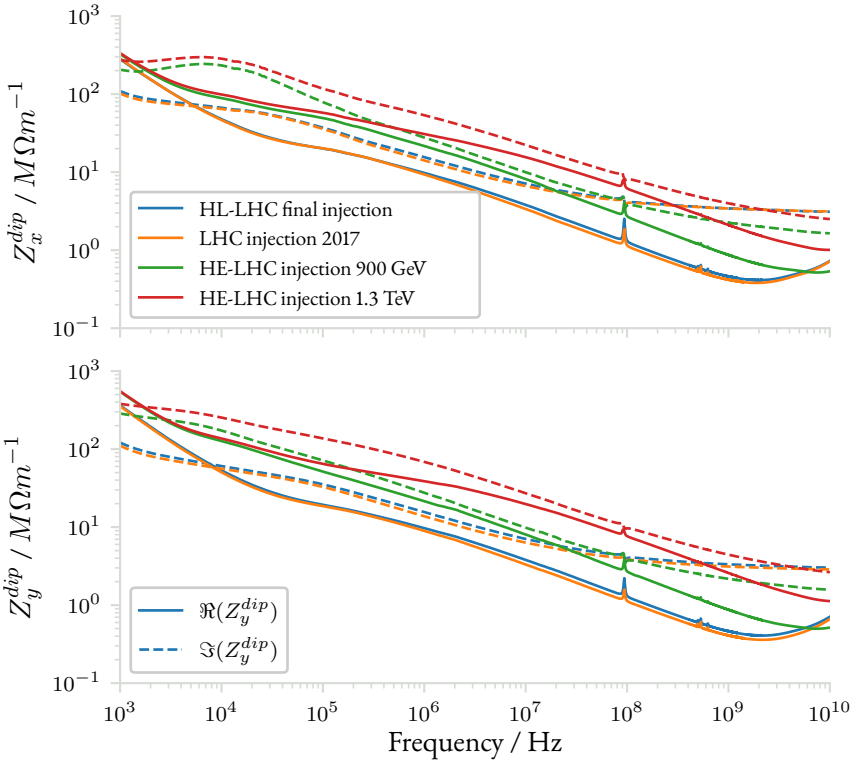

Figure 4.10: Horizontal (top plot) and vertical (bottom plot) transverse dipolar impedance as a function of frequency for the the HE-LHC injection energy options. The models are compared to the 2017 LHC and the HL-LHC models. Solid lines represent the real part and dashed lines the imaginary part.

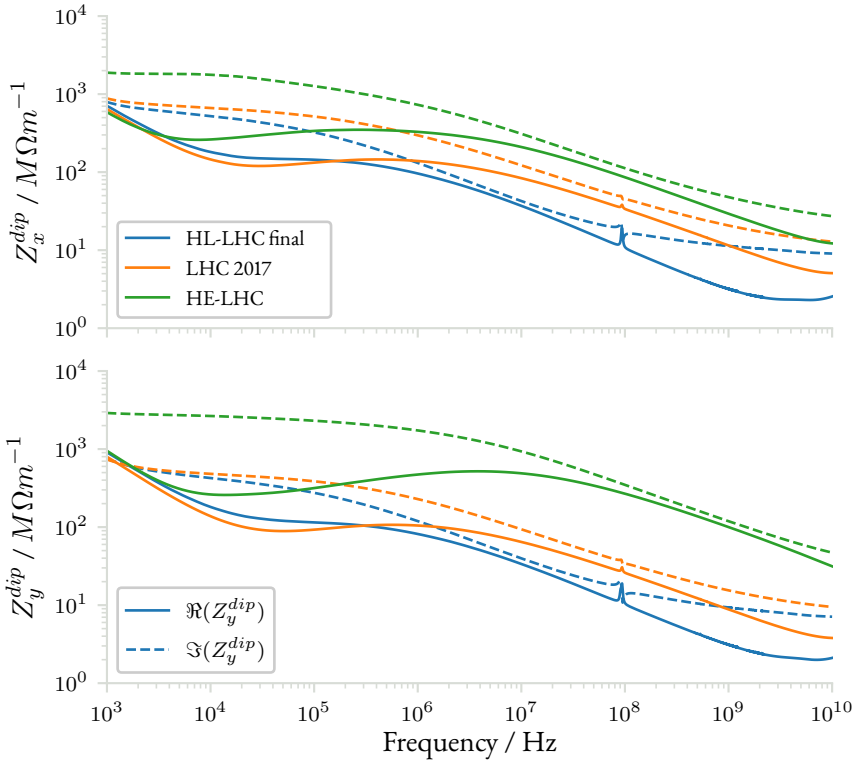

Figure 4.11: Horizontal (top plot) and vertical (bottom plot) transverse dipolar impedance as a function of frequency for the HE-LHC top energy. The model is compared to the 2017 LHC and the HL-LHC models. Solid lines represent the real part and dashed lines the imaginary part.

4.3.2 Mode coupling instability in the HE-LHC

The impedance models were used to estimate the stability limits at the different energies. We will highlight here the results for the mode coupling instability at $Q' = 0$. Additional results on the Landau damping requirements and multi-bunch stability can be found in [6, 12, 15, 153].

The horizontal instability growth rate as a function of intensity for the different considered energies are presented in Fig. 4.12. The TMCI intensity threshold is found when the growth rate becomes non-zero. At the injection energies of 450 GeV and 1.3 TeV, the thresholds are found at 8×10^{11} p.p.b. and 6.4×10^{11} p.p.b. Compared to the nominal bunch intensity of 2.3×10^{11} p.p.b., the two injection energy scenarios have therefore large stability margins.

The top energy is the most constraining case from the beam stability point of view. The TMCI threshold is found at 2×10^{11} p.p.b. in the vertical plane, a value below the nominal bunch intensity. Using the transverse damper mitigates the mode coupling instability but as we saw in part 2.5.1, a slow instability then appears below the threshold. Chromaticity and Landau damping from octupole magnets can be used to stabilize the beam and mitigate these single bunch instabilities.

However the beam stabilization with Landau octupoles become more challenging as the beam energy increases [140]. The effective frequency spread provided by the octupoles scales as $1/\gamma^2$. An HL-LHC type octupole would therefore be $\sim$4 times less efficient with an HE-LHC beam. Novel instability mitigation techniques are therefore being considered. For example an electron lens would create a frequency spread from the electromagnetic interaction of the proton beam with a high brightness low energy electron beam [132, 133, 134]. An RF quadrupole is an other option to increase Landau damping [110, 130]. While the octupole magnets create a frequency spread dependent on the transverse actions of the beam J_x and J_y, an RF quadrupole generates a spread dependent on the longitudinal action J_z. For higher energies the transverse actions are much smaller than the longitudinal one: for example in HL-LHC there is a factor $\sim 10^4$ between the two [129].

We saw with the High-Energy LHC study that beam coupling impedance poses a challenge for beam stability in future high energy machines. New and robust mitigation techniques will be needed to maintain stability margins and allow for optimal machine operation.

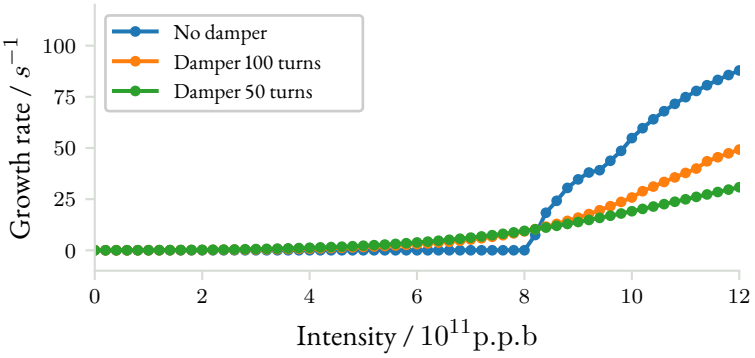

(a) 450 GeV injection energy.

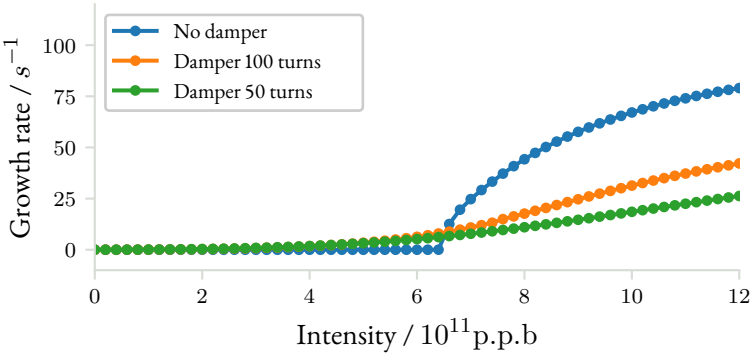

(b) 1.3 TeV injection energy.

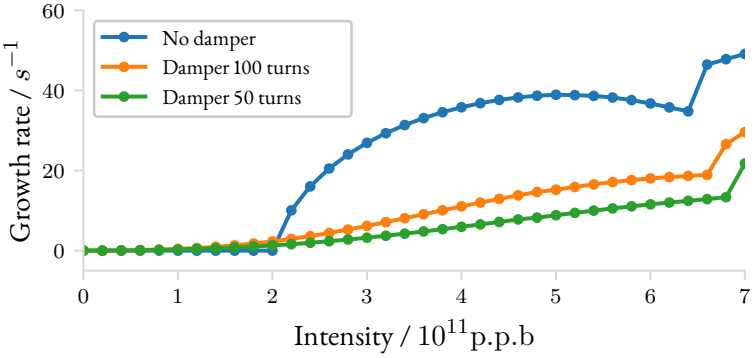

(c) 13.5 TeV top energy.

Figure 4.12: Instability growth rate in the vertical plane as a function of bunch intensity. The top plot is for the 450 GeV injection option, the central plot for the 1.3 TeV injection option and the bottom plot for the 13.5 TeV top energy. Three different transverse damper settings are represented: damper deactivated and damping times of 100 and 50 turns. The mode coupling instability appears for the cases without the transverse damper, at 8×10^{11} p.p.b. and 6.4×10^{11} p.p.b. for the two injection energies considered. At top energy it appears at 2×10^{11} p.p.b., an intensity smaller than the nominal bunch intensity.

5 Conclusion

This work presented advancements on the understanding of transverse impedance induced instabilities in the Large Hadron Collider. In particular the Transverse Mode Coupling Instability was investigated for the current and future large colliders at CERN.

We first validated the simulation codes for the study of coherent beam instability in the LHC and highlighted their limitations. This study was performed for two types of instabilities, the head-tail and the mode coupling ones. The effect of the transverse damper was also included in the simulations. Different impedance models were used, and in particular the LHC impedance model. The results showed good agreement between the PyHEADTAIL tracking simulations and the Vlasov solver DELPHI.

The mode coupling instability was then investigated for the LHC with simulations and measurements. Simulations for different machine configurations highlighted the predominant role of the collimators on the machine impedance and the mode coupling instability. The TMCI intensity threshold was predicted to be found at 3×10^{11} protons per bunch, more than two times the single bunch intensity used during Run II (2015-2018). Measurements of the tune shift as a function of intensity were performed at the LHC top energy. Different collimator configurations were tested to modify the machine impedance. From these measurements the impedance induced tune shift was found to be higher than predicted from simulations by 20 % to 60 % depending on the beam and plane. Despite the larger tune shifts with respect to predictions, the TMCI intensity threshold was still higher than the used bunch intensities.

The impedance at top energy of some single collimators were also measured at multiple occasions during Run II. This measurement method and the subsequent data processing allowed to measure the impedance induced tune shifts to a level of a few 10^{-5}. The results for the different collimators are within a factor of two from the impedance model predictions.

Measurements at top energy in the LHC pose time and machine protection constraints. A measurement of the head-tail instability was therefore performed at the injection energy to scan a larger chromaticity range. The results obtained with this method are also within a factor of two from predictions.

We concluded from the combination of the different measurements that the LHC model underestimates the machine impedance by a factor of 1.3 to 1.5. During Run II, the LHC was operated with at least two times more Landau octupole current than predicted from impedance and instability simulations. Missing impedance sources can therefore explain a part of this factor, but other destabilizing mechanisms need also to be investigated.

For the High-Luminosity LHC project, the impedance will be a critical aspect. The beams will be two times more intense than the design value. To cope with this brightness increase and maintain margins for coherent beam stability, an impedance reduction of the collimators is planned. We saw with simulations that in the final stage of the HL-LHC upgrade the mode coupling instability threshold is at 8.4×10^{11} protons per bunch, a value four times higher than the projected single bunch intensity. Intermediate scenarios corresponding to the staged implementation of the upgrade and to different

collimator jaws materials were also simulated. They all showed an increase of the TMCI threshold, but still smaller than the one obtained with the full upgrade.

The beneficial effect of the collimators impedance reduction was also demonstrated with measurements in the LHC. A tune shift measurement with a set of opened collimators was performed. The machine impedance was reduced to a level similar to the one that will be reached during Run III (2021-2013). We saw that the tune shift versus intensity could be reduced with this configuration.

Moreover the impedance of a single collimator prototype was also measured with beam in the LHC. This prototype was installed to confirm the choice of new low resistivity metallic materials for the collimation upgrade. The beneficial effects of these low resistivity materials compared to the current carbon based collimators has been shown.

Finally, impedance and mode coupling instability simulations were performed for the High-Energy LHC, a proposed future collider. We saw that because of the machine protection constraints, the impedance can increase by a factor up to ten over a large frequency range compared to current colliders. This results from the tight collimator gaps required to protect the machine. In consequence coherent stability margins will be much lower than in the LHC and HL-LHC. Novel beam stabilization techniques should therefore be investigated.

A Impedance of two collimators with different orientations

A.1 Introduction

The LHC makes use of many collimators to protect the cold magnets from particle losses. Because of their tight gaps, they contribute to a sizeable portion of the beam coupling impedance at top energy. These collimators also have different orientations, gaps and Twiss beta functions.

Because of these differences in optics and gaps, the quadrupolar impedance might increase or decrease the tune shifts, assuming that those can be derived from the sum of the dipolar and quadrupolar components of the impedance.

We will derive expressions for the impedance of a combination of two flat structures, the first one horizontal and the second one vertical. This structure approximate the case of two LHC collimators. We will rely on simple geometric considerations and on Yokoya factors [151] for flat structures to derive these simple expressions.

A.2 Simple derivation of the total impedance of the structure

Let S be a source particle of coordinates (x_S, y_S) and T a test particle with coordinates x_T, y_T as was pictured in Fig. 2.1. For a flat, multilayered, axisymmetric structure, the wall impedance can be written

$$Z_x = Z_x^{dip} x_S + Z_x^{quad} x_T \tag{A.1}$$

$$Z_y = Z_y^{dip} y_S + Z_y^{quad} y_T \tag{A.2}$$

We now assume that we dispose of two identical flat structures, the first with horizontal plates and the second with vertical plates. They will be referred as 1 and 2 throughout the paper.

The second structure impedance components are then

$$Z_{x,2}^{dip} = Z_{y,1}^{dip}\,, \tag{A.3}$$

$$Z_{x,2}^{quad} = Z_{y,1}^{quad}\,, \tag{A.4}$$

$$Z_{y,2}^{dip} = Z_{x,1}^{dip}\,, \tag{A.5}$$

$$Z_{y,2}^{quad} = Z_{x,1}^{quad}\,. \tag{A.6}$$

$$\tag{A.7}$$

Moreover the structure being flat, we have the following relations between dipolar and quadrupolar impedances [103, 151]

$$Z_{x,1}^{dip} = -Z_{x,1}^{quad}\,, \tag{A.8}$$
$$Z_{y,1}^{dip} = 2Z_{y,1}^{quad}\,, \tag{A.9}$$
$$Z_{x,1}^{dip} = Z_{y,1}^{quad}\,, \tag{A.10}$$
$$\tag{A.11}$$

We can now sum the impedances of structures 1 and 2

$$Z_{x,tot}^{dip} = \left(\frac{\beta_{x,1}}{\langle\beta_x\rangle}\right) Z_{x,1}^{dip} + \left(\frac{\beta_{x,2}}{\langle\beta_x\rangle}\right) Z_{x,2}^{dip}\,, \tag{A.12}$$
$$Z_{x,tot}^{quad} = \left(\frac{\beta_{x,1}}{\langle\beta_x\rangle}\right) Z_{x,1}^{quad} + \left(\frac{\beta_{x,2}}{\langle\beta_x\rangle}\right) Z_{x,2}^{quad}\,, \tag{A.13}$$
$$Z_{y,tot}^{dip} = \left(\frac{\beta_{y,1}}{\langle\beta_y\rangle}\right) Z_{y,1}^{dip} + \left(\frac{\beta_{y,2}}{\langle\beta_y\rangle}\right) Z_{y,2}^{dip}\,, \tag{A.14}$$
$$Z_{y,tot}^{quad} = \left(\frac{\beta_{y,1}}{\langle\beta_y\rangle}\right) Z_{y,1}^{quad} + \left(\frac{\beta_{y,2}}{\langle\beta_y\rangle}\right) Z_{y,2}^{quad}\,. \tag{A.15}$$

Using the previous relations, the impedances can all be expressed as a function of structure 1 dipolar impedance component

$$Z_{x,tot}^{dip} = \left(\frac{\beta_{x,1}}{\langle\beta_x\rangle}\right) Z_{x,1}^{dip} + \left(\frac{\beta_{x,2}}{\langle\beta_x\rangle}\right) Z_{y,1}^{dip}\,, \tag{A.16}$$
$$Z_{x,tot}^{quad} = -\left(\frac{\beta_{x,1}}{\langle\beta_x\rangle}\right) Z_{x,1}^{dip} + \frac{1}{2}\left(\frac{\beta_{x,2}}{\langle\beta_x\rangle}\right) Z_{y,1}^{dip}\,, \tag{A.17}$$
$$Z_{y,tot}^{dip} = \left(\frac{\beta_{y,1}}{\langle\beta_y\rangle}\right) Z_{y,1}^{dip} + \left(\frac{\beta_{y,2}}{\langle\beta_y\rangle}\right) Z_{x,1}^{dip}\,, \tag{A.18}$$
$$Z_{y,tot}^{quad} = \frac{1}{2}\left(\frac{\beta_{y,1}}{\langle\beta_y\rangle}\right) Z_{y,1}^{dip} - \left(\frac{\beta_{y,2}}{\langle\beta_y\rangle}\right) Z_{x,1}^{dip}\,. \tag{A.19}$$

Moreover we have $Z_{x,1}^{dip} = Z_{y,1}^{quad}$ and $Z_{y,1}^{dip} = 2Z_{y,1}^{quad}$, $Z_{y,1}^{dip} = 2Z_{x,1}^{dip}$ and the previous equations become

$$Z_{x,tot}^{dip} = \frac{1}{\langle\beta_x\rangle}(\beta_{x,1} + 2\beta_{x,2}) Z_{x,1}^{dip}\,, \tag{A.20}$$
$$Z_{x,tot}^{quad} = \frac{1}{\langle\beta_x\rangle}(-\beta_{x,1} + \beta_{x,2}) Z_{x,1}^{dip}\,, \tag{A.21}$$
$$Z_{y,tot}^{dip} = \frac{1}{\langle\beta_x\rangle}(2\beta_{y,1} + \beta_{y,2}) Z_{x,1}^{dip}\,, \tag{A.22}$$
$$Z_{y,tot}^{quad} = \frac{1}{\langle\beta_x\rangle}(\beta_{y,1} - \beta_{y,2}) Z_{x,1}^{dip}\,. \tag{A.23}$$

The total impedance for horizontal and vertical planes is thus

$$Z_{x,tot}^{dip+quad} = \frac{1}{\langle \beta_x \rangle}(3\beta_{x,2}) Z_{x,1}^{dip} \,, \tag{A.24}$$

$$Z_{y,tot}^{dip+quad} = \frac{1}{\langle \beta_x \rangle}(3\beta_{y,1}) Z_{x,1}^{dip} \,. \tag{A.25}$$

$$\tag{A.26}$$

A.3 Impedance of the single vertical collimator

A collimator is called vertical when its two jaws have a horizontal orientation because in this case, the cleaning is made in the vertical plane. In the following examples, it will be referred as collimator 1. In the LHC, the TCSG.D4L7.B1 is a vertical collimator so we can use its impedance as a base for our examples. The four components Z_x^{dip}, Z_x^{quad}, Z_y^{dip} and Z_y^{quad} are showed in Fig. A.1.

Figure A.1 shows that the horizontal dipolar and quadrupolar impedance are opposite signs whereas the vertical quadrupolar impedance is half the dipolar impedance. In this case the horizontal tune shift, proportional to $Z_x^{dip} + Z_x^{quad}$ would be zero.

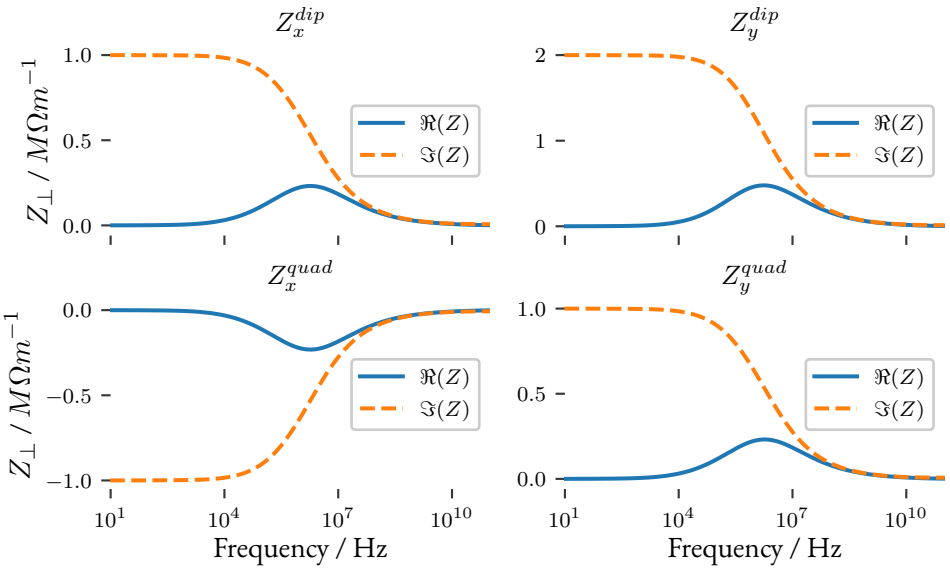

Figure A.1: Collimator impedance before weighting by β functions.

A.4 Case of two collimators with identical Twiss beta functions

We now take the case of a combination of the two identical collimators described in part A.2. We will assume that the average horizontal and vertical betatron function $\langle\beta_x\rangle$ and $\langle\beta_y\rangle$ are equal to 1 in all the following examples. In this first example we put the β functions equal to 1 for both planes and in both collimators. The quadrupolar impedance is now zero for both planes and the dipolar impedances are three times the single vertical collimator of Sec. A.3.

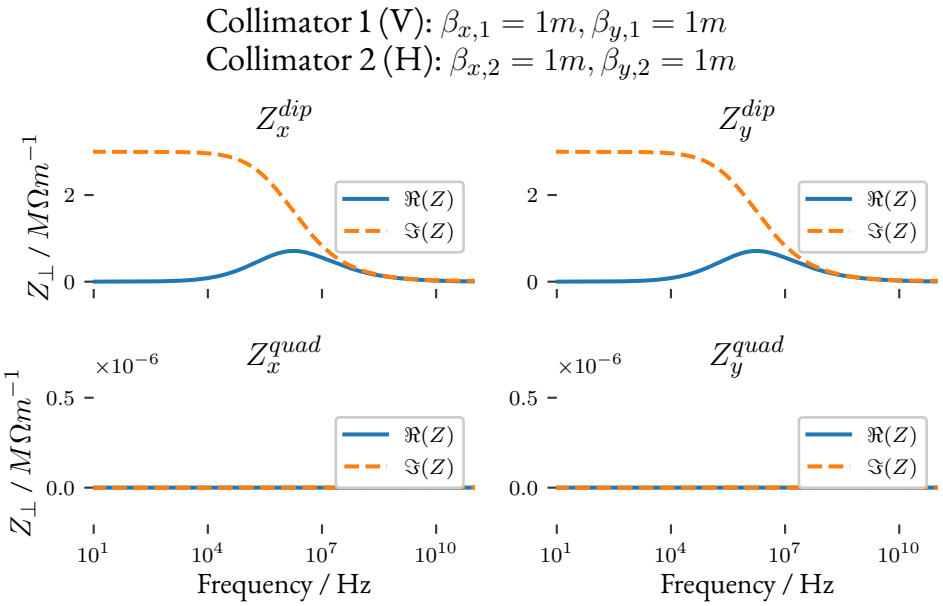

Figure A.2: Example of two collimators with identical β functions.

A.5 Case of two collimators with different Twiss beta functions

We now take the case of different β functions in both collimators. Figures A.3 and A.4 show two different cases. In the first case, the horizontal quadrupolar impedance has an opposite sign to the dipolar impedance. In consequence the tune shift induced by the dipolar impedance will be reduced if we take the quadrupolar impedance into account. This is can also be seen in the vertical impedance.

Changing the β functions of the second collimator can lead to a very different situation. Figure A.4 doesn't exhibit this compensation of the dipolar impedance by the quadrupolar component. The quadrupolar impedance would even worsen the tune shifts in the horizontal plane.

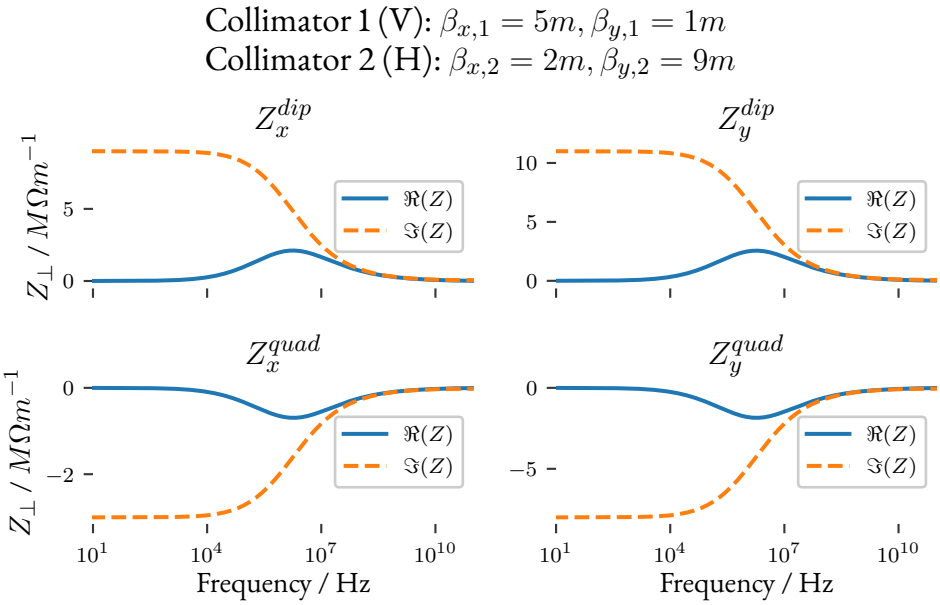

Figure A.3: Example of two collimators with different β functions. This case mimics an association of two LHC collimators, the TCSG.D4L7 and the TCSG.B4L7, which are respectively vertical and horizontal collimators.

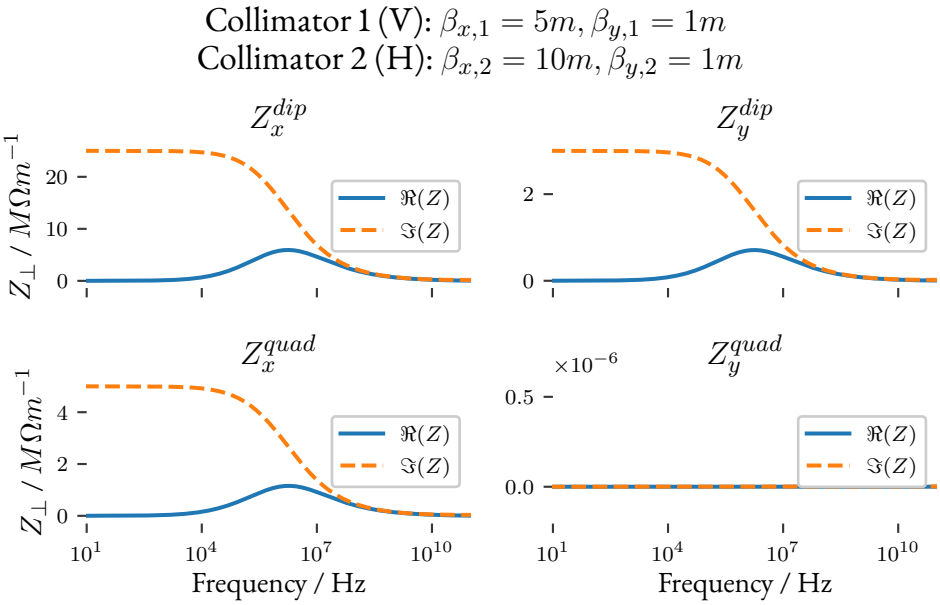

Figure A.4: Example of two collimators with different β functions.

A.6 Conclusion

We saw that the impedance of a pair of flat structures with different orientations can lead to tune shifts compensation or adjonction depending on the optics functions used in each structure. For the LHC and its numerous collimators, this means that the quadrupolar part of the impedance might partially compensate the effects of the dipolar impedance on the tune shifts. This depends of course as well on the collimators gaps used.

B Beam parameters for instability simulations

B.1 Parameters for simulations with an inductive impedance model

Table B.1: Machine and beam parameters for DELPHI simulations with an inductive impedance model.

Parameter	Value
Impedance	
Impedance model	$Z_x^{dip}(\omega) = j25\,\mathrm{M\Omega\,m^{-1}}$
Machine	
Circumference / m	26 658.8832
Transverse tunes $Q_{x,y}$	62.31/60.32
Momentum compaction factor α_c	3.48×10^{-4}
RF voltage / MV	12
Harmonic number	35 640
Synchrotron tune Q_s	1.909×10^{-3}
Beam	
Number of bunches	1
4 σ bunch length / ns	1.0
Bunch intensity / p.p.b.	10^5
Chromaticity Q'	0 and –10
Chromatic shift for $Q' = -10$	
$\xi = \frac{Q'}{Q_{x0}}$	$-10/62.31 = -0.16$
$\eta = \alpha_p - \frac{1}{\gamma^2}$	$3.48 \times 10^{-4} - 1/6927^2 = 3.48 \times 10^{-4}$
$f_\xi = \frac{1}{2\pi}\xi\frac{\omega_\beta}{\eta} = \frac{\omega_0}{2\pi}\frac{\xi Q_{x0}}{\eta}$	$-350\,\mathrm{MHz}$

B.2 Parameters for TMCI simulations with the LHC impedance model

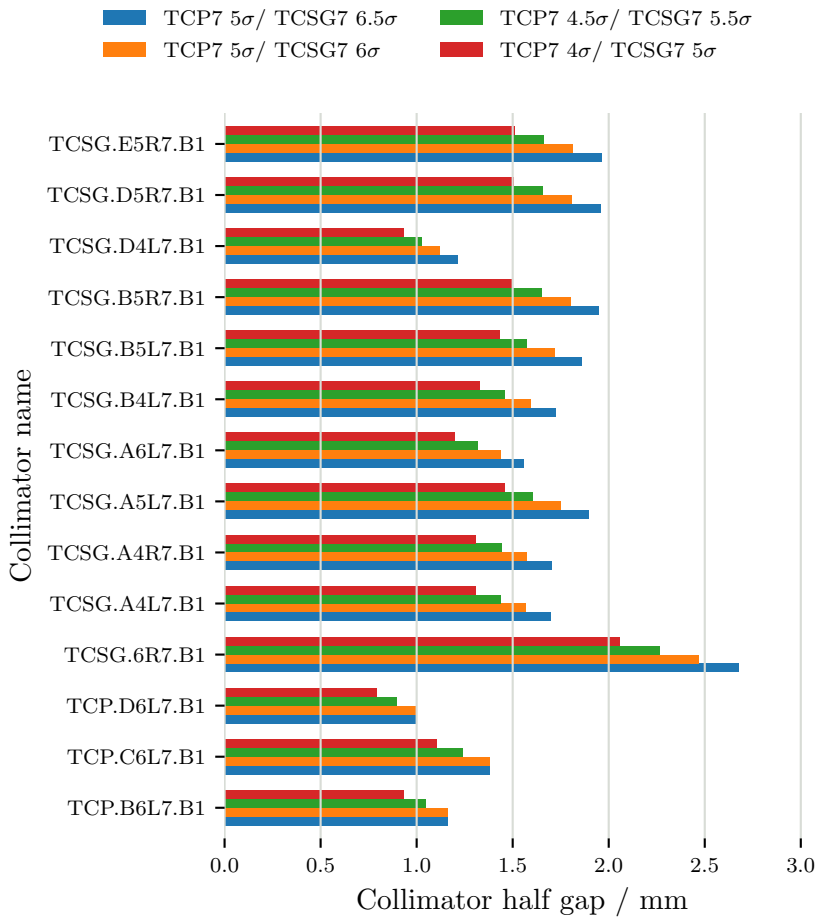

Figure B.1: Physical gaps of the LHC IR7 collimators in mm for the different scenarios investigated. The nominal LHC configuration in 2017 is displayed in blue, whereas the other colors show tighter collimators settings. Only the primary and secondary collimators of IR7 settings were modified and are thus showed in the figure. In the tightest setting presented here the collimator gaps are reduced by ≈25 %.

B.3 Comparison of collimator gaps for the TMCI measurement

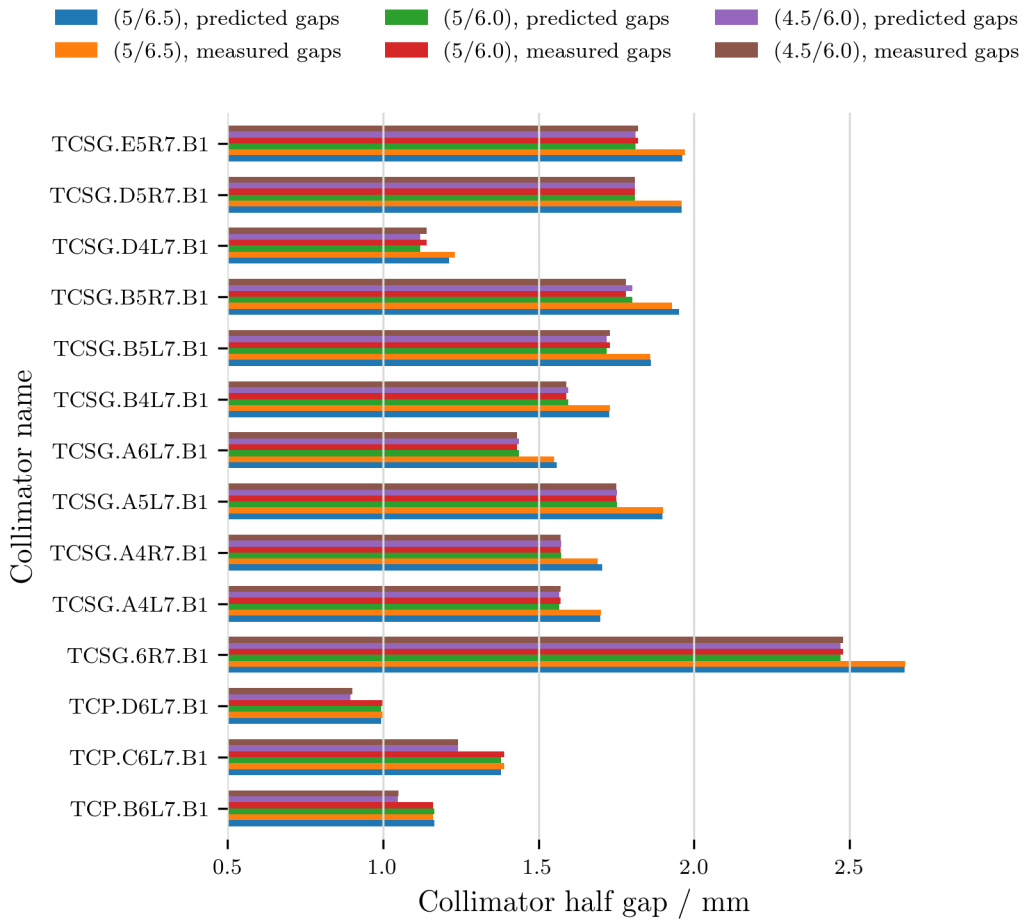

Figure B.2: Physical gaps of the LHC IR7 collimators in mm for the configurations given in Tab. 3.2. The collimator gaps measured in the machine are compared to the one resulting from a scaling with $n_{\sigma,coll}$ of the gaps and which were used for instability predictions described in the previous part. The difference between the gaps measured in the machine and the predicted ones are of the order of 1 %.

B.4 Collimator gaps and beam parameters for the HL-LHC TMCI simulations

Table B.2: Gaps in σ_{coll} for the primary and secondary collimators in LHC and HL-LHC

Collimator family	LHC[1]	HL-LHC [1]
Primary	5	6.7
Secondary	6.5	9.1

[1] The normalised emittance used to compute the collimators gaps are different between LHC and HL-LHC. In LHC $\varepsilon_n^{LHC} = 3.5\,\mu\text{m}$ whereas in HL-LHC $\varepsilon_n^{HL-LHC} = 2.5\,\mu\text{m}$. If the Twiss beta function is kept constant for the considered collimator, then $\sigma_{coll}^{LHC}/\sigma_{coll}^{HL-LHC} = \sqrt{\frac{\varepsilon_n^{LHC}\gamma^{LHC}}{\varepsilon_n^{HL-LHC}\gamma^{LHC}}} = 1.22$. This beam size reduction leads to a larger collimator setting to maintain similar physical gaps.

Table B.3: LHC and HL-LHC machine and beam parameters for TMCI simulations with DELPHI.

Parameter	LHC	HL-LHC
Machine		
Circumference / m	26 658.8832	
Transverse tunes $Q_{x,y}$	62.31/60.32	
Momentum compaction factor α_c	3.225×10^{-4}	3.455×10^{-4}
RF voltage / MV	12	16
Harmonic number	35 640	
Synchrotron tune Q_s	1.838×10^{-3}	2.04×10^{-3}
Beam		
Number of bunches	1	
$4\,\sigma$ bunch length / ns	1.08	
Bunch intensity / 1×10^{11} p.p.b.	0 to 10	
Chromaticity Q'	0 to 5	

B.5 Collimator gaps and beam parameters for the HE-LHC impedance model and stability simulations at injection energy

Table B.4: Gaps in σ_{coll} for the primary and secondary collimators at injection energy in LHC, HL-LHC and HE-LHC

Collimator family	LHC[1]	HL-LHC [1]	HE-LHC 450 GeV[1]	HE-LHC 1.3 TeV[1]
Primary	5.7	6.7	5.7	9.7
Secondary	6.7	7.9	6.7	11.4

[1] The normalised emittance used to compute the collimators gaps are different between LHC and HL-LHC/HE-LHC. In LHC $\varepsilon_n^{LHC} = 3.5\,\mu\text{m}$ whereas in both HL-LHC and HL-LHC $\varepsilon_n = 2.5\,\mu\text{m}$.

Table B.5: LHC, HL-LHC and HE-LHC machine and beam parameters at injection energy.

Parameter	LHC	HL-LHC	HE-LHC 450 GeV	HE-LHC 1.3 TeV
Machine				
Circumference / m	26 658.8832			
Transverse tunes $Q_{x,y}$	62.31/60.32			
Momentum compaction factor α_c / 10^{-4}	3.225	3.455	3.5	
RF voltage / MV	6	8	10	10
Harmonic number	35 640			
Synchrotron tune Q_s / 10^{-3}	1.838	2.04	6.333	3.748
Beam				
Number of bunches	-	-	1	
4 σ bunch length / ns	1.2	1.08	1.2	
Bunch intensity in 10^{11} p.p.b.	-	-	0 to 12	
Chromaticity Q'	-	-	0	

B.6 Collimator gaps and beam parameters for the HE-LHC impedance model and stability simulations at injection energy

Table B.6: Gaps in σ_{coll} for the primary and secondary collimators in HL-LHC and HE-LHC

Collimator family	LHC[1]	HL-LHC[1]	HE-LHC[1]
Primary	5	6.7	6.7
Secondary	6.5	9.1	9.1

[1] The normalised emittance used to compute the collimators gaps are different between LHC and HL-LHC/HE-LHC. In LHC $\varepsilon_n^{LHC} = 3.5\,\mu\text{m}$ whereas in both HL-LHC and HL-LHC $\varepsilon_n = 2.5\,\mu\text{m}$.

Table B.7: LHC, HL-LHC and HE-LHC machine and beam parameters at top energy.

Parameter	LHC	HL-LHC	HE-LHC
Machine			
Impedance model[1]	LHC 2017	HL-LHC v1.3	HE-LHC
Circumference / m		26 658.8832	
Transverse tunes $Q_{x,y}$		62.31/60.32	
Momentum compaction factor α_c	3.225×10^{-4}	3.455×10^{-4}	3.5×10^{-4}
RF voltage / MV	12	16	16
Harmonic number		35 640	
Synchrotron tune Q_s	1.838×10^{-3}	2.04×10^{-3}	1.472×10^{-3}
Beam			
Number of bunches	-	-	1
$4\,\sigma$ bunch length / ns		1.08	1.2
Bunch intensity / 1×10^{11} p.p.b.	-	-	0 to 7
Chromaticity Q'	-	-	0

[1] Impedance models are available at [143].

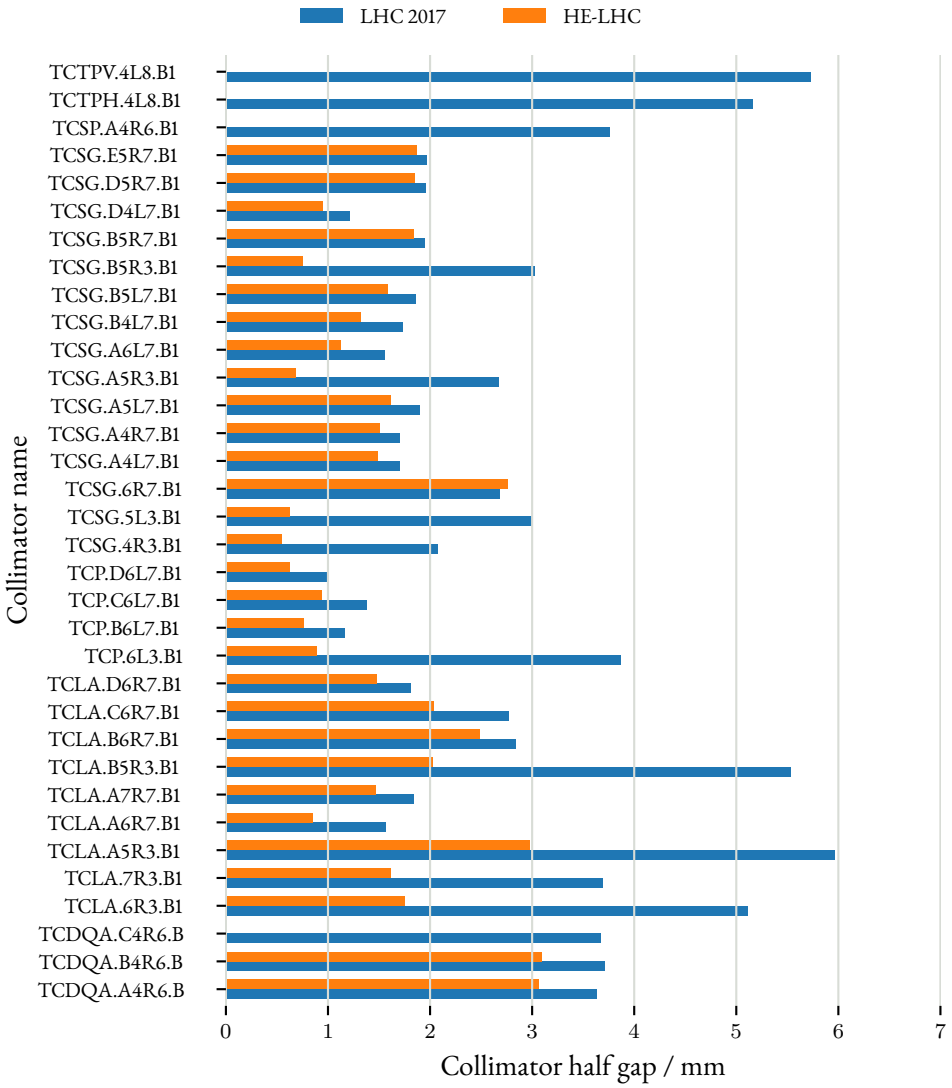

Figure B.3: Comparison of the physical gaps of the LHC and HE-LHC collimators at top energy. Because of the higher beam energy and therefore smaller beam size, the gaps for HE-LHC are much tighter.

C Results of collimators measurements

C.1 Results of TCP measurements

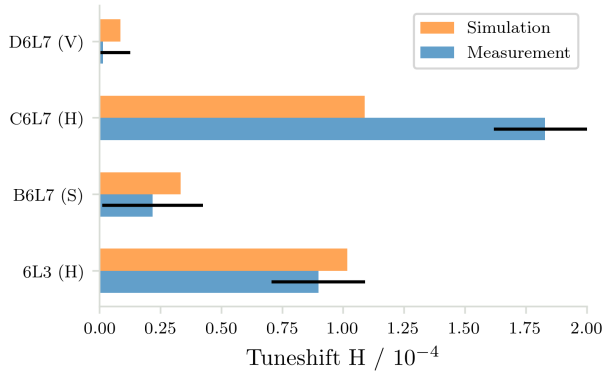

(a) Beam 1 horizontal

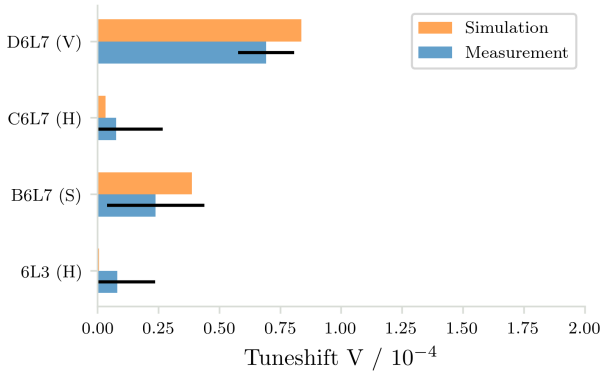

(b) Beam 1 vertical

Figure C.1: Measurements results of the beam 1 TCP collimators induced tune-shifts.

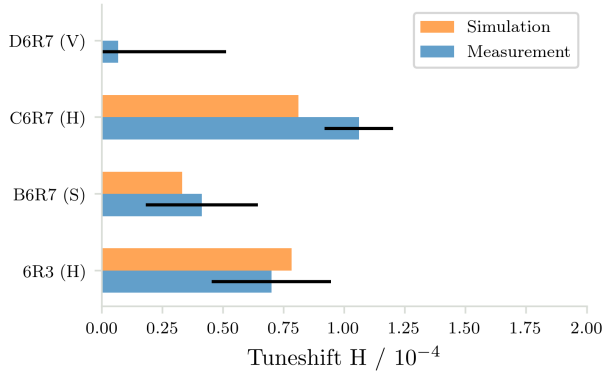

(a) Beam 2 horizontal

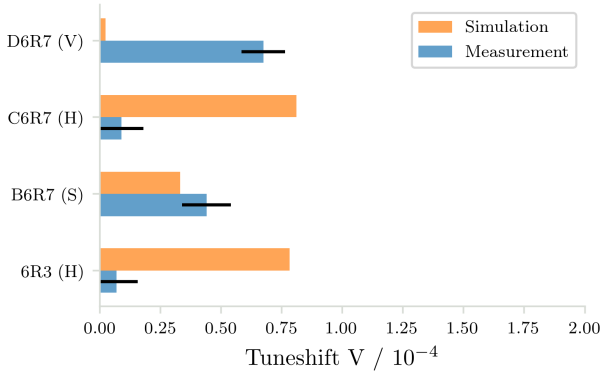

(b) Beam 2 vertical.

Figure C.2: Measurements results of the beam 2 TCP collimators induced tune-shifts.

C.2 Results of TCSG measurements

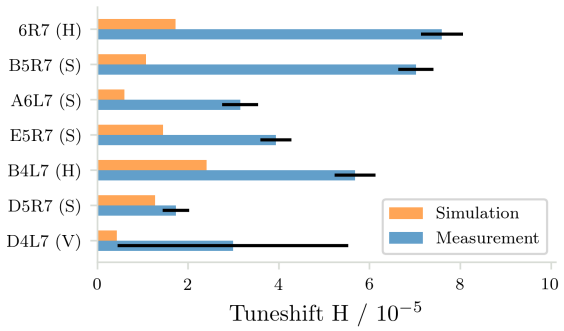

(a) Beam 1 horizontal, bunch 0

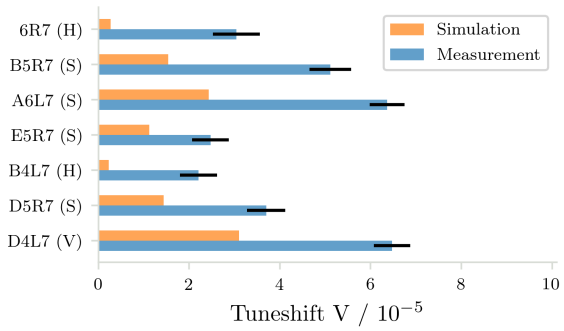

(b) Beam 1 vertical, bunch 0

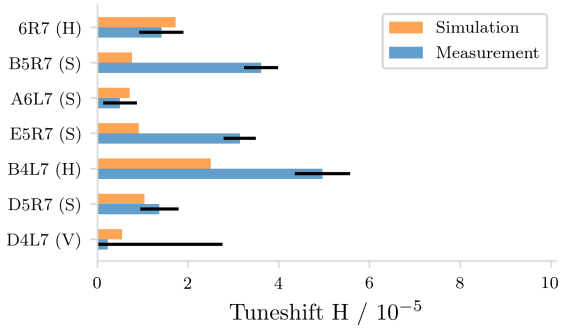

(c) Beam 1 horizontal, bunch 72

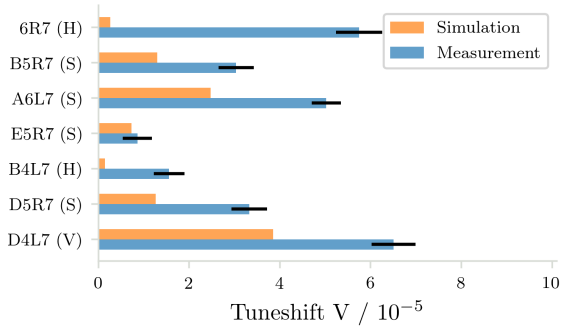

(d) Beam 1 vertical, bunch 72

Figure C.3: Measurements results of the beam 1 TCSG collimators induced tune-shifts.

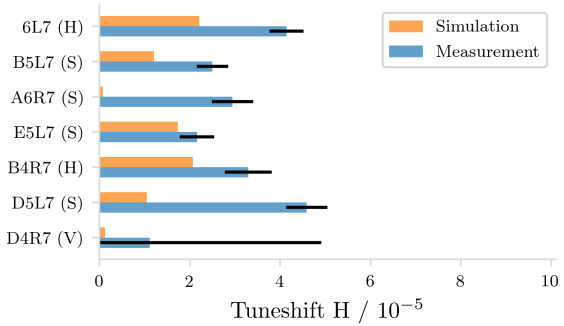

(a) Beam 2 horizontal, bunch 7

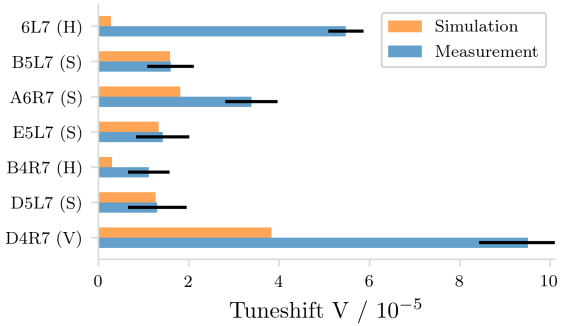

(b) Beam 2 vertical, bunch 7

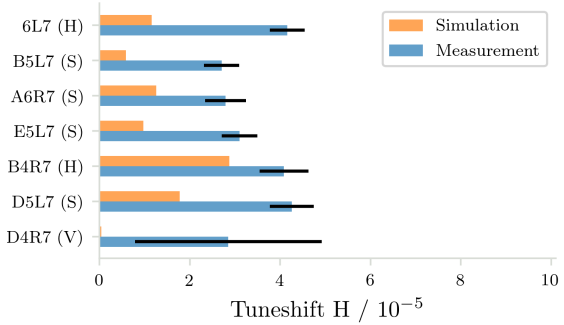

(c) Beam 2 horizontal, bunch 79

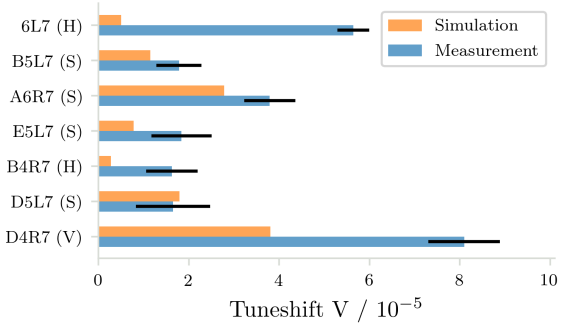

(d) Beam 2 vertical, bunch 72

Figure C.4: Measurements results of the beam 2 TCSG collimators induced tune-shifts.

D Effect of beam distribution slicing in PyHEADTAIL simulations

D.1 Introduction

Stability simulation presented in part 2.5.2 for the LHC impedance and wake model showed a discrepancy at high bunch intensity between the codes DELPHI and PyHEADTAIL. The convergence of the simulations was therefore checked with the two approaches.

D.2 Slicing in the PyHEADTAIL code

As explained in part 2.3.1, in PyHEADTAIL the bunch is divided in several thousand of macroparticles. When applying the effect of wakefields, the macroparticles are grouped in longitudinal slices. All macroparticles within a slice receive the same kick from the wakefield.

The default slicer used for stability simulations with PyHEADTAIL is the UniformBinSlicer. With this function all slices have the same length and the number of macroparticles per slice varies according to the bunch charge distribution. Figure D.3 shows the slicing of a bunch made of 1×10^6 macroparticles using 21 slices. The bunch has a Gaussian longitudinal distribution as can be seen in the upper plot with the number of macroparticles per slice. The slices at the edges of the longitudinal space have a low number of macroparticles. This is confirmed by the bottom plot of Fig. D.3: the slices with index 0 to 3 and 18 to 20 have no macroparticle.

This absence of macroparticles and the charge difference between slices can introduce numerical noise in the simulations. Because of the Gaussian shape of the longitudinal distribution, increasing the number of slices has little effect on the number of macroparticle in the edge slices.

The PyHEADTAIL code also includes a UniformChargeSicer module. In this case each slice will have a different length but they will all contain the same number of macroparticles. Figure D.2 shows the slicing of the same bunch with this slicer. The top plot shows that indeed all slices have the same number of macroparticles. However slices at the center of the distribution are much shorter that those located at the edges of the distribution to ensure the uniform density.

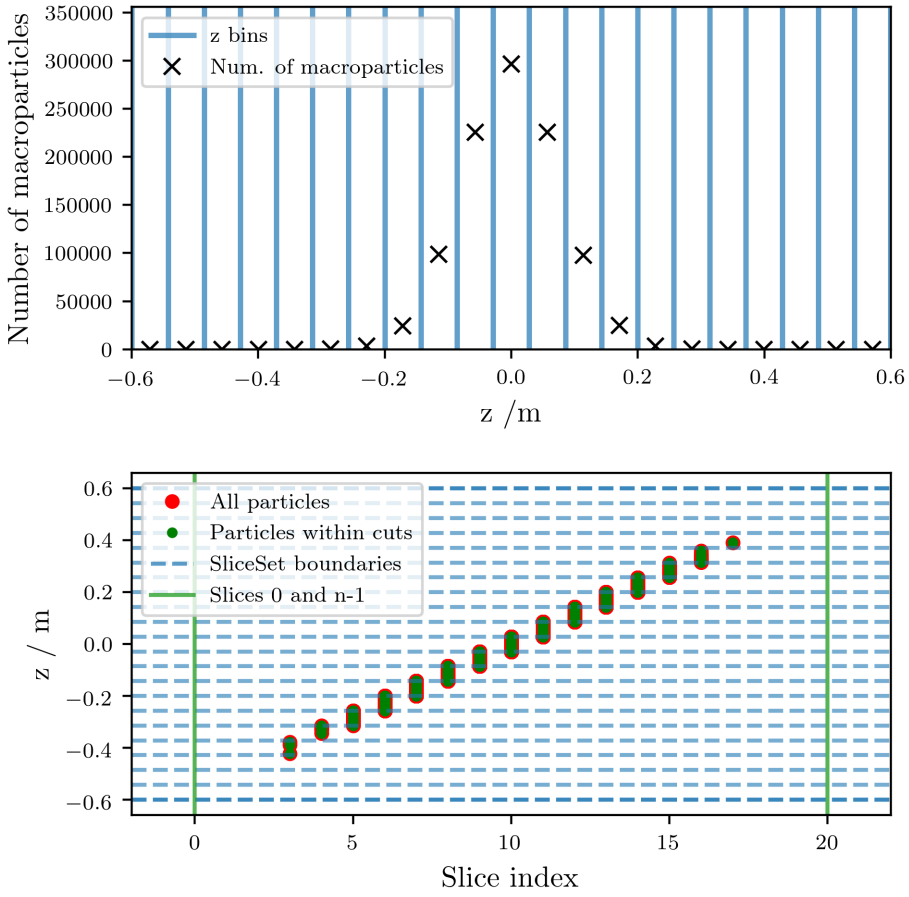

Figure D.1: Particle distribution with the `UniformBinSlicer` in PyHEADTAIL. Top plot shows the number of macroparticles in each slice, as well as the longitudinal limits of the slices. Bottom plot shows the longitudinal position of each macroparticle as a function of the slice index.

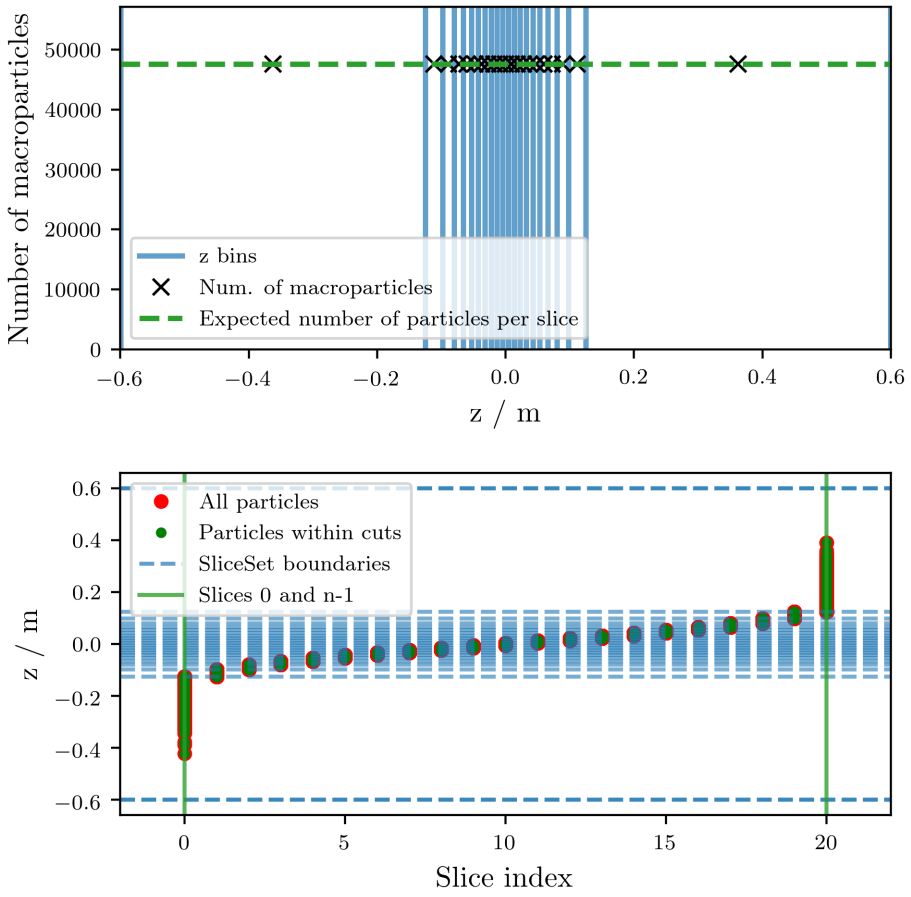

Figure D.2: Particle distribution with the `UniformChargeSlicer` in PyHEADTAIL. Top plot shows the number of macroparticles in each slice, as well as the longitudinal limits of the slices. Bottom plot shows the longitudinal position of each macroparticle as a function of the slice index.

D.3 Effect of slicing on the LHC stability simulations

To try understand the discrepancy found between DELPHI and PyHEADTAIL simulations showed in part 2.5.2, a convergence study was made first using the UniformBinSlicer in PyHEADTAIL. The number of bins used for the longitudinal slicing was scanned from 100 to 2000 with few steps. Figure ?? shows the results for this first scan: the most unstable mode growth rate is plotted as a function of bunch intensity. The curves correspond to the different number of slices used.

The results of the convergence study with the UniformBinSlicer don't show any improvement compared to the 1000 bin case.

The UniformChargeSlicer was then used in PyHEADTAIL. Figures D.4 to D.7 show the resulting mode frequency shifts and most unstable mode growth-rate for 1000 to 2000 bins. The results are compared to DELPHI simulation results.

When the number of slices is increased, the results start to converge towards DELPHI simulation results. Using more than 1600 bins with this slicer type appears to ensure the results convergence.

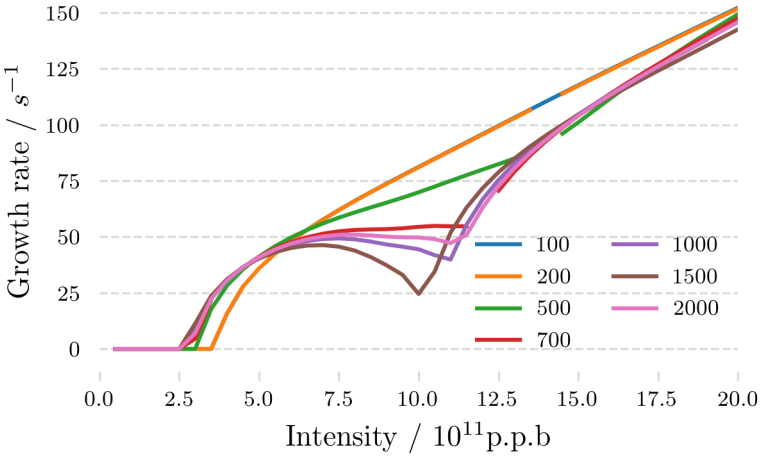

Figure D.3: Most unstable mode growth-rate versus bunch intensity versus intensity for the LHC impedance model. The `UniformBinSlicer` is used, changing the number of bins. No improvement to the convergence is made even for bin numbers larger than 1000.

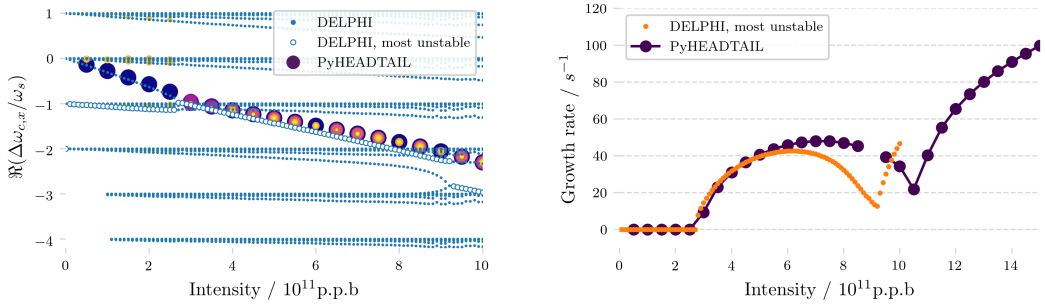

(a) Real part

(b) Impedance

Figure D.4: Real part of the mode frequency shift (left plot) and most unstable mode growth-rate (right plot) versus intensity for the LHC impedance model. The `UniformBinSlicer` is now used, with 1000 bins.

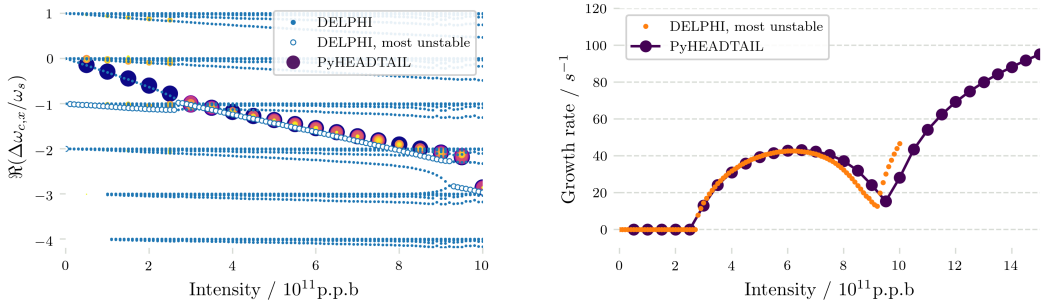

(a) Real part

(b) Impedance

Figure D.5: Real part of the mode frequency shift (left plot) and most unstable mode growth-rate (right plot) versus intensity for the LHC impedance model. The `UniformBinSlicer` is now used, with 1400 bins.

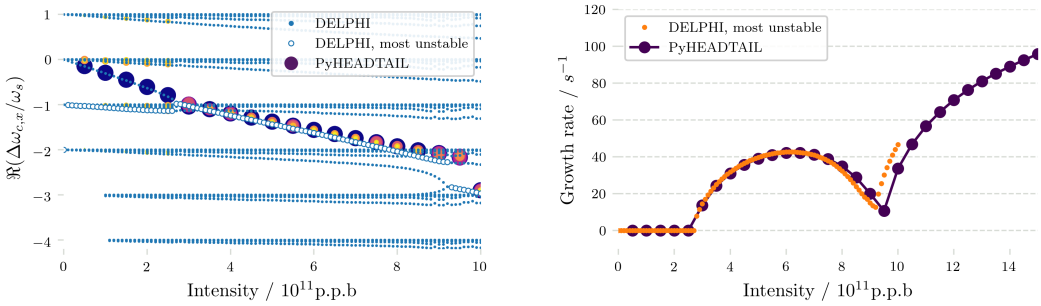

(a) Real part (b) Impedance

Figure D.6: Real part of the mode frequency shift (left plot) and most unstable mode growth-rate (right plot) versus intensity for the LHC impedance model. The `UniformBinSlicer` is now used, with 1600 bins.

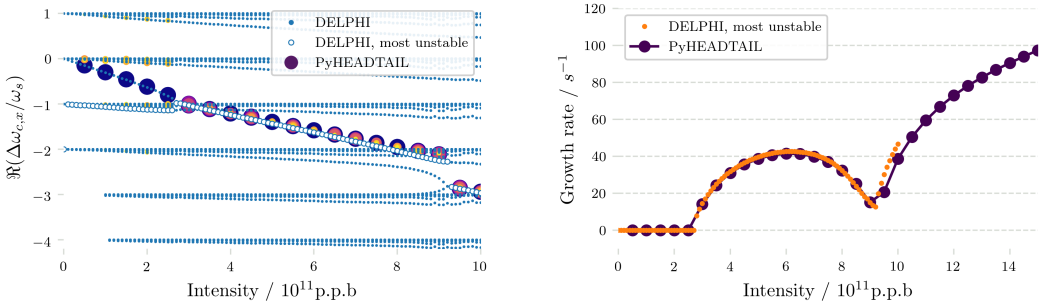

(a) Real part (b) Impedance

Figure D.7: Real part of the mode frequency shift (left plot) and most unstable mode growth-rate (right plot) versus intensity for the LHC impedance model. The `UniformBinSlicer` is now used, with 2000 bins.

D.4 Conclusion

The convergence study made with the two beam slicers available in `PyHEADTAIL` showed a great difference when applied to the LHC impedance model. With the `UniformBinSlicer`, results diverge from `DELPHI` simulations whereas the `UniformChargeSlicer` allowed to obtain converges results using at least 1600. We saw that when the number of slices with the `UniformBinSlicer` is increased, bins sampling the edges of the distribution can be empty. This could introduce numerical artefacts leading to the discrepancy found in part 2.5.2. The issue could be solved by using the `UniformChargeSlicer` in `PyHEADTAIL`. With this slicer, all bins have the same number of macroparticles. With enough slices, results were found to be close to `DELPHI` predictions.

Acronyms

ADT	LHC transverse damper
CFC	Carbon-fiber reinforced carbon
FCC	Future Circular Collider
HE-LHC	High Energy LHC
HL-LHC	High Luminosity LHC
LHC	Large Hadron Collider
MKQA	LHC tune kicker
Mo	Molybdenum
MoGr	Molybdenum-graphite
PS	Proton Synchrotron
SPS	Super Proton Synchrotron
TCP	Primary collimator
TCPPM	Primary collimator, MoGr and BPM
TCSG	Secondary collimator
TCSPM	Secondary collimator, Mo coated MoGr and BPM
TCTPH	Tertiary collimator, horizontal, with BPM
TCTPV	Tertiary collimator, vertical, with BPM
TiN	Titanium-nitride
TMCI	Transverse Mode Coupling Instability

Glossary

β	Particle speed in unit of c
c	Speed of light
$\Delta\omega_c$	Coherent frequency shift
$E = \sqrt{p^2c^2 + m_0^2c^4}$	Particle total energy. E_0 designates the synchronous particle energy
ε	Beam emittance
$\varepsilon_n = \beta\gamma\varepsilon$	Normalized beam emittance
$\gamma = \frac{1}{\sqrt{1-\beta^2}}$	Particle Lorentz factor
m_0	Particle mass
N_b	Individual bunch intensity
$p_0 = \gamma m_0 v$	Synchronous particle momentum
$q = +e$	Particle charge, taken as one elementary charge
ρ	Beam bending radius
s	Particle curvilinear position
θ	Particle azimuthal angle along the ring
v	Particle velocity
$W_{x,y}$	Transverse wake field
$Z_{x,y}$	Transverse impedance
x, y, z	Position offsets from the synchronous particle
σ_z	RMS bunch length, in m
$\tau_b = \frac{4\sigma_z}{\beta c}$	Full bunch length, in s
δ_{skin}	Skin depth
μ_0, ϵ_0	Vacuum permeability and permittivity
ρ_c	Material resistivity
Z_0	Free space impedance
$\alpha_{x,y}, \beta_{x,y}, \gamma_{x,y}$	Horizontal/Vertical Twiss parameters
α_p	Momentum compaction factor
$(B\rho)$	Beam magnetic rigidity
$D_{x,y}$	Horizontal/Vertical dispersion function
$\eta = \alpha_p - \frac{1}{\gamma^2}$	Beam slippage factor
$\gamma_t = \sqrt{1/\alpha_p}$	Transition energy gamma
$\mu_{x,y}$	Horizontal/Vertical phase advance
ω_0	Beam angular revolution frequency
$\omega_{\beta_{x,y}} = Q_{x,y}\omega_0$	Angular betatron frequency
$\omega_{\xi_{x,y}} = Q'_{x,y}\omega_0$	Horizontal/Vertical angular chromaticity
$Q'_{x,y} = \xi_{x,y}Q_{x0,y0}$	Horizontal/Vertical beam chromaticity

$Q_{x0,y0}$	Unperturbed Horizontal/Vertical transverse tunes
$\xi_{x,y}$	Horizontal/Vertical beam chromaticity
h	RF cavity harmonic number
ω_s	Beam synchrotron angular frequency
$\phi_{RF} = h\omega t$	RF cavity phase
$Q_s = \frac{\omega_s}{\omega_0}$	Beam synchrotron tune
$T_s = \frac{1}{Q_s}$	Synchrotron period

Bibliography

1. O. Aberle et al. "Collimation for the LHC High Intensity Beams". *Proceedings of the 46th ICFA Advanced Beam Dynamics Workshop on High-Intensity and High-Brightness Hadron Beams*. Sept. 2010. URL: https://accelconf.web.cern.ch/accelconf/HB2010/papers/moib03.pdf.
2. C. Accetura. "Observations of Mo Coating from DTI, Politeknik and CERN Productions". Presentation at the Impedance Meeting. CERN, Geneva, Switzerland, 1 Feb. 2019. URL: https://indico.cern.ch/event/794863/.
3. D. Amorim. "Benchmarks between DELPHI and Recent TMCI Studies". Presentation at the 103rd HSC Section Meeting. CERN, Geneva, Switzerland, 6 Mar. 2017. URL: https://indico.cern.ch/event/615438/.
4. D. Amorim. "Comparison of Predictions of Current Impedance Model to Beam Based Measurements". Presentation at the 30th Impedance Working Group. CERN, Geneva, Switzerland, 5 Mar. 2019. URL: https://indico.cern.ch/event/802620/.
5. D. Amorim. "Hadron Collective Effects Studies for the LHC and FCC-hh Project". CERN-THESIS-2016-258. MA thesis. Grenoble, France: Institut Polytechnique de Grenoble, 24 Aug. 2016. URL: https://cds.cern.ch/record/2252474/.
6. D. Amorim. "Impedance Model and Beam Stability". Presentation at the FCC Week 2019. Crowne Plaza, Brussels, Belgium, 16 July 2019. URL: https://indico.cern.ch/event/727555/contributions/3452809/.
7. D. Amorim. "Study of the Destabilising Effet of the Resistive Transverse Damper with DELPHI". Presentation at the 104th HSC Section Meeting. CERN, Geneva, Switzerland, 27 Mar. 2017. URL: https://indico.cern.ch/event/625631/.
8. D. Amorim, S. Antipov, N. Biancacci, and B. Salvant, eds. *HL-LHC Impedance and Related Effects*. CERN-ACC-NOTE-2018-0087. Dec. 2018. URL: https://cds.cern.ch/record/2652401/.
9. D. Amorim, N. Biancacci, K. Li, and E. Métral. "Improvement of the Analytic Vlasov Solver DELPHI". *Proceedings of the 8th International Particle Accelerator Conference*. 2017. DOI: 10.18429/jacow-ipac2017-thpab005. URL: https://cds.cern.ch/record/2289471/.
10. D. Amorim et al. *MD 2490: Measurement of the TMCI Threshold at Top Energy*. Technical report. Geneva, Switzerland: CERN.
11. D. Amorim et al. *MD 3318: Impedance Contribution of Secondary and Tertiary Collimators*. Technical report. Geneva, Switzerland: CERN.
12. D. Amorim et al. "Single-Beam Transverse Collective Effects for HE-LHC". In: *ICFA Beam Dynamics Newsletter* 72, 2017, pp. 151–174. URL: https://cds.cern.ch/record/2315727/.

13. S. Antipov. "Effect of Surface Roughness on TCSPM Tune Shift Measurement". Presentation at the Impedance Meeting. CERN, Geneva, Switzerland, 20 Apr. 2018. URL: https://indico.cern.ch/event/721640/.

14. S. Antipov. "Impedance Measurements of TCSPM". Presentation at the 90th Collimation Upgrade Specification Meeting. CERN, Geneva, Switzerland, 28 July 2017. URL: https://indico.cern.ch/event/656269/.

15. S. Antipov. "Instability Growth Rates". Presentation at the HE-LHC Design Review. CERN, Geneva, Switzerland, 11 Dec. 2017. URL: https://indico.cern.ch/event/674475/contributions/2805075/.

16. S. Antipov. "Machine Impedance and HOM Power Update". Presentation at the 7th HL-LHC Collaboration Meeting. CIEMAT, Madrid, Spain, Nov. 2017. URL: https://indico.cern.ch/event/647714/contributions/2646112/attachments/1558633/2452416/Machine_impedance_and_HOM_power_update_7th_HL-LHC_Meeting.pdf.

17. S. Antipov. "Study of the Destabilising Effet of the Resistive Transverse Damper with NHTVS". Presentation at the 104th HSC Section Meeting. CERN, Geneva, Switzerland, 27 Mar. 2017. URL: https://indico.cern.ch/event/625631/.

18. S. A. Antipov, S. Nagaitsev, and A. Valishev. "Single-Particle Dynamics in a Nonlinear Accelerator Lattice: Attaining a Large Tune Spread with Octupoles in IOTA". In: *Journal of Instrumentation* 12, Apr. 2017, P04008. ISSN: 1748-0221. DOI: 10.1088/1748-0221/12/04/P04008. arXiv: 1604.08565. URL: http://arxiv.org/abs/1604.08565.

19. S. Antipov et al. "Low-Impedance Collimators for HL-LHC". *Proceedings of the 9th International Particle Accelerator Conference*. 2018. DOI: 10.18429/jacow-ipac2018-weygbe4. URL: http://jacow.org/ipac2018/doi/JACoW-IPAC2018-WEYGBE4.html.

20. G. Apollinari et al., eds. *High-Luminosity Large Hadron Collider (HL-LHC): Technical Design Report V. 0.1*. CERN Yellow Reports: Monographs. CERN, Geneva, Sept. 2017. DOI: 10.23731/CYRM-2017-004. URL: https://cds.cern.ch/record/2284929/.

21. S. Arsenyev and D. Schulte. "Broadband Impedance of Pumping Holes and Interconnects in the FCC-Hh Beamscreen". In: *Journal of Physics: Conference Series* 1067, Sept. 2018, p. 022003. ISSN: 1742-6588, 1742-6596. DOI: 10.1088/1742-6596/1067/2/022003. URL: http://stacks.iop.org/1742-6596/1067/i=2/a=022003?key=crossref.8c91e2b7c140878dd605a0e19f10ebd9.

22. S. Arsenyev, O. Boine-Frankenheim, and D. Schulte. "FCC-hh Transverse Impedance Budget". *Proceedings of the 9th International Particle Accelerator Conference*. Vancouver, Canada, 2018. DOI: 10.18429/jacow-ipac2018-mopmf029. URL: http://jacow.org/ipac2018/doi/JACoW-IPAC2018-MOPMF029.html.

23. R. Barlow et al. *Control of the MKQA Tuning and Aperture Kickers of the LHC*. Technical report CERN-TE-Note-2010-001. CERN, Dec. 2009. URL: https://cds.cern.ch/record/1232062/.

24. R. Bartolini and F. Schmidt. *A Computer Code for Frequency Analysis of Non-Linear Betatron Motion*. Technical report SL-Note-98-017-AP. CERN, 4 Feb. 1998. URL: https://cds.cern.ch/record/702438/.

25. H. Bartosik et al. "TMCI Thresholds for LHC Single Bunches in the CERN SPS and Comparison with Simulations". *Proceedings of the 5th International Particle Accelerator Conference*. Dresden, Germany, 16 June 2016. URL: https://cds.cern.ch/record/1742183/ (visited on 27/03/2019).

26. M. Benedikt and F. Zimmermann. "Proton Colliders at the Energy Frontier". In: *Nuclear Instruments and Methods in Physics Research Section A: Accelerators, Spectrometers, Detectors and Associated Equipment* 907, Nov. 2018, pp. 200–208. ISSN: 01689002. DOI: 10.1016/j.nima.2018.03.021. URL: https://linkinghub.elsevier.com/retrieve/pii/S0168900218303577.

27. M. Benedikt et al., eds. *Future Circular Collider*. Vol. Volume 3: The Hadron Collider (FCC-hh). CERN, Dec. 2018. URL: https://cds.cern.ch/record/2651300/.

28. M. Benedikt et al., eds. *Future Circular Collider*. Vol. Volume 2 : The Lepton Collider (FCC-ee). CERN, Dec. 2018. URL: https://cds.cern.ch/record/2651299/.

29. J. S. Berg and F. Ruggiero. "Stability Diagrams for Landau Damping". *Proceedings of the 17th Particle Accelerator Conference*. Vancouver, Canada, 11 June 1997. URL: https://cds.cern.ch/record/328011/.

30. A. Bertarelli. "Novel Materials for Collimators at LHC and Its Upgrades". *Proceedings of the 54th ICFA Advanced Beam Dynamics Workshop on High-Intensity, High Brightness and High Power Hadron Beams*. East-Lansing, USA, Nov. 2014. URL: https://cds.cern.ch/record/2112203/.

31. G. Besnier, J. L. Laclare, and C. Limborg. "Stability Criterion for Intense Electron Bunches in an Inductive Turbulent Regime". *AIP Conference Proceedings*. Vol. 367. AIP, Upton, NY, USA, 1996, pp. 204–214. DOI: 10.1063/1.50306. URL: http://aip.scitation.org/doi/abs/10.1063/1.50306.

32. G. Besnier. "Contribution à La Théorie de La Stabilité Des Oscillations Longitudinales d'un Faisceau Accéléré En Régime de Charge d'espace". PhD thesis. Rennes, France: Université de Rennes, 1978. URL: http://www.sudoc.fr/042205522.

33. G. Besnier, D. Brandt, and B. Zotter. "The Transverse Mode Coupling Instability in Large Storage Rings". In: *Particle Accelerators* 17, 1985, pp. 51–77. URL: https://cds.cern.ch/record/154782/.

34. G. Besnier and B. Zotter. *Oscillations Longitudinales d'une Distribution Elliptique, Couplées Par Un Résonateur : Application Au Calcul de l'allongement de Faisceaux Intenses*. Technical report CERN-ISR-TH-82-17. CERN, 1982. URL: https://cds.cern.ch/record/141457/.

35. N. Biancacci. "Improved Techniques of Impedance Calculation and Localization in Particle Accelerators". CERN-THESIS-2014-043. PhD thesis. Rome, Italy: Università degli Studi di Roma "La Sapienza", Apr. 2014. URL: https://cds.cern.ch/record/1704527.

36. N. Biancacci. "TCSG Impedance: Measurements vs. Predictions". Presentation at the 63rd LHC Beam Operation Committee. CERN, Geneva, Switzerland, 21 June 2016. URL: https://indico.cern.ch/event/543915/.

37. M. Brice. "FCC-hh Beam Screen Prototype". CERN-PHOTO-201604-074. Apr. 2016. URL: https://cds.cern.ch/record/2145407.

38. R. Bruce et al. "Reaching Record-Low β^* at the CERN Large Hadron Collider Using a Novel Scheme of Collimator Settings and Optics". In: *Nuclear Instruments and Methods in Physics Research Section A: Accelerators, Spectrometers, Detectors and Associated Equipment* 848, Mar. 2017, pp. 19–30. ISSN: 01689002. DOI: 10.1016/j.nima.2016.12.039. URL: https://linkinghub.elsevier.com/retrieve/pii/S0168900216313092.

39. O. Brüning et al., eds. *LHC Design Report*. CERN Yellow Reports: Monographs. CERN, Geneva, 2004. DOI: 10.5170/CERN-2004-003-V-1. URL: https://cds.cern.ch/record/782076/.

40. X. Buffat. "Transverse Instabilities". Presentation at the 9th LHC Operations Evian Workshop. Evian-les-Bains, France, 1 Feb. 2019. URL: https://indico.cern.ch/event/751857/contributions/3259409/.

41. X. Buffat et al. *Impact of the ADT on the Beam Quality with High Brightness Beams in Collision (MD2155)*. Technical report CERN-ACC-NOTE-2018-0005. CERN, Geneva, Switzerland: CERN, Feb. 2018. URL: https://cds.cern.ch/record/2304603/.

42. A. Burov. "Nested Head-Tail Vlasov Solver". In: *Physical Review Special Topics - Accelerators and Beams* 17:2, 25 Feb. 2014. ISSN: 1098-4402. DOI: 10.1103/PhysRevSTAB.17.021007. URL: https://link.aps.org/doi/10.1103/PhysRevSTAB.17.021007.

43. E. Carideo. "Effect of the Actual Taper Geometry on the Collimator Impedance and Octupole Thresholds of LHC and HL-LHC". Presentation at the 161st HSC Section Meeting. CERN, Geneva, Switzerland, 26 Nov. 2018. URL: https://indico.cern.ch/event/775773/.

44. E. Carideo. "Simulations of the LHC Collimators Geometric Impedance". Presentation at the Impedance Meeting. CERN, Geneva, Switzerland, 20 Apr. 2018. URL: https://indico.cern.ch/event/721640/.

45. F. Carra. "Status of TCSPM Prototype Production". Presentation at the 80th Collimation Upgrade Specification Meeting. CERN, Geneva, Switzerland, 9 Dec. 2016. URL: https://indico.cern.ch/event/591788/.

46. L. R. Carver et al. "Transverse Beam Instabilities in the Presence of Linear Coupling in the Large Hadron Collider". In: *Physical Review Accelerators and Beams* 21:4, Apr. 2018. ISSN: 2469-9888. DOI: 10.1103/PhysRevAccelBeams.21.044401. URL: https://link.aps.org/doi/10.1103/PhysRevAccelBeams.21.044401.

47. L. Carver et al. "Current Status of Instability Threshold Measurements in the LHC at 6.5 TeV". *Proceedings of the 7th International Particle Accelerator Conference*. Busan, South Korea, 2016. DOI: 10.18429/jacow-ipac2016-tupmw011. URL: https://cds.cern.ch/record/2207391/.

48. L. Carver et al. "Instability Observations in the Large Hadron Collider During Run 2". *Proceedings of the 9th International Particle Accelerator Conference*. 2018. DOI: 10.18429/jacow-ipac2018-thpaf057. URL: http://jacow.org/ipac2018/doi/JACoW-IPAC2018-THPAF057.html.

49. A. W. Chao. *Physics of Collective Beam Instabilities in High Energy Accelerators*. Wiley, New York, NY, 1993. ISBN: 0-471-55184-8. URL: http://www.slac.stanford.edu/~achao/wileybook.html.

50. Y.-H. Chin. *Hamiltonian Formulation For Transverse Bunched Beam Instabilities In The Presence Of Betatron Tune Spread*. Technical report CERN-SPS-85-9. CERN, May 1985. URL: https://cds.cern.ch/record/160217/.

51. Y.-H. Chin. *Transverse Mode Coupling Instabilities in the SPS*. Technical report CERN-SPS-85-2-DI-MST. CERN, 1985. URL: https://cds.cern.ch/record/157995/.

52. M. Conte and W. W. MacKay. *An Introduction to the Physics of Particle Accelerators*. 2nd edition. World Scientific, Singapore, 2008. ISBN: 978-981-277-961-8.

53. S. Dailler. "Cross Section of an LHC Dipole". Apr. 1999. URL: https://cds.cern.ch/record/842530/.

54. Dassault Systèmes. *CST Particle Studio*. 2019. URL: https://www.cst.com/products/cstps/.

55. L. Drøsdal. "LHC Injection Beam Quality During LHC Run I". PhD thesis. Oslo, Norway: Oslo University, 3 Mar. 2015. URL: https://cds.cern.ch/record/2118801/.

56. D. A. Edwards and M. J. Syphers. *An Introduction to the Physics of High Energy Accelerators*. Wiley, New York, NY, 1993. ISBN: 978-0-471-55163-8. DOI: 10.1002/9783527617272.

57. S. Furuseth et al. *MD3288: Instability Latency with Controlled Noise*. Technical report CERN-ACC-NOTE-2019-0011. CERN, Geneva, Switzerland: CERN, Mar. 2019. URL: https://cds.cern.ch/record/2670123/.

58. J. Gareyte, J.-P. Koutchouk, and F. Ruggiero. *Landau Damping Dynamic Aperture and Octupole in LHC*. Technical report LHC-Project-Report-91. Geneva: CERN, Feb. 1997. URL: https://cds.cern.ch/record/321824/.

59. J. Gareyte and F. J. Sacherer. "Head-Tail Type Instabilities in the CERN PS and Booster". *Proceedings of the 9th International Conference on High-Energy Accelerators*. SLAC, Stanford, USA, May 1974. URL: https://cds.cern.ch/record/322647/.

60. J.-P. Garnier. "Instabilités cohérentes dans les accélérateurs circulaires". PhD thesis. Grenoble, France: Institut National Polytechnique de Grenoble, 1987. URL: https://inis.iaea.org/collection/NCLCollectionStore/%5C_Public/20/012/20012271.pdf.

61. L. C. W. Group. *LHC Collimation Project Website*. 2018. URL: https://lhc-collimation-project.web.cern.ch/.

62. J. Guardia-Valenzuela. "Surface Observations of Mo Coated Samples". Presentation at the Impedance Meeting. CERN, Geneva, Switzerland, 20 Apr. 2018. URL: https://indico.cern.ch/event/721640/.

63. J. Guardia-Valenzuela et al. "Development and Properties of High Thermal Conductivity Molybdenum Carbide Graphite Composites". In: *Carbon* 135, Aug. 2018, pp. 72–84. ISSN: 00086223. DOI: 10.1016/j.carbon.2018.04.010. URL: https://linkinghub.elsevier.com/retrieve/pii/S0008622318303555.

64. W. Herr. "Introduction to Landau Damping". *Proceedings of the CERN Accelerator School Advanced Accelerator Physics Course*. CERN, Trondheim, Norway, 2014. DOI: 10.5170/CERN-2014-009.377. URL: https://cds.cern.ch/record/1982428/.

65. G. W. Hill. "On the Part of the Motion of the Lunar Perigee Which Is a Function of the Mean Motions of the Sun and Moon". In: *Acta Mathematica* 8, 1886, pp. 1–36. ISSN: 0001-5962. DOI: 10.1007/BF02417081. URL: http://projecteuclid.org/euclid.acta/1485888530/.

66. W. Höfle. "Transverse Feedback in the HL-LHC Era". Presentation at the 5th Joint HiLumi LHC-LARP Meeting. CERN, Geneva, Switzerland, 28 Oct. 2015. URL: https://indico.cern.ch/event/400665/.

67. A. Hofmann and G. Muelhaupt. "Observation of the Head-Tail Instability at the Cambridge Electron Accelerator". *Proceedings of the 8th International Conference on High-Energy Accelerators*. Sept. 1971, pp. 306–307. URL: https://inspirehep.net/record/73320/.

68. A. Jeff et al. "First Results of the LHC Longitudinal Density Monitor". In: *Nuclear Instruments and Methods in Physics Research Section A: Accelerators, Spectrometers, Detectors and Associated Equipment* 659:1, Dec. 2011, pp. 549–556. ISSN: 01689002. DOI: 10.1016/j.nima.2011.08.055. URL: https://linkinghub.elsevier.com/retrieve/pii/S0168900211017165.

69. R. D. Kohaupt. *Simplified Presentation of Head-Tail Turbulence*. Technical report DESY M-80/19. DESY, Oct. 1980. URL: https://inspirehep.net/record/156772/.

70. S. S. Kurennoy. "Impedance Issues for LHC Beam Screen". In: *Particle Accelerators* 50, Jan. 1995, pp. 167–175. URL: https://cds.cern.ch/record/1120216/.

71. A. Kurtulus. "Procedure for Coating Measurements with H011 Cavity and Pressure Effect". Presentation at the Impedance Meeting. CERN, Geneva, Switzerland, 1 Feb. 2019. URL: https://indico.cern.ch/event/794863/.

72. J.-L. Laclare. "Bunched Beam Coherent Instabilities". *Proceedings of the CERN Accelerator School on Accelerator Physics*. CERN, Oxford, UK, 1987. DOI: 10.5170/CERN-1987-003-V-1.264. URL: http://cds.cern.ch/record/611596/.

73. L. Landau. "On the Vibrations of the Electronic Plasma". In: *Journal of Physics USSR* 10, 1946, pp. 25–34.

74. A. Latina. "Introduction to Transverse Dynamics". Course at the Joint Universties Accelerator School. Archamps, France, Jan. 2019. URL: https://indico.cern.ch/event/779575/.

75. S. Lee. *Accelerator Physics*. 3rd edition. World Scientific, Singapore, 2012. ISBN: 978-981-4374-94-1.

76. T. Levens, K. Łasocha, and T. Lefèvre. "Recent Developments for Instability Monitoring at the LHC". *Proceedings of the International Beam Instrumentation Conference*. Barcelona, Spain, Sept. 2016, pp. 852–855. DOI: 10.18429/JACoW-IBIC2016-THAL02. URL: https://cds.cern.ch/record/2313358/.

77. LHC Collimation Working Group. *Impedance Inputs*. 2017. URL: https://lhc-collimation-upgrade-spec.web.cern.ch/lhc-collimation-upgrade-spec/Impedance.php.

78. K. Li, G. Rumolo, and H. Bartosik. "Introduction to PyHEADTAIL". Course at the US Particle Accelerator School. Hampton, VA, USA, Jan. 2015. URL: http://kli.web.cern.ch/kli/.

79. K. Li, G. Rumolo, and H. Bartosik. "Wake Fields and Impedances". Course at the US Particle Accelerator School. Hampton, VA, USA, Jan. 2015. URL: http://kli.web.cern.ch/kli/.

80. P. Loïez, P. Rakosy, and L. Guiraud. "Beam Screens for the LHC Beam Pipes". May 1997. URL: https://cds.cern.ch/record/39110/.

81. M. Lonza. "Multi-Bunch Feedback Systems". *Proceedings of the CERN Accelerator School on Digital Signal Processing*. CERN, 2008. DOI: 10.5170/CERN-2008-003.285. URL: http://cds.cern.ch/record/1100539/.

82. G. Mazzacano. "Update on Mo Coating Resistivity Measurements on Different Substrates". Presentation at the Impedance Meeting. CERN, Geneva, Switzerland, 20 Apr. 2018. URL: https://indico.cern.ch/event/721640/.

83. A. Mereghetti et al. *MD 1875: Impedance Contribution of Single IR7 Collimators*. Technical report. Geneva, Switzerland: CERN.

84. E. Métral. "Destabilising Effect of the Resistive Transverse Damper". Presentation at the 102nd HSC Section Meeting. CERN, Geneva, Switzerland, 10 Feb. 2017. URL: https://indico.cern.ch/event/612111/.

85. E. Métral. "Effect of Space Charge on the CERN LHC and SPS Transverse Instabilities: Simulations vs. Measurements". Presentation at the Space Charge 2017 Workshop. TU Darmstadt, Darmstadt, Germany, Oct. 2017. URL: https://indico.gsi.de/event/5600/.

86. E. Métral. *Landau Damping for TMCI: with vs. without Transverse Damper*. Technical report CERN-ACC-NOTE-2019-0018. CERN, Geneva, Switzerland: CERN, May 2019. URL: https://cds.cern.ch/record/2674776.

87. E. Métral. "Longitudinal Dynamics". Course at the Joint Universties Accelerator School. Archamps, France, Jan. 2019. URL: https://indico.cern.ch/event/779575/.

88. E. Métral. "TMCI Far above the Intensity Threshold". Presentation at the LIS Meeting. CERN, Geneva, Switzerland, 1 Dec. 2008. URL: https://espace.cern.ch/be-dep-workspace/abp/HSC/Meetings/TMCIFarAboveTheIntensityThreshold_LIS_01-12-08.pdf.

89. E. Métral and D. Möhl. "Transition Crossing". In: *Fifty Years of the CERN Proton Synchrotron: Volume 1*. CERN Yellow Reports: Monographs. CERN, Geneva, Switzerland, 2011. DOI: 10.5170/CERN-2011-004. URL: https://cds.cern.ch/record/1359959/.

90. E. Métral and G. Rumolo. "Wake Fields and Impedances". Course at the US Particle Accelerator School. Albuquerque, NM, USA, June 2009. URL: https://emetral.web.cern.ch/emetral/USPAS09course/WakeFieldsAndImpedances.pdf.

91. E. Métral et al. "Destabilising Effect of the LHC Transverse Damper". *Proceedings of the 9th International Particle Accelerator Conference*. Vancouver, Canada, 2018. DOI: 10.18429/JACoW-IPAC2018-THPAF048. URL: https://cds.cern.ch/record/2648696/.

92. E. Métral et al. "Space Charge and Transverse Instabilities at the CERN SPS and LHC". *Proceedings of the 13th International Computational Accelerator Physics Conference*. Oct. 2018. DOI: 10.18429/jacow-icap2018-supag01. URL: http://jacow.org/icap2018/doi/JACoW-ICAP2018-SUPAG01.html.

93. E. Métral et al. *Summary of the Half-Day Internal Review of LHC Performance Limitations Linked to Transverse Collective Effects) during Run II*. Technical report CERN-ACC-NOTE-2017-0005. CERN, 29 Nov. 2016. URL: https://cds.cern.ch/record/2242249/.

94. E. Métral et al. *Update of the HL-LHC Operational Scenarios for Proton Operation*. Technical report CERN-ACC-NOTE-2018-0002. CERN, Jan. 2018. URL: https://cds.cern.ch/record/2301292/files/CERN-ACC-NOTE-2018-0002.pdf.

95. M. Migliorati, E. Belli, and M. Zobov. "Impact of the Resistive Wall Impedance on Beam Dynamics in the Future Circular e^+ e^- Collider". In: *Physical Review Accelerators and Beams* 21:4, Apr. 2018. ISSN: 2469-9888. DOI: 10.1103/PhysRevAccelBeams.21.041001. URL: https://link.aps.org/doi/10.1103/PhysRevAccelBeams.21.041001.

96. B. Mikulec et al. "LHC Beams from the CERN PS Booster". *Proceedings of the 23rd Particle Accelerator Conference*. Vancouver, Canada, May 2009. URL: http://accelconf.web.cern.ch/AccelConf/PAC2009/papers/tu6pfp086.pdf.

97. E. Mobs. "The CERN Accelerator Complex - August 2018". OPEN-PHO-ACCEL-2018-005. Aug. 2018. URL: https://cds.cern.ch/record/2636343/.

98. M. Morrone. "FCC-hh Beam Screen Design". Presentation at the FCC week 2019. Crowne Plaza, Brussels, Belgium, 26 June 2019. URL: https://indico.cern.ch/event/727555/contributions/3452779/.

99. A. Mostacci. "Beam-Wall Interaction in the LHC Liner". CERN-THESIS-2001-014. PhD thesis. Rome, Italy: Universita degli Studi di Roma "La Sapienza", 2001. URL: http://weblib.cern.ch/abstract?CERN-THESIS-2001-014.

100. N. Mounet. "DELPHI: An Analytic Vlasov Solver for Impedance-Driven Modes". 7 May 2014. URL: https://cds.cern.ch/record/1954277/ (visited on 27/03/2019).

101. N. Mounet. "Status of the Impedance-Damper Model". Presentation at the LHC Beam Operation Committee. CERN, Geneva, Switzerland, 14 Aug. 2012. URL: https://lhc-beam-operation-committee.web.cern.ch/lhc-beam-operation-committee/minutes/Meeting46-14_08_2012/damper_wake_model_Aug14_2012.pdf.

102. N. Mounet. "The Good, the Bad and the Ugly –a DELPHI Update". Presentation at the 181st HSC Section Meeting. CERN, Geneva, Switzerland, 1 July 2019. URL: https://indico.cern.ch/event/827061/.

103. N. Mounet. "The LHC Transverse Coupled-Bunch Instability". PhD thesis. Lausanne, Switzerland: École Polytechnique Fédérale de Lausanne, Mar. 2012. URL: https://cds.cern.ch/record/1451296/files/CERN-THESIS-2012-055.pdf.

104. N. Nakamura. "Effects of Longitudinal and Transverse Resistive-Wall Wakefields on ERLS". *Proceedings of ERL09*. Ithaca, New York, USA, 2009. URL: http://accelconf.web.cern.ch/AccelConf/ERL2009/papers/js205.pdf.

105. K.-Y. Ng. *Physics of Intensity Dependent Beam Instabilities*. World Scientific, Hoboken, NJ, 2006.

106. A. Oeftiger. "Single-Bunch Stability With Direct Space Charge". Poster at the ICFA mini-workshop on Impedances and Beam Instabilities in Particle Accelerators. Benevento, Italy, Sept. 2017. URL: https://cds.cern.ch/record/2290575/.

107. OMC Team. *Beta-Beat.src: Many Scripts and Files for Optics Correction Scheme*. 30 Apr. 2019. URL: https://github.com/pylhc/Beta-Beat.src.

108. L. Palumbo, V. G. Vaccaro, and M. Zobov. "Wake Fields and Impedance". In: *Proceedings of the CERN Accelerator School 5th Advanced Accelerator Physics Course*. CERN, Rhodes, Greece, 1994. DOI: 10.5170/CERN-1995-006.331. URL: http://cds.cern.ch/record/276437/.

109. S. Papadopoulou et al. "Modelling and Measurements of Bunch Profiles at the LHC". In: *Journal of Physics: Conference Series* 874, July 2017, p. 012008. ISSN: 1742-6588, 1742-6596. DOI: 10.1088/1742-6596/874/1/012008. URL: http://stacks.iop.org/1742-6596/874/i=1/a=012008?key=crossref.1b160fc4fda440b74094ee34b18b2960.

110. K. Papke and A. Grudiev. "Design of a RF Quadrupole Resonator for Landau Damping in HL-LHC". *Proceedings of 18th International Conference on RF Superconductivity*. Lanzhou, China, 2018. DOI: 10.18429/jacow-srf2017-mopb004. URL: http://jacow.org/srf2017/doi/JACoW-SRF2017-MOPB004.html.

111. C. Pellegrini. "On a New Instability in Electron-Positron Storage Rings (The Head-Tail Effect)". In: *Il Nuovo Cimento A Series 10* 64:2, Nov. 1969, pp. 447–473. ISSN: 0369-3546, 1826-9869. DOI: 10.1007/BF02754905. URL: http://link.springer.com/10.1007/BF02754905.

112. F. J. Perez Rodriguez, P. Chiggiato, C. Garion, and J. Fernandez Topham. *Preliminary Beam Screen and Beam Pipe Engineering Design: Deliverable D4.3*. Technical report CERN-ACC-2019-0023. Geneva: CERN, Oct. 2017. URL: https://cds.cern.ch/record/2655296.

113. PyHEADTAIL development team. *PyHEADTAIL*. 2018. URL: https://github.com/PyCOMPLETE/PyHEADTAIL.

114. S. Redaelli. "Beam Cleaning and Collimation Systems". Course at the Joint Accelerator School on Beam Loss and Accelerator Protection. Newport Beach, CA, USA, Nov. 2014. URL: http://uspas.fnal.gov/.

115. S. Redaelli. "Beam Cleaning and Collimation Systems". *Proceedings of the Joint International Accelerator School on Beam Loss and Accelerator Protection*. 2016. DOI: 10.5170/CERN-2016-002.403. URL: https://e-publishing.cern.ch/index.php/CYR/article/view/243.

116. S. Redaelli. "Update on Collimation Layouts and Results from Operational Prototypes". Presentation at the 7th HL-LHC Collaboration Meeting. CIEMAT, Madrid, Spain, Nov. 2017. URL: https://indico.cern.ch/event/647714/contributions/2633146/attachments/1558620/2452818/SRedaelli_2017-11-15.pdf.

117. S. Redaelli et al. *Staged Implementation of Low-Impedance Collimation in IR7: Plans for LS2*. Technical report CERN-ACC-NOTE-2019-0001. CERN, Geneva, Switzerland: CERN, Jan. 2019. URL: https://cds.cern.ch/record/2654779/.

118. S. Redaelli et al. "Collimation Upgrades for HL-LHC". *Proceedings of the 2014 LHC Performance Workshop*. CERN, Geneva, Switzerland, 2015. DOI: 10.5170/CERN-2015-002.225. URL: http://cds.cern.ch/record/2031211/.

119. C. Roderick, L. Burdzanowski, and G. Kruk. "The CERN Accelerator Logging Service - 10 Years in Operation: A Look at the Past, Present and Future". *Proceedings of the 14th International Conference on Accelerator and Large Experimental Physics Control Systems*. Oct. 2013. URL: https://cds.cern.ch/record/1611082/.

120. A. Romano et al. “Electron Cloud Buildup Driving Spontaneous Vertical Instabilities of Stored Beams in the Large Hadron Collider”. In: *Physical Review Accelerators and Beams* 21:6, June 2018. ISSN: 2469-9888. DOI: 10.1103/PhysRevAccelBeams.21.061002. URL: https://link.aps.org/doi/10.1103/PhysRevAccelBeams.21.061002.

121. J. R. Rumble, ed. *Electrical Resistivity of Pure Metals*. 99th Edition (Internet Version 2018). CRC Press/Taylor & Francis, Boca Raton, FL., 2018. ISBN: 978-1-138-56163-2.

122. F. J. Sacherer. “A Longitudinal Stability Criterion for Bunched Beams”. In: *IEEE Transactions on Nuclear Science* 20:3, 1973, pp. 825–829. ISSN: 0018-9499. DOI: 10.1109/TNS.1973.4327254. URL: http://ieeexplore.ieee.org/document/4327254/.

123. F. J. Sacherer. “Bunch Lengthening and Microwave Instability”. In: *IEEE Transactions on Nuclear Science* 24:3, June 1977, pp. 1393–1395. ISSN: 0018-9499, 1558-1578. DOI: 10.1109/TNS.1977.4328955. URL: http://ieeexplore.ieee.org/document/4328955/.

124. F. J. Sacherer. “Methods for Computing Bunched-Beam Instabilities”. *Proceedings of the 1st International School of Particle Accelerators "Ettore Majorana"*. CERN-SI-BR-72-5. Sept. 1972. URL: https://cds.cern.ch/record/322545/.

125. F. J. Sacherer. “Transverse - Part II: Bunched Beams”. *Proceedings of the 1st International School of Particle Accelerators "Ettore Majorana"*. 1st International School of Particle Accelerators "Ettore Majorana" CERN-77-13. Erice, Italy, 1977, pp. 198–218. DOI: 10.5170/CERN-1977-013.198. URL: https://cds.cern.ch/record/864422/.

126. B. Salvachua et al. “LHC Collimation Cleaning and Operation Outlook”. *Proceedings of the 4th LHC Operations Evian Workshop*. Evian-les-Bains, France, Dec. 2012. URL: https://cds.cern.ch/record/2302435/.

127. B. Salvant. “Impedance Model of the CERN SPS and Aspects of LHC Single-Bunch Stability”. PhD thesis. Lausanne, Switzerland: École Polytechnique Fédérale de Lausanne, 4 Mar. 2010. URL: https://cds.cern.ch/record/1274254/.

128. M. Sands. *The Head-Tail Effect: An Instability Mechanism In Storage Rings*. Technical report SLAC-TN-69-008. SLAC, Mar. 1969. URL: https://inspirehep.net/record/54938.

129. M. Schenk, A. Grudiev, K. Li, and K. Papke. “Analysis of Transverse Beam Stabilization with Radio Frequency Quadrupoles”. In: *Physical Review Accelerators and Beams* 20:10, Oct. 2017. DOI: 10.1103/PhysRevAccelBeams.20.104402. URL: https://link.aps.org/doi/10.1103/PhysRevAccelBeams.20.104402.

130. M. Schenk. “A Novel Approach to Landau Damping of Transverse Collective Instabilities in Future Hadron Colliders”. PhD thesis. École Polytechnique Fédérale de Lausanne, Feb. 2019. URL: https://cds.cern.ch/record/2665819.

131. M. Schenk. “Beam Dynamics Simulations With The Pyheadtail And Pyecloud Macroparticle Codes”. Seminar presentation. KEK, Tsukuba, Japan, 5 July 2017. URL: https://www2.kek.jp/accl/seminar/file/PyHEADTAIL_PyECLOUD_2.pdf.

132. V. D. Shiltsev. *Electron Lenses for Super-Colliders*. Particle Acceleration and Detection. Springer, New York, 2016. 188 pp. ISBN: 978-1-4939-3315-0.

133. V. Shiltsev, Y. Alexahin, A. Burov, and A. Valishev. "Landau Damping of Beam Instabilities by Electron Lenses". In: *Physical Review Letters* 119:13, Sept. 2017. ISSN: 0031-9007, 1079-7114. DOI: 10.1103/PhysRevLett.119.134802. URL: https://link.aps.org/doi/10.1103/PhysRevLett.119.134802 (visited on 12/07/2019).

134. V. Shiltsev et al. "Tevatron Electron Lenses: Design and Operation". In: *Physical Review Special Topics Accelerators and Beams* 11, 10 Oct. 2008. DOI: 10.1103/physrevstab.11.103501. URL: http://arxiv.org/abs/0808.1542.

135. M. Solfaroli Camillocci. "LHC Nominal Cycle". *Proceedings of the 6th LHC Operations Evian Workshop*. CERN, Evian-les-Bains, France, 15 Dec. 2015. URL: https://cds.cern.ch/record/2294513/.

136. R. J. Steinhagen. "Tune and Chromaticity Diagnostics". *Proceedings of the CERN Accelerator School on Beam Diagnostics*. CERN, 2009. DOI: 10.5170/CERN-2009-005.317. URL: http://cds.cern.ch/record/1213281/.

137. G. Stupakov. "Wakefields and Collective Beam Instabilities". Course at the US Particle Accelerator School. Northern Illinois University, IL, USA, Jan. 2019. URL: http://uspas.fnal.gov/materials/19Knoxville/Knoxville-Wakefields.shtml.

138. R. Talman. "The Influence of Finite Synchrotron Oscillation Frequency on the Transverse Head-Tail Effect". In: *Nuclear Instruments and Methods in Physics Research* 193:3, Mar. 1982, pp. 423–435. ISSN: 01675087. DOI: 10.1016/0029-554X(82)90234-8. URL: https://linkinghub.elsevier.com/retrieve/pii/0029554X82902348.

139. C. Tambasco. "Update on BTF Measurements and Understanding". Presentation at the 163rd HSC section meeting. CERN, Geneva, Switzerland, 10 Dec. 2018. URL: https://indico.cern.ch/event/778893/.

140. C. Tambasco et al. "Landau Damping Studies for the FCC: Octupole Magnets, Electron Lens and Beam-Beam Effects". *Proceedings of the 9th International Particle Accelerator Conference*. Vancouver, Canada, 2018. DOI: 10.18429/jacow-ipac2018-thpaf074. URL: http://jacow.org/ipac2018/doi/JACoW-IPAC2018-THPAF074.html.

141. The CLIC collaboration. "The Compact Linear Collider (CLIC) - 2018 Summary Report". In: *CERN Yellow Reports: Monographs*, 2018. DOI: 10.23731/CYRM-2018-002.

142. D. Tommasini. *The PS Booster, PS and SPS Magnets for the next 25 Years*. Technical report CERN-TE-Note-2010-003. CERN, 18 Jan. 2010. URL: https://cds.cern.ch/record/1233948/.

143. Transverse Impedance and Stability team. *IRIS Repository*. 2018. URL: https://gitlab.cern.ch/IRIS.

144. D. Valuch and M. Soderen. "ADT ObsBox Data Acquisition". Presentation at the 79th LHC Beam Operation Committee. CERN, Geneva, Switzerland, 13 June 2017. URL: https://indico.cern.ch/event/645898/.

145. A. Vlasov. "On the Kinetic Theory of an Assembly of Particles with Collective Interaction". In: *Journal of Physics USSR* 9:1, 1945, pp. 25–40.

146. J. Wenninger. "LHC Parameter Reproducibility". *Proceedings of the 7th LHC Operations Evian Workshop*. Evian-les-Bains, France, 2016. URL: https://cds.cern.ch/record/2293510/.

147. J. Wenninger. "Machine Protection and Operation for LHC". *Proceedings of the Joint International Accelerator School on Beam Loss and Accelerator Protection*. Jan. 2016. DOI: 10.5170/CERN-2016-002.377. arXiv: 1608.03113. URL: http://arxiv.org/abs/1608.03113.

148. H. Wiedemann. *Particle Accelerator Physics*. 4th edition. Springer, Berlin, 2015. ISBN: 978-3-319-18316-9. DOI: 10.1007/978-3-319-18317-6.

149. A. Wolski. "Linear Dynamics in Particle Accelerators". Course at the University of Liverpool. Liverpool, UK, Nov. 2012. URL: http://pcwww.liv.ac.uk/~awolski/.

150. A. Wolski and D. Newton. "Design of Electron Storage and Damping Rings". Course at the US Particle Accelerator School. Fort Collins, Colorado, USA, June 2013. URL: http://uspas.fnal.gov/materials/13CSU/Lecture6.pdf.

151. K. Yokoya. "Resistive Wall Impedance of Beam Pipes of General Cross Section". In: *Particle Accelerators* 41, Apr. 1993, pp. 221–248. URL: https://cds.cern.ch/record/248630/.

152. C. Zannini, K. Li, and G. Rumolo. "Effects of an Asymmetric Chamber on the Beam Coupling Impedance". *Proceedings of the 3rd International Particle Accelerator Conference*. New Orleans, LA, USA, May 2012. URL: https://cds.cern.ch/record/1451303/.

153. F. Zimmermann et al., eds. *Future Circular Collider*. Vol. Volume 4 : The High-Energy LHC (HE-LHC). CERN, Dec. 2018. URL: https://cds.cern.ch/record/2651305/.

154. B. Zotter. *Impedances and Wakes in High-Energy Particle Accelerators*. World Scientific, Singapore, 1998. ISBN: 978-981-02-2626-8.